Identification and Quantitative Classification of Europa's Microfeatures: Implications for Microfeature Formation Models and the Europa Clipper Flagship Mission

by

Jessica Lynn Noviello

A Dissertation Presented in Partial Fulfillment
of the Requirements for the Degree
Doctor of Philosophy

Approved June 2019 by the
Graduate Supervisory Committee:

Alyssa R. Rhoden, Co-Chair
Philip Christensen, Co-Chair
David A. Williams
Mark Robinson
Paul Scowen

ARIZONA STATE UNIVERSITY

August 2019

ABSTRACT

Jupiter's moon Europa is an active target of research because of its unique geology and its potential for habitability. Europa's icy chaos disrupts and transforms the previous terrain, suggesting melting is involved. Chaos occurs alongside several types of endogenic surface features. These microfeatures are under <100 km^2 in area and include uplifts and domes, pits, spots, and hybrid features. The distribution of microfeatures is known in the ~10% of the Europa's surface that are covered by the regional mosaics ("RegMaps"). The efforts to connect microfeature formation to any kind of heat transport in Europa are confounded because microfeatures are difficult to identify outside of RegMaps because of low image resolutions. Finding microfeatures outside of RegMaps would provide new observational constraints for microfeature formation models.

First, I mapped microfeatures across four of Europa's RegMaps and validated them against other mapping datasets. Microchaos features are the most numerous, followed by pits, domes, then hybrids. Spots are the least common features, and the smallest. Next, I mapped features in low-resolution images that covered the E15RegMap01 area to determine error rates and sources of omission or misclassification for features mapped in low-resolution images. Of all features originally mapped in the RegMap, pits and domes were the least likely to be re-mapped or positively identified (24.2% and 5%, respectively). Chaos, spots, and hybrids were accurately classified over 70% of the time. Quantitatively classifying these features using discriminant function analysis yielded comparable values of accuracy when compared to a human mapper. Finally, nearest-neighbor clustering analyses were used to show that pits are clustered in all regions, while chaos, domes, and hybrids vary in terms of their spatial clustering.

This work suggests that the most likely processes for microfeature formations is either the evolution of liquid water sills within Europa's ice shell or cryovolcanism. Future work extending to more areas outside of the RegMaps can further refine microfeature formation models. The detection of liquid water at or near the surface is a major goal of multiple upcoming Europa missions; this work provides predictions that can be directly tested by these missions to maximize their scientific return.

ACKNOWLEDGMENTS

There are many people I want to thank who have befriended, loved, mentored, and guided me through graduate school and all that came before. Your time, affection, gifts, letters, and laughter gave me happy memories that I will hold onto forever. Thanking you does not seem like enough repayment.

To those who came before, for their wisdom and their patience when I needed to lean on them: Kimberly Ward-Duong, Amber Keske, Danika Wellington, Nathan Williams, Julie Mitchell, Michael Veto, Mark Neveu, Svetlana Skolyar-Neveu, Heather Meyer, Cameron Mercer, Viranga Perera, Amanda Truitt, Alex Spacek, Jacqueline Monkiewicz, Piyanat "Boom" Kittiwisit, Thomas Mozdzen, Divya Allu Peddinti, Kristen Bennett, Brett Carr, Matt Walker, Lynnae Quick, Ali Nabivizadeh, and Patrick Gasda.

To those who will soon finish their own work and move on to great things, for your support, your inclusion, and our adventures together: Alyssa Anderson, Nari Miller, Enzo Cataldo, Sean Czarnecki, Travis Gabriel, Lena Heffern, Daniel Dunlap, Mariah Heck, Samantha Jacob, Hannah Kerner, Jacob Adler, Alexandra Pye, Joel Leonard, Abigail Weibel, Srinidhi Ravi, Soumya Ray, Thomas Ruberto, Melissa Sedler, Genevieve Studer-Ellis, Stephen West, Kristen Whitney, Alana Williams, Edward Buie II, Sean Peters, Theresa Fisher, Jonathan Ho, Rhonda Holton, Marisol Juarez Rivera, Laurence Tognetti, Scott Dickenshied, Jon Hill, the amazingly talented software developer Paul F. Wren, Hema Werner, and all my friends not listed here.

To the people who served as leaders with me on SESE Graduate Council, for your friendship, teamwork, and all the work you do that no one praises: Meghan Guild, Kara

Brugman, John Christoph, Kevin Hubbard, Crystyl Fudge, Lucia Perez, Nivedita Mahesh, Megan M. Miller, Gregory Vance, and Angel Garcia-Romero.

To the colleagues in the Ronald Greeley Center for Planetary Studies, for your knowledge, friendship, and patience: Amy Zink, David Nelson, and Kyle Guzman.

To the L'SPACE team, for showing me the difference that education and opportunity can make to everyone and allowing me to share it: Sheri Klug-Boonstra, Dann Garcia, Garrett Nez, Katherine Kretke, and Sanlyn Buxner.

To all the students I have taught, either in person during the lab courses or through the L'SPACE program, for the joy and experience you brought me when I taught you, with particular thanks to: Jessica Maschino, Angelica Berner, the SEDS Chapter at Arizona State University, Joe Holland, and Alicia Hyatt.

To the staff of the School of Earth and Space Exploration at Arizona State University, for all the work you do to keep SESE running and for being the people I could rely on in stressful moments: Becca Dial, Camelia Skiba, Meg Hufford, Karin Valentine, Ernest Cisneros, Chris Skiba, Ric Alling, Sue Selkirk, and Tess Calvert.

To my teachers outside of the classroom, for giving me the knowledge, space, and encouragement for me to discover who I am: Marc Huisken, Steve Desch, Christy Till, Heather Throop, Sherman Mohler, Jenny Borst, Benji Paysnoe, Raphael D'Sa, the Arizona chapter of the Southwest Paleontological Society, the ASU PokémonGo Community, and Grace Gee and Cola. You are the friends I never expected to have.

To those who advised me, for your patience, humor, feedback, support, and teachings: Alyssa Rhoden, David A. Williams, Mark Robinson, Phil Christensen, Paul Scowen, Erik Asphaug, Jim Bell, Michael Edwards, Leona Aiken, Olivier Barnouin,

Carolyn Ernst, Lindy Elkins-Tanton, David B. Weishampel, Michael Nolan, Deborah Savage, and all my professors at Johns Hopkins and at Arizona State University.

To all the women who have served on the National Board of the Delta Xi Phi Multicultural Sorority, Inc., especially Nikita De Barros, Vicki Nelson, Emily Mennenga, Monica Longoria, Ivy Sanchez, Ambrosia Solis, and Kaitlin DeFoor for your example, empathy, and support in everything DXP and beyond since 2016.

To the family I chose, for your belief in me and for your strength when I had none of my own: Josie Fuschetto, Laura Cignarale, Rachel LeCover, Jenny Verniero, Kellen McGee, Eddie Brooks, Ji-Yeung Kim, Daniel Berman, Sierra Ferguson, Vishaal Singh, Kyle Mohr, Alyssa Sherry, Aleisha Johnson, Stephanie Holaday, Anna Brunner, Hannah Shamloo, Zachary Torrano, Monte McRae, Madeline Marquadt, Emilie Dunham, Kristen Hidalgo-Munroy, Liza Kurtz, Christina Forbes, Eric Wan, Ami Cox, and David Shear.

To the family I was born to: my brother Donald, my sister Kristen, my mother Regina, my father Don, and my uncles, aunts, cousins, and grandparents. Thank you for motivating me to seek out my own knowledge and for always pushing me.

This research was conducted in partial fulfillment of the requirements for the Degree of Doctor of Philosophy in the School of Earth and Space Exploration at Arizona State University, Tempe, Arizona. Primary financial support was provided by NASA grants: COLDTech grant NNX17AF70G and Solar System Workings grant NNX15AH91G. Additional support was provided by the School of Earth and Space Exploration as part of a teaching assistantship, and by the Lucy Trojan Asteroid Mission through the Lucy Student Pipeline and Competency Enabler (L'SPACE) program.

TABLE OF CONTENTS

Page

CHAPTER Page

Page

APPENDIX

LIST OF TABLES

Table Page

LIST OF FIGURES

Figure Page

CHAPTER 1

INTRODUCTION

It is late on the night of January 8, 1610. Galileo Galilei is peering through his *occiale*, a telescopic instrument of his own creation. He had observed Jupiter the night before and made detailed notes about its position relative to the stars in the sky around it. This night, however, three of the stars had changed position from the night before. In his own words, Galileo was "seeing the same three 'stars' as the previous night but [was] puzzled by the apparent motion of Jupiter relative to them." Over the next eight days he continued to observe these wandering stars, and even discovered a fourth one that appeared to orbit Jupiter. On March 13, 1610, he published his observations in his brief paper *Sidereus Nuncius*, the "Starry Message." The middle "star" Galileo had first observed was the first European observation of the moon known today as Europa. The four moons observed were named Io, Europa, Ganymede, and Callisto; today that group is collectively called the Galilean satellites after the man credited with their discovery.

Four hundred years later, humanity is still fascinated by Jupiter's moons, particularly Europa. Though multiple missions have examined its surface, significant questions remain about how it formed, how it has evolved, how its geologic features were (or are) created, and what its capacity for extraterrestrial life might be. This work will present new evidence about Europa's geology and address these questions to provide more information to the planetary community and help prepare for the upcoming NASA missions.

1.1 Previous Spacecraft Exploration of Europa

The first spacecraft image of Europa was taken in December 1973 by the photopolarimeter instrument on the *Pioneer 10* mission (Figure 1-1; Fimmel et al., 1974; Fimmel et al., 1980). Though the image resolution was coarse (160 km/pix), the images showed that Europa's surface was heterogeneous in albedo. The *Pioneer 11* mission followed in 1974. One of the biggest findings of the Pioneer missions was that the surface of Europa is dominated by water ice (Fanale et al., 1977; Cassen et al., 1979; Cassen et al., 1980; Clark, 1980). These missions sent enough data back to intrigue planetary scientists and led to proposals to build future missions to target Europa for further investigation.

The *Voyager 1* and *2* missions, both launched in 1977, acquired the highest-resolution images up to that time of Europa. These images revealed a high-albedo surface with long linear ridges that scarred the surface and a surprisingly low number of craters (Lucchita and Soderblom, 1982; Alexander et al., 2009). Curved ridges called cycloids were also observed, and Europa is still the only known planetary body that has these geologic features. The bright surface, the crispness of the ridges, and the lack of craters suggested that the surface was geologically young (Lucchita and Soderblom, 1982). Modeling work (Zahnle et al., 2003; Bierhaus et al., 2009) has produced estimates that the surface is between 40 and 90 million years old, making it one of the youngest surfaces in the solar system. Lucchita and Soderblom (1982) also noted the presence of dark spots scattered on Europa's surface and named them *lenticulae* after the Latin word for freckles. Debates began regarding the origin of these linear features and the lenticulae (Lucchita and Soderblom, 1982), the thickness of the water ice shell (Squyres et al.,

Figure 1-1: The first spacecraft image taken by the *Pioneer 10* mission. Obtained in December 1973. Included here under the commons license.

1983; Helfenstein and Parmentier, 1985), and whether this moon could support a liquid water ocean (Cassen et al., 1979; Cassen et al., 1982).

The *Galileo* mission was sent to resolve, or at least address, these questions. After a six-year journey, *Galileo* arrived at Jupiter in 1995 and took measurements and photographs of all four Galilean satellites until its descent into Jupiter's atmosphere in 2003. *Galileo*'s camera, the Solid State Imager (SSI; Belton et al., 1992) took images of Europa's surface at a range of resolutions ranging from 9 m/pix to 30 km/pix. The dark, mottled areas noted by Lucchita and Soderblom (1982) were found to be an entirely new feature type called icy chaos, another geologic feature unique to Europa (Figure 1-2). SSI also revealed a hemispheric dichotomy in albedo. In the images with resolutions under 250 m/pix, individual features such as domes and pits became visible, as well as smaller chaos features and low-albedo, small features called spots. These features were studied and detailed in multiple scientific papers in the post-*Galileo* age (Pappalardo et al., 1998; Rathbun et al., 1998; Greenberg et al., 1999; Greeley et al., 2000; Spaun, 2002; Greenberg et al., 2003; Singer et al., 2010; Culha and Manga, 2016; Noviello et al., 2019; Singer et al., in review). Evidence from the magnetometer instrument indicated that Europa had an electrically conducive interior (Khurana et al., 1998; Kivelson et al., 1999; Kivelson et al., 2000). This evidence, combined with the information regarding its density and moment of inertia, suggests that Europa has a layer of salty liquid water that spanned globally. The characterization of this global ocean and how it interacts with the surface have driven much of the investigation of Europa in the past two decades and led to new questions. How is heat transferred through the ocean and the ice shell? Does water or other material from the ocean enter the ice shell or reach the surface? If so, then under

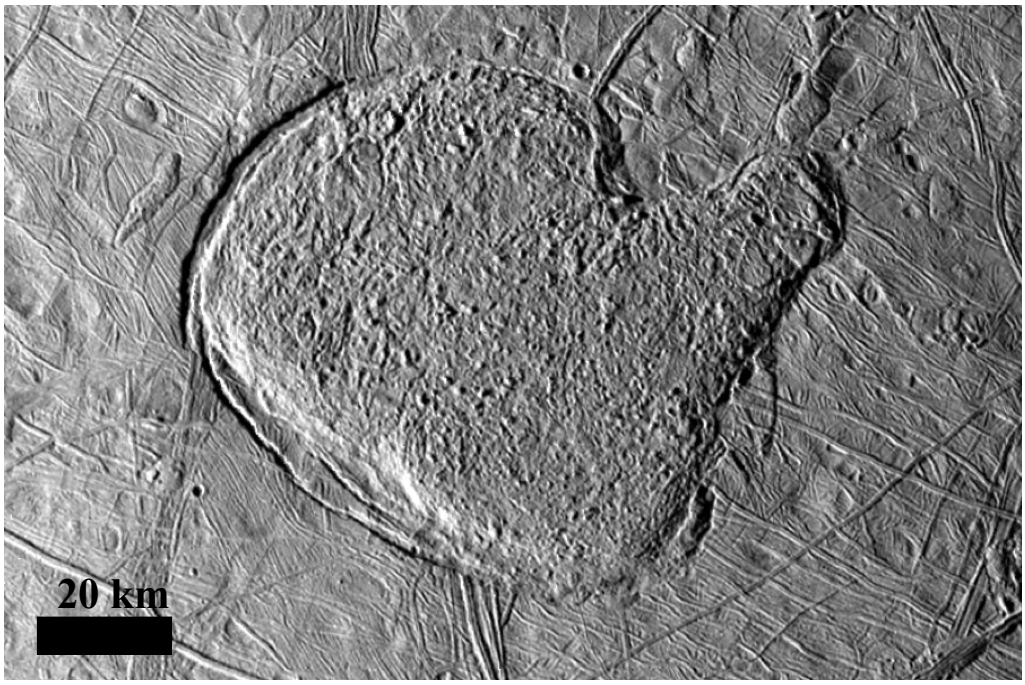

Figure 1-2: Icy chaos on Europa. This is Murias Chaos, found in the northern leading hemisphere in the E15RegMap02 area. This feature is elevated an estimated 400-600 m above the surrounding terrain. Images: 4326r and 4300r from the *Galileo* mission. Illumination from the left, north is up.

what conditions? What features are most closely associated with heat and material transport?

Many of these questions may be answered by studying Europa's icy chaos. Chaos itself is a thoroughly scrutinized geologic feature on Europa because it shows clear evidence of melt via some form of heating. Some chaos features exhibit rafts, which are pieces of the pre-existing ice shell that have been translated and rotated as the chaos feature formed; a good example of this is Conamara chaos (Figure 1-3). These rafts could only exist if the feature had at some point melted at least the top layer of the ice shell, moved the pieces around, and then froze them into place. For this reason, chaos has been linked with heat transport on Europa. When heat and ice meet, the result is often liquid water, which makes chaos an interesting target for astrobiology studies as well. Large chaos features have been studied extensively (Greenberg et al., 1999; Riley et al., 2000; Greeley et al., 2000; Spaun, 2002; Figueredo et al., 2002; Figueredo and Greeley, 2004; Collins and Nimmo, 2009; Schmidt et al., 2011; Bunte, 2013), but descriptions of smaller chaos features are less common in the literature. Small chaos features occur alongside pits, domes, and spots; in this work they are collectively referred to as microfeatures, to emphasize that these features include some which are not albedo-dominated features. Whatever process is driving Europa's geologic surface evolution, these microfeatures are a part of that story.

1.2 Europa's Physical Properties

Europa's radius is accepted as 1561 km (Seidelmann et al., 2007), about the same size as Earth's moon. Despite a global water/ice layer, its bulk density is accepted at 3.0 g/cm^3, and it has a moment of inertia factor of $C = 0.346 \pm 0.005$, which both suggest that

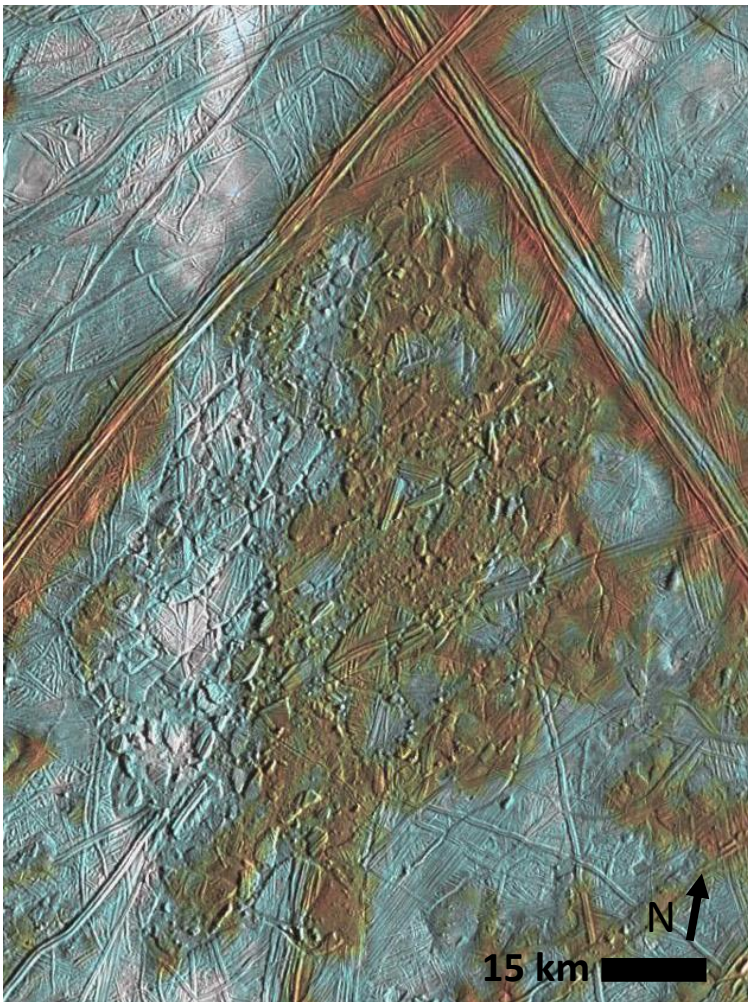

Figure 1-3: Conamara Chaos as imaged by the *Galileo* mission. This is an archetype for bright, platy chaos on Europa. The polygonal structures in its interior are called rafts, and the low-lying material they sit in is called the hummocky matrix. The red indicates the presence of salts (enhanced color in the image). Illumination from the right. Image credit: NASA/JPL/University of Arizona.

Europa is compositionally heterogeneous and differentiated (Anderson et al., 1998; Kivelson et al., 2000; Kargel et al., 2000). Data from the Galileo mission's magnetometers detected a small induced magnetic field, suggesting the presence of a global, liquid water ocean laden with salts underneath the ice shell (Khurana et al., 1998). Gravity data was used to probe the moment of inertia of the moon (Anderson et al., 1998; Kivelson et al., 2000; Kargel et al., 2000) and constrained the combined thickness of the ice shell and ocean to be between 80 and 180 km (Anderson et al., 1998), although the most widely accepted value is 160 km (Figure 1-4). Many subsequent questions therefore focused on estimating the thickness of the ice shell in an effort to better understand the physical characteristics of the ocean itself and the processes that affect Europa. Estimates of ice shell thickness range between 3 km and 30 km (Ojakangas and Stevenson, 1989; Pappalardo et al., 1998; Greeley et al., 2000; Greenberg et al., 2002; Hussman et al., 2002; Tobie et al., 2003). A thick silicate mantle likely encompasses a metallic core; the boundary layer between this silicate layer and the bottom of the liquid water ocean remains uncharacterized.

Europa's position near Jupiter and other Galilean satellites causes interesting gravitational interactions. Like Earth's moon, Europa is tidally locked, meaning the same side of Europa faces Jupiter throughout its orbit. Its orbital period around Jupiter is roughly 3.5 days, and its average orbital radius is 670,900 km. Its orbital path is slightly elliptical (eccentricity of 0.009). As such, Europa's orbital angular frequency is not constant, and it cannot always point the same face exactly toward Jupiter, and Europa's tidal bulge shifts east and west as Europa orbits Jupiter. As well, the small variation in the distance from Jupiter, a massive planet, causes the ice shell itself to flex up and down 30

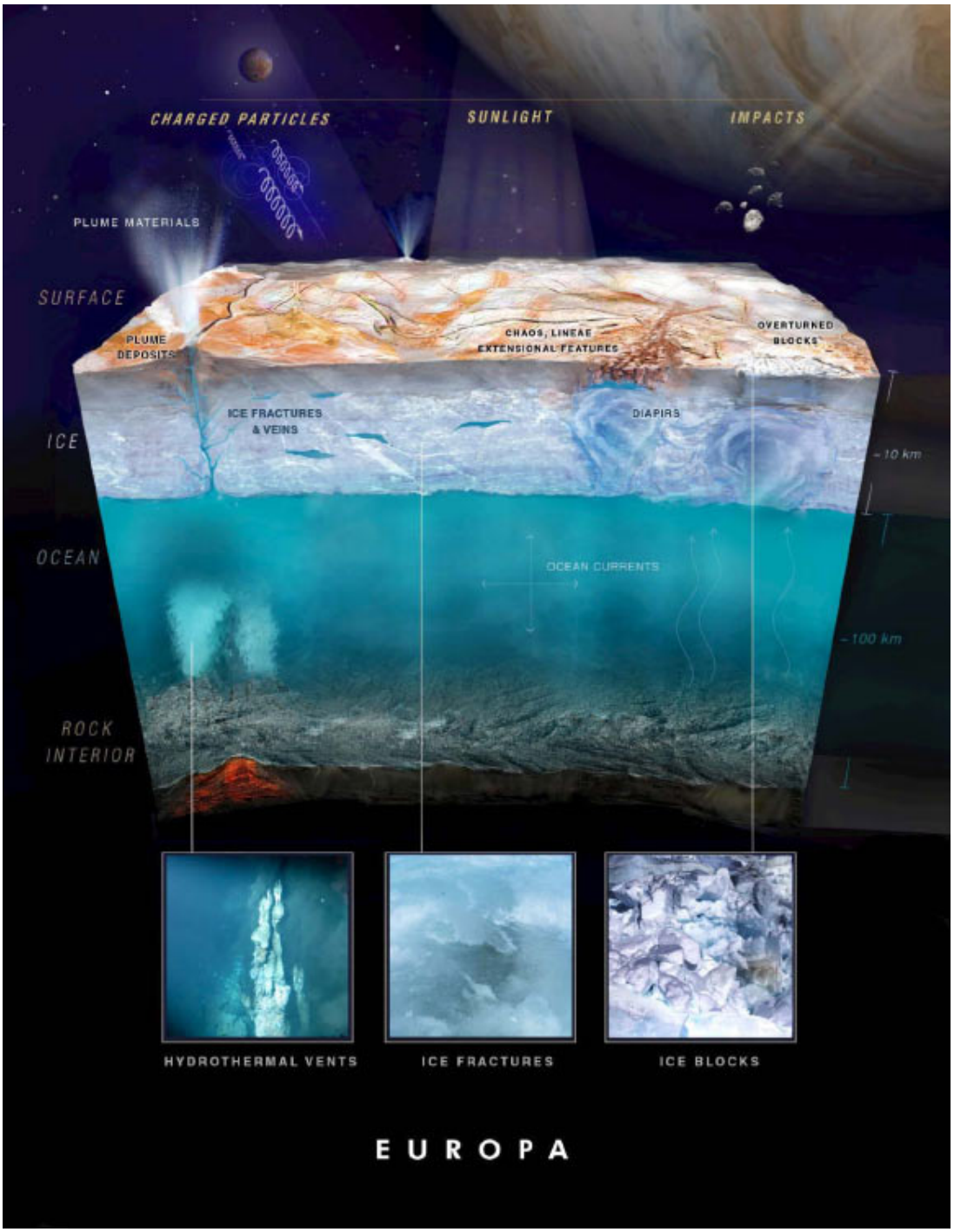

Figure 1-4: Cross-section of Europa's theorized ice shell, ocean, and ocean floor, along with some speculations as to the underlying activity. Credit: Hand et al., 2017; NASA.

m during every orbit. This amount of flexure creates much heat via friction; this kind of heat generation is called tidal heating and is the dominant source of heat on Europa. Tidal dissipation would eventually circularize Europa's orbit, except for Europa's interaction with Io and Ganymede. Europa is locked into a Laplace resonance (Laplace, 1805) with these two moons. For every one orbit Ganymede makes, Europa makes two, and Io makes four, putting these three into a 1:2:4 resonance with each other. The resonant interactions between the moons maintain Europa's non-zero eccentricity and sustain tidal heating. The heating and flexing are thought to drive the tectonics and geologic formations of microfeatures on Europa.

1.3 Context for this work

Understanding the origin of the microfeatures and their role in Europa's tidal heating beings with mapping. Mapping and classification of microfeatures mapped in the regional mosaics on Europa (the "RegMaps") is a relatively straightforward method and has been completed by at least four independent teams. The ones discussed most extensively in this work are: Greenberg et al., 2003; Culha and Manga, 2016; Singer et al., in review; and the one created by this author. These RegMaps in total cover ~10% of Europa's surface (Doggett et al., 2009); in this work, the total area mapped and analyzed amounts to 6.8% of Europa's surface because of the exclusion of RegMap-resolution images that cover large chaos areas (Conamara, Mannanán, etc.). These maps have been used to formulate theories as to how these features have formed and to provide observational constraints for formation models.

Chaos and microfeature formation models were first proposed in the late 1990s, soon after the first data from the *Galileo* mission arrived on Earth. At that point, little was

known about any of the features on Europa's surface, but the details of microfeatures—then called lenticulae in the literature—were obscured by the more fundamental questions related to Europa's overall structure and underlying geologic processes. Chaos is thought to be at least partially associated with heat and material transport, so studying chaos could lead to a deeper understanding of Europa's internal processes and its evolution. Chaos could also be related to tectonics on Europa, but more work is needed to clarify this. Other features, primarily domes, were also examined for any clues related to Europa's subsurface.

In the late 1990s and early 2000s, two main ideas regarding chaos formation competed for acceptance in the Europa community, and their implications regarding ice shell thickness and Europa's endogenic processes differ greatly. What these two ideas have in common is that neither can fully explain all instances of chaos and microfeatures, and without imaging data from more of Europa's surface, it is difficult to determine which model is superior. The two most prominent theories at the time of this writing are diapirism and liquid water sills. The most prominent models, their assumptions, and their predictions are detailed here.

1.4 Summary of Models

The following is a review of the literature surrounding potential ideas for microfeature formation processes. Table 1-1 summarizes the main ideas of these formation models, the major evidence for and against them, and the predictions they make that can be tested with available observational data.

1.4.1 Convection and diapirism formation models

Model Name	Main Points	Evidence in Favor	Evidence Against	Testable Predictions
Convection and Diapirism	- Warm ice rises through an ice shell between 3 and 30 km thick - Domes and chaos form above diapir, pits form when the diapir disappears	- Explains variety of microfeatures forming close together - Explains elevated topography of large chaos features (Murias Chaos)	- Chaos is found in many sizes, but diapirs are likely uniform in size - Numerical models fail to reproduce observed features of the correct size	- More chaos would be found near Europa's poles since tidal heating on Europa should be higher at the poles (drives diapirism)
Cryovolcanism	- Similar to diapirism, except with active flows of cryolava	- Explains hybrid features as effusive cryovolcanic features - Dome sizes/topography match models	- Unclear from current work if it can explain features other than domes - No evidence of flows observed	- Some features will have evidence of recent effusive flows - Domes are a typical size/topography
Melt-through	- A thin (< 3 km) ice shell is breached directly by the liquid water ocean - Ocean heat may be provided by hydrothermal vents	- Accounts for large range of chaos sizes - Accounts for observed disruption of chaos and presence of tilted/rotated rafts - Explains salts on Europa's surface	- Cannot easily explain positive elevation changes - Ocean currents are too weak to cause block translation - Heat from plume is quickly dissipated in Europa's ocean	- More chaos would be found near Europa's poles - Direct observation of raft translation/rotation in chaos
Liquid Water Sills	- Liquid water collects at a shallow depth in ice shell and forms a sill - Water travels up via a fracture, pushed by ocean pressure, or melts *in situ* - Sill's evolution causes changes to the surface	- Explains large chaos (Thera Macula) and microfeatures of all types - Explains the presence of salts in chaos, hybrids, spots -Explicitly explains hybrid features	- Must explain how liquid water rises through ice, even though doing so is gravitationally unstable - Must more explicitly explain the range of sizes for chaos	- Pits are clustered on Europa - Domes are larger than pits, chaos is largest of all - Pit clusters should be noticeably warmer in thermal data

Table 1-1: Summary of microfeature formation models on Europa.

One of the earliest proposed models involved solid-state convection-driven transport of heat and material through the ice shell. In this model, warm ice rises through the surrounding colder, denser ice shell, similar to how magma rises through Earth's brittle lithosphere. It was first proposed by Pappalardo et al. (1998) in a Nature paper, based on the widespread distribution of chaos and domes, their apparent random spacing, and what they observed to be a generally uniform size. This paper was also the first to suggest that chaos and other microfeatures could be genetically related. From their observations, they proposed that these features form when a warm ice diapir rises through an ice shell between 3 and 10 km thick and causes the overlying surface to warp upwards (domes) and/or break to form the rafts observed in some chaos.

This work was expanded on by Rathbun et al. (1998), who specifically examined the sizes of 42 domes in the immediate vicinity of Conamara chaos (10°N, 275°W). This area was not studied in this body of work. They noted that some of these domes were simple uplifts, and that some appear "as though something is disrupting the terrain," which could imply cracked domes (Rathbun et al., 1998). They too noted that some domes have smooth, surrounding moats of low-albedo material. They also noted that the domes' radii peaked between 3 and 4 km. From these observations, Rathbun et al. (1998) suggested that a Europan diapir that forms a feature less than 10 km in radial size must be formed by a diapir with a radius less than 4 km that originates at a depth of no more than "a few tens" of kilometers (Rathbun et al., 1998), and that it could take between 10^4 and 10^5 years to form a dome. On a broader scale, they also suggested the ice itself may be convecting, but pointed out a potential issue in the diapirism hypothesis: a small diapir will cool faster than a large one because it has a larger surface area to volume ratio. This

means that small diapirs might cool down and stop rising before they reach Europa's surface, or even close to it. Rathbun et al. (1998) suggested that this could account for the isolated nature of domes and could lead to a restriction in the overall number of domes in general.

Modeling work built on these observations and looked more closely at the factors that could contribute to diapirism within the ice shell, particularly thermal and compositional variations. One study found that partial melt produced in the rising diapirs will disrupt the surface, creating different lenticulae and chaos, even when the average ice thickness is over 20 km (Sotin et al., 2002). This process may be exacerbated by localized heating from tidal heating effects within a diapir, and that it is this localized heating that is much more responsible for forming microfeatures (Mitri and Showman, 2008). This study said that chaos and domes could form on Europa by this process but failed to explain how they form. This paper also failed to explain, or even mention, how pits and spots may form, suggesting that chaos formation may be a different process from the one that forms other microfeatures.

A later study specifically connected domes to diapirism, stating that domes and other lenticulae are formed by diapirism related to solid-state convection within the ice shell, potentially along with partial melting and disaggregation of the icy lithosphere (Pappalardo and Barr, 2004). These authors also note that there are two types of domes. Domes of the first type have different textures from the surrounding ridged plains and a typically lower albedos, with heights estimated between 40 and 100 m. These domes may have been formed from extrusions related to diapiric upwellings (Pappalardo and Barr, 2004). Domes of the second type preserve the pre-existing terrain, where the older

surfaces are warped upwards, but not destroyed. Pappalardo and Barr (2004) called these the intrusive domes. They also introduced the possibility that impurities in the ice could be responsible for forming domes around the observed sizes and topographies seen in the actual lenticulae, suggesting a thermally-induced compositional buoyancy (Pappalardo and Barr, 2004). This detail could be applicable to large chaos areas on Europa as well (Schenk and Pappalardo, 2004).

A successful model needs to consider both the thermal environment of the ice shell and the composition of the ice itself, as these parameters are coupled together through equations that describe the strength of the ice and any convection occurring within it. Han and Showman (2005) used numerical simulations to study the effects of salinity on convection within Europa's ice shell. Their numerical models produced uplifts and pits with 100–500 m of topographic relief, with diameters that ranged between 10–30 km. These diameters belong to features that are too large to be considered microfeatures. Additionally, there is a clear drop-off in the numbers of both domes and pits as the diameters approach 10 km, suggesting that there are few, if any, domes and pits that would fit into that size range. What this paper did conclude is that the ice needs a temperature and a compositional (salinity) contrast to get any buoyancy to raise a diapir through the ice shell. Concurrent work by the same team focused on chaos formation, specifically the effects that the rigidity of the ice has on the ice shell has on the process (Showman and Han, 2005). They found that rafty and hummocky chaos can be formed if there is melt in the presence of "substantial surface strain" generated by stresses that they modeled in the range of 0.2–1 bar. The source of this strain is the tidal flexing that Europa experiences as it orbits Jupiter, and evidence of these stresses is seen in the many

bands, cycloids, and ridges that cross Europa's surface. This model struggles to explain pits and domes however, as the ones produced in the models are too large (30–100 km in diameter) and never occur in isolation at any diameter.

If stress and strain could be involved in chaos formation, then tidal heating and dissipation may be involved as well, an idea originally proposed by Sotin et al. (2002). Han and Showman (2010) used a series of two-dimensional numerical simulations to study tidal dissipation in Europa's ice shell, and found that temperatures within plumes can reach melting temperatures under "plausible tidal flexing amplitude" (1.25×10^{-5} in Han and Showman, 2010), which could lead to partial melting and the formation of chaos. Pre-existing fracture zones greater than 6 km deep can concentrate tidal dissipation, increasing the size of a chaos feature. While this addition can explain well the formation of large chaos features, it fails to explain domes, pits, spots, or microchaos. Furthermore, any model that predicts tidal heating plays an important role in chaos formation would imply that there should be more chaos near the poles of Europa, as the tidal strain rates would be highest there (Collins and Nimmo, 2009).

There are several problems with the diapirism hypothesis. One, the sizes of diapirs would not be expected to vary. The size of a diapir is controlled by the thermal boundary layer of the setting. Europa's environment as a whole will not change much; even variation in the thickness of the ice shell will change the diapir's size by, at most, tens of percent. The large range of chaos features is a problem diapirism models have yet to overcome. As discussed previously, the composition of the ice can change its rheologic properties in ways that are not yet well-constrained. The hummocky interiors of chaos features are often lower in elevation than the surrounding terrain or rafts, but no models

have explained why without invoking some element of material removal. Moreover, this material should be higher than the background and plates if compositional convection and plastic yielding are important in chaos formation. The rafts within chaos could also be difficult to explain; as the plates translate and tilt, they may sink into the warm ice substrate (Collins et al., 2000).

Diapiric activity should also vary with regard to location on Europa; for example, diapirism should be more active at the poles (Collins and Nimmo, 2009). If diapirism is responsible for creating microfeatures on Europa, then there should be more microfeatures in areas where there should be more diapiric activity. Finding more chaos features outside of the RegMap areas of Europa would directly test predictions made regarding the locations of chaos on Europa, helping to support or refute the diapirism hypothesis.

1.4.2 Cryovolcanism

Ice-dominated volcanism, or cryovolcanism, is an offshoot from diapirism. Cryovolcanism is defined as "…the eruption of liquid or vapor phases (with or without entrained solids) of water or other volatiles that would be frozen solid at the normal temperature of the icy satellite's surface" (Geissler, 2000). In this model, instead of simply pushing the surface up and melting it passively, as happens in diapirism, the cryomagma breaches the surface and exudes out as cryolava. The confirmation of a cryovolcano on the dwarf planet 1 Ceres (Neveu and Desch, 2015; Ruesch et al., 2016) and dwarf planet Pluto (Singer et al., 2016) and Charon (Desch and Neveu, 2017) shows that this process is present in the solar system. The question is whether or not it is at least possible on Europa. Cryovolcanism was suggested as a source for the mottled terrain

visible in the *Voyager* (Lucchita and Soderblom, 1982) and *Galileo* (Greeley et al., 1998) data, though in many cases the inspection of these potential cryovolcanic features in higher-resolution images revealed them to be something unrelated. Certain domes and dome-like features on Europa have been included as evidence for this process (Fagents, 2003; Quick and Marsh, 2016; Quick et al., 2017), along with discoloration on bands and ridges (Buratti and Golombek, 1988) that are also present on Europa's surface. These domes are 3–10 km in diameter and are estimated from photoclinometry studies to be 40 to 100 m tall (Fagents et al., 1998; Singer et al., in review). While some domes exhibit characteristics consistent with effusive cryovolcanism (Fagents, 2003; Quick and Marsh, 2016), other origins of these features cannot be ruled out.

One of the biggest obstacles for understanding cryovolcanism is how liquid water ascends through an ice shell. As liquid water is denser than water ice (the dominant component of Europa's ice shell), the liquid water should remain in the gravitationally stable position underneath the ice shell. The presence of salts, particularly ammonia (Croft et al., 1988; Kargel, 1992; Kargel, 1995), would increase the buoyancy of the fluid, causing it to rise more easily through the ice; however, there is little evidence for significant amounts of ammonia, methane, nitrogen, or methanol on Europa. The materials that do exist—sulfur compounds (Carlson et al., 1999; Carlson et al., 2002) and magnesium and sodium salts (McCord et al., 1998a; McCord et al., 1998b; McCord et al., 2002)—would not significantly decrease the density of the liquid. Instead, Fagents (2003) investigated the possibility that salty, liquid water was pressurized, either directly from the ocean or from a pocket of liquid water in the ice shell, and pushed out to the surface, causing the potentially cryovolcanic features (Greenberg et al., 1998). The excess

pressurization could come from tidal stresses flexing the ice shell, from liquid water freezing into water ice, or from a combination of the two. While the models themselves at this time were simple, they did show that cryovolcanism is possible on Europa under a range of conditions, but is likely a localized event (Fagents, 2003).

To continue this earlier work, Quick and Marsh (2016) performed many numerical simulations to determine in cryomagma could travel through Europa's ice shell and showed that it is possible on Europa. They tracked the evolution of the cryomagma to determine its potential to carry material to the surface, particularly salts, as this knowledge would determine whether the salt present on Europa's surface is endo- or exogenic in origin. This paper also built on the ideas proposed by Fagents (2003) that fractures and dikes could be used by more than one cryomagmatic ascension, and that domes and uplifts could be the result of multiple magmatic ascensions. A follow-up paper specifically examined this question, and whether domes could be the result of cryovolcanism on Europa (Quick et al., 2017). Previous papers (Greenberg et al., 2003; Pappalardo and Barr, 2004) noted the presence of cracked domes on Europa, which are domes that retain the original terrain and appear as "punched up" through the ice shell. These may be the result of diapirism. Instead, Quick et al. (2017) focused on the domes that appear to have cracks and surfaces that are inconsistent with the surrounding terrain, as their origins are less clear. They gave particular attention to the rates of dome relaxation, assuming certain viscosities, temperatures, and crystallization percentages, important and interconnected parameters in any rheological study. They found that their modeled domes matched a Europan dome after 1.5 simulation years of relaxation, and that the domes' average radius was 3 km, a size consistent with previous results. While

the authors do acknowledge early that at least some of the domes could be formed from diapirism, the range of dome morphologies could suggest more than one process at work.

Cryovolcanism is still a relatively young model idea for microfeature formation on Europa, and much work still needs to be done to fully understand its implications for Europa's subsurface. One shortcoming of the model at the moment is that it fails to explain the occurrence of pits and spots, and most instances of chaos. It is also not clear if cryovolcanism has a role in forming larger chaos features (e.g., Figueredo et al., 2002) or if it is strictly limited to dome formation.

1.4.3 Melt-through Model

The melt-through model was a prominent idea for chaos formation on Europa in the late 1990s and early 2000s. It was inspired by icebergs floating in Earth's high-latitude oceans (Carr et al., 1998; Greeley et al., 1998), which could explain the relative positions of rafts within chaos and their positive relief relative to the matrix surrounding them. It would also explain the low albedo of and the presence of salts within some chaos, as these could be the result of the salty ocean spilling out onto the surface. This arrangement necessitates a thin ice shell and a high heat flux to melt large areas of the ice, in direct contrast with the thick ice shell and slow movement of diapirism. While the melt-through model is conceptually easier to grasp, the problems with it are more extensive, and the more recent literature all but ignores it.

The most serious problem with the melt-through model is that of the heat source. For the ice shell to melt and stay at least semi-solid for long enough to move and rotate rafts, an enormous amount of energy is required (Pappalardo et al., 1999; Collins et al., 2000). Maintaining the temperature of Europa's surface at 270 K would take a heat flux

of approximately 300 W m^{-2} (Goodman et al., 2004), roughly 1000 times as high as the estimated amount of heat produced from tidal flexing (Nimmo and Giese, 2005) and 25 times the solar insolation. A thicker shell would also have the problem that the bottom of the heating column would infill from the bottom up as the melting moves towards the surface (Collins and Nimmo, 2009); above a certain shell thickness, this infilling will happen faster than the melting, and the melt-through model will fail.

Hydrothermal plumes could be a source of heating on the bottom of the ice shell. To understand how, consider a source of heat on Europa. If Europa's silicate mantle is as dissipative as Io's, its sister moon, then it could generate as much as 7 TW of heat from tidal flexing. This heat would then have to travel from the mantle/ocean boundary to the bottom of the ice shell, a journey of more than 100 km. Thomson and Delaney (2001) first suggested that these hydrothermal plumes would rise through the ocean, which was itself undergoing stratification and destratification events. They proposed that chaos formed during periods where the ocean allowed for the efficient transfer of heat from the mantle to the bottom of the ice shell. After reaching the base of the ice shell, the hydrothermal plume would begin to melt the ice. Goodman et al. (2004) showed that even when the hydrothermal plumes began as a narrow cylinder, once it reached the base of the ice shell, the heat would begin to spread laterally out, thus decreasing the heat supplied to any particular spot. This lowered heat flux (0.1–10 W m^{-2}) is insufficient to cause melt-through. Supplying more heat to the initial plume would only increase the lateral extent of the plume at the base of the ice shell. Goodman et al. (2004) also attempted to estimate the expected chaos size-frequency distribution given constraints on hydrothermal plume size and found that while a power-law distribution of plume

lifetimes could explain large chaos areas, it failed to explain chaos areas smaller than 10 km in diameter. Finally, Lowell and DuBose (2005) showed that the lower gravity on Europa as compared to Earth would actually create weaker hydrothermal plume sources. None of these papers considered the presence of currents in Europa's oceans, which would dissipate heat within the ocean and prevent the top of the plume from ever reaching the bottom of the ice shell at all (Soderlund et al., 2014). With all this evidence stacked against them, it seems unlikely that hydrothermal plumes are directly responsible for chaos formation on Europa.

Still, many people have tried to make this model work. O'Brien et al. (2002) studied the melting process and determined that an ice shell 6 km thick could be completely melted through in ~10^4 years by concentrating all of Europa's heat output into an area 200 km across. They also demonstrated that the melting would happen significantly faster than the ice infilling would, thus surmounting both of the main problems with the model. However, this study had serious flaws. One, the amount of heat, while large, is insufficient to retain open water at Europa's surface (Goodman et al., 2004). Two, the grid spacing in the code used was too spatially coarse to resolve the heat conduction as it neared the surface, and caused the grid spacing to become numerically unstable. Further study (Goodman et al., 2004) using an adaptive grid spacing showed that the ice will reach an equilibrium thickness on the order of 100 m for the values used in O'Brien et al. (2002), but failed to show that the melt-through model as originally proposed (Carr et al., 1998; Greenberg et al., 1999; Thomson and Delaney, 2001), in which liquid water is directly exposed at Europa's surface, could physically happen.

Recent analysis by Soderlund et al. (2014) investigated the idea that Europa's ocean currents could be a previously unrecognized heat source. Due to Europa's rotation, the ocean should have hemispherical currents similar to Hadley cells on Earth. According to their models, the ocean in the equatorial region should, in a time-averaged sense, convect more vigorously than in other places, which will lead to a homogeneous temperature at the base of the ice shell (the top of the ocean). This increase in heat flux could intensify melting near the equator, eventually lead to thinning and breaching of the ice shell in low-latitude regions (Soderlund et al., 2014). If this is true, then more chaos or microfeatures in general should be found closer to the equator than elsewhere.

More chaos in the equatorial region is not a conclusive sign of melt-through, however, as there could be ice pumps active on Europa. Ice pumps in Antarctica are responsible for more than a 50% contribution to the thickness of marine ice in certain ice shelves (Oerter et al., 1992), and could be thickening Europa's ice shell in certain places. As currents move within Europa's oceans, they carry colder, fresher water from high latitudes to lower latitudes, where it then freezes, negating any thinning brought about by a higher heat flux (Soderlund et al., 2014). Because water will preferentially reject impurities when freezing, the new ice is fresher than the older ice, and could be a trigger for compositionally-driven diapirism in Europa's ice shell. Thus, a large population of chaos at low latitudes on Europa could suggest either melt-through or diapirism.

While the melt-through model has flaws, it does a good job of explaining certain characteristics of chaos. If the icy shell is melted, the rafts should be able to move, rotate, and tilt fairly easily, even if the driving mechanism behind it is not well-constrained. Pits will form as a consequence of melting, but how melting can form domes and chaos

features that are higher than the surrounding terrain is unknown. The presence of salts is a hard constraint that at least some liquid water is associated with chaos formation; this model explains how the liquid water breaches the surface. Most relevant to this study, however, is the connection between tidal heating and chaos formation. Melt-through events may be more common in areas where tidal heating is concentrated, but in the presence of strong oceanic currents, melt-through events could be more common around the equator (Soderlund et al., 2014). If locations of chaos are well-correlated with these areas of increased tidal heating, then it follows that chaos formation and tidal heating are related. Yet again, finding chaos across a wide range of sizes would significantly improve the understanding of chaos formation.

1.4.4 Sill Formation Model

The final major, relevant model for potential microfeature formation on Europa is the sill model (Schmidt et al., 2011; Michaut and Manga, 2014; Manga and Michaut, 2017), partially inspired by subglacial lakes on Earth. The early steps of this process are the same as that of diapirism: a thermal plume rises through the ice shell and melts some of the surrounding ice, downwarping the surface above the head of the plume because of the volume change associated with pressure melting. The pressurized lens is then "sealed" by the resulting hydraulic gradients and driving forces. The brittle ice shell above the lens is cracked by the combined stressors of diurnal tides, transient pressure, wedging in preexisting cracks, and interactions with preexisting terrain, allowing some of the briny liquid in the lens to spill out onto the surface. The stressors and the temperature gradient of the liquid infilling can also cause the edges of the surface expression of the lens to calve off. Finally, the lens freezes and the surface above it is modified a final time.

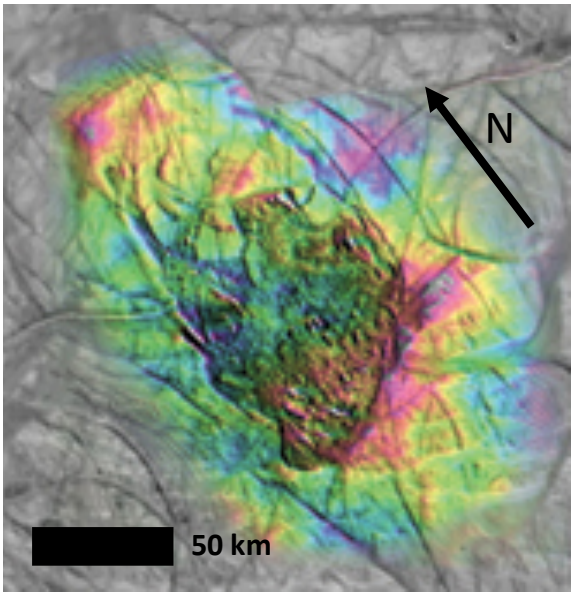

Figure 1-5: Thera Macula chaos on Europa. The northern region of this feature is a potential area of active chaos formation currently happening on Europa. Thera Macula is low-lying relative to the surrounding terrain, suggesting that the ice shell is being forced down. The color is artificial enhancement to emphasize topography; purples and reds indicate higher elevations. Illumination from the top right. Image credit: Paul Schenk/NASA.

This model in its entirety was first proposed by Schmidt et al. (2011), though the framework comes from the diapirism model (Pappalardo et al., 1998; Head and Pappalardo, 1999; Rathbun et al., 1998; Collins et al., 2000; Sotin et al., 2002; Schenk and Pappalardo, 2004; Pappalardo et al., 2004; Han and Showman, 2005; Collins and Nimmo, 2009; Han and Showman, 2010), with aspects of briny liquid mobilization (Head and Pappalardo, 1999; Collins et al., 2000; Fagents, 2003; Han and Showman, 2005; Collins and Nimmo, 2009; Buffo et al., 2019) incorporated.

The original sill model focused on large chaos features on Europa, particularly Conamara Chaos and Thrace and Thera Maculae. The most important prediction of this model is that Thera Macula (Figure 1-5) is actively forming chaos; its concentric fracture system surrounding the feature and the absence of a continuous moat implies that ice disaggregation is currently happening. This chaos formation is likely most concentrated towards the northern end of Thera Macula, as there are aspects that suggest that it was still actively freezing at the time of the *Galileo* mission. If the lens was still liquid when *Galileo* visited this region of Europa, then there should be visible changes in the morphology of Thera Macula upon return. Documenting the changes of this feature between past and future missions would be strong evidence in favor of the sills model. Finally, the ice may not have to be melted by the diapir to create a liquid water sill within Europa's ice shell; a pressurized ocean may be able to push liquid water up through fractures within the ice shell, with the momentum from the ocean pressure overcoming any negative buoyancy (Collins et al., 2000; Fagents, 2003; Michaut and Manga, 2014). The ocean pressure is caused by the thickening of the ice shell (Manga and Wang, 2007; Allu Peddinti and McNamara, 2019), which reduces the available volume of the ocean

layer, forcing the incompressible water to expand into fractures and move upward as a vertical dike. When it reaches a height of neutral buoyancy in the ice shell, the water layer begins to extend laterally, forming a sill (Michaut and Manga, 2014; Manga and Michaut, 2017).

One failing of the model as described by Schmidt et al. (2011) is that is does not explicitly describe how pits, domes, spots, and small chaos features form, though they note that their model "could be extended to other features." Subsequent papers worked to connect microfeatures on Europa to the sills model (Michaut and Manga, 2014; Manga and Michaut, 2017). In forming these microfeatures, a general series of events needs to occur (Michaut and Manga, 2014):

1. Liquid water must intrude into the ice shell. Note that this water could be melted *in situ* by a diapir (Schmidt et al., 2011) or pushed up through a fracture by a pressurized ocean (Michaut and Manga, 2014; Manga and Michaut, 2017).
2. The weight of the liquid water then deforms the elastic layer of the ice shell, and the ice above will experience viscous relaxation.
3. Stresses from the sill's formation widen the opening, allowing some material to spill out onto the surface and creating a disrupted surface.
4. The sill begins to solidify. Depending on the depth of the sill within the elastic layer, the ice above will either depress and form a pit (deep sill), or the freezing ice will increase the volume of the sill, warping the surface upwards and forming a dome (shallow sill; Manga and Michaut, 2017).

The timescales of these steps depend on the volume of the sill, the injection rate of the dike, the depths of the sill, the overpressure of the ocean, the viscosity of the ascending fluid, the size of the fracture or diapir, the strength of the ice surrounding the sill, and the temperature gradient within the ice shell. Michaut and Manga (2014) estimated some of these parameters to place time constraints on microfeature formations. This analysis was limited in that they used a two-dimensional code to estimate these values; hence the units for volume and volume injection rates are m^2 and $m^2\ s^{-1}$, respectively. Michaut and Manga (2014) estimated that to create the observed sizes and heights of a typical dome or pit, the sill volume must range between 10^6 and 10^7 m^2. For a sill injection rate of 1 $m^2\ s^{-1}$, that puts the time for sill emplacement between 10^6 and 10^7 seconds, or between 11.6 and 116 days, assuming the dike width is between 0.1 and 1 m. The time to freeze this sill was modeled as a function of sill thickness and evaluated for different depths from Europa's surface. All of these timescales were on the order of 10^{13} seconds, or 3.17×10^5 years, significantly longer than the time it took to inject the sill. On these long timescales the ice shell can behave elastically, allowing for the formation of domes and pits that can retain the preexisting terrain (Michaut and Manga, 2014). The potential for uneven freezing within the sill could mean that some areas of the overlying ice shell experience more fracturing as a result of the freezing, and this coupled with localized effects of diurnal stresses could lead to the surface breaking down to the sill, allowing some of the liquid to spill out. In this way, chaos can be formed.

The final main sill-model paper expanded on the nature of the sills themselves, suggesting that the could be saucer-shaped (Manga and Michaut, 2017), a model based on seismic images in sedimentary basins on Earth. In this model, the initial intrustion of

water rises until it is no longer buoyant or rheologically constrained, after which it forms a laterally-extended ellipsoidal shell. The transition between crack and laccolith comes when the free-surface of the elastic ice layer affects stresses and their upward propagation. Like the previous model, the sill is at a shallow enough depth in the elastic sheet that the overlying ice drives deformation. In this model, domes and chaos are more readily formed at the surface because the overlying ice bends readily as it becomes easier for stresses to propagate upwards rather than out. When radial stress is maximum, the overlying ice layer fractures and can form inclined sheets, in some cases creating the rafts observed in some chaos features.

Assuming that the volume and pressure of the sill doesn't change in the transition between original crack to final laccolith, then a consistent relationship between the depth of the sill (d) and the radius (R) of the feature it creates can be expressed as:

$$R \approx 2.4\, d$$

This implies that features of the same size should be formed by sills at the same depth, where depth is defined as the top of the sill. The variation in final morphology is determined by the way the sill's weight is compensated, as will be explained later. According to this model, this laccolith-formation stage is a relatively short one, estimated to range between 16 minutes and 2.75 hours (Manga and Michaut, 2017). At this stage, the surface relief caused by the intrusion of liquid water into the ice shell is estimated at 23 m at the most (Manga and Michaut, 2017), too small to explain the ~10^2 m estimated from photoclinometry (Fagents et al., 1998; Singer et al., 2010; Singer et al., in review). The observation that there are inclined ice sheets implies that the overlying ice is fractured, so the thickness of the elastic ice layer decreases over time.

Eventually, the liquid in the sill will begin to freeze. At this point the overlying ice is likely to fracture, and the likelihood increases as R increases. Assuming that the ice tensile strength is on the order of 10^6 Pa, then the overlying ice will begin to fracture when the stresses from a freezing sill exceed this limit, which will happen in a freezing time that ranges from 10^6–10^8 seconds (12 days to 3 years), a time range that is an order of magnitude longer than the previous model version suggested. At this point the formation mechanics of domes and pits vary. If water intrudes into the ice shell and if part of the weight of the sill is supported by elastic flexure, then the surface will rise and form a dome. This step can add additional height to the already upwarped surface, allowing the dome to reach the observed heights (Fagents et al., 1998; Singer et al., 2010; Singer et al., in review). If the sill is isostatically compensated, then there should be little, if any, topographic relief. If the underlying ice layer cannot support the weight of the sill, then the weight will cause the ice to warp downwards, and a pit will form (Figure 1-6). An important point is that this model predicts that a sill that forms a pit must still be liquid at the time a pit forms, else the freezing sill will push the overlying ice upwards until there is little to no visible relief.

As more liquid freezes, the ice above the sill cracks, temporarily reducing stress. This increase in pressure squeezes out some liquid onto the surface, which forms chaos and spots. This version also explains an additional microfeature class introduced in Culha and Manga (2016) called hybrids, which have attributes of both domes and chaos features. These hybrid features may represent a transitional state between domes and chaos, but if they do, then the question is whether the hybrid is a dome changing into a chaos or a chaos turning into a dome. These features typically also have a low albedo like

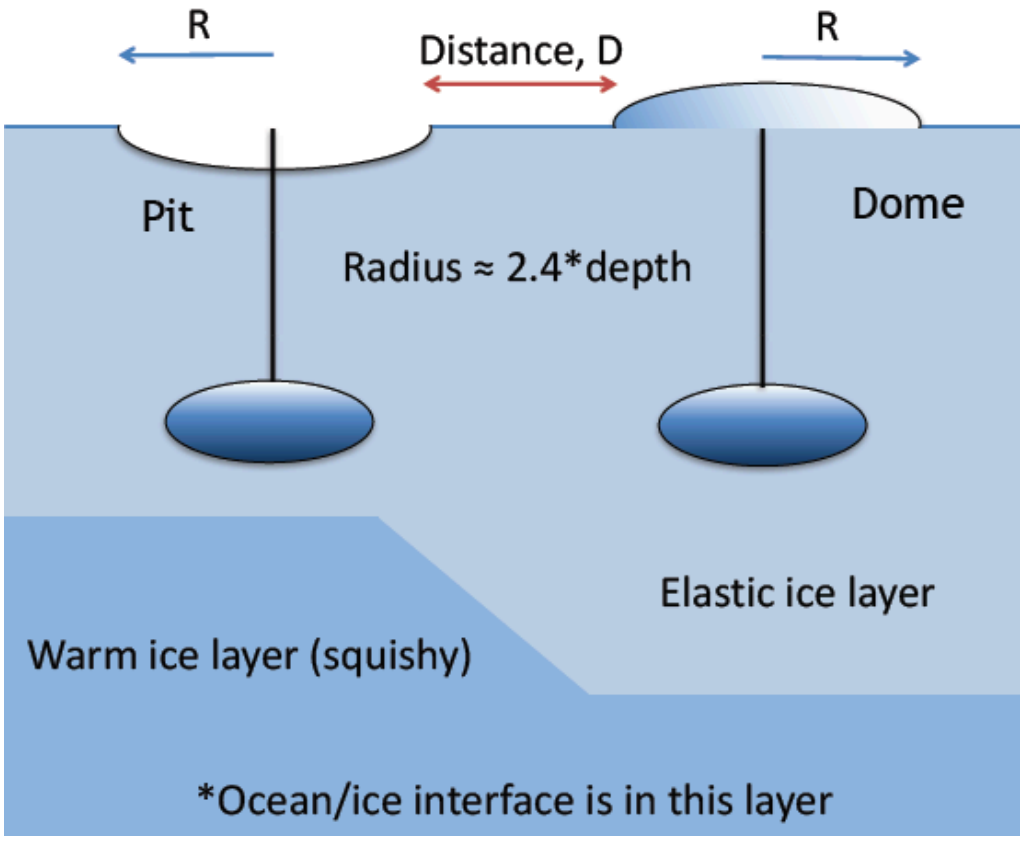

Figure 1-6: Schematic of the liquid water sill mode's implications for ice shell thickness on Europa. In this model, microfeatures of the same size will be formed by sills at equivalent depths in Europa's ice shell. The difference in microfeature type is determined by the way the weight of liquid water is compensated by the elastic ice layer. If it is thin underneath the sill, the sill will warp the ice shell down and form a pit. If the elastic ice layer is thick underneath the sill, then the weight will be compensated from below and force expansion upwards, forming domes and chaos features. Model by Manga and Michaut (2017), figure by J. L. Noviello.

chaos and spots, suggesting at least some commonalities. This model explains the formation of all types of microfeatures and is directly applicable to small-scale features, though they do suggest that large chaos terrains have a different origin (Manga and Michaut, 2017).

Manga and Michaut (2017) suggested four testable hypotheses from their modeling studies. The first is that pits should have smaller mean radii than domes, as the downward deflection of the sill during a pit's formation should contract the lateral extent of the sill. The second is that domes should be more numerous than pits because domes should be easier to form in general. Domes work after intruding water has frozen and has not been isostatically compensated, while a pit forms when the liquid water is still liquid and the underlying ice has a thin elastic thickness, hence why the weight fails to be compensated. As the freezing time for a sill is not indefinite, then pits should be short-lived, hence they should be less numerous. The third prediction is that pits should be clustered in space, as the sills are likely to form where there is a thin lithosphere and a high heat flux. As these places are presumably not widespread or large on Europa, and assuming that pits form in this way, then observable pits should be expected to be clustered together in areas that meet these conditions. Finally, the larger sills that form the larger microfeatures should lead to larger blocks and a greater degree of disruption, as the stresses on the overlying ice shell from a freezing sill should increase as the radius of the sill increases. They also suggest how large chaos features form, and predict that this could be the result of multiple sills merging together and collectively disrupting a surface larger than one sill alone could (Manga and Michaut, 2017).

1.5 Future Mission Plans

Some of the predictions made by these microfeature formation models can be tested using the data that has already been returned from previous missions, but the sparseness of the data prevents definitive conclusions. Near-future missions to Europa will provide new observations of Europa's surface, garnering evidence for and against heating, tidal, and feature formation models by providing observational constraints. Both the National Aeronautics and Space Administration (NASA; NRC, 2011) and the European Space Agency (ESA, 2005) have named Europa as an important target of future exploration; these missions are detailed here.

NASA's Flagship class Europa Clipper mission will focus almost exclusively on this icy moon, unlike the JUICE mission (Figure 1-7). As of 2019, the updated trajectory for Europa Clipper begins with a launch in 2022 and contains a total of 46 Europa flybys, 4 of Ganymede, and 9 of Callisto over 3.7 years of flight, including travel time (Bayer et al., 2018). In July 2015 nine instruments were selected to fly on this mission; in March 2019, the ICEMAG magnetometer instrument was descoped to a smaller magnetometer, leaving eight instruments as proposed on the mission. These instruments will study the plasma environment of the Jupiter system (PIMS; Westlake et al., 2016), the chemical properties of Europa's atmosphere (SUDA, Kempf et al., 2014; Europa-UVS, Pappalardo et al., 2017) and surface (MISE, Pappalardo et al., 2017; SUDA; Europa-UVS), the thickness and structure of the ice shell (REASON, Schroeder et al., 2016), the thermal properties of Europa's surface (E-THEMIS, Christensen et al., 2017), and Europa's geology (EIS; Turtle et al., 2016). Combined, these instruments will provide the clearest picture of Europa and touch on the major questions of the solar system, including

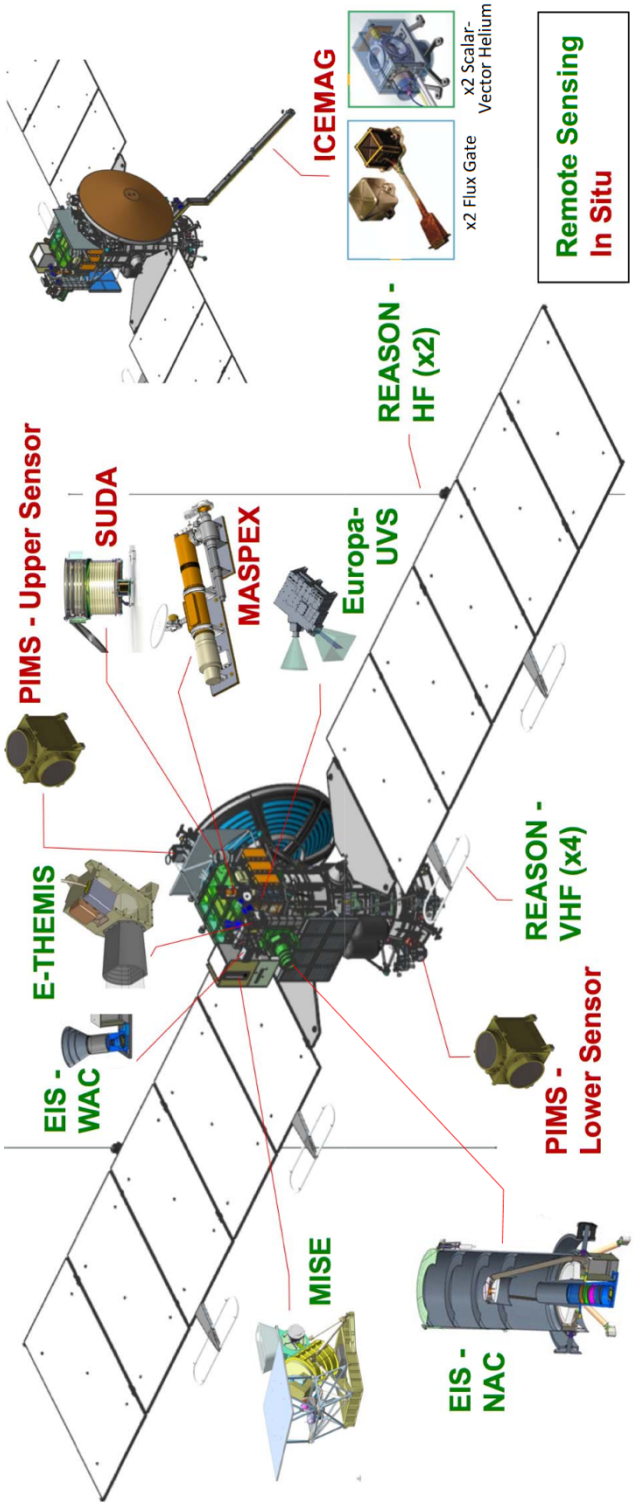

Figure 1-7: Proposed instruments of the *Europa Clipper* Flagship mission. As of March 2019, the ICEMAG magnetometer has been descoped in to a smaller magnetometer. The other instruments are still slated to fly. Figure from NASA.

whether or not Europa is capable of supporting life and the geophysics of ocean moons in the outer solar system.

The final planned step for future Europa exploration is the Europa Lander, which is currently in the development stage. This mission would have three main goals: to search for evidence of life on Europa, to assess the habitability of Europa via *in situ* techniques, and to characterize the surface and subsurface to enable future robotic exploration (Hand et al., 2017). The proposed instruments it would carry include an organic compositional analyzer, a microscope for life detection, a vibrational spectrometer, a contextual remote sensing instrument, and geophysical sounding system, and infrastructure sensors for science (Pappalardo et al., 2013; Hand et al., 2017). The target launch date for this mission is later than 2025, meaning it will follow the Europa Clipper mission at a much later date. This dataset would further constrain ice shell properties from a structural and compositional standpoint, refining existing models and opening the possibility for additional models to be developed.

Concurrently with these NASA missions, ESA's Jupiter Icy Moons Explorer (JUICE) is currently under development with a selected launch window in 2022. This mission will last for 11 years, 3.5 of which will be spent in the Jupiter system. Thought JUICE's main target will be Ganymede, the mission will do two flybys of Europa over 36 days in early 2030. Its main purpose will be to study the composition of Europa's non-ice chemicals with a particular focus on the chemistry "essential to life, including organic molecules" (Grasset et al., 2013). It will also image the surface geology to identify appropriate landing sites for future exploration, and attempt subsurface measurements of Europa's ice shell thickness in its most active locations using subsurface radar sounding

at closest approach (Grasset et al., 2013). This mission will complement the data collected by the Clipper and Lander missions, and provide a short time gap between subsequent measurements, allowing for a constrained estimation of the rates of certain geologic processes on Europa, including microfeature formation.

1.6 Organization of Dissertation

This thesis is broken down into the major components of the work done in fulfillment of the requirements for the doctoral degree in geological sciences (concentration: planetary geology) of the School of Earth and Space Exploration at Arizona State University. This chapter served as the introduction to the work, providing contextual background on the history of Europa exploration, the geology observed on the surface, the proposed formation models for some of these geologic features, and the potential for future exploration. The first main chapter is an in-depth description of the acquisition and morphometric analysis of the microfeature dataset used in further analysis in the rest of the thesis. This dataset was collected in RegMap images and validated against three additional, independently collected datasets. The second main chapter is a description of the collection and analysis of a second microfeature dataset, this one in low-resolution (≥1.5 km/pix) images, rather than RegMap images. This second dataset was collected in an area for which microfeatures had already been mapped in the RegMap images, allowing for a direct calculation of omission and classification errors to be calculated. The third main chapter introduces a multivariate classification analysis that can sort quantitatively the microfeatures identified on Europa. The test is first trained on the RegMap dataset and then used to classify the low-resolution features, allowing for a comparison between human and computer accuracy rates. The fourth main chapter

returns to the RegMap dataset and performs multiple clustering analyses on them to determine the spatial clustering of different microfeature types across RegMaps. Finally, the conclusion summarizes the results and offers predictions that can be directly tested with images and data taken by the Europa Clipper and potential Europa Lander missions. This work is intended to be used in mission planning for these missions, as well as model constraints, expansion of a usable dataset to previously unmapped areas of Europa, and the introduction of robust statistical tests to the study of icy satellites.

1.7 Brief Summary of Results

Four of Europa's RegMaps areas were mapped, and together this area accounts for 6.43% of Europa's total surface area. A total of 691 classified microfeatures were identified and validated. The most numerous feature type was microchaos (239), almost equaled in number by pits (217), followed by domes (116), hybrids (90), and spots (29). Chaos and hybrid features are larger on average than the other microfeatures, and also have lower average normalized reflectance values. Pits and domes are around the same size, aspect ratios, and normalized reflectances. Spots are the fewest, smallest, and darkest of all the microfeature types studied. In addition, there are two distinct types of hybrid features, one more chaos-like and the other more dome-like. This work suggests that the underlying microfeature formation process or processes are more consistent with cryovolcanism and the sills models than with diapirism.

Much of the uncertainty in microfeatures formation models lies in the lack of data, specifically images where these microfeatures are apparent. Low-resolution images present an opportunity to potentially map additional microfeatures outside of the traditional RegMap areas. To investigate the different sources of error and the

corresponding error rates, an independent dataset was created of the E15RegMap01 region mapping features in four low-resolution images; this dataset was then compared to the RegMap dataset. Roughly 70% of chaos, spots, and hybrids that were originally mapped in the RegMap dataset were also mapped in the low-resolution dataset. Moreover, chaos features were accurately classified as chaos 60% of the time in low-resolution images. Pits and domes were mapped as little as 5% of the time, and were never recognized correctly as pits or domes. As many as 25% of the microfeatures that were mapped in low-resolution ended up being false positive "phantom" microfeatures that were not associated with any microfeature in the RegMap dataset. This work provides confidence levels to studies that seek to map microfeatures outside of RegMap areas.

It may be possible to increase the accuracy of these mapping tests if there was a quantifiable classification framework for these microfeatures, even in low-resolution images. This would reduce the overall uncertainty in mapping outside of RegMaps and the variability between different mapping datasets. Using a selected multivariate analysis (discriminant function analysis, or DFA), the microfeatures were evaluated for their statistically significant quantitative differences and how well those differences separated the microfeature groups. Except in cases where the groups being compared were very similar (e.g., the pits and domes), the quantitative classification was able to sort between the feature types with an accuracy that was above and beyond what could be expected from random chance. Overall the computer is adept at separating between chaos/spots/hybrids and pits/domes, but is less successful when sorting features within those groups. The accuracy rate of sorting features using this quantitative classification

approach was also compared to a human using a traditional mapping and classification approach. In the end, the computer was more accurate at identifying pits and domes out from the LowRes dataset than the human did, but otherwise was comparable to a human mapper.

Finally, the predictions of one formation model in particular were examined in more detail. The sills model implies that liquid water exists underneath certain features, mainly pits, on Europa. Determining the likelihood of this being true is critical to understand more about Europa's potential for habitability, as well as how heat and material transfer potentially work in ice shells. The different microfeature types across the four RegMaps were analyzed for degree of clustering via a nearest neighbor clustering analysis, and the average minimum distances between features types were computed. Monte Carlo simulations were also run to provide synthetic datasets to allow for comparisons to the observed dataset. While in general all microfeature types were reported as clustered, pits were the only ones that were clustered in all four RegMaps studied. The average minimum distances between pits to other pits were consistently lower than the average minimum distances between pits to any other feature type. Finally, the Monte Carlo runs consistently had average minimum distances that were significantly larger than the observed distances. This all suggests that pits are definitely clustered on Europa. This document concludes with a summary of the chapters and predictions for future Europa missions to evaluate.

CHAPTER 2

MICROFEATURE MAPPING IN REGMAP IMAGES

2.1 Introduction

Europa's surface is peppered with hundreds of endogenic features including chaos features, which are present across a large range of sizes, and small features collectively referred to as lenticulae. Chaos features are defined as irregular polygons with a hummocky or platy interior texture and are often but not always associated with areas of low albedo (Greenberg et al., 1999; Prockter et al., 1999; Greeley et al., 2000; Figueredo et al., 2002) and a higher concentration of salts (Hand and Carlson, 2015). The rafts inside of platy chaos features are the remains of previous terrain that the chaos feature disrupted during its formation. Chaos features have been extensively studied in terms of their morphology (Head et al., 1999; Greenberg et al., 1999; Spaun, 2002; Figueredo et al., 2002; Collins and Nimmo, 2009; Singer et al., in review), potential formation mechanisms (Head and Pappalardo, 1999; Greeley et al., 2000; Riley et al., 2000; Spaun 2002; Figueredo et al., 2002; Collins and Nimmo, 2009; Schmidt et al., 2011), locations and clustering (Greenberg et al., 1999; Spaun et al., 1999; Riley et al., 2000; Soderlund et al., 2014; Culha and Manga, 2016; Leonard et al., 2017; Noviello et al., 2017), observational constraints (Neish et al., 2012; Bunte, 2013; Noviello et al., 2018; Leonard et al., 2018), and relation to Europa's geologic history (Head and Pappalardo, 1999; Prockter et al., 1999; Greeley et al., 2000; Spaun, 2002; Greenberg et al., 2003; Figueredo and Greeley, 2004; Spaun et al., 2004; Collins and Nimmo, 2009; Schmidt et al., 2011; Leonard et al., 2018; Singer et al., in review). This terrain type is estimated to cover between 20% (Figueredo and Greeley, 2004) and 40% (Riley et al., 2000) of

Europa's surface. Chaos is easily identifiable in the moderate resolution (220–230 m/pix) images of Europa across most lighting angles (Neish et al., 2012), enabling detailed data collection efforts across ~10% of Europa's surface (Doggett et al., 2009; Neish et al., 2012). Large chaos features are visible in low resolution (≥1.5 km/pix) images (Neish et al., 2012), so these features have been mapped globally (Riley et al., 2000; Bunte, 2013; Leonard et al., 2017), but little is known about their details or the global distribution of any other non-linear feature type.

Other features occur alongside chaos, and have been subdivided into specific types (Pappalardo et al., 1998; Greeley et al., 2000; Figueredo and Greeley, 2004; Spaun, 2002; Greenberg et al., 2003; Collins and Nimmo, 2009; Culha and Manga, 2016) primarily based on qualitative assessment of their morphologies (Figure 2-1). Small chaos (microchaos) are small areas with disrupted terrain and often irregular edges (Figure 2-1A). Uplifts and domes are features with positive relief (Figure 2-1B; Greeley et al., 2000; Greenberg et al., 2003; Singer et al., 2010;). Uplifts are usually more polygonal, while domes are more elliptical. Pits are generally elliptical features with negative topographical relief (Figure 2-1E; Greeley et al., 2000; Greenberg et al., 2003; Singer et al., 2010; Singer et al., in review). Spots are elliptical areas that have low albedo, but without any discernable interior structure (i.e. a hummocky interior or rafts) and no obvious topography (Figure 2-1F; Greeley et al., 2000; Greenberg et al., 2003; Singer et al., 2010; Singer et al., in review). A recent mapping study of selected regions of Europa revealed an additional category of hybrid features, in which a distinct dome or uplift is present within a chaos feature (Figure 2-1C and Figure 2-1D; Culha and Manga, 2016). Some of these features had previously been considered domes or uplifts with

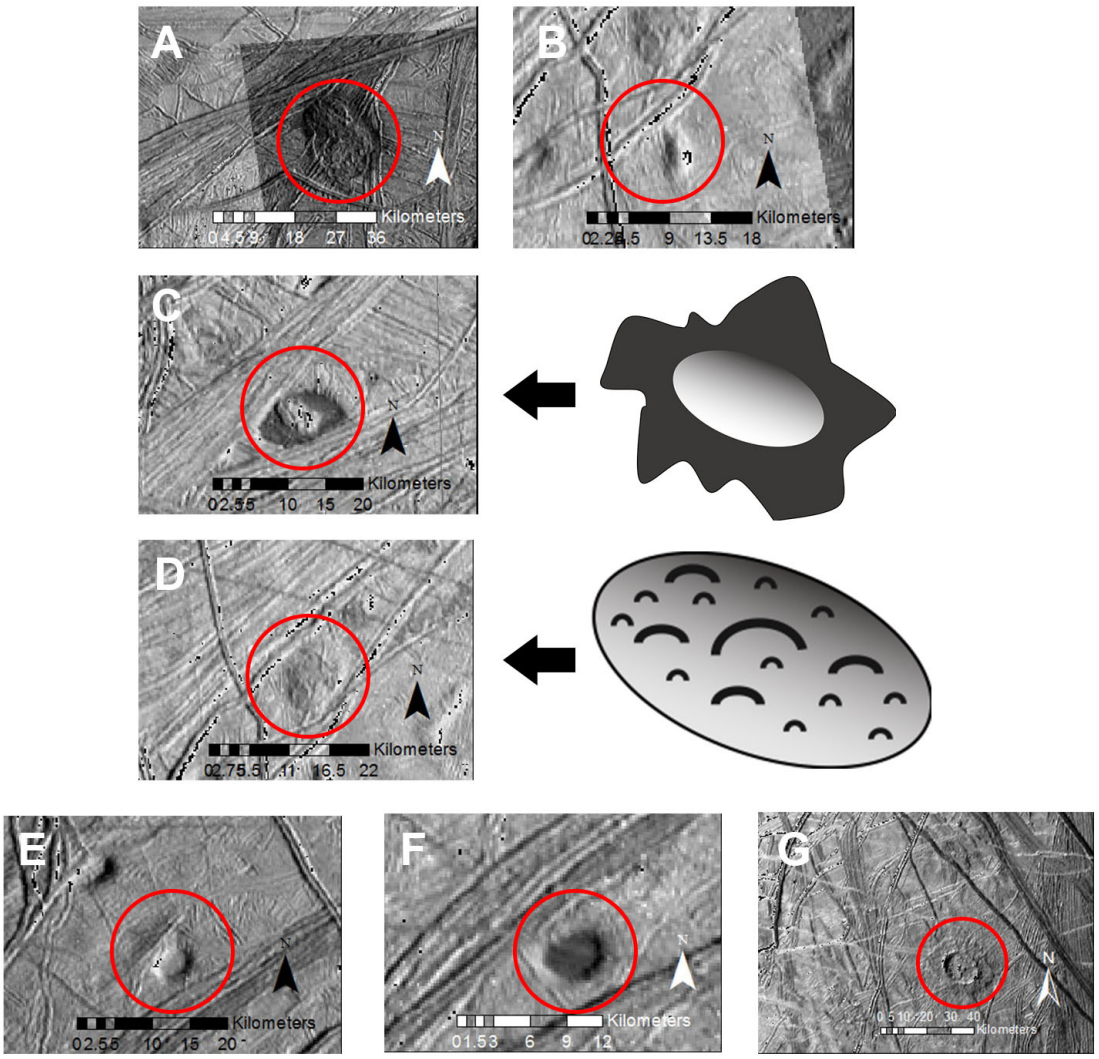

Figure 2-1: Examples of microfeatures seen in the four RegMaps on Europa's surface. A) Chaos, classified as such by the hummocky interior and clear disruption of the previous terrain (sun from right). B) A dome, characterized by its positive topography (sun from right). C) Type I hybrid morphology, characterized by a positive topographic feature inside of a dark "halo" (sun from right). The halo can be smooth or have a hummocky appearance. D) Type II hybrid morphology, characterized by a positive topographic feature with a fully disrupted surface, akin to the hummocky interior of the chaos feature in A (sun from bottom right). The visible cracks are inconsistent with the surrounding terrain. E) A pit, characterized by its negative topography (sun from top left). F) A spot, characterized by consistent albedo and lack of interior disruption (sun from bottom right). G) A crater on Europa (sun from top left).

cracked surfaces (Rathbun et al., 1998; Greenberg et al., 2003; Quick et al., 2017), but not until recently were they considered a separate type. Much of the literature refers to these features, especially pits, spots, and domes, as lenticulae. This language is avoided here, so as not to exclude small chaos features and to emphasize that not all of these features studied are albedo features.

The process of chaos formation disrupts and transforms the previous terrain. This can be interpreted as evidence that some kind of melting is involved, implying the presence of liquid water or warm ice near Europa's surface. Initial models for chaos formation invoked full melt through of a thin ice shell (Greenberg et al., 1999; Collins et al., 2000; O'Brien et al., 2002; Nimmo and Giese, 2005) or a warm-ice diapir rising through a thick ice shell (Pappalardo et al., 1998; Figueredo et al., 2002; Schenk and Pappalardo, 2004; Showman and Han, 2005; Singer et al., 2010; Soderlund et al., 2014; Singer et al., in review). These two models explained some characteristics of chaos features, but there remained other aspects that neither model could fully explain (Collins and Nimmo, 2009).

A more recent model, specifically designed to address the formation of large chaos features, invokes local melt water formed by a rising diapir that disaggregates the overlying ice (Schmidt et al., 2011). As the convective plume reaches its minimum depth in the ice shell, the overlying surface is deflected downward to compensate for the decrease in volume caused by the ice melting into a liquid melt lens. As the melt lens begins to collapse, ice blocks cleave off from the surrounding ice shell. As the water lens refreezes, the blocks above rotate, and domes form in between the disrupted ice blocks and at the margins of hummocky chaos. This mandates that the sill is much larger than

the domes themselves, as the domes form in between the large ice blocks. It is not clear if this method of dome formation can account for domes that appear isolated, or if it necessitates that domes must be clustered above the location of the sill. The work also briefly notes that the scale of the ascending plumes and the preexisting terrain accounts for the range of chaos morphologies, and could explain domes, but does not explain pits or spots. Finally, while the model can explain the formation of larger chaos features such as Conamara and Thera Macula, it is unclear if this model could be applied to microchaos (chaos under 100 km^2 in area) or any of the microfeatures. As this work is focused on microfeatures, the Schmidt et al. (2011) sills model is disregarded at present, but is included in the suite of models that invoke liquid water in the formation of surface features. Another liquid water model, discussed in more detail later, specifically focuses on microfeatures and their relationship to each other (Manga and Michaut, 2017); this model is explored in detail.

The similar range of sizes and clustering patterns of small chaos features, domes, pits, and spots have led to the hypothesis that they may be genetically related (Pappalardo et al., 1998; Rathbun et al., 1998; Collins and Nimmo, 2009; Singer et al., 2010; Schmidt et al., 2011; Michaut and Manga, 2014; Manga and Michaut, 2017; Noviello et al., 2017; Singer et al., in review). Understanding how one forms could lead to an understanding of the entire microfeature formation process. Similar to large chaos features, one proposed mechanism for microfeature formation is solid-state convection, in which a warm-ice diapir rises through Europa's ice shell (Pappalardo et al., 1998; Rathbun et al., 1998). The warm ice will rise until it reaches a point of neutral buoyancy, at which point it will begin to spread out laterally. Additional studies have suggested that variations of this process

could partially melt the ice above the diapir's head, either due to localized compositional impurities and brine mobilization (Head and Pappalardo, 1999; Pappalardo et al., 2004) or from the localized effects of tidal heating (Sotin et al., 2002). Further work demonstrated that tidal heating can enhance the effects of partial melting (Sotin et al., 2002; Mitri and Showman, 2008; Han and Showman, 2010), which may concentrate melt within the diapir, creating chaos and potentially other microfeature types.

Another proposed mechanism for forming microfeatures involves liquid water rather than warm ice (Schmidt et al., 2011; Manga and Michaut, 2017). In this model, an over-pressurized ocean (Manga and Wang, 2007; Michaut and Manga, 2014) pushes liquid into Europa's ice shell via a conduit or a pre-existing fracture (Quick and Marsh, 2016; Craft et al., 2016; Culha and Manga, 2016; Manga and Michaut, 2017). The liquid water eventually reaches a point of neutral buoyancy within the ice shell, and spreads out laterally to form a subsurface volume of liquid water (i.e. a sill). The mass influx from the liquid water and subsequent freezing changes the water volume and, consequently, the morphology at the surface. Different stages of the sill's evolution can cause different microfeatures to form on the surface above it. Early in the process, a pit or dome forms, depending on how the liquid water pocket is compensated (Manga and Michaut, 2017). Then during freezing, either a dome forms (Schmidt et al., 2011; Manga and Michaut, 2017), or the surface is breached to form a chaos feature (Manga and Michaut, 2017), depending on whether or not part of the weight is supported by elastic flexure in the ductile upper ice shell.

More recent work (Quick and Marsh, 2016; Quick et al., 2017) has examined the possibility that some domes are the result of cryovolcanism on Europa. Previous studies

(Rathbun et al., 1998; Pappalardo and Barr, 2004) have noted that domes can present in slightly different morphologies; some are texturally different material from the surrounding plains, typically with a lower albedo. These domes may also occur with surrounding "moats" of lower albedo, which may be more consistent with hybrid features. The other type of domes retains the pre-existing terrain on the upwarped surfaces (called "punched through" in Quick et al., 2017). The domes that retain the original terrain may have been created as the result of viscous extrusions of cryolava onto Europa's surface (Quick et al., 2017), an idea expressed earlier for the large chaos feature Murias chaos (Figueredo et al., 2002). Cryovolcanism can also explain the dark "moats" around some of the hybrid features, as it is merely the extent of the cryolava flow. If correct, cryovolcanism can potentially explain both hybrid features and domes, and may even explain bands and ridges as manifestations of subsurface cryomagmatic processes associated with diapirism (Quick and Marsh, 2016).

Each of these proposed formation mechanisms is associated with predictions and assumptions for microfeature characteristics, discussed in detail in Section 2.4.2. Hence, geographical and morphological information about microfeatures can help constrain their formation mechanism. Chaos clustering near the poles could imply that tidal heating is necessary to form chaos (Collins and Nimmo, 2009), while a more random or dispersed global distribution could implicate sills, as they could form anywhere. Although microfeatures have been mapped in several studies, there is significant variation between individual mapping data sets, especially as technology has improved to allow for more quantitative studies to be conducted.

Having one complete, validated geomorphic map of microfeatures on Europa that represents all previous work can facilitate discussions regarding feature distribution, size, and morphologies, and could help form and focus science objectives for the upcoming Europa Clipper mission (Phillips and Pappalardo, 2014; Pappalardo et al., 2016). To fulfill this need, geomorphic map of Europa's microfeatures, including small chaos features ($\leq$ 100 km^2), has been created and merged with three previous maps (Greenberg et al., 2003; Culha and Manga, 2017; Singer et al., in review) to create a validated, digitized map of microfeatures on Europa within the regional mosaics ("RegMaps") that cover ~10% of the surface. Next, morphological information was obtained for each feature, including area, diameter, and normalized reflectance. Finally, these observational findings and their implications for formation models are presented. This work seeks to improve the understanding of how Europa's microfeatures form, and assess whether different types of features form in related or distinct processes, by identifying statistically significant morphologic indicators of each type. This work presents new constraints that future modeling efforts on microfeature formation should address and serves as the basis for future work on quantitative classification of these features.

2.2 Materials and Methods

2.2.1 Data and mapping

All the images used in this study came from the *Galileo* SSI instrument. Only images taken with the clear filter (611 nm; Belton et al., 1992) were used. Images were taken in *Galileo*'s 15th and 17th orbits, both of which had Europa as its central target; these images make up the regional map mosaics. Table 2-1 shows the average image characteristics for the images included in each RegMap; for details of each image used,

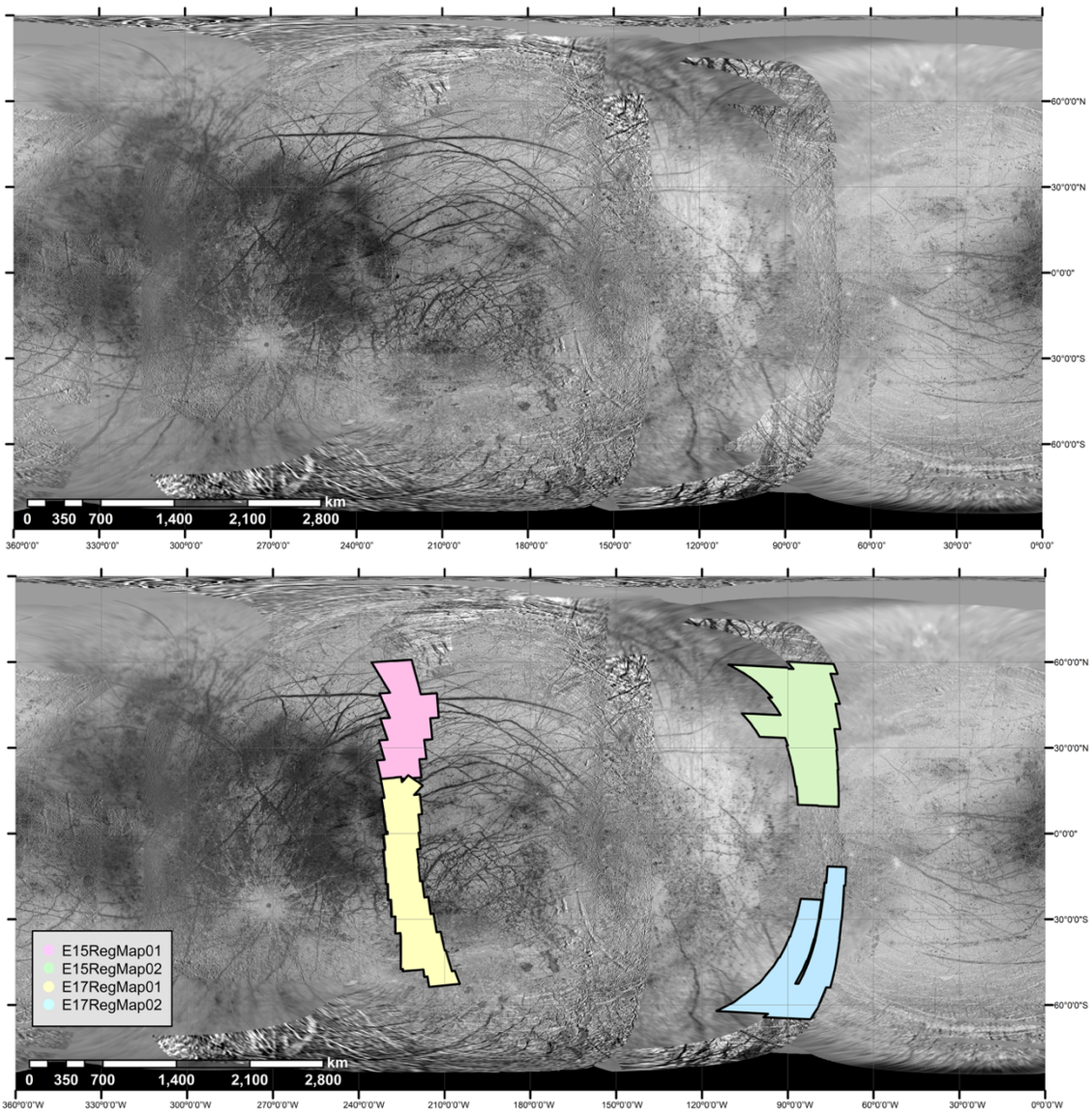

Figure 2-2: Mapped areas on Europa. Top: The USGS (2002) basemap of Europa. Bottom: The same basemap with polygons overlain to show our study areas. Pink: E15RegMap01. Green: E15RegMap02. Yellow: E17RegMap01. Blue: E17RegMap02.

Table 2-1: Average characteristics of the RegMap images used for mapping

Region	Average Resolution (m/px)	Average Phase Angle (deg)	Average Emission Angle (deg)	Average Incidence Angle (deg)
E15RegMap01	231.12	63.15	37.60	77.46
E15RegMap02	237.33	100.54	37.47	78.12
E17RegMap01	218.20	72.35	20.30	77.92
E17RegMap02	222.31	92.62	28.15	79.51

Table 2-2: The central meridians used for projecting the RegMap images

Region	Central Meridian Mapping Longitude
E15RegMap01 (trailing, northern hemisphere)	222°W
E15RegMap02 (leading, northern hemisphere)	83.5°W
E17RegMap01 (trailing, southern hemisphere)	220.7°W
E17RegMap02 (leading, southern hemisphere)	79.5°W

see Appendix B. This data set enables mapping of both the northern (0° to 55°N) and southern (0° to 65°S) latitudes at two separate longitudes (~90°W and ~230°W) on Europa. For a visual representation of the areas mapped, see Figure 2-2.

Because the resolutions of regional mapping images were degraded for inclusion in the USGS basemap of Europa (USGS, 2002), the raw *Galileo* images were imported and tied to the basemap at full resolution, which involved a series of steps. First, the raw regional mapping images were downloaded from the Planetary Data System (PDS) and converted into cube files for processing using the open-source United States Geological Survey (USGS) software ISIS3 (Torson and Becker, 1997; Anderson et al., 2004). Pointing information was attached to the raw cubes and basic I/F calibration was completed; see Appendix C for a more detailed explanation. Once the images were photometrically corrected, they were each imported into ArcGIS and aligned to their respective locations, using the USGS Europa basemap (USGS, 2002) as reference. The boundaries of potential features were mapped as polygons in ArcGIS. Each feature was then classified into one of seven categories, based on its apparent morphology (Fig. 2-1).

1. Chaos: a feature with a clear disruption of its interior area, with no clear evidence of topographic changes (i.e. shadows) across the feature, and without evidence of an elevation change within the feature. No distinction is made here between platy chaos and hummocky chaos (Spaun 2002; Prockter and Schenk, 2005).
2. Dome: a feature with an apparent shadow gradient across it, with the bright side on the sun-facing side, indicating positive topography. While previous work (Greenberg et al., 2003; Singer et al., in review) noted all features that exhibit

positive topography, some of them were classified as uplifts, rather than domes, due to their angular shape. Some of these features are included in this data set if it is clear that the uplift is its own independent feature (i.e. distinct from a nearby ridge system). There is no distinction noted here between domes and uplifts in the overall analysis done here, but the differences are noted in the data set itself.

3. Pit: an oval- to circle-shaped feature with an apparent shadow gradient across it, with the dark side on the sun-facing side, indicating negative topography.
4. Spot: an enclosed feature with consistent, dark albedo across the entirety of the feature. Presumably the formation of the spot modified the surface to the point where the previous terrain is completely erased because the present spot lacks any obvious signs of further disruption or topography changes.
5. Hybrid: a feature with the typical disrupted interior of chaos that surrounds a topography high or low. Culha and Manga (2017) first identified this microfeature type as dome/chaos, which can appear as hummocky or smooth. This definition differs from theirs in that here a feature is only classified as hybrid if there was clearly a dome/pit inside of the confines of the surrounding chaos, or if a feature appeared to be a dome/pit with a disrupted surface inconsistent with the appearance of the surrounding terrain. Thus, two two different morphologies for hybrid features are reported (Figure 2-1C and 2-1D). Note: only dome/chaos hybrids were observed in the study areas, although it doesn't rule out the possibility of a pit/chaos hybrid feature outside of the areas of study.
6. Unclassified: a feature with characteristics indicative of a microfeature (e.g., small, round or polygonal, clear delineation from other features) that could not be

confidently classified into a specific morphological type at the resolutions available.

7. Crater: a circular feature with negative topographic relief with a well-defined edge (crater rim). This rim is elevated along the entire perimeter of the feature. A central peak may or may not be present, and its absence does not preclude the classification of a crater. Though craters were noted in the data set, they were not included in the analyses as they are formed by an exogenic process, and it is assumed that microfeatures are formed from an endogenic one.

In selecting which quantitative characteristics to extract from the maps, focus was placed on those that seem to vary between feature types and are easily obtained using native ArcGIS tools. Area and perimeter were calculated with the Shapes and Graphics tool (see below). The minimum bounding geometry (MBG) tool was used to extract the maximum length and maximum width of the smallest rectangle that encloses each feature (Figure 2-3), dimensions which we used to calculate the aspect ratio of these rectangles (henceforth called eccentricity): the ratio of the maximum width of a feature divided by its maximum length. Finally, the zonal statistics (ZS) tool was used to retrieve information about the normalized reflectance (the apparent albedo) of each feature. Note that the normalized reflectance of a feature, while similar to, is not equivalent to a feature's albedo, as it requires photometric corrections that were not performed on the images here because of a lack of photometric constraints for Europa.

The ZS tool notes the digital number (DN) value of each pixel within a feature and calculates a number of metrics about that group of pixels. Here only mean, median,

standard deviation, and range are reported, though ZS has the ability to output many more metrics. The DNs in this case represent the I/F of the pixel as captured by the *Galileo* SSI camera and corrected using commands in USGS ISIS3 (Anderson et al., 2004); see Appendix C for more information. The final numbers are divided by 65,536, the maximum DN a 16-bit pixel can have, so that all normalized reflectance values are a ratio. A smaller ratio indicates that a feature has a lower overall normalized reflectance (i.e. appears darker). In order to map the entirety of the elliptical domes and pits, parts of the feature that were covered in shadow were also included, lowering the normalized reflectance values for those features. Therefore, the numbers presented here could be considered a minimum value for normalized reflectance. In particular, values for pits and domes may be more representative of the shadows caused by topography than the true albedo of Europa's surface within the feature. Shadowing from topography increases near the terminator, but features are spread throughout the images so there should be no bias towards additional shadowing from topography for any given feature type.

Before extracting data from the images, four sinusoidal projections were applied, one centered on the central meridian of each of the regions studied (Snyder and Voxland, 1994). Table 2-2 shows the central meridian of each region studied. The sinusoidal projection preserves both shape and size, with the distortion of features increasing with lateral distance from the central meridian, and at high latitudes (poleward of ±60°) (Snyder and Voxland, 1994). However, as different projections yield different values for area and perimeter, the best measurements are those that are independent of projection. The Graphics and Shapes tool (Jenness, 2011) was used in place of the usual Area and Perimeter calculations tools, which calculates the true area of polygons and lengths of

lines as they lay on the sphere independent of projection. Unfortunately, the tool was not able to calculate the maximum length and width of each polygon, so for those measurements; the value computed in the sinusoidal projection was chosen instead. When comparing the areas and perimeters of the features calculated using the sinusoidal projection to those acquired using the Graphics tool, the values were similar to within <1 km^2 (for area) and <1 km (for perimeter), and the majority were the same to within half those values. Because of the similarities in the values, and because only those two measurements could not be acquired with the Graphics tool, the few measurements that are projection-dependent can be used with confidence.

As an aside, the images were also processed using a series of custom codes written in MATLAB to remove the linear "darkening" trend. When the data of the apparent albedos was collected from the zonal statistics, there was no significant relative difference between the values collected from the ISIS3 corrected images reported later in this document and the values collected from the MATLAB corrected images (i.e. the overall differences between the microfeature groups were constant). Because the ISIS3 software is widely used in the community, the only values reported here are the normalized reflectance values taken in the ISIS3 corrected images; however, the MATLAB code is provided in Appendix D for completeness.

2.2.2 Validating the data set

To ensure accuracy in the classifications of mapped features, the feature data set was compared to three other data sets (Greenberg et al., 2003; Culha and Manga, 2016; Singer et al., in review), which first required that the data set collected by Greenberg et al. (2003) was digitized. In general, the features that were included in the final analysis

were those that were mapped in at least two out of the four datasets, allowing for exceptions if a feature is clearly present but only included in any one of the four data sets. The reason for this level of validation is primarily to account for the advance in technology that occurred between the creations of different data sets, and to allow for the maximum number of verified features to be counted in the final tally. The largest difference between the data sets is the number of features. Some data sets completely omitted features that at least two others included. The oldest data set (Greenberg et al., 2003) was most prone to this. Another reason for omission of features between data sets is that different data sets mapped in slightly different areas. For example, even if all data sets included the same RegMap, there were some areas within the RegMap where only two data sets overlapped. It was not clear if the other data sets failed to map features because they were outside of a predetermined study range, or if the creators did not see any features there. There were also some features that are clearly present, but extend beyond the RegMap images. Such features were excluded from the data set on the basis that one could not retrieve complete information about those features within images of the same resolution. Finally, Greenberg et al. (2003) did not include spots and chaos in their data set, so those feature types could only be compared between three data sets overall. Singer et al. (in review) included spots as a separate category, but they were analyzed as part of the chaos group because they were so few in number. Similarly, the only two data sets that included "hybrids" as a category were ours and the Culha and Manga (2017) data set, though the definitions of a hybrid feature presented here are different. As a result, some flexibility was built-in to accommodate the differences in the data sets.

The second difference between data sets lay in determining the boundaries of the features. The largest variation existed in the chaos features, especially in both RegMap02 regions, where there are multiple large chaos features—larger than the area covered by the RegMap images—that intersect the RegMap. Chaos features are irregularly shaped, and it is not clear in some cases where the boundary of one chaos feature ends and another begins. In these cases, only chaos features that were clearly distinct from one another were mapped in the data set. This led to some chaos features being omitted. The chaos feature sizes and shapes also varied between data sets, as the boundaries themselves were often inconsistent between data sets, especially between that of ours and Culha and Manga's (2016). In those cases, the polygons from the data set belonging to this author were included for consistency. Because the Greenberg et al. (2003) data set was digitized by this author, the features are not exactly the same shape and size as the authors originally mapped them, though every effort was taken to remain as true to the original as possible. In some cases, it was unclear what feature they mapped, and therefore some of their features (~5% of the total) were omitted from the digitization. For the most part, pits and domes were consistent in shape and size across data sets, as were spots when they were noted. Slight variations existed in orientation of the pits and domes, but the overall location was consistent across datasets.

Once the final data set was validated, all features larger than 100 km^2 in area were removed, which is equivalent to a circle with a diameter of 11.2 km. This size cut-off was chosen to narrow the data set to a size range that was applicable to all microfeatures in order to explore the relationship between feature types. Because this smaller size range is the focus, these features are collectively referred to as microfeatures. This term is based

on the fact that these features look small in the images of Europa that are currently available. Note that the Europa Clipper mission will return images with resolutions better than 50 m/pix over 95% of the surface (Turtle et al., 2016; Bayer et al., 2018), at least four times better than the resolution of the images used here. The higher resolution images may reveal even smaller features that were not visible in the currently available images; therefore, the term "microfeature" is likely a temporary one.

Finally, after validating the data sets and setting the size range, the characteristics of the data were determined. In the context of statistics, the sample refers to the features mapped in this study, which represent a subset of the entire population of features. For each characteristic we quantified, an "error" was computed that estimates the expected amount of variation in the measurements within each microfeature group. To calculate error, the standard error (SE) equation of $SE = \frac{\sigma}{\sqrt{N-1}}$ was used, where σ is the sample standard deviation of the data and N is the total number of features being analyzed. The factor of $\frac{1}{\sqrt{N-1}}$ converts the sample standard deviation into the unbiased estimate of the true population standard deviation from the available sample.

Reported here (Table 2-3) are the overall number of features of each type in each RegMap, and the average areas, diameters, eccentricities, and normalized reflectances of each of these feature types. Also included is how many features were excluded from the study as a result of the size cut-off, and to what category they belonged. In the case of chaos, the number that contained any evidence of rafts are also reported. Also included is information on the maximum lengths of these features overall, as this may be the measurement used to determine average feature sizes in previous studies (Carr et al.,

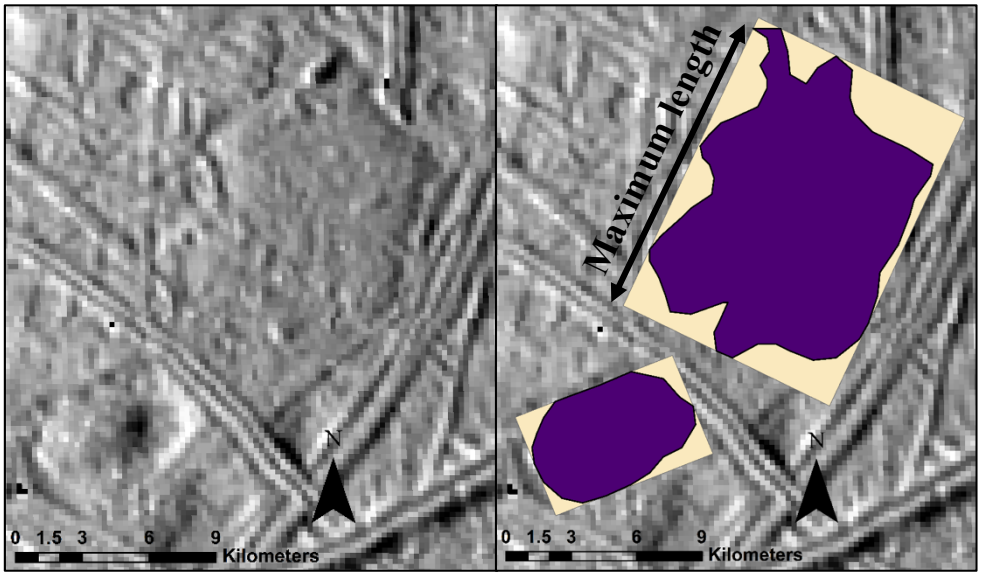

Figure 2-3: FID #52 and 53 in E15RegMap02. Some polygons drawn in ArcGIS overlying the rectangles created by the minimum bounding geometry (MBG) tool. The maximum length of a feature is defined as the length of the rectangle. Sun angle is from the top.

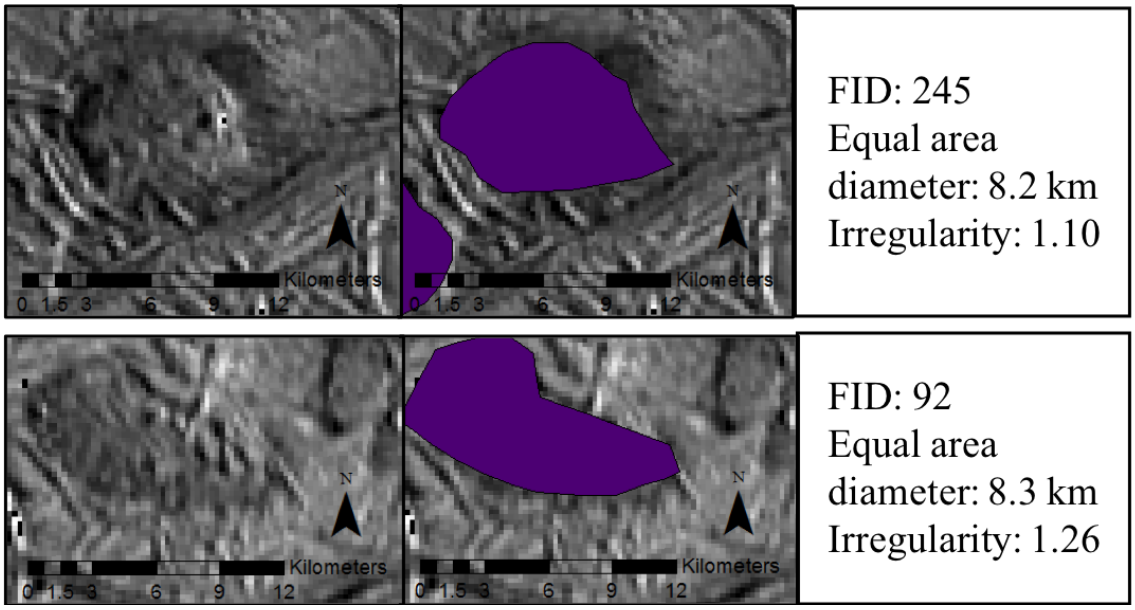

Figure 2-4: Visualization of the irregularity measurement using two features from E15RegMap01. These two features have the same equal area diameter, but their different shapes mean they have very different irregularity measurements. These features are both chaos, illustrating some of the variety of chaos feature shapes.

1998; Greeley et al., 1998; Pappalardo et al., 1998; Spaun, 2002); the visual of this measurement is shown in Figure 2-3.

Also developed here is a method to quantify the shapes of microfeatures, specifically a feature's irregularity. Qualitatively speaking, chaos features in particular tend to have irregular shapes whereas other microfeature types are more elliptical. Initially the diameter of a circle of equal area is calculated, represented by the equation: $Diam. = 2 * \sqrt{\frac{Area}{\pi}}$, for each microfeature as a way to consistently speak about the size of the feature. This information is used again to calculate the circumference of an equal-area circle. A feature's perimeter is then divided by the equal-area circle circumference. This will yield a ratio with a minimum value of 1.0, indicative of a perfect circle. A feature with a higher perimeter-to-circumference ratio will be more irregularly shaped (Figure 2-4).

2.3 Results

2.3.1 E15RegMap01, northern trailing hemisphere

All four data sets included features in this region (Figure 2-5). There are 306 total verified features in E15RegMap01 (Table 2-3). 27 chaos features and two hybrid features were excluded because they exceeded the size limit of 100 km^2, leaving 277 features in the data set. The most numerous feature type was pits (119), followed by chaos (68); domes, hybrids, and spots were less numerous and had similar numbers of features (33, 34, and 23, respectively). Chaos and hybrid features in this region are significantly larger than the domes, pits, and spots, which are all around the same size in both area and diameter. The eccentricities of all microfeature types do not differ significantly. Out of all

Region	Feature Type	Total number of features (number excluded on size)	Average Area (km^2)	Average Diameter (km)	Eccentricity (Aspect ratio)	Average Normalized Reflectance
E15RegMap01 Area: 356,529.51 km^2	Chaos	95 (27) Rafts: 11	51.0±2.4	7.9±0.2	0.67±0.03	0.339±0.012
	Domes	33 (0)	24.0±2.8	5.2±0.3	0.65±0.04	0.440±0.023
	Hybrids	36 (2)	40.4±3.3	7.0±0.3	0.67±0.02	0.358±0.016
	Pits	119 (0)	29.4±1.6	5.9±0.2	0.67±0.04	0.483±0.011
	Spots	23 (0)	18.8±1.6	4.8±0.2	0.68±0.05	0.278±0.020
E15RegMap02 Area: 613,109.02 km^2	Chaos	209 (120) Rafts: 30	43.5±2.5	7.2±0.2	0.68±0.03	0.416±0.011
	Domes	30 (0)	14.4±2.0	4.0±0.3	0.63±0.04	0.443±0.020
	Hybrids	25 (1)	35.1±4.1	6.4±0.4	0.65±0.03	0.403±0.019
	Pits	10 (0)	7.5±1.3	3.0±0.3	0.68±0.06	0.486±0.051
	Spots	1 (0)	9.1*	3.4*	0.84*	0.3*
E17RegMap01 Area: 630,229.91 km^2	Chaos	134 (65) Rafts: 21	51.7±2.9	7.9±0.2	0.67±0.03	0.377±0.012
	Domes	33 (1)	18.1±3.0	4.4±0.3	0.72±0.03	0.417±0.019
	Hybrids	23 (1)	36.4±4.9	6.5±0.4	0.64±0.03	0.385±0.018
	Pits	21 (0)	21.1±3.6	4.8±0.4	0.70±0.04	0.402±0.026
	Spots	4 (0)	10.7±3.6	3.5±0.6	0.60±0.03	0.448±0.023
E17RegMap02 Area: 490,409.50 km^2	Chaos	13 (0) Rafts: 0	47.3±8.1	7.4±0.7	0.69±0.05	0.318±0.026
	Domes	21 (0)	19.5±2.2	4.8±0.3	0.75±0.03	0.398±0.029
	Hybrids	10 (0)	35.1±5.4	6.5±0.5	0.68±0.07	0.340±0.037
	Pits	67 (0)	17.5±1.4	4.5±0.2	0.66±0.02	0.387±0.014
	Spots	1 (0)	6.7*	2.9*	0.50*	0.07*

Table 2-3: Summary of microfeature characteristics by RegMaps. The number within the parentheses for each RegMap represent the number of features that were excluded because they exceeded the maximum size of a microfeature.

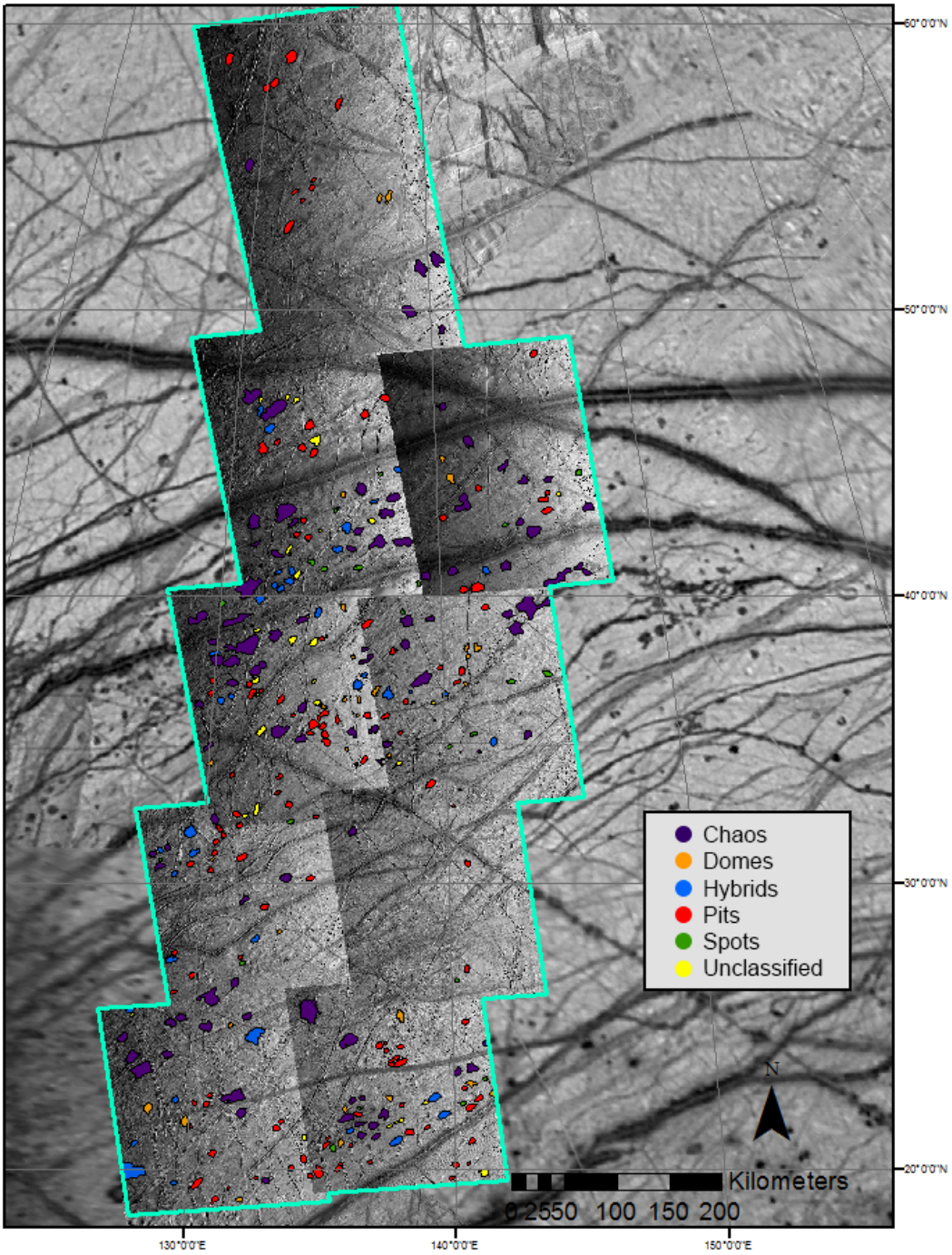

Figure 2-5: E15RegMap01, with mapped features shown as polygons. Purple polygons are chaos. Orange polygons are domes. Blue polygons are hybrids. Red polygons are pits. Green polygons are spots. Yellow polygons are potential features that were mapped, but left unclassified. No craters were observed in this region.

68 microchaos features mapped, 11 (16%) had evidence of rafts, but all features only had one or two, and the resolution of the images made it difficult to resolve any details about them.

In this region, the spots have the lowest mean normalized reflectance (i.e. they appear darker), followed by chaos and hybrids. Pits and domes have significantly higher normalized reflectance values than chaos, spots, and hybrids, making them appear brighter overall, although the reflectance values are affected by shadows and brightening related to their topography. As one side of pits and domes is directly illuminated, while chaos, hybrids, and spots are generally flat, the observation that pits and domes are brighter is consistent lighting and imaging geometries of the images. Pits and domes do differ significantly from each other in terms of normalized reflectance, with pits having the higher normalized reflectance.

2.3.2 E15RegMap02, northern leading hemisphere

All four studies mapped in this region (Figure 2-6), but each study had slightly different boundaries, resulting in some areas where this data set only overlapped with one other. There are 282 total verified features in E15RegMap02, with 160 that are less than 100 km^2 (Table 2-3), fewer than were in E15RegMap01. Chaos features are by far the most numerous feature type in this region (89), with similar, smaller numbers of domes and hybrids (30 and 24, respectively). In stark contrast to E15RegMap01, there were only 10 pits and 1 spot identified in this region, and 7 craters. This region sits within what appears to be a larger platy chaos region that extends well beyond the limits of the RegMap (Riley et al., 2000; Leonard et al., 2017; Leonard et al., 2018), which may contribute to the high number of features that are over 100 km^2. Chaos formation

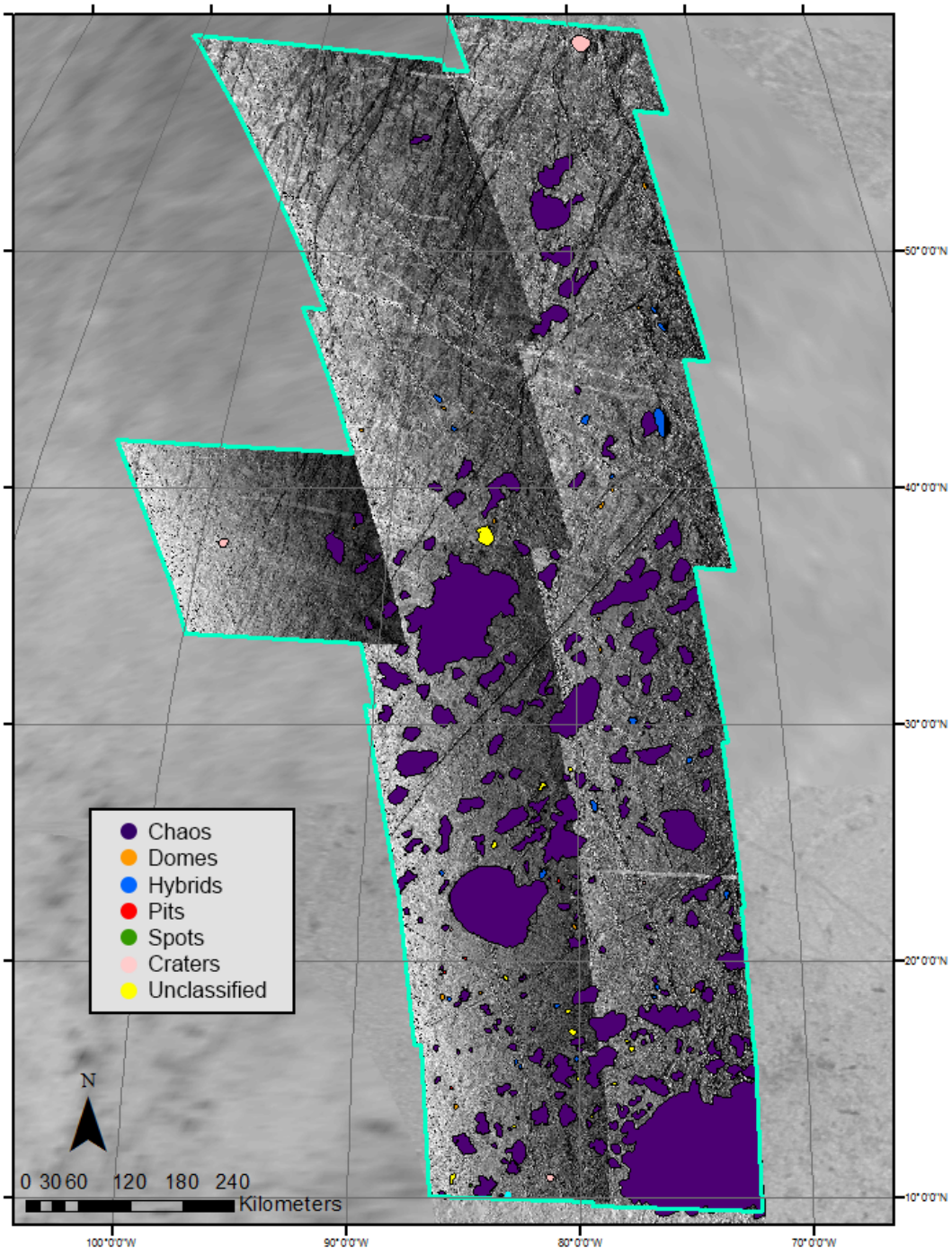

Figure 2-6: E15RegMap02, with mapped features shown as polygons. Purple polygons are chaos. Orange polygons are domes. Blue polygons are hybrids. Red polygons are pits. Green polygons are spots. Pink polygons are craters. Yellow polygons are potential features that were mapped, but left unclassified.

destroys preexisting terrain, so the presence of a large zone of chaos likely contributed to the overall lower numbers of identifiable microfeatures in this region. The eccentricities of all microfeature types do not differ significantly in this region either. Out of all the microchaos features mapped, 30 (34%) of them had evidence of rafts.

The chaos features are significantly affected by the size cut-off; 120 chaos features and one hybrid feature were removed when the size cut-off was imposed. Even below the size cut-off, chaos and hybrids are on average larger than the domes, pits, and spots, which are all around the same size in both area and diameter. This is consistent with the results in E15RegMap01. Pits in this region are 2 to 4 times smaller, on average, than pits in all other regions. The feature types with the lowest normalized reflectance values are spots, hybrids, and chaos features, with pits and domes both significantly brighter, and pits having the highest normalized reflectance.

2.3.3 E17RegMap01, southern trailing hemisphere

All four studies mapped in this region (Figures 2-7A and B), but not all mapped down to the same latitude. There are 216 total verified features in this region, including one crater, and 149 of these are less than 100 km^2 (Table 2-3). Chaos features are the most numerous (69), with about half as many domes (32) and a third as many pits and hybrids mapped and validated (22 and 21, respectively). Of the features that exceeded the size limit, all but two were chaos. One of the remaining features belonged to the hybrid class, and one was a particularly large uplift, the only one over 100 km^2 in any of the four mapped regions. Once again, the chaos and hybrid features are significantly larger than the domes and pits, which are all around the same size in both area and diameter, consistent with the results from other regions. The spots (4 in total) are significantly

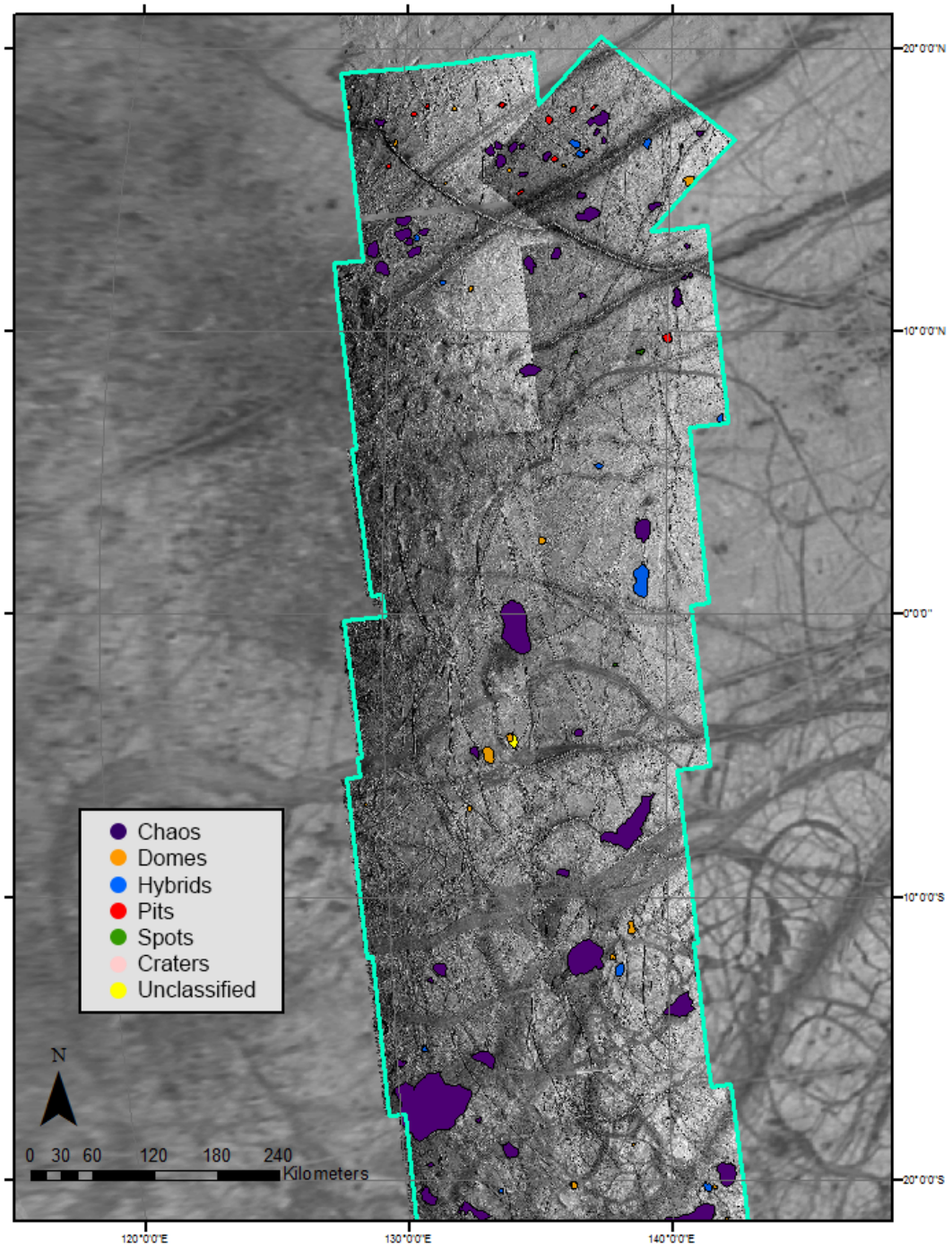

Figure 2-7A: The top section of E17RegMap01, with mapped features shown as polygons. Purple polygons are chaos. Orange polygons are domes. Blue polygons are hybrids. Red polygons are pits. Green polygons are spots. Pink polygons are craters. Yellow polygons are potential features that were mapped, but left unclassified.

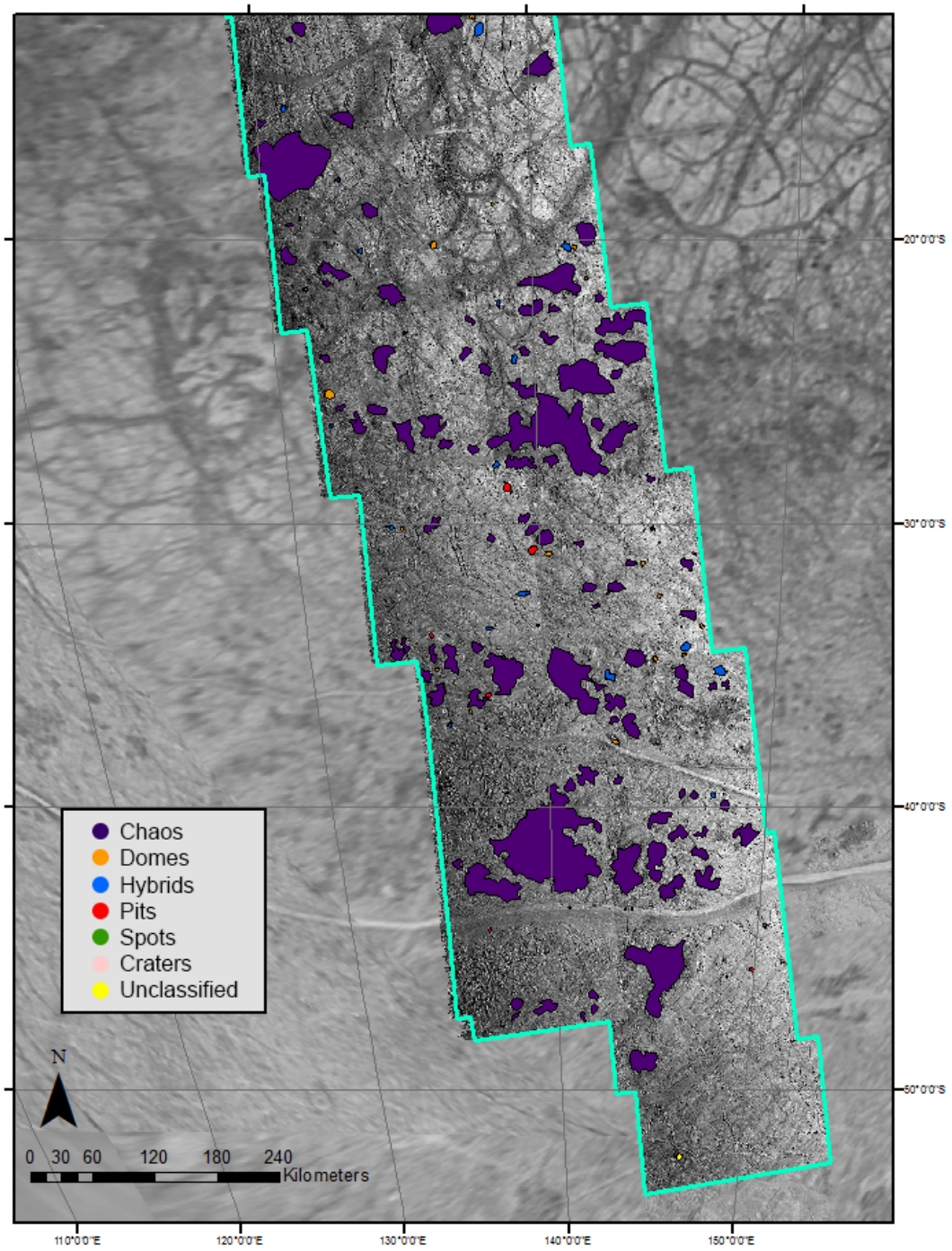

Figure 2-7B: The bottom section of E17RegMap01, with mapped features shown as polygons. Purple polygons are chaos. Orange polygons are domes. Blue polygons are hybrids. Red polygons are pits. Green polygons are spots. Pink polygons are craters. Yellow polygons are potential features that were mapped, but left unclassified.

smaller in area and diameter than any other feature type, another consistent result across the regions. The domes and pits in this region also have an eccentricity that is significantly different from chaos, hybrids, and spots. Spots have a significantly lower eccentricity than all other microfeatures. Out of all microchaos features mapped, 21 (30%) had evidence of rafts.

The normalized reflectance of chaos is the lowest of all the features, followed by hybrids. Domes and pits are around the same normalized reflectance value, though domes are slightly brighter. This could indicate that the pits in this region are deeper than in other regions, and their large shadows are lowering the overall mean normalized reflectance values. According to these values, the spots have the highest normalized reflectance in this region, but this could be because of a small sample size, which is associated with higher errors.

2.3.4 E17RegMap02, southern leading hemisphere

In this region (Figures 2-8A and B), there are significantly fewer features than in any other, and they are consistently smaller than in the other regions. Out of the 125 total features in E17RegMap02, only one – a crater - was excluded based on size (Table 2-3). This region also had the most overall number of craters (12). Pits are the most numerous features (67), and there are a third as many domes (21). In general, all features are significantly less numerous than in any other region. Domes outnumber both chaos and hybrid features (13 and 10, respectively), the only region where this is observed. The chaos and hybrid features are significantly larger than the domes, pits, and spots, which are all around the same size in both area and diameter. The eccentricities of chaos and hybrids do not differ significantly to any other feature type, but the eccentricities of

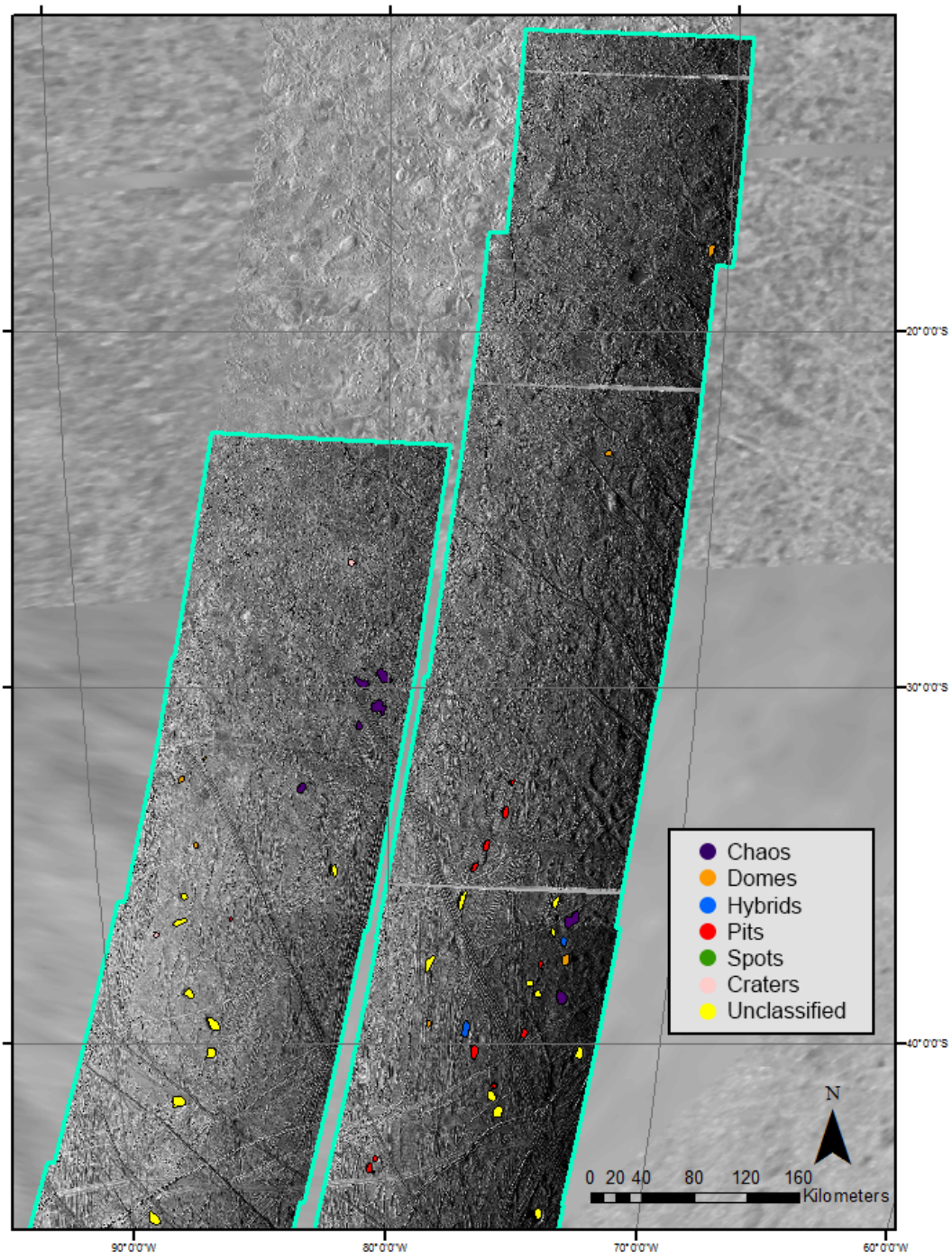

Figure 2-8A: The top section of E17RegMap02, with mapped features shown as polygons. Purple polygons are chaos. Orange polygons are domes. Blue polygons are hybrids. Red polygons are pits. Green polygons are spots. Pink polygons are craters. Yellow polygons are potential features that were mapped, but left unclassified.

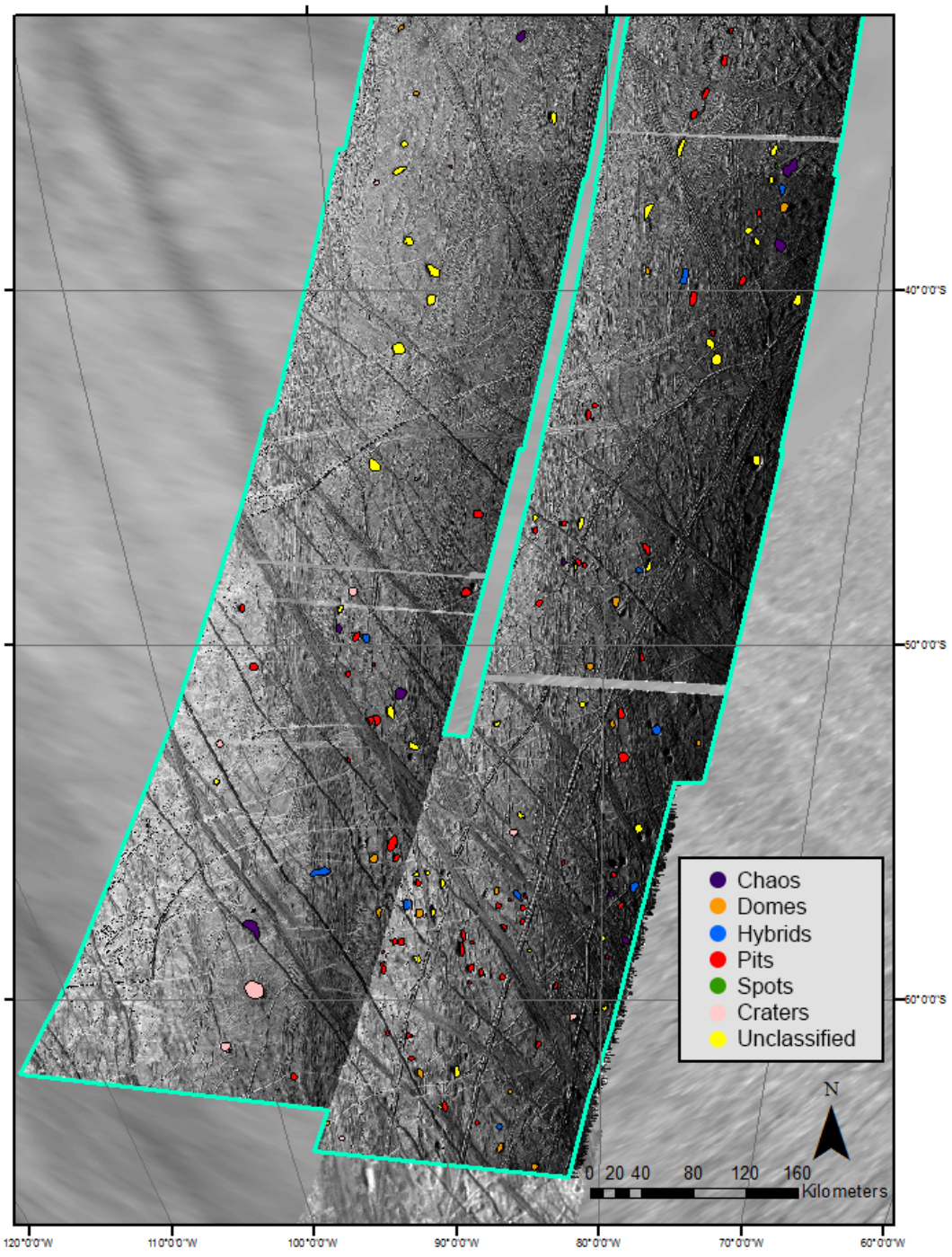

Figure 2-8B: The bottom section of E17RegMap02, with mapped features shown as polygons. Purple polygons are chaos. Orange polygons are domes. Blue polygons are hybrids. Red polygons are pits. Green polygons are spots. Pink polygons are craters. Yellow polygons are potential features that were mapped, but left unclassified.

domes and pits are significantly different from each other. Out of all microchaos features, none had clear evidence of rafting. Chaos features, and one spot, are the darkest features in this region, and hybrid features are slightly brighter than chaos. Domes and pits are, on average, the brightest feature types in this region.

2.3.5 Overall observations

Comparing across all four mapped regions, chaos is the most numerous feature type, almost equaled in number by pits. However, chaos features are more consistently numerous whereas pits are spatially heterogenous. Spots are the least common, overall, and most spots are concentrated in one region (E15RegMap01). Domes are most consistent in terms of their spatial distributions, with roughly equal numbers in all regions, even those with fewer total features. Overall values are provided in Table 2-4.

In the area histogram (Figure 2-9), the bin sizes are 5 km^2, and the data points on the histogram represent the centers of the bins. Chaos and hybrid features are significantly larger than the domes, pits, and spots, which are all around the same size in both area and diameter. The size distribution of pits and domes both indicate a higher concentration of features at smaller sizes, but no features under 1 km can be confidently measured due to the resolution limit. The size distribution of spots is also clustered at small sizes; it both ascends to and descends from its peak more gradually, and there are no spots larger than 35 km^2. Pits have a definite peak between 10 and 15 km^2, while domes have a broader peak between 5 and 25 km^2. Hybrids have a small peak around 25 km^2, but above this size the distribution is uniform until it gradually drops off at larger sizes. Chaos dominates in number at large areas, though there is at least one pit and one

Table 2-4: Overall characteristics of microfeatures in the four RegMaps. Italicized text represents the subgroups of Type I and Type II hybrid features and are included in the hybrid (all) count, as they are not separate features.

Feature Type	Number of features	Average Area (km^2)	Average Diameter (km)	Eccentricity	Average Normalized Reflectance	Average Irregularity
Chaos	239	48.2±1.5	7.6±1.5	0.68±0.04	0.377±0.007	1.16±0.01
Domes	116	19.1±1.3	4.6±0.2	0.68±0.06	0.427±0.011	1.10±0.01
Hybrids (all)	90	37.5±2.1	6.7±0.2	0.66±0.04	0.374±0.010	1.12±0.01
Hybrids: Type I	*25*	*38.8±5.1*	*6.7±0.5*	*0.65±0.11*	*0.369±0.021*	*1.15±0.02*
Hybrids: Type II	*65*	*37.0±2.2*	*6.7±0.2*	*0.66±0.07*	*0.376±0.022*	*1.11±0.01*
Pits	217	23.9±1.1	5.2±0.1	0.67±0.05	0.445±0.010	1.10±0.01
Spots	29	16.9±1.5	4.5±0.2	0.67±0.06	0.295±0.021	1.13±0.02
TOTAL	691					
Total area studied: 2,090,277.94 km^2 (6.43% of Europa's surface area)						

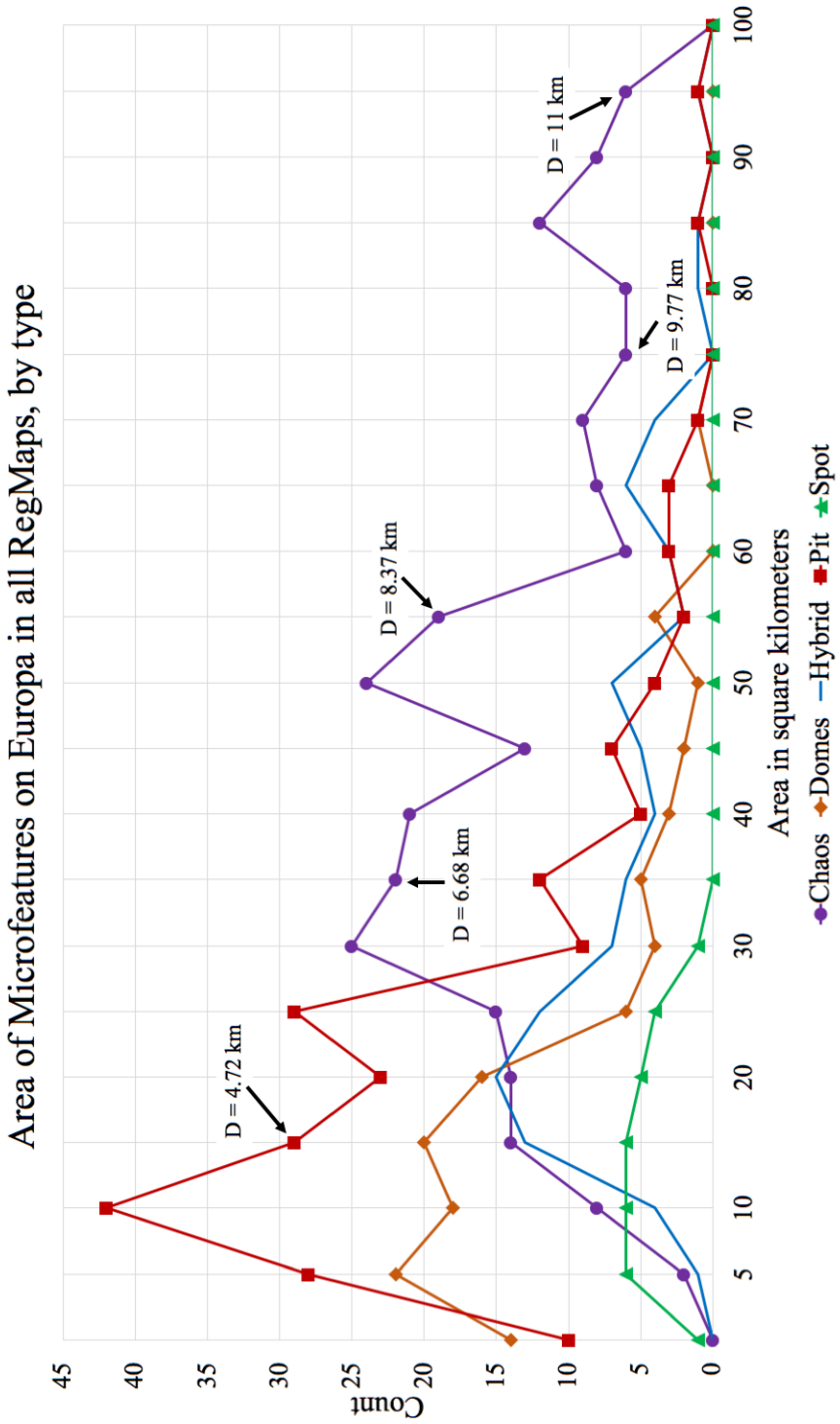

Figure 2-9: A line histogram showing the areas of microfeatures in the four RegMaps studied here, separated by type. Bin sizes are consistent throughout the chart and represent areas of 5 km^2.

hybrid feature that reach at least 90 km^2 in area (excluding the dome that was removed due to size cut-off constraints in E17RegMap01). Chaos has a roughly normal distribution, with a clear peak between 50 and 60 km^2. The rise up to the peak is roughly linear, and after the peak the counts remain approximately uniform until the upper size limit of 100 km^2. There is an imposed truncation in the chaos distribution due to the size cut-off at 100 km^2, which is expected as chaos features are known to exist above the size cut-off. All other feature types decline in number at large sizes and are, therefore, unaffected by the imposed size limit. There is also a steep drop off in the number of features observed below a few km^2, which may be a resolution effect (see also, discussion in Section 2.4.1). A similar size distribution was reported by Singer et al. (in review).

The maximum lengths of features (Figure 2-10) were also examined. The maximum length of a feature is likely to be larger than the equal area diameter as a feature can be eccentric or shaped irregularly. The equal area circle diameter does not retain information related to how a feature is shaped, but the maximum length is more sensitive to these differences. Maximum length is also an easier measurement to envision, and previous studies may have considered the lengths of these features while describing their sizes. Like the areas, the majority of the features of all types cluster around small sizes. Pits and domes peak between 4 and 7 km in maximum length, while hybrids and spots peak between 5 and 7 km. Only chaos features peak around 10 km, a "typical size" reported in past studies (e.g., Pappalardo et al., 1998; Riley et al., 2000; Spaun 2002; Collins and Nimmo, 2009; see discussion in 2.4.2), though it is noted that only small chaos was considered in this study. Even so, these peaks are broader than those seen in the area histogram, implying a broad range of sizes.

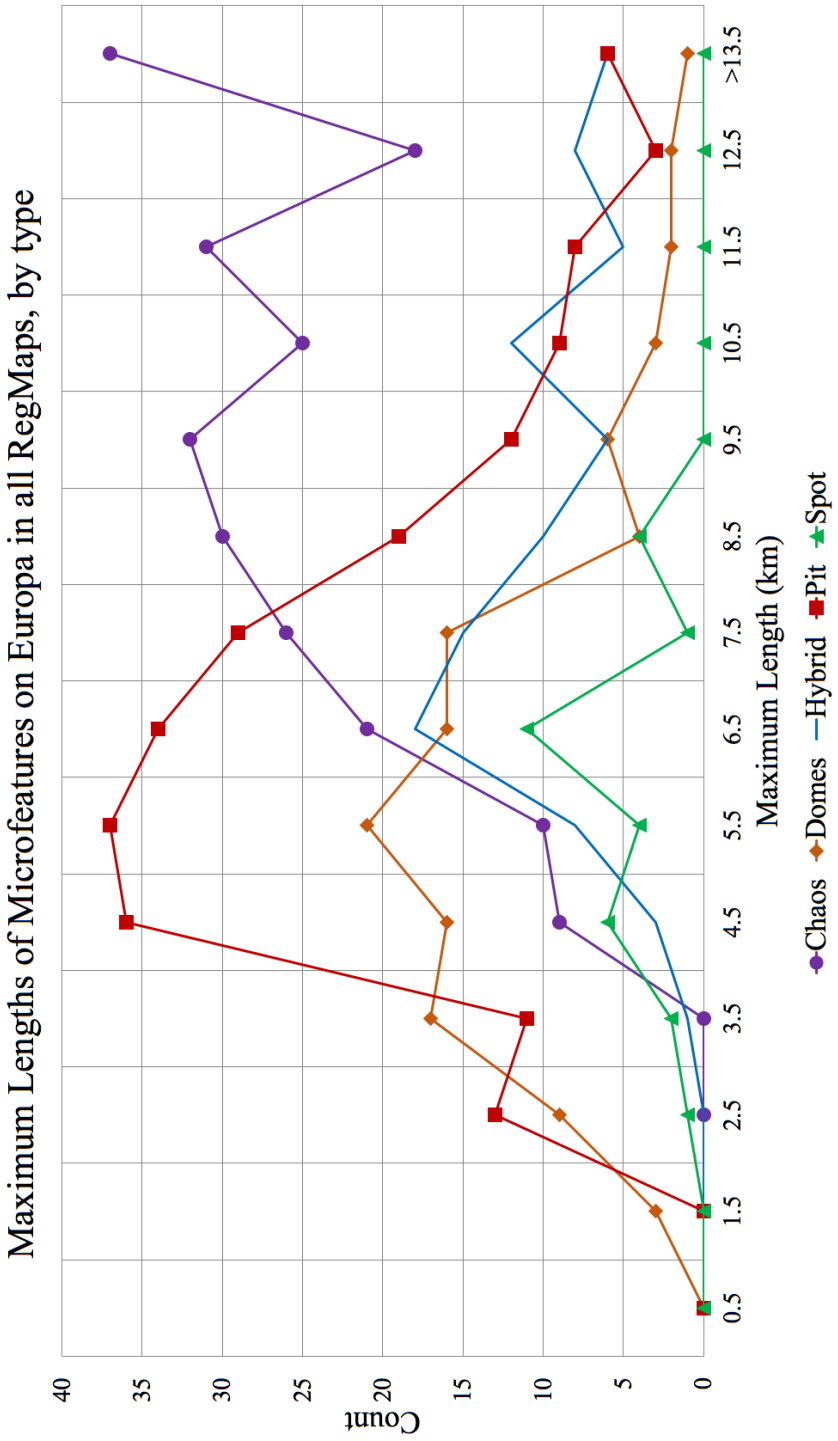

Figure 2-10: A line histogram showing the maximum lengths of microfeatures in the four RegMaps studied here, separated by type. The points represent the center of the bin. Bins are the same size and represent distances of 1 km in length.

Overall, spots are the darkest features, although they are also the least numerous features, which makes them susceptible to large errors due to a small sample size. In all four study areas, chaos and hybrids have around the same normalized reflectance values, although chaos is slightly darker. This shared characteristic suggests a common process affecting the formation of chaos, spots, and hybrid features. Domes and pits have roughly the same values of normalized reflectance, with pits being slightly brighter than domes. The higher normalized reflectance of pits may be because of their geometry; there is more area within pits that reflects sunlight, which is both a function of their topography (i.e. the depth and symmetry of an individual pit) and the lighting angle of the image. An asymmetrical pit may have one side that reflects more sunlight than the other, while a non-nadir lighting angle could increase the amount of the sunlight in the pit. In E15RegMap02, the normalized reflectance values are higher on average than in the other regions, indicating that this region was more illuminated than other regions were, which resulted in a brighter set of images even after photometric correction. It could also increase the length of a dome's shadow, another reason for why the dome's average normalized reflectance value is slightly lower than that of pits.

2.3.6 Locations of microfeatures

In order to compare the number of features below and above the equator, the features in the data set were separated into these two latitudinal groups based on its latitude, regardless of the RegMap in which a feature was mapped. There are more than twice as many features above the equator than below it (480 features above compared to 211 below), even though the total area mapped in the southern hemisphere was larger than the total area mapped in the northern hemisphere. The same was done with longitude

to compare the number of features in the leading hemisphere to the number in the trailing hemisphere. Once again, there was a large discrepancy in the number of features between the two hemispheres; there are 425 features in the trailing hemisphere, and 266 in the leading hemisphere. The total area mapped in the trailing hemisphere is smaller than the total area mapped in the leading hemisphere. Possible reasons for these population size differences are discussed in Section 2.4.1.

2.3.7 Eccentricity and irregularity of features

Overall, eccentricities do not vary between microfeature types, though this does not hold true for each region. Domes and pits had the smallest irregularity measurement of all the features. Chaos has the highest average irregularity of all the feature types, which is significantly higher than pits, domes, and hybrids. Spots have a high irregularity value, but with a small data set, the error is high. These results are consistent with the qualitative result that chaos is irregularly shaped. It also suggests that the average irregularity of chaos features is significantly different from that of domes and pits. Hybrid features have an intermediate average irregularity value, but are more similar to the average domes and pit irregularity values overall.

2.3.8 Hybrids

In simplest terms, hybrids are a blend between a chaos feature and a dome, but not all hybrid features combine chaos and domes in the same ratio. What has here been defined as Type I hybrid morphology shows an elliptical, topographically-positive feature within a dark "moat" that is usually smoother than the surrounding terrain. This "moat" can be smooth or hummocky, similar to the interiors of some chaos features. The domes and uplifts within these hybrid features usually have a disrupted surface, though it is not

true of every case, and are smaller than the full extent of the "moat." The Type II hybrid morphology shows a dome or an uplift with a significantly disrupted surface, and lacks the "moat" characteristic of the Type I hybrids. While some domes retain the evidence of a cross-cutting ridge or trough, the Type II hybrid features show a disruption pattern that is inconsistent with the surrounding terrain. These features have been noted previously in the literature; Greenberg et al. (2003) described these kinds of features as cracked domes.

Overall, there are 65 Type II hybrids and 25 Type I hybrids, a ratio of about 2.5:1. The only region where Type I hybrids outnumber Type II hybrids is E17RegMap01. In all regions, there is no significant difference in size between the two hybrid types; indeed, the equivalent diameter for both types is identical. There is also no significant difference in the eccentricities of the two hybrid types. The Type I hybrid features have a significantly lower average normalized reflectance than the Type II hybrids, as the "moats" are dark and exhibit little variation in topography or albedo, as opposed to the dome-like Type II hybrid features. Type I hybrid features also have higher irregularity than the Type II hybrid features, and share a value more similar to that of chaos.

2.4 Discussion

In this study, four data sets of microfeatures in Europa's four RegMap areas were merged together to create the most robust data set possible. The shape files are available in an online supplement. In total, a total of mapped, validated, and characterized 691 microfeatures across Europa's surface. These observations are presented as constraints for present and future modeling efforts.

2.4.1 Implications of microfeatures characteristics

Small chaos features and pits are the most numerous types of microfeatures across the four regions studied, although pits are spatially heterogeneous whereas chaos is more consistently prevalent across all regions. Pits are sometimes numerous even in regions that have fewer microfeatures overall, making up anywhere from 6% to 54% of the microfeatures in a given region. In contrast, the number of domes and hybrids are relatively uniform across all four regions, and spots are always much less prevalent than other microfeature types.

To further explore spatial differences in the number and character of microfeatures, it is important to first consider potential sources of observational bias. First, there is an extensive area of dispersed chaotic terrain in the leading hemisphere between ~10°N and ~30°S (as mapped by e.g., Riley et al., 2000), which reduces the mappable area in E15Regmap02 and E17Regmap01. No individual microfeatures could be confidently mapped within this broad region of surface disruption, which could partially explain why fewer microfeatures were identified in the southern hemisphere and the leading hemisphere, and the fewest in the south leading hemisphere (E17RegMap02). In addition, the presence of many large chaos features, which were mapped but excluded from the reported feature counts, were much more numerous in the north leading hemisphere than in other regions. The presence of these larger features leaves less area in which to identify microfeatures, so they may also contribute to the smaller number of features observed in the leading hemisphere. Therefore, the relative numbers of observed microfeatures may be more suggestive of a difference in the character of chaos features, from clusters of microchaos to discrete large chaos features to diffuse regions of disruption, across Europa's surface.

Separate from the issues of observational bias, there appears to be a spatial difference in the character of chaos features. While microfeatures are more concentrated in the northern and trailing hemispheres, large chaos features are more numerous in the leading hemisphere, especially in the E15RegMap02 area (Riley et al., 2000; Leonard et al., 2017). From previous mapping studies (Riley et al, 2000; Figueredo and Greeley, 2004; Collins and Nimmo, 2009; Culha and Manga, 2016; Leonard et al., 2017), the largest chaos features are mapped close to Europa's equator, including Conamara and Manannán. The largest chaos features mapped in this study were in the E15RegMap02 and E17RegMap01 regions, which are in the northern, leading quadrant and southern, trailing quadrants, respectively. Thera and Thrace Maculae lie in between the two southern RegMaps studied here, but they are more fully situated in the trailing hemisphere.

It is interesting that the quadrants with the larger features are diagonal to each other, which may point to a symmetric heating source driving the formation of these larger chaos features. Part of the reason for this could be attributed to differences in the ice shell properties in these regions; if fractures penetrate deeper where tidal stresses are larger, sills could form in higher numbers or with different depths and sizes that contribute to the prevalence of larger chaos. It could also be that there is a concentration of heat at low-latitudes on Europa, perhaps as a result of latitudinal heterogeneity (Soderlund et al., 2014), and this heat creates the larger chaos features. Concentrations of large chaos features have been previously noted (e.g., Schenk et al., 2008) near 120°W and 300°W in support of a polar wander scenario, which could be interpreted to support diapirism, as tidal heating is most concentrated near the poles (Collins and Nimmo,

2009). While there appear to be no obvious correlations between the locations of large chaos patches to predictions regarding the equilibrium ice thickness (e.g., Ojakangas and Stevenson, 1989), the limited spatial extent of this mapping project makes it difficult to address and characterize global processes that could drive microfeature formation, and an extensive modeling project addressing these issues is outside the scope of this manuscript.

The morphology of chaos features may also suggest a difference in the formation process between large and small-scale features. Chaos has two different, well-documented morphologies: platy (e.g., Conamara chaos) and hummocky (e.g., Murias chaos). Roughly 41% of the surface area of Conamara chaos is platy (Spaun et al., 1998), a typical value among larger chaos features (Spaun, 2002). Some clear examples of platy chaos were identified at smaller sizes (<100 km^2) within the regional mapping data set, a result consistent with the identification of individual rafts within some smaller chaos features around Conamara (Tognetti et al., 2017; Leonard et al., 2018). Even when potential rafts were found, however, they were not numerous and it was difficult to note any details about them, a result also reported in Leonard et al. (2018). The lack of discernable rafts within small chaos features could potentially be a result of image resolution, or it could point to a difference in the way surface disruption occurs during the formation of large and small-scale chaos features. The fact that rafts in small-scale features have been identified in proximity to the archetypical example of platy chaos (i.e. Conamara) may also suggest that microchaos can develop as part of the formation of large-scale features, with morphologies dictated by the formation process of the large features.

In the model of Manga and Michaut (2017), pits form as an intermediate phase of microfeature formation in which liquid water is present within the ice shell. That model implies that the differences in pit density in different regions represents a heterogeneity in the presence of liquid water within the shell, perhaps suggesting that regions with fewer pits have not experienced recent endogenic activity. Note that the region with the fewest pits (E15RegMap02) also has the largest number of craters, lending credence to the idea that the surface is older, with less endogenic activity in the recent past than other regions. Although that region is affected by the presence of large chaos features potentially reducing the area in which features can be identified, the decline in the number of pits relative to other regions is much more drastic than for other feature types.

No evidence was found to support past assertions that microfeatures have a typical diameter of 10 km (Carr et al., 1998; Greeley et al., 1998; Pappalardo et al., 1998; Spaun, 2002). Instead, it was found that microfeature types vary in their typical sizes, each type presents over a fairly wide range of sizes, and only chaos features display any size characteristics consistent with typical diameter of 10 km. Chaos and hybrid features are significantly larger than pits, domes, and spots across all regions studied. The average sizes of domes and pits are within each other's error bars. Even when considering the maximum lengths of the features, only chaos features peaked around 10 km, while all other features peaked at significantly smaller sizes. A better estimate for the average size of microfeatures of all types is 2–6 km in terms of equal area diameter, and 4–9 km in terms of maximum lengths.

Because the pixel scale of the images was at least 218 m/pix, and assuming a five-pixel detection limit, the smallest feature that could be confidently identified in this study

is ~1 km in diameter, as reported by Singer et al. (in review). The rapid decrease in number of features observed as area drops below roughly 10 km^2 could indicate that there is a minimum size associated with the formation of microfeatures, but the detection limit within the regional mapping images may also play a role. Singer et al. (2010) looked for pits and domes in the limited set of higher resolution images across Europa, including ones that cover parts of the RegMaps, and did not find features of increasingly smaller size. Even though the results of Singer et al. (2010) and this study are consistent, this team has only looked at roughly 7% of Europa's total surface, and smaller features could exist outside of these areas studied.

Many previous chaos mapping studies (Head and Pappalardo, 1999; Greenberg et al., 1999; Prockter et al., 1999; Spaun et al., 1999; Greeley et al., 2000; Riley et al., 2000; Spaun, 2002; Figueredo et al., 2002; Greenberg et al., 2003; Figueredo and Greeley, 2004; Spaun et al., 2004; Collins and Nimmo, 2009; Schmidt et al., 2011; Culha and Manga, 2016; Leonard et al., 2017) note that chaos features typically have low albedo, although there are counterexamples (e.g., Conamara chaos). A higher albedo does not exclude a feature from being classified as chaos, and instead introduces a new dimension to understanding chaos and its relation to other microfeatures. Chaos, spots, and hybrid features have similar normalized reflectance values, which may support the claim that their formation involves a similar process. Additionally, their normalized reflectances are lower than those of pits and domes. Comparisons can be made within this data set because the imaging geometry is similar and the same photometric corrections were applied to all of the images. The normalized reflectance values may not be the same in

images with different imaging geometries or lighting conditions, and the normalized reflectances reported may not be well-correlated with albedo.

Lower albedo terrain on Europa is usually associated with reddish-brown material, which has been interpreted as evidence of salts on Europa's surface (McCord et al., 2002; Dalton et al., 2005; Carlson et al., 2005; Carlson et al., 2009; Hand and Carlson, 2015). Brine inclusion has been suggested as a feature of chaos formation (Head and Pappalardo, 1999; Han and Showman, 2005) because the inclusion of salts and other impurities will lower the melting temperature of ice, making it easier for surface disruption to occur. The fact that domes and pits have higher average normalized reflectances than chaos, hybrids, and spots may imply that briny, liquid water is only brought to the surface during the formation of the latter features. However, the idea that liquid water in the shallow subsurface plays a role in the formation of pits and domes, as in the model of Michaut and Manga (2014), cannot be ruled out, particularly because normalized reflectance is dependent on photometric correction and viewing geometry, and thus, may not be an accurate indicator of lower albedo material.

The source of liquid water within the ice shell is still undetermined. Liquid could form as partial melt at the top of a rising diapir within a convecting ice shell, or ocean water could be injected into the ice shell by an overpressurized ocean through a pre-existing fracture in the ice. Work by Hand and Carlson (2015) shows that the reddish-brown color is more consistent with sodium chloride irradiated over long periods of time in Europa's environment, and argues that it is evidence that Europa's ocean is in direct contact with the surface. This interpretation is more consistent with the liquid water sill hypothesis (Schmidt et al., 2011; Michaut and Manga, 2014; Manga and Michaut, 2017)

than with the *in situ* partial melt one. Still, the possibility that the salts are hydrated sulfate salts (McCord et al., 2002; Dalton et al., 2005) or sulfuric acid hydrate (Carlson et al., 2005) cannot be ruled out.

2.4.2 Predictions associated with formation models

Multiple studies (Pappalardo et al., 1998; Rathbun et al., 1998; Pappalardo et al., 2004; Collins and Nimmo, 2009, and references therein; Schmidt et al., 2011; Culha and Manga, 2016; Manga and Michaut, 2017) have suggested that all of these microfeature types are related. They could be different stages of one process occurring on Europa, or the same process yielding different results because of the particular environment in a certain location. These observations are now compared to the predictions and assumptions of the main formation models: diapirism, cryovolcanism, and sill formation.

Pappalardo et al. (1998) first suggested that the different microfeatures are genetically related, and that domes and chaos were especially indicative of a warm-ice diapir within a convecting ice shell between 3 and 10 km thick. One piece of evidence in favor of this model was that the microfeatures appeared to be around the same size, between 7 and 15 km in diameter, in an area centered at 15°N and 270°W (Conamara region). This region is not included in the data set. Broadly speaking, microfeatures are similarly sized, but most features are smaller than the range reported by Pappalardo et al. (1998), and that chaos features are substantially larger than other feature types. Hence, if all microfeatures are formed though diapirism, the diapirs would need to be capable of producing smaller surface features (e.g., 4–7 km across), consistent with the sizes observed outside the Conamara region.

Rathbun et al. (1998) studied 42 domes in the same region. Their findings corroborated the diapirism model in that the features were a consistent size, but they noted a potential problem: diapirs small enough to have formed the observed domes would have lost their heat too quickly, even before they reached the surface. Hence, while small diapirs could explain the presence of small isolated domes, the domes should be rare. Rathbun et al. (1998) also noted that some of the domes had surrounding "moats," which is more consistent with the definition of hybrids than domes. Domes and hybrids are roughly half as numerous than microchaos and pits, but they are much more common than spots.

Later work examined the roles that concentrated tidal heating (Sotin et al., 2002; Mitri and Showman, 2008; Han and Showman, 2010), plasticity of the ice shell (Showman and Han, 2005), and salinity (Pappalardo and Barr, 2004; Han and Showman, 2005) have on the ability of a diapir in a convecting ice shell to produce the observed microfeatures. In general, these papers focused primarily on chaos and dome formation, and only one explicitly mentioned the formation of pits (Showman and Han, 2004). None addressed the formation of spots. Han and Showman (2005) used numerical simulations to show that a diapir with sufficient temperature and salinity contrast to the surrounding ice would become buoyant enough to form uplifts and pits with 100–500 m of relief, consistent with later mapping results (Schenk and Pappalardo, 2004; Singer et al., 2010; Singer et al., in review). However, they were unable to create features with the diameters observed here; all their features were between 10 and 30 km in diameter (78.5 km^2 and 706.9 km^2 in area, respectively), almost exclusively outside of the range examined here. While there are chaos features in this size range, there are almost no domes and pits that

are those sizes. Furthermore, in a later study, they were unable to produce any isolated pits or uplifts/domes of any diameter (Showman and Han, 2005), which is inconsistent with the observations. Based on the current modeling results, the small sizes and prevalence of pits and domes are inconsistent with the diapir formation model. However, because chaos features and hybrids are typically larger than other microfeature types, diapirism cannot be ruled out as a formation mechanism for chaos.

Quick and Marsh (2016) investigated whether the cracked domes (called Type II hybrid features here) could have been formed by cryovolcanism. They used numerical simulations to first verify that cryomagma can ascend within Europa's ice shell. They found that warm ice can move through Europa's lithosphere, and that its speed is comparable to ascent velocities of terrestrial magma diapirs moving through Earth's mantle (Quick and Marsh, 2016). On Earth, dikes and pre-existing fractures can be used repeatedly by multiple magma ascensions, eventually forming features such as shield volcanoes. A similar process could happen on Europa, and domes could be the result of repeated eruptions of cryolava on the surface (Quick and Marsh, 2016). Later work on dome relaxation revealed that the model dome topographic profiles match the estimated dome heights observed on Europa. Moreover, they found that the average dome radius is 3 km, consistent with these observations (Quick et al., 2017). They also investigated the compositional evolution of the cryomagma inside of a diapir, as an eruption could bring material to the surface from Europa's interior, and provided more evidence that the salts observed on Europa's surface are endogenic (Quick and Marsh, 2016). Cryovolcanism is consistent with the sizes of domes and hybrid features, and it provides a natural explanation for the lower normalized reflectance of hybrid features. However, this model

does not provide a natural mechanism for forming chaos features, pits, or spots, which would suggest multiple processes or different manifestations of cryovolcanism in order to explain all microfeature types. Additionally, no evidence of flow features was observed. Additionally, work by Rathbun et al. (2010) that studied the thermal inertia of Europa's surface was not able to detect any thermal evidence of recent (< 100 years) outflows, even though there was evidence to suggest that flows as small as 100 km^2 should have been visible.

The microfeature formation model proposed by Manga and Michaut (2017) invokes the presence of a liquid water sill, in which the depth of the sill relative to the surface and the strength of the ice layer containing the sill control whether a dome or a pit is formed. A sill that forms at a shallower depth will have more support from the ice beneath it, allowing it to expand upwards and outwards, increasing the positive relief of the overlying ice and the lateral extent of the feature itself. This arrangement will form a dome. A sill that forms deeper in the ice shell, near the boundary between brittle and ductile ice layers, will not have the bottom support to grow, so it will instead become deeper, with a lesser lateral extent. This negatively warps the surface above the sill, forming a pit. However, the evolutionary stage of the sill and the radius of the sill itself can affect the appearance and size of the feature it potentially creates; as the liquid water freezes, the model predicts that pits will evolve into domes. Hence, pits could indicate pockets of deeper liquid water whereas domes could indicate shallow liquid water or frozen sills that initially created pits.

This model also predicts that domes should be larger than pits (Manga and Michaut, 2017). The model first relates the depth of the sill to the size of the feature. If

there exist two sills at the same depth in the ice shell where, because of differences in the depth of the elastic layer of Europa's ice shell, one sill formed a dome and the other formed a pit, then the dome should have a larger diameter despite the same sill depth. This is because the weight of the liquid water in the sill will cause the ice underneath the sill to warp downward, causing "the intrusion's lateral extent [to] decrease a few tens of percent" (Manga and Michaut, 2017). Pits and domes are not significantly different in either average overall area or average diameter, which disagrees with the model prediction. Additionally, the model suggests that larger water bodies are more likely to lead to disaggregation of the surface, forming chaos features. Because larger sills form larger surface features, chaos features should be larger on average than the other microfeature types. These results are consistent with this prediction. Chaos is, on average, larger than domes and pits, implying that the sills that form chaos are larger than sills that form pits and domes. Smaller chaos features may be formed from a single sill or a combination of a couple of small sills, while larger chaos (e.g., Thrace Macula) may be formed from many sills merging together to form a sill complex, or via a separate process altogether. The ratio between blocky and hummocky chaos at various sizes could provide more clues to the formation of chaos features.

The sill model (Manga and Michaut, 2017) also supplies a continuum of microfeature formation involving the evolution of liquid water pockets within Europa's ice shell. The model states that chaos and domes are both end-stage microfeature types, and both pits and domes can form as an intermediate stage. Assuming the process takes less time than Europa's surface age, the most numerous feature type is most likely to represent the end stage of this continuum process. Therefore, these results would imply

that microchaos is the most common end stage, as it outnumbers all other features. It could also be that it is easier to create microchaos from domes than Manga and Michaut (2017) suggest. If the shallow water sills create domes that crack while the liquid water is freezing (effectively overpressurizing the sill itself), fractures would be created on the dome's surface, which could be the origin of the cracked dome Type II hybrid feature. The overpressures in the freezing sill could also lead to the remaining liquid to escape through the fractures, where it could become the low-albedo material seen around the Type I hybrid features and within the matrix of microchaos (Manga and Michaut, 2017).

Careful attention should be paid to hybrid features in general. Their classification has evolved from domes with "moats" (Rathbun et al., 1998; Quick et al., 2017) and cracked domes (Pappalardo et al., 2004; Greenberg et al., 2003) to an independent feature type (Culha and Manga, 2016; this study). The range of hybrid morphologies and the fact that hybrid features exhibit similarities to both chaos and domes support the idea that they are intermediate features between domes and small chaos. According to the Manga and Michaut model (2017), domes may turn into chaos features, and hybrids could represent this transition. Hybrids are similar in number to domes, and have intermediate sizes between domes and chaos features. The presence of two different morphologies also supports this idea. The formation ideas from the previous paragraph could apply, but they are not the only explanations for hybrids. The Type I hybrid features with their dark "moats" could reflect the progressive cracking of the surface from the outside in, as would happen as the sill freezes and overpressure increases. This explains why the dome in the center is often disrupted as well, as the surface would have been affected at an earlier stage as the sill was growing. Cryovolcanism cannot be ruled out either, especially

in the formation of hybrids and domes, as the "moats" could be interpreted as the surface's response to an effusion of cryolava (Quick et al., 2017). Without more information, it is difficult to say for sure which formation mechanism is more likely.

Both pits and domes are supposed to form as intermediate features, while the weight of the liquid water sill warps the surface before it later freezes. However, pits are almost as numerous as small chaos features, whereas domes are only half as numerous as microchaos or pits. Hence, these results suggest that domes are not the most common end state and calls into question the hypothesis that domes would form during multiple phases of microfeature evolution. Instead, these results support the idea that the formation of pits, and not domes, is the more-commonly taken route between an unaltered surface and the conclusion of microfeature emplacement, likely as a chaos feature. Alternatively, it is also possible that the domes that would form from the sills underneath current pits simply have not frozen yet to form the domes, suggesting that microfeature formation is relatively recent.

This begs the question of why there are fewer domes than expected, relative to chaos and pits. Domes are predicted to form as an intermediate stage of microfeature evolution when a sill in emplaced higher in the ice shell (Manga and Michaut, 2017). It is more challenging to get large volumes of water to a higher level in the ice shell, which means that it would be harder to form domes than pits. Domes are also hypothesized to form when the sill freezes, even if the surface expression of the sill had been a pit during the liquid phase. Hence, some pits may have turned into domes. Therefore, one might expect a correlation between older surfaces (i.e., those less affected by recent endogenic

activity) and higher numbers of domes relative to pits. In any case, the reduced number of domes compared to chaos and pits must be fully explained by any formation model.

One observation that could shed more light on the relationship between hybrids, domes, and chaos features is the potential change in the numbers of features in the same regions studied here once Europa Clipper returns data from Europa in the mid- to late-2020s. If the number of hybrids relative to domes has increased, then it could mean that domes are changing into hybrid features. Recalculating the ratio between Type I and Type II hybrid features could also be telling. If it is assumed that the microfeatures form along a continuum, then the end stage feature type should be the most numerous. If there are more Type I hybrids relative to Type II hybrids or vice versa in the future, it could be interpreted as evidence for the progression of microfeature formation, and for the direction of formation (i.e., do domes turn into chaos or does chaos turn into domes?). If the ratio remains roughly the same, it could mean that there is no continuum, or that these features form at the same rate.

2.4.3 Implications for formation of microfeatures

Several key characteristics of microfeatures have been identified, some of which have not been previously noted in the literature, that can serve as constraints for future modeling efforts.

1. **Chaos and hybrid features are larger than pits, spots, and domes.** Chaos is the only microfeature that presents at scales larger than 100 km^2, and the peak size is larger than that of domes and pits. This indicates that whatever process creates chaos and hybrids typically affects a larger area on Europa's surface during their formation. The relative sizes of different feature types may indicate

that disruption events are more likely to occur for larger features. One hypothesis, presented by Manga and Michaut (2017), is that the merging of multiple sills would weaken the overlying ice, leading to the cracked and hummocky surfaces characteristic of chaos and hybrid features. However, any formation model would also need to explain smaller chaos features and the domes that form within Type I hybrids.

2. **Chaos is the most common type of microfeature, and the second most common is pits.** The relatively high frequency of chaos features may indicate that chaos formation is the most likely end state in a progression of microfeature formation, as suggested by Manga and Michaut (2017), or that conditions for chaos formation are more readily met than for other feature types. A future model needs to explain why chaos is more common than other features, and why pits are more numerous than domes, which is counter to the prediction of Manga and Michaut (2017). The relative ages of different regions – with high pit density indicative of more recent endogenic activity – could potentially account for the larger number of pits relative to domes. However, the region that had the highest number of craters, E17RegMap02, had the fewest overall features but the second highest number of pits, so the relationship between crater-based age and the presence of liquid water within the shell is not obvious.
3. **Chaos and hybrid features are irregularly shaped.** The irregularity of microfeatures is now quantified and reveals that pits, spots, and domes are generally more elliptical in nature (though they can be polygonal), while chaos and hybrid features often have irregular shapes and wavy perimeters, even if they

are not bounded by a ridge system. Merging sills (e.g., Manga and Michaut, 2017) could be useful in explaining this observation. Multiple ellipsoidal-shaped sills could merge to make an irregular surface expression, depending on their sizes, depths in the ice shell, and relative orientations. Furthermore, microchaos features are far more likely to have hummocky, rather than platy, interiors.

4. **Hybrid features come in two distinct types.** What here has been termed Type I hybrids have a dome surrounded by a dark "moat," which presents as hummocky chaos. In this case, the majority of the domes inside of the hybrids show a disrupted surface themselves, indicating that the dome is simply raised from the previous chaotic terrain. This interpretation implies that the domes are younger than the chaos feature, although the domes may have formed in direct response to chaos formation. Type II hybrids present as domes with severely disrupted surfaces, which have higher normalized reflectance than the Type I hybrids. Because features tend to darken over time when exposed to radiation (Hand and Carlson, 2015), the fact that these Type II hybrids are not as dark as Type I hybrids or chaos suggests that the Type II hybrids could be younger than the Type I hybrids. Another possibility is that Type II hybrids have simply not experienced any surface rupture that allowed material to flow over the surface, since that is the material that would darken over time.
5. **Spots are the rarest and smallest of all microfeature types.** Spots also have consistently low normalized reflectance value across all four RegMaps, similar to chaos features and hybrids, perhaps indicating a common process that occurs in the formation of all three types. Previous models (Schmidt et al., 2011; Manga

and Michaut, 2017) have posited that spots are formed when the surface is minimally disrupted after the spot is formed, such that it remains mostly flat. An alternative hypothesis is that spots are the result of surface disruption but that the scale of the event is below the resolution limit of currently available images. In that case, spots are simply small chaos features whose interiors have not been fully resolved, rather than a distinct feature type.

2.5 Conclusion

In an effort to understand the underlying process or processes that govern microfeature formation on Europa, all visible microfeatures in the E15RegMap01, E15RegMap02, E17RegMap01, and E17RegMap02 regions were mapped. These microfeatures were classified into chaos, domes, hybrids, pits, spots, or left them unclassified; craters were also noted where present. Data sets from other studies (Greenberg et al., 2003; Culha and Manga, 2016; Singer et al., in review) were incorporated to validate these features and ensure high robustness and accuracy of the final feature database. These results show that chaos and hybrids are larger than all other microfeature types, while pits and domes are around the same size, and spots are the smallest overall. Pits and domes are smaller than the "typical" size reported in past studies (Greenberg et al., 2003; Culha and Manga, 2016). Chaos is the most numerous microfeature, followed by pits, then domes, then hybrids, and finally, spots. The average normalized reflectance values of chaos, spots, and hybrid features are significantly lower than pits and domes, consistent across all regions studied. It was also found that there are more microfeatures in the northern hemisphere than the southern, and more in the trailing

hemisphere than the leading one, although the presence of large chaos features may be introducing an observational bias.

These results were compared to predictions made by some microfeature formation models. Diapirsm may explain microchaos and domes, but the predicted sizes of these features are larger than the observed sizes, and numerical models of diapirism have not reproduced pits and spots. Extrusive expressions of cryovolcanism on Europa (Quick et al., 2017) may explain the formation of domes, as their predicted heights and radii match the profiles of those domes produced by the model. Unfortunately, this model does not yet explain pits, spots, or microchaos, and is presently only supported by observations of domes, equivalent to diapirism. Finally, a sill model (Manga and Michaut, 2017) explains the presence of all microfeature types as part of the sill's evolution, including the presence of hybrids as a transitional feature type, and can explain the overall numbers and sizes of microfeatures observed. However, the large number of pits relative to domes in some areas suggests that regional characteristics may exert some control on whether domes form or that some regions may have experienced less endogenic modification in the recent past than others. From these observations, the cryovolcanism and sill models are most consistent with these results.

Future mapping work should address whether or not microfeatures can occur on Europa at sizes smaller than 1 km in diameter and the degree of clustering of microfeatures on Europa. Mapping efforts can also be expanded to areas that were not included in this study, with particular attention paid to the appearance and morphology of hybrid features and the addition of normalized reflectance measurements. This data set will serve as the basis of future geophysical and statistical modeling efforts, which will

inform future mission planning including both the upcoming Europa Clipper and potential future lander missions.

CHAPTER 3

MICROFEATURE MAPPING IN LOWRES IMAGES

3.1 Introduction

The RegMap mosaics on Europa only account for ~10% of its total surface area (Doggett et al., 2009), and while they are good resources for geomorphic mapping on Europa, their value is limited by their extent. Most of the images outside the RegMaps are significantly lower resolutions (>1 km/pix). This does not preclude the ability to measure large-scale features such as cycloids or ridges, but smaller features are difficult to find and identify, as many of them are below the resolution limit of the image. Many microfeature formation models would benefit from additional observational constraints, including but not limited to the locations of additional microfeatures outside of RegMap areas.

Many studies have mapped the locations of large chaos features (Greeley et al., 2000; Riley et al., 2000; Spaun, 2002; Figueredo et al., 2002; Figueredo and Greeley, 2004; Soderlund et al., 2014; Leonard et al., 2017; Leonard et al., 2018), but the results of mapping studies in general are greatly affected by the imaging parameters. Hoppa et al. (2001) described the limitations on accurate chaos identification, and concluded that the identification of chaotic terrain is strongly dependent on the observational parameters of the area, particularly the resolution and the incidence angle of the image. When the incidence angles in images were increased from 75° to 82° in one area, 33% more regions of chaos were identified. When the resolution was increased by a factor of 3.6 in a different region, the amount of chaos identified increased seven-fold.

To account for these potential inconsistencies, Riley et al. (2000) placed firm constraints on the images selected for use in their chaos mapping study and only used images with <200 m/pixel resolution and incidence angles >55°. Similarly, Figueredo and Greeley (2004) included only high-resolution, high incidence angle RegMap images of Europa acquired during several of Galileo's Europa flybys. However, more work needed to be done to address observational constraints on chaos to expand mapping to include non-RegMap images. Neish et al. (2012) performed a comparative analysis to find the identification limits for chaos mapping as a function of resolution and incidence angle. To study the effects of observational parameters on chaos identification, they mapped chaos regions in RegMap images, RegMap images artificially degraded to the level of a low-resolution image, and images originally taken at low-resolutions. In cases when the resolution was low (~1.5 km/pix) but the incidence angle was high (about ≥70°), large chaos was easily identified. In images with low incidence angles (≤30°), however, chaos could not be identified if the resolution was 250 m/pix or less (Neish et al., 2012).
As detailed as that study was, there are still unknown limits on microfeature and, by extension, microchaos identification. The chaos regions identified in Neish et al. (2012) were all upwards of 1500 km^2, significantly larger than the microchaos features that were identified in the RegMaps and described in earlier text. It is therefore unclear if the limits described in the paper can equally apply to microchaos. Additionally, this and other papers have focused only on chaos; none have mentioned the identification limits for other microfeature types in low-resolution images.

Learning how to correctly interpret the low-resolution *Galileo* images opens up a significant amount of usable data that has not yet been fully studied. Increasing the

amount of data about the locations and characterizations of known features helps to constrain models that predict how these features formed, which connects to the amount of heat and materials are transported within Europa's ice shell, and to the geophysics of an icy world. Geologic and geomorphic maps of Europa (USGS, 2002; Bunte, 2013) show the locations of the largest and most obvious geologic features on Europa. One of the features that could be connected to both heat and material transport is chaos. Large chaos features have been mapped and characterized (Greenberg et al., 1999; Collins et al., 2000; Riley et al., 2000; Figueredo et al., 2002; Collins and Nimmo, 2009), but little attention has been paid to the smaller chaos features scattered across the surface. Other studies have reported on the characteristics and locations of pits and domes (Rathbun et al., 1998; Greenberg et al., 2003; Singer et al., 2010; Noviello et al., 2019).

This chapter is devoted to addressing the limits of microfeature identification in low-resolution images by creating a dataset of features in low-resolution images and comparing them to the dataset collected in the RegMap images for the same area. Directly comparing these two datasets will help determine the main sources of error and quantify uncertainty when mapping microfeatures in low-resolution images. These errors are that of omission, where a feature is entirely excluded from a dataset because it is invisible in the images; that of misclassification, where a feature is identified but assigned to a group that is inconsistent with the same microfeature in a RegMap; and that of false positives, where a feature is mapped in a low-resolution but has no corresponding microfeature in RegMap images. These error rates can then be applied to future efforts to map microfeatures outside of RegMap areas to provide additional constraints for microfeature formation and heat and material transfer models.

3.2 Methods

3.2.1 Image selection

One RegMap region was selected as a low-resolution (LowRes" mapping "test case." E15RegMap01 was selected because it contained the highest number of microfeatures and an absence of large chaos features, as the locations of large chaos has been reported on previously (Riley et al., 2000; Greeley et al., 2000; Spaun, 2002; Bunte, 2011; Neish et al., 2012; Leonard et al., 2017; Leonard et al., 2018). As with the RegMap images, only images taken with the Galileo SSI (Belton et al., 1992) were included, and only those taken with the clear filter. Based on parameters provided by Neish et al. (2012), the LowRes images that were included in the analysis had to cover at least part of the RegMap, have resolutions between 1.4 and 1.7 km/pixel, and have similar incidence angles to those of the images used in the RegMaps.

Because of the lack of images of this area of Europa, no single image exists that meets all three criteria. Instead, four images were used for the LowRes mapping, as they collectively cover the full study area; details are provided in Table 3-1. Maps showing the E15RegMap01 study area and the LowRes images' overlap with E15RegMap01 are shown in Figures 3-1 and 3-2. Two of the images have similar incidence angles, but the other two have significantly lower incidence angles. A change in the lighting conditions on any planetary body, especially a high-albedo target such as Europa, can enhance or obscure shadows and albedo features to an observer, significantly changing the geologic and geomorphic interpretations of the surface. For areas covered with images with different parameters, the error rates will be different. Thus, the results presented here should be considered the minimum error rates for global studies of microfeatures.

Table 3-1: Average characteristics of the LowRes images used for mapping

Image ID	Galileo Orbit Acquired	Phase Angle (°)	Emission Angle (°)	Incidence Angle (°)	Incidence Angle Range (°)	Pixel Resolution (m)
5139r	G1	37.72	32.36	30.29	2.1416–69.86	1572.85
5126r	C3	37.72	24.15	21.14	0.02–54.31	1571.76
5113r	G1	37.30	27.41	61.65	36.73–116.92	1572.13
5100r	G1	37.25	35.43	67.68	38.39–120.74	1573.27

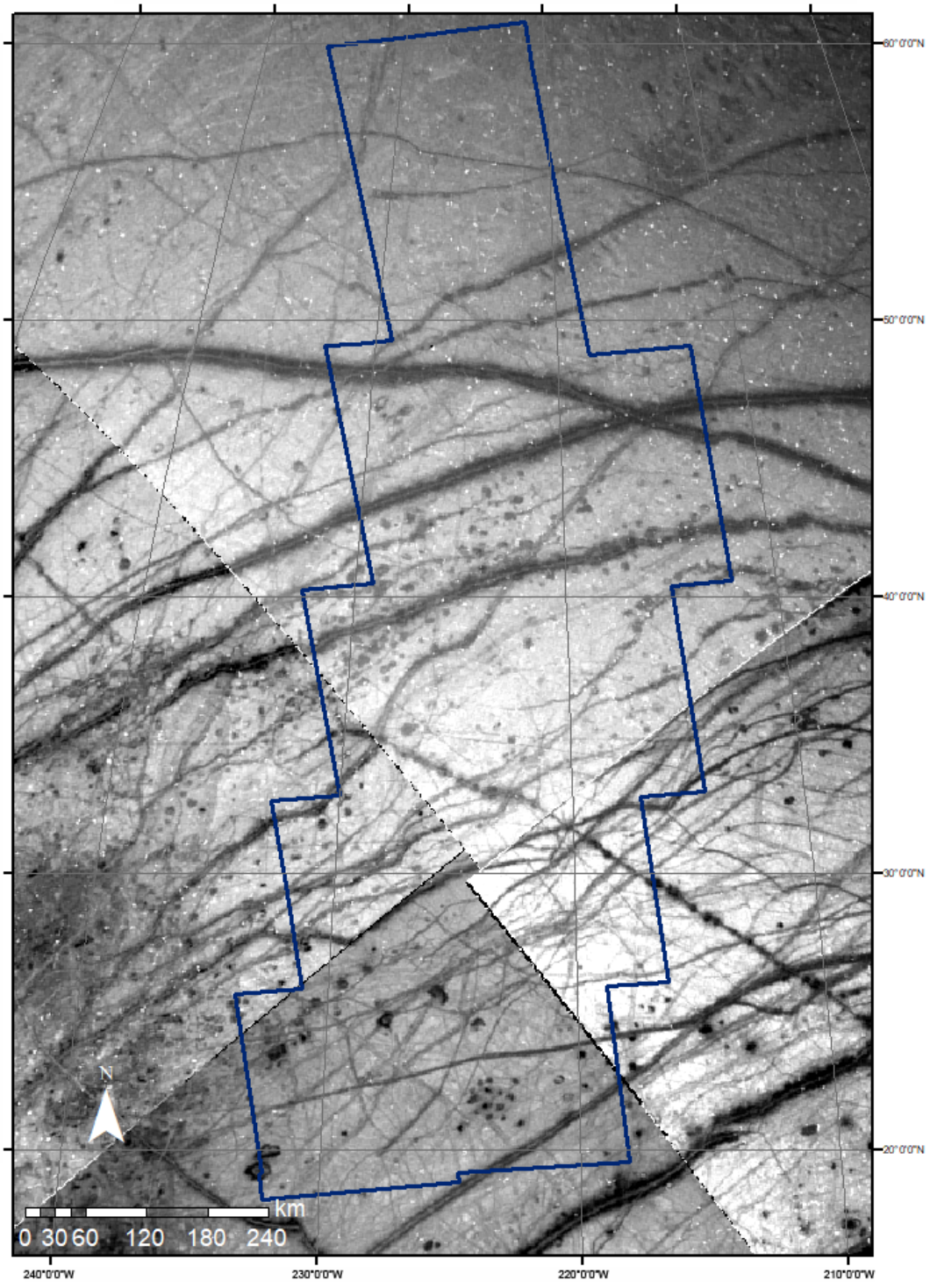

Figure 3-1: The E15RegMap study area (with navy blue outline) with LowRes images overlain. No single image covered the entire study area, hence why four total images were used. Details about these images are provided in Table 1.

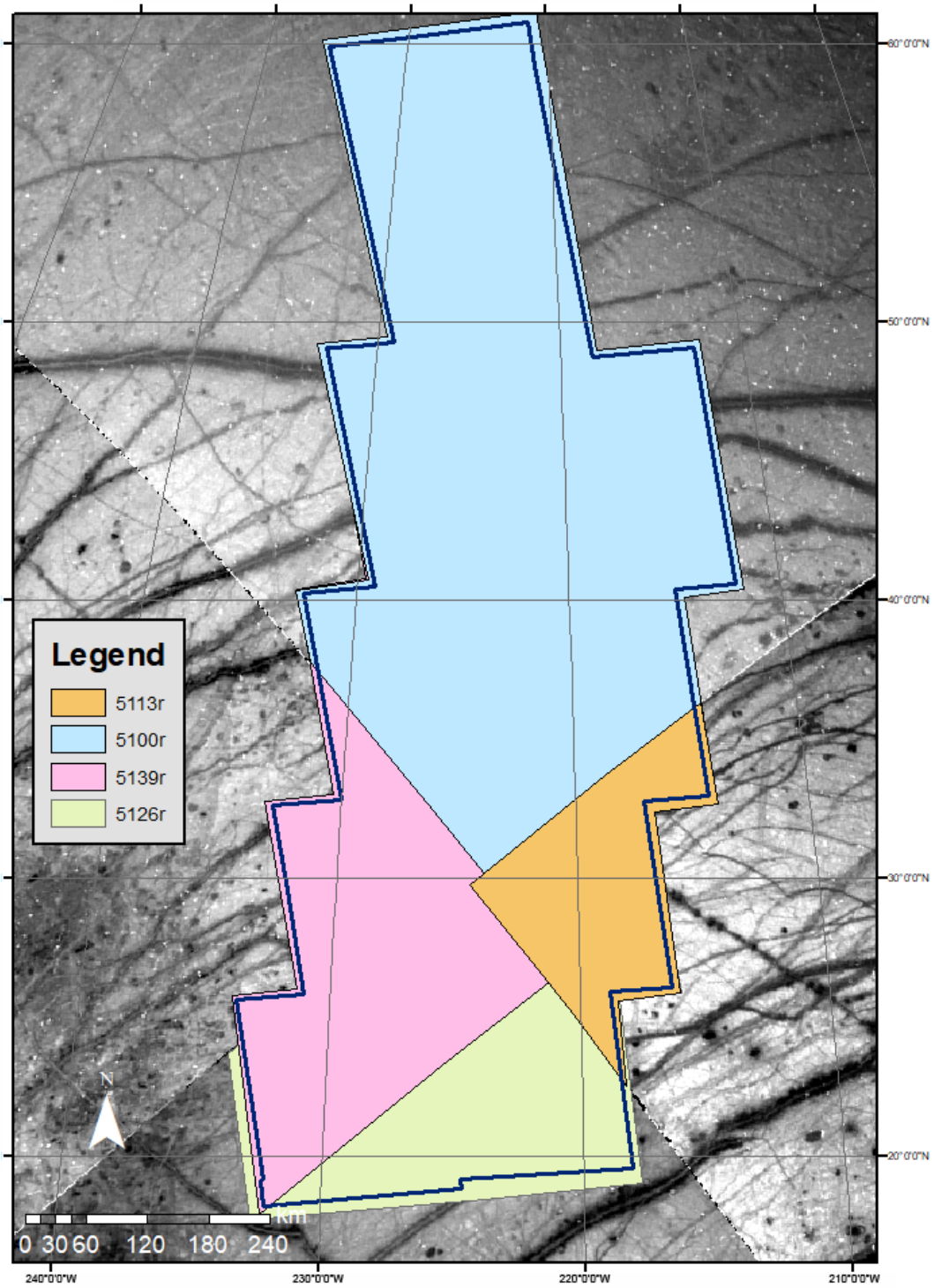

Figure 3-2: The E15RegMap study area (navy blue outline) with LowRes coverage polygons overlain. This represents which parts of E15RegMap01 were mapped in which image.

3.2.2 Mapping in LowRes images

To place observational constraints on identifying and classifying microfeatures in low-resolution images, a new dataset was collected, this time using LowRes images that covered the same areas as the RegMaps. The LowRes data were collected using the same mapping protocols as was used in the RegMap mapping approach and applying the same classification parameters to the mapped features. Another category, Phantom Features, is added in the LowRes mapping to reflect features that were mapped in LowRes but that corresponded to areas that lacked any detectable feature in the RegMap images. This is a better choice for three distinct reasons: 1) there now exist two datasets collected at different image resolutions, allowing for easy comparison between features mapped at both levels; 2) the number of features mapped in the RegMap images that were not mapped in the LowRes images, and the reasons for these omissions, can now be constrained; and 3) the number of false positive "features" mapped in LowRes images that were not mapped in the RegMap images can now be constrained.

The same parameters were calculated for the LowRes data as the RegMap data so as to allow for easy comparison. These are: spherical area, spherical perimeter, maximum length, maximum width, aspect ratio (eccentricity), the morphometric ratios, mean normalized reflectance, median normalized reflectance, range of normalized reflectance values, and standard deviation of normalized reflectance values. One caveat is that even though some feature types (e.g., chaos) had features above and below the 100 km^2 area size cut-off, only true microfeatures were analyzed.

A rule of thumb in mapping is that it should be possible to identify and map any feature that is larger than five times the resolution of the image. In the case of this

LowRes mapping, the images had an average resolution of 1.57 km/pix, meaning that any feature with a lateral extent ≥ 7.85 km should be visible, even in low-resolution images. This number can change based on the way that lateral extent is defined. Here, the estimated minimum detection size of a feature was lowered to 7.5 km across because the "size" used here is the equal area diameter. This value is usually smaller than the maximum distance across, but better accounts for the two-dimensional reality of a mapped feature. For completeness, the number of microfeatures that exceed this detection limit are discussed in the next section.

3.2.3 Review of the E15RegMap01 dataset

The RegMap dataset was used to assess the LowRes dataset for completeness and accuracy. The total number of mapped features in E15RegMap01 is 339, and 310 of these features were under the size cut-off of 100 km^2. Of these microfeatures, 277 of them are classified, meaning there are 33 mapped but unclassified features included in the E15RegMap01 dataset. These included the 68 microchaos features, the 33 domes, the 34 hybrids, the 119 pits, and the 23 spots described in detail in Chapter 2. There are two ways to describe size: the diameter of a circle with equal area to the feature, and the maximum length of the feature. The total number of microfeatures of any type in this dataset (including unclassified) that were larger than 7.5 km in equal area diameter is 81, 26.1% of the total number of mapped features. The total number of features of any type in this dataset (including unclassified) that were over 7.5 km in maximum length is 165, 53.2% of the total number of mapped features. Thus, before the LowRes mapping begins, it is already expected that at least 112 features will be omitted, more if the unclassified

features are included, and will likely be closer to 200 depending on which definition of size is applied.

3.3 Results

3.3.1 LowRes mapping and identification

In total, 214 features were mapped in LowRes; this map is shown in Figure 3-3. The equivalent diameter of these features ranged from 2.33 km to 21.25 km (Figure 3-4). The features were then given provisional classifications based on their appearance in the low-resolution images which were then checked against their classifications from the RegMap mapping, which is assumed to be more robust. The type breakdowns of these features are provided in Table 3-2, but as they are not all true microfeatures, they are not considered further.

This left 186 microfeatures in the analyzed dataset; their type breakdowns are provided in Table 3-3. The LowRes-mapped microfeatures contained 84 features classified as chaos, 11 features classified as domes, six features classified as hybrids, six features classified as pits, 53 features classified spots, and 26 features that were mapped but left unclassified. Of these 186 microfeatures, 70 (37.6%) of the features mapped are above 7.5 km under the assumption that diameter is equal to that of a circle of equivalent area. These 70 features include: 55 chaos (78.6%), two domes (2.9%), four hybrids (5.7%), no pits, two spots (2.9%), and seven unclassified features (10.0%). A histogram of all microfeature diameters including unclassified is shown in Figure 3-5. As a large part of the dataset would have been excluded if the five-pixel detection limit was followed, the rule was disregarded. Indeed, the smallest feature mapped in this dataset was 2.33 km in diameter, well below the five-pixel detection limit. A more appropriate

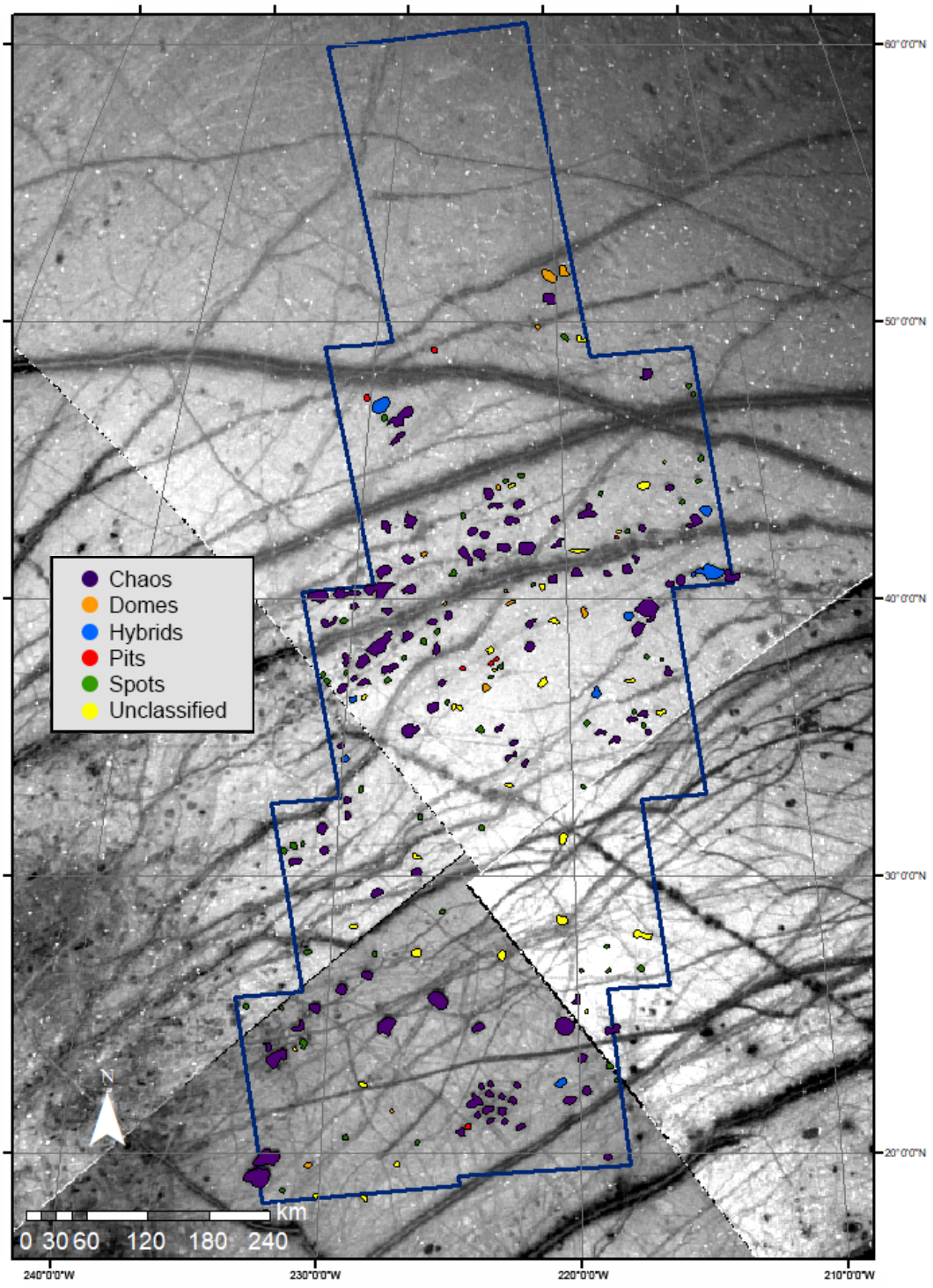

Figure 3-3: A map showing all features mapped in the LowRes dataset. The features whose boundaries extend outside of the RegMap limits were excluded from the dataset prior to analysis, as well as any features whose area was above 100 km^2.

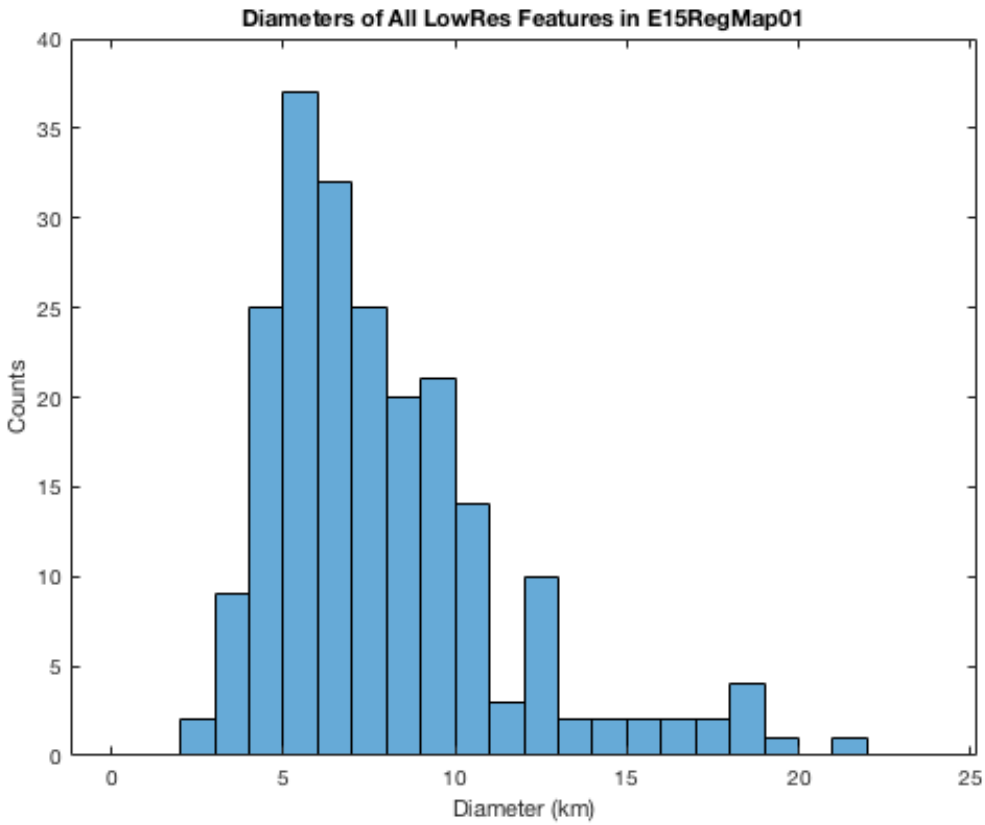

Figure 3-4: Histogram of equal-area circle diameters, all mapped LowRes features. These are all features mapped, including those above the microfeatures size cut-off. Bin sizes are 1 km.

rule for detecting features on a bright surface such as Europa could therefore be as small as 2.5 km in diameter if the feature has an apparent albedo that differs significantly from the background. Out of the 186 features mapped in LowRes, 46 were ultimately classified as "phantom" features, meaning they were mapped as a feature in the LowRes mapping, but upon closer inspection using RegMap images were not associated with a microfeature.

3.3.2 Missed features

A total of 195 features that were mapped in the RegMap were not mapped in the LowRes (Figure 3-6). Out of these 195 missed features, 193 are under the microfeature size cut-off, and 187 are above 2.5 km in diameter. The distribution of the diameters of the missed features is Gaussian with a peak between 5 and 6 km (Figure 3-7) and qualitatively matches with the distribution of the microfeatures mapped in LowRes. Out of all the missed features, 15 (7.8%) of them were chaos, 25 (13.0%) of them were domes, 12 (6.2%) of them were hybrids, 113 (58.5%) of them were pits, six (3.1%) of them were spots, and 22 (11.4%) were unclassified.

3.3.3 Find rates

To better assess the completeness of the LowRes dataset compared to a RegMap dataset, a "find rate" was calculated using this formula:

$$Find\ Rate = \left(1 - \left(\frac{Number\ missed}{Total\ number\ in\ RegMap}\right)\right) * 100$$

The find rates for all categories are given in the last row of Table 3-3. Only true microfeatures were considered in the find rate calculation, as this study is focused on finding microfeatures outside of RegMap areas.

Table 3-2: Count breakdown of all features mapped in LowRes in E15RegMap01

Data Set	Total features	Chaos (%)	Domes (%)	Hybrids (%)	Pits (%)	Spots (%)	Unclassified (%)
E15RegMap01	339	95 (28.0)	33 (9.7)	36 (10.6)	119 (35.1%)	23 (6.8%)	33 (9.7)
LowRes features (classified in low-resolution images)	214	108 (50.5)	12 (5.6)	8 (3.7)	6 (2.8)	53 (24.8)	27 (12.6)
Missed features	195	17 (8.7)	25 (12.8)	12 (6.2)	113 (57.9)	6 (3.1)	22 (11.3)

Table 3-3: Count breakdown of all microfeatures mapped in LowRes in E15RegMap01

Data Set	Total features	Chaos (%)	Domes (%)	Hybrids (%)	Pits (%)	Spots (%)	Unclassified (%)
E15RegMap01	310	68 (21.9)	33 (10.6)	34 (11.0)	119 (38.4%)	23 (7.4%)	33 (10.6)
LowRes features (classified in low-resolution images)	186	84 (45.2)	11 (5.9)	6 (3.2)	6 (3.2)	53 (28.5)	26 (14.0)
Missed features	193	15 (7.8)	25 (13.0)	12 (6.2)	113 (58.5)	6 (3.1)	22 (11.3)
Find rate	x	77.9%	24.2%	65.7%	5.0%	73.9%	x

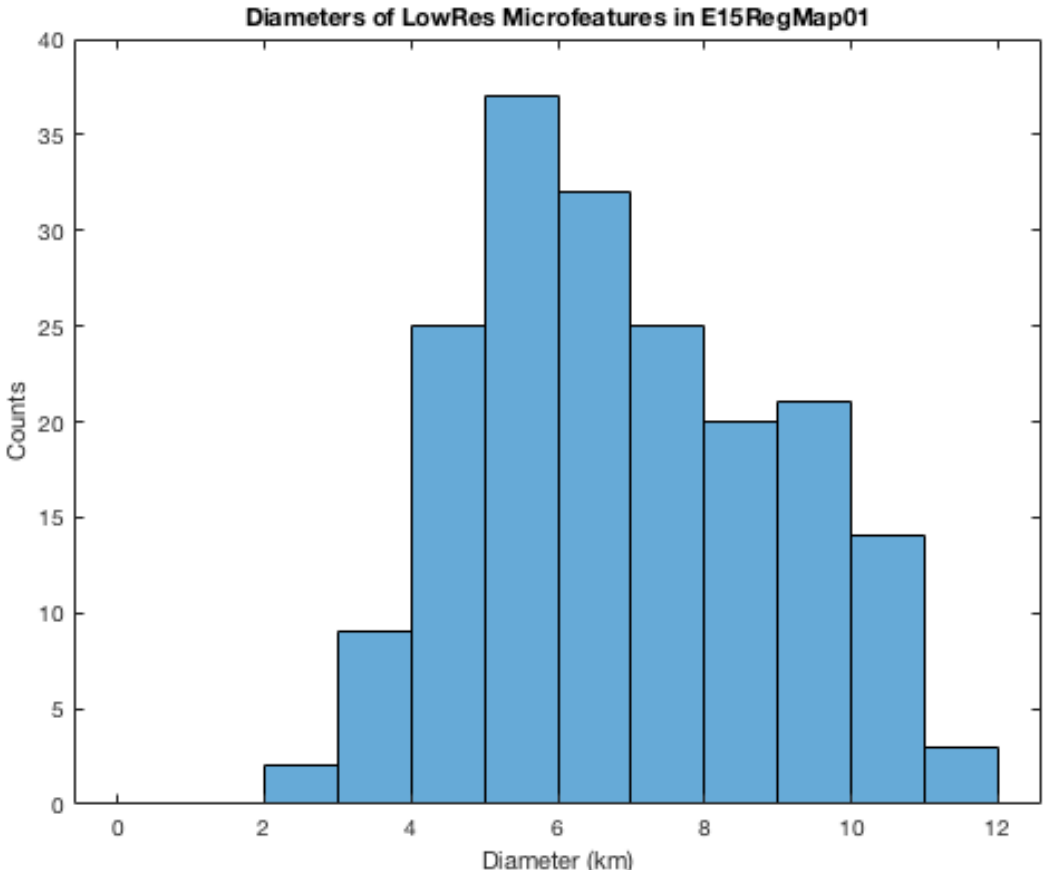

Figure 3-5: Histogram of equal-area circle diameters, all mapped LowRes microfeatures. Bin sizes are 1 km.

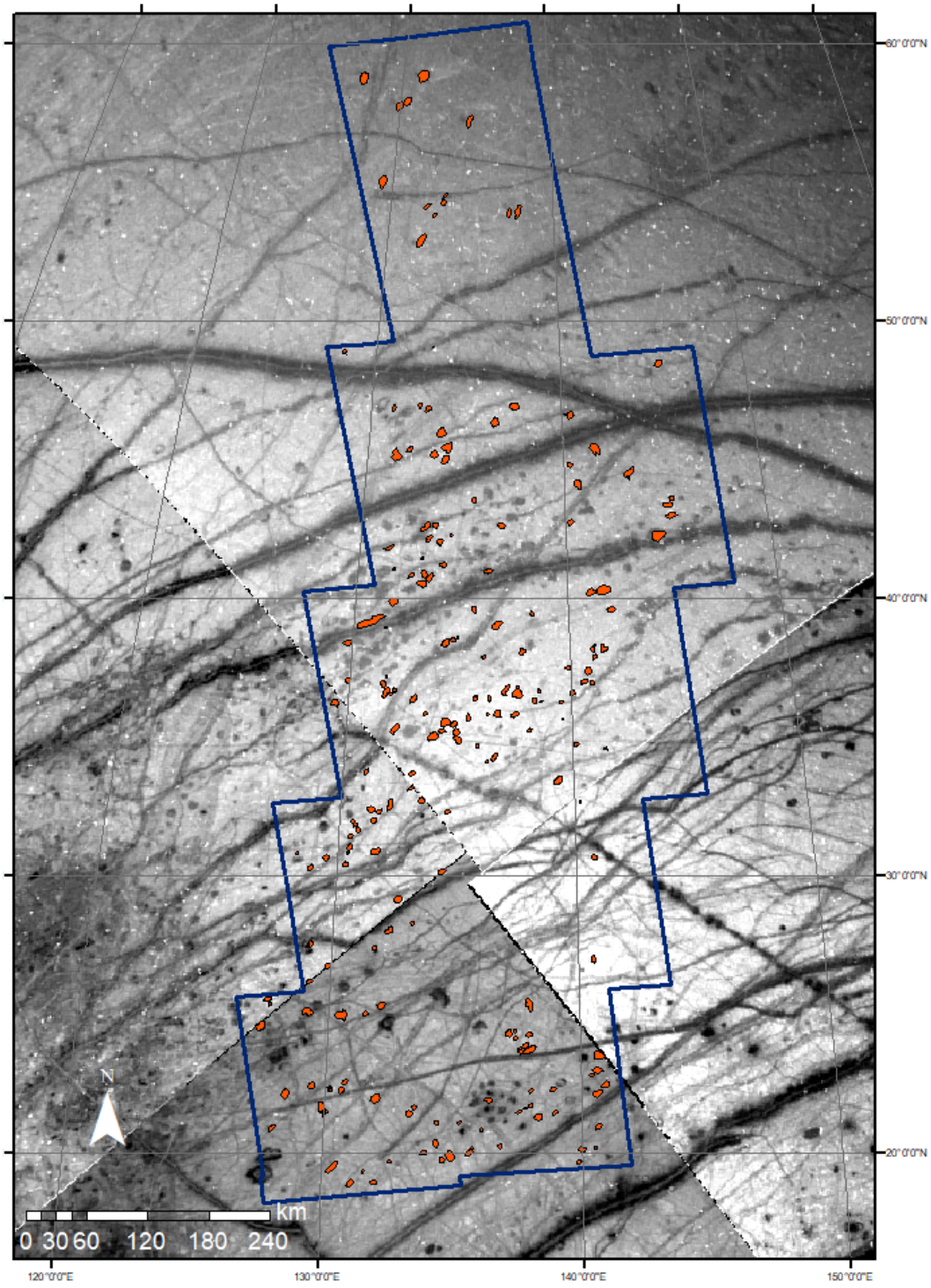

Figure 3-6: All features (in orange) of the E15RegMap01 study area missed in LowRes mapping of the same area.

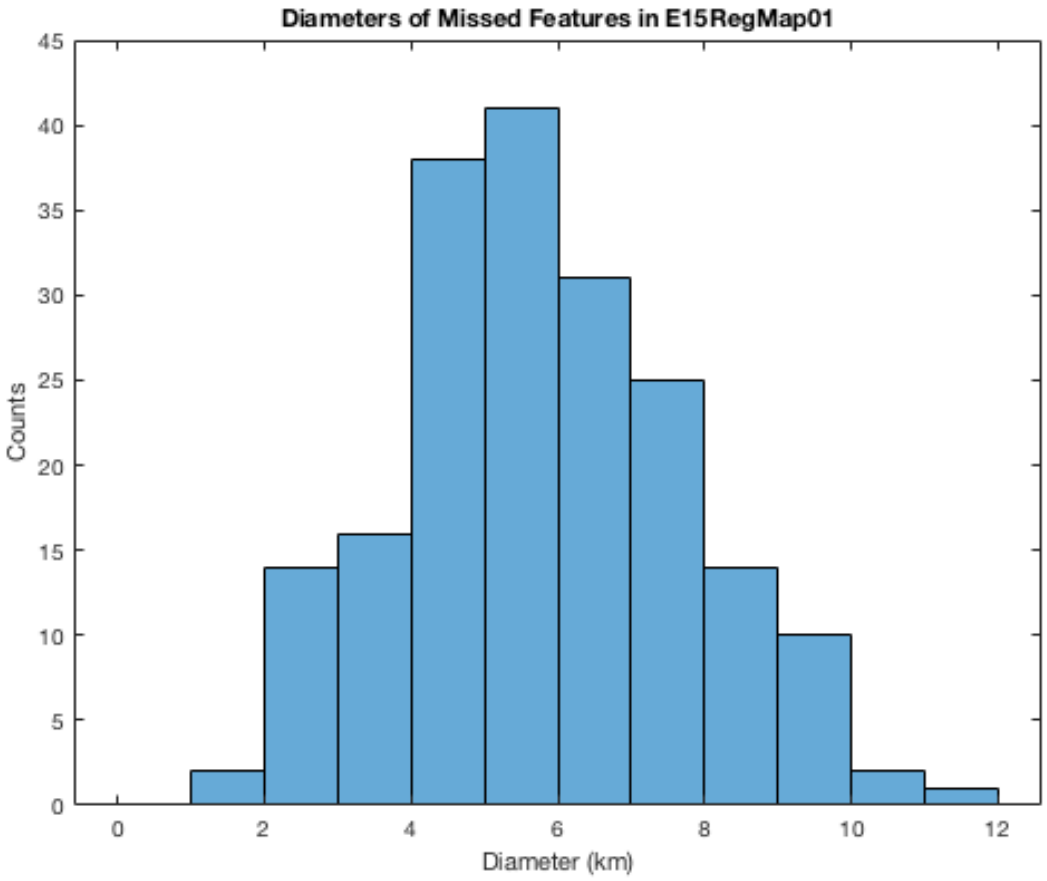

Figure 3-7: Histogram of equal-area circle diameters, all missed RegMap microfeatures. Bin sizes are 1 km.

Only features that were mapped in both LowRes and had a corresponding feature in the RegMap dataset, regardless of the accuracy of the classification, were considered as "found," else they were considered "missed." This is to reflect the presence of false positives (the phantom features) in the LowRes dataset that were mapped as features but had no corresponding morphology in the RegMap images. Accuracy of mapping is discussed in a later section. For some microfeature groups, the number of features mapped in LowRes exceeds the total number of features that were mapped in the RegMap and the number of missed features. Spots are an ideal example of this; the 53 spots identified in low res far exceeds the total number of mapped spots in the RegMap images. In some of these cases, the features were misclassified, falsely increasing the number of spots reported in that microfeature type. In other cases, the features belonged to the phantom category because they did not correspond to a microfeatures in the RegMap. Chaos, hybrids, and spots were found at relatively high rates (65.7–77.9%), even if these features were misclassified, but domes and pits were found at very low rates, 24.2% and 5.0%, respectively. The hybrid features that were omitted all belonged to the Type II (cracked dome) subcategory.

3.3.4 Accuracy

Showing that features can be found at all is the beginning. The next step is to determine how often the classifications done in LowRes are consistent with the RegMap classifications. When considering microfeatures mapped and classified in LowRes, the number of matches becomes 61 out of 186 (32.8%) when including unclassified features, and 61 out of 160 (38.1%) when unclassified features were excluded. Some microfeatures groups were mapped more accurately than others. Chaos features were correctly mapped

and classified 50 out of 84 times (59.5%), domes were correct one out of 11 times (9.1%), hybrids were correct one out of six times (16.7%), pits were correct zero out of six times (0.0%), and spots were correct nine out of 53 times (17.0%). The decision to divide by the total number of features identified for that type in LowRes is motivated by the need to know how many features can be expected to be misclassified rather than simply omitted. This information is included in Table 3-4 in the boxes highlighted in green.

It is important to note that these numbers merely reflect the number of microfeatures found. When the features above the size cut-off are included, the number of correctly classified features and the percentage classified correctly also increase, but not significantly. This result is not surprising; larger features are easier to identify, and their defining attributes are also more visible than smaller features. The overall number correct in the entire population, including features over 100 km^2, is 80 out of 214 (37.4%). Chaos are correctly mapped 66 out of 108 times (61.1%), but the total number of "chaos" found in LowRes (108) is higher than the number found in the RegMap images (95, with 68 of them considered microchaos). Domes, hybrids, pits, and spots do not change the number correctly identified, but as there are more features included, these percentages either decrease or remain the same.

There appears to be a correlation between size of a feature and the chance it is accurately classified in LowRes images. As area increased from 10 to 100 km^2, the accuracy of the classification increased. A simple linear model (slope = 16.15, 95% CI:[0.80, 31.51]; y-intercept = 0.6679, 95% CI:[0.38, 0.96]) yields a high positive

Table 3-4: Classification accuracy breakdown of all microfeatures mapped in LowRes. The columns across represent the classifications in the RegMap dataset, and the rows down represent the classifications made in the LowRes dataset. The values highlighted in green are the ones whose classifications matched between the two datasets.

	Total	Chaos Counts (%)	Dome Counts (%)	Hybrid Counts (%)	Pit Counts (%)	Spot Counts (%)	Unclassi-fied Counts (%)	Phantom Counts (%)
Micro-chaos	84	50 (59.5)	9 (10.7)	6 (7.1)	0 (0.0)	6 (7.1)	6 (7.1)	7 (8.3)
Dome	11	1 (9.1)	1 (9.1)	1 (9.1)	0 (0.0)	0 (0.0)	2 (18.2)	6 (54.5)
Hybrid	6	3 (50.0)	2 (33.3)	1 (16.7)	0 (0.0)	0 (0.0)	0 (0.0)	0 (0.0)
Pit	6	1 (16.7)	1 (16.7)	0 (0.0)	0 (0.0)	0 (0.0)	0 (0.0)	4 (66.7)
Spot	53	7 (13.2)	8 (15.1)	1 (1.9)	4 (7.5)	9 (17.0)	7 (13.2)	17 (32.1)
Unclassi-fied	26	8 (30.8)	3 (11.5)	0 (0)	1 (3.8)	2 (7.7)	0 (0.0)	12 (46.2)
Phantom	46	7 (15.2)	6 (13.0)	0 (0)	4 (8.7)	17 (37.0)	12 (26.1)	x

correlation (r_{sq} = 0.78, $r_{sq., adj.}$= 0.75) between accuracy and size. Figure 3-8 shows the number of correct classifications per bin, where each bin represents 10 km^2, the (61.1%), but the total number of "chaos" found in LowRes (108) is higher than the number found in the RegMap images (95, with 68 of them considered microchaos). Domes, hybrids, pits, and spots do not change the number correctly identified, but as there are more features included, these percentages either decrease or remain the same.

Relative accuracy is the percentage of classifications correct versus the total number of features within that size bin. What these graphs show is that the size of a feature contributes to how accurately that feature is classified, though a relatively large feature area is no guarantee of correctness.

3.3.5 Chaos identification

As chaos is the focus of many formation models that imply liquid water, heat, and material transport on Europa, special attention is paid to them. In the LowRes mapping dataset, chaos is correctly identified and classified as chaos 66 out of 108 times (61.1%) when all potential chaos features are considered. 24 potential chaos features were above the 100 km^2 size cut-off and were removed from further analysis. The number of potential chaos features that were truly chaos in the RegMap images is 50 out of 84 (59.5%). Chaos mapped in LowRes was most often misclassified as a hybrid (6 out of 84 times, 7.1%) and as a spot (6 out of 84, 7.1%). Once, two hybrid features near each other were classified as a larger chaos feature in LowRes mapping. Chaos was never misclassified as a pit but was misclassified as a dome nine out of 84 times (10.7%). When it was misclassified as a dome, the "chaos" feature mapped corresponded to the dome's shadow in all but one of the cases. Seven out of 84 times (8.3%) a potential chaos feature

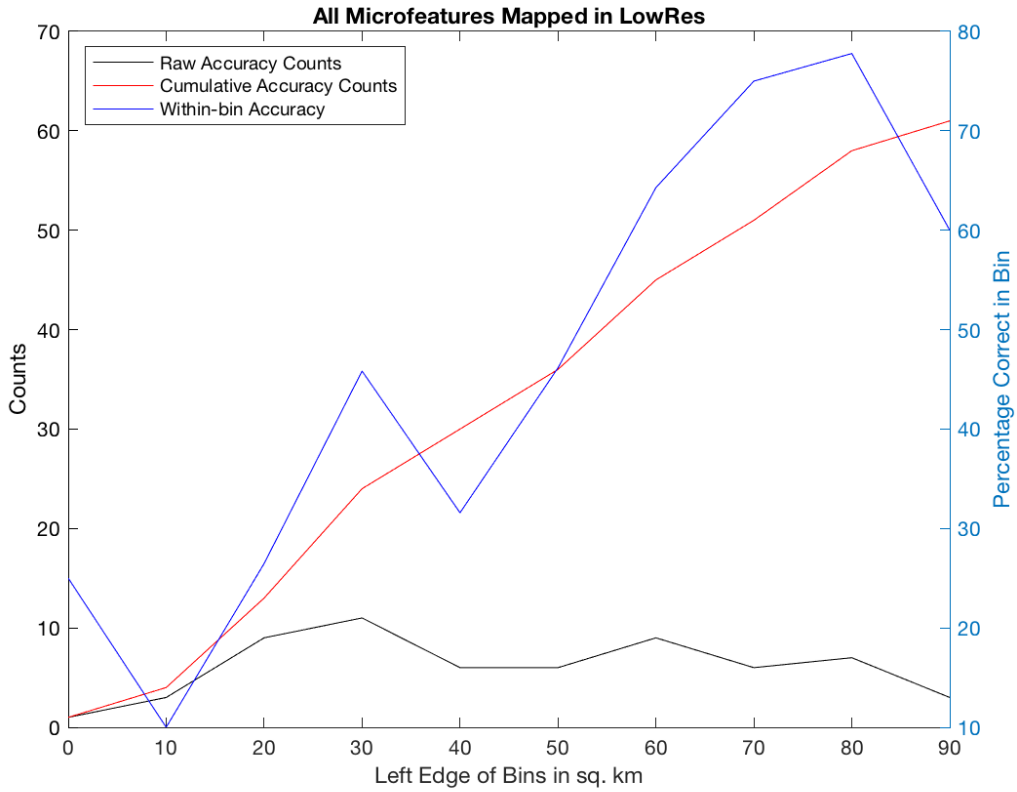

Figure 3-8: Accuracy of LowRes classification as a function of size, shown as a line histogram. The bins represent 10 km^2 in area, and are plotted at the left edge of the bin (e.g., the measurements for the 20–30 km^2 bin are plotted on the 20 km^2 line). Accuracy is defined as when a feature mapped and classified in LowRes is mapped in the same place as another feature with the same classification. The black line represents the raw counts per bin (number of correct cross-classifications), and the red line represents the cumulative number of correct cross-classifications for all the bins. The blue line represents the percentage of correct cross-classifications per bin relative to the total number of cross-classifications per bin. The blue line follows the scale on the right y-axis. The trend is that as microfeature size increases, the number of correct classifications (the accuracy) also increases.

belonged to the “unclassified” group in the RegMaps. Six out of 84 times (7.1%), a feature called chaos in LowRes was revealed as a phantom feature in the RegMap. These phantoms were associated with ridges three times (50%) of the time, with a generally rough area on Europa’s surface once (16.7%). The other two times (33.3%) were both associated with low albedo areas of the plains, but where there were no obvious microfeatures. These numbers are provided in Table 3-4.

3.3.6 Other microfeature types

Hybrids were correctly identified once out of six times (16.6%). Features mapped as hybrid features were truly chaos features three out of six times (50%), and twice a hybrid feature was mapped as a dome (33.3%). Hybrids mapped in LowRes were never truly an unclassified or a phantom feature. Spots were correctly classified as spots nine out of 53 times (17.0%). They were misclassified as chaos seven out of 53 times (13.2%), as hybrids once (1.9%), as domes eight times (15.1%), as pits four times (7.5%), and as an unclassified feature nine times (17.0%). Out of all microfeatures, spots had the highest chance of truly being a phantom feature in the RegMaps, as this occurred 17 out of 53 times (32.1%).

Out of the 11 domes in the LowRes microfeature dataset, only one (9.1%) of them was also classified as a dome in the RegMap images. One (9.1%) of these false domes was truly a chaos feature, one (9.1%) was truly a hybrid feature, two (18.2%) were mapped but unclassified, and 6 (54.6%) were phantom features. Two of these phantom features were revealed as a bright spot within a ridge that was obscured in the LowRes images. Similarly, though six features were called pits in LowRes, none were truly pits in the RegMap images. One (16.7%) was a dome, where the dark shadow of the dome was

interpreted as the dark area within a pit, one (16.7%) was a chaos, and the remaining four (66.7%) were all phantom areas in the RegMap. This, coupled with the knowledge that domes and pits both had a low find rate, suggests that information necessary to accurately map and identify pits and domes is obscured or absent in the LowRes images. These numbers are given in Table 3-4.

3.3.7 Unclassified features

There was a total of 26 unclassified features in the LowRes dataset. Roughly half (14 out of 26, 53.8%) of these LowRes unclassified features were mapped features in the RegMap images. Eight of these (30.8%) were chaos, three (11.5%) were domes, none were hybrids, one (3.8%) was a pit, and two (7.7%) were spots in the RegMap dataset. The remaining 12 features that were unclassified in the LowRes dataset belonged to the phantom feature category, which is examined further in the next section. Examining the classifications from the RegMap dataset, a total of fifteen unclassified features were identified as potential features in LowRes imaging. Six of these (40%) were misclassified as a potential chaos feature, two (13.3%) were misclassified as potential domes, and the remaining seven (46.7%) were misclassified as potential spots. This information is provided in Table 3-4.

3.3.8 Phantom features

The phantom features are those that were mapped as features in LowRes but had no corresponding microfeature in the RegMaps. A total of 51 of these are reported here out of 214 features mapped in LowRes (23.8%). This number initially suggests that roughly a quarter of features mapped in LowRes have a chance of being a non-feature in higher resolution images. Five out of the 51 features were above the 100 km^2 maximum

size for microfeature classification, and the remaining 46 features (90.2%) are examined further to determine common reasons for mapping a featureless area as a feature in LowRes. A brief breakdown of these numbers is provided in Table 3-4.

As stated previously when discussing the other microfeature types, seven of these phantom features (15.2%) were classified as chaos features in LowRes. Six were classified as domes (13.0%), none were classified as hybrids, four were classified as pits (8.7%), 17 were classified as spots (37.0%), and 12 of these features (26.1%) were left as unclassified in LowRes. Spots is therefore the category most likely to have these false positives, though the possibility is present in every feature group. This finding is consistent with the expectations prior to mapping, as the number of features called spots was known to be higher than the true number of spots mapped in the RegMap.

Often (16 out of 51 times, 31.4% for all phantom features; 12 out of 46, 26.1% for phantom microfeatures), a phantom feature was associated with a ridge on Europa, either the shadow of a single or a location where multiple ridges intersect. While all efforts were made to exclude ridges from being misclassified as microfeatures, in low-resolution images with inconsistent lighting, ridges are not always recognizable. This is especially true for the thinner ridges (total width less than 2 km) or where dark spots that could indicate a feature juts out perpendicularly to the ridge; this is shown in Figure 3-9. Four out of 46 times (8.7%) there was an anomalous dark spot in otherwise smooth terrain or there was a feature mapped in an area that was full of generally rough (though not fully chaotic) terrain. These dark areas were mistakenly classified as chaos or spots because of their low apparent albedo. Twice (4.3%), a bright spot within a ridge was mistaken for the bright side of a pit or a dome. The remaining 28 times a potential feature was mapped

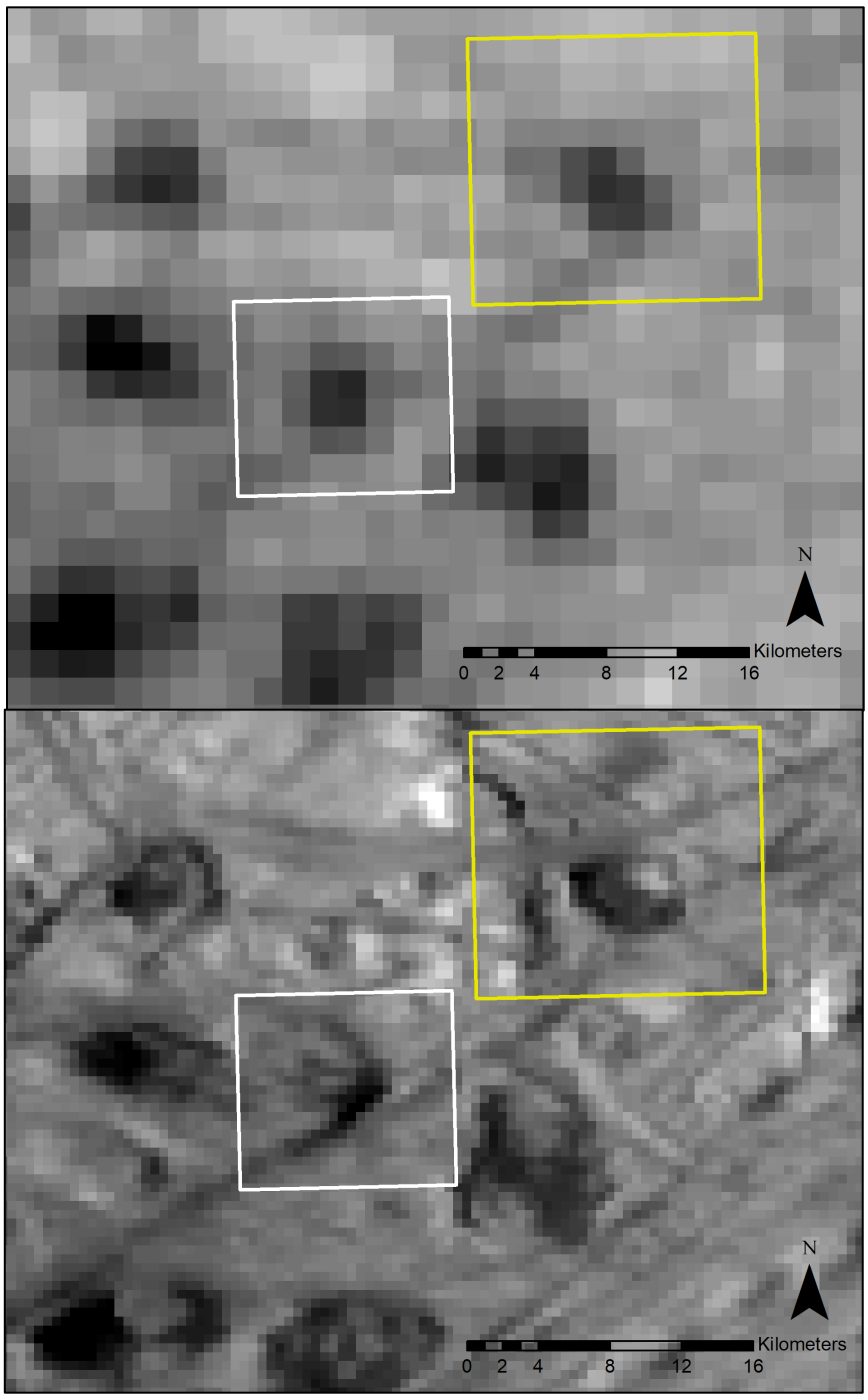

Figure 3-9: Example of a false positive (ridge) in a LowRes image of Europa. Top: two potential features (within the boxes) mapped in LowRes imaging in the E15RegMap01 region (image 5126r). Bottom: the same areas in the RegMap images. The yellow box represents a true feature even in RegMap images, but the white box outlines a non-feature. This is an example of mistaking shadows from a ridge as an independent feature in LowRes mapping.

and turned out to be a featureless area of Europa are true errors. These were marked as phantom regions with no obvious morphology to reference in the RegMaps. These account for 60.9% of all of the phantom feature areas. An example of this is shown in Figure 3-10.

3.4 Discussion

Part of the issue for why there are so many competing ideas for chaos formation models is the lack of data. Efforts to map microchaos outside of the RegMap areas (Bunte, 2013; Leonard et al., 2017; Leonard et al., 2018) have been completed, but at the time of this writing there is no certain way to verify that the features called microchaos on these maps are truly microchaos. Lighting conditions and the subjective approaches between individual mapping datasets can also affect the identification of chaos, and microfeatures in general (Hoppa et al., 2001; Neish et al., 2012). This study helps to put constraints on the certainty of these classifications, identifies the limitations of such an approach, and provides suggestions for further work. The ultimate deliverable of this work will be a map of all chaos, micro- and otherwise, with a confidence level attached to all the features represented on the map. These robust observations will provide firm limitations that need to be explained by chaos and microfeature formation models, in turn advancing the state of knowledge of Europa's geophysics, heat and material transport processes, and surface evolution.

Chapter 2 of this dissertation presented information about features in the RegMaps, and this chapter presents the information in a new dataset mapped in low-resolution images covering the same areas for comparison purposes. The numbers presented and discussed here represent the maximum average error rate for LowRes

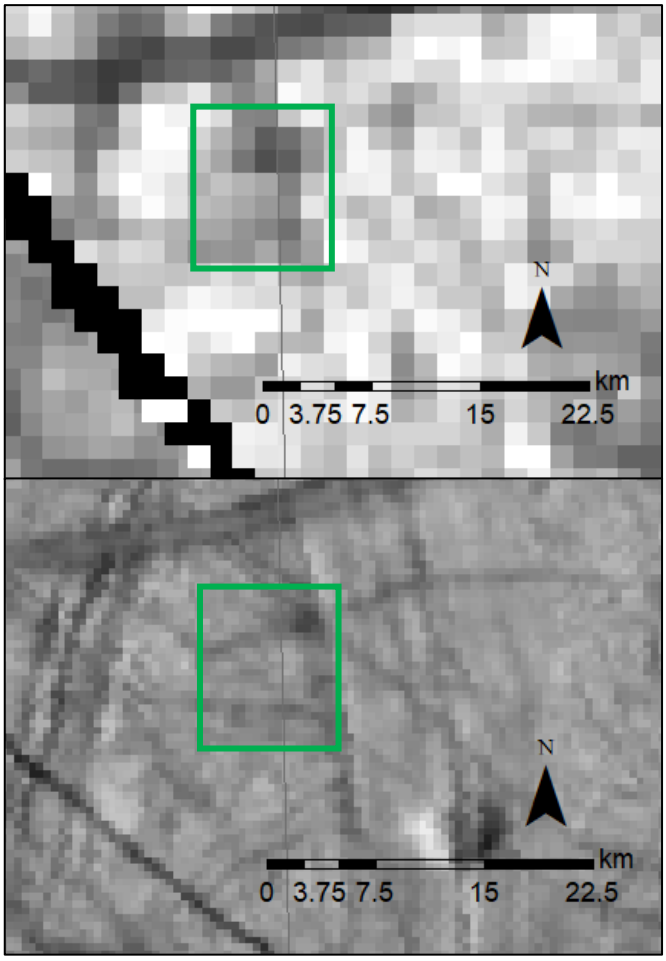

Figure 3-10: Example of a false positive (phantom feature) in a LowRes image of Europa. Top: a potential chaos feature (within green box) mapped in LowRes imaging in the E15RegMap01 region (image 5113r). Bottom: the same area in the RegMap images. This is an example of mistakenly mapping an area in the LowRes images that has no corresponding morphology in the RegMap images.

mapping studies. E15RegMap01 was selected because it had the highest number of microfeatures in the RegMap mapping project, and thus the most opportunity to find multiple features in LowRes images. It also provided the most chances for mistakes, and the best chance of quantifying those mistakes, hence why these values represent what is probably a typical error rate for LowRes mapping of microfeatures on Europa's surface. This approach is most successful in regions that have not been severely disrupted by large chaotic terrain and chaos features, linear geologic features such as bands and ridges, or areas of proposed tectonic activity, including subsumption (Kattenhorn and Prockter, 2014). These areas are likely to have few microfeatures in general because of large-scale surface modifications, and as the presence of ridges is a significant source of error in mapping, are best avoided for maximal success in microfeature mapping.

3.4.1 Mapping study

Out of the all the microfeatures initially mapped in the E15RegMap01 region, including those left unclassified initially, number 310. Out of these, 193 were not mapped in the LowRes data set. These missed features are curious, as there does not appear to be a clear size cut-off below which a majority of features are missed. If it was difficult to identify features below a certain diameter size, the histogram of missed features would show a plateau in the histogram up to that size, and above that the missed counts would start to decrease, signaling few missed features. This is not observed. This suggests that the five-pixel rule of thumb often used in mapping studies is not valid for Europa, so long as the mapped feature has an apparent albedo that is significantly different from the background. On Europa, it is possible to map down to as small as 2.5 km, though the accuracy of these classifications is likely very low.

Some feature types were more easily mapped. Chaos, hybrids, and spots were all identified at relatively high rates that range from 65.7% to 77.9%. Conversely, pits and domes were found at very low rates, 5.0% and 24.2%, respectively. This implies that chaos and chaos-related features are relatively easy to find, even in low-resolution images. Pits and domes, however, even when they are large, are difficult to map in low-resolution images. When they are mapped, it is mostly by accident, as they are often confused as a chaos or a chaos-related feature because the shadow of the pit or dome is mapped instead and misclassified as a chaos, hybrid, or spot.

This segues into an important point: that not all dark features mapped in low-resolution images are chaos or chaos-related features. Out of the 84 so-called microchaos features mapped in LowRes, 50 of them (59.5%) were verified as chaos in the RegMap dataset. Out of the remaining 34 false positives, roughly a third were either truly a hybrid feature or a spot in the RegMap images. The remaining 22 false positive features turned out to be either domes (9), unclassified (6), or phantom (7). Unclassified features are those that were mapped but not confidently assigned to a group even in the RegMap dataset, suggesting that there will be features present for which significantly higher resolution images are needed to resolve the presence and/or type of feature. The final class, the phantom features, is particularly interesting and deserves its own elaboration; this discussion is provided later in this section.

17 chaos features that were mapped in the RegMap images were missed in the LowRes mapping. Two of them were larger than 100 km^2 in area, so were not included in the RegMap microfeature dataset. The remaining 15 were then examined more closely to determine why they were missed. Two of these chaos features were associated with an

anomalously bright spot in the LowRes images; these bright spots corresponded to the illumination of a topographic high nearby, and the chaos feature's shape and relatively low normalized albedo was lost. This is likely a result of the change in illumination angles between the RegMaps and the LowRes imaging. Two more chaos features were too close to ridges and did not appear as a separate feature in the LowRes images. Four of these chaos features were indistinguishable from the background terrain in the LowRes images. When examining these features more closely, these chaos features also had higher median and mean normalized reflectances, emphasizing the importance of a change in the albedo of a surface to identify a feature. The remaining nine chaos features should have been mapped and were simply omitted. One of these features was in an area covered by two different images. That chaos was clearly visible in one of these images and invisible in the other. Future mappers should utilize the simultaneous information from all images available, even if the area is already thought of as "covered" to minimize errors like this in the future.

This is yet more information to show how important imaging angles are for identifying microchaos features in LowRes images. The feature that was missed in one image but visible in another is an interesting example. At first glance, the results seem to contradict the findings of Neish et al. (2012), as the feature was missed in the image with the higher incidence angle (5113r, inc. angle = 61.65°) and was found in an image with a much lower incidence angle (5139r, inc. angle = 30.29°). Importantly, these values only represent the average incidence angle across an image that spans thousands of square kilometers. A subsequent inspection of the incidence angles of specifically the parts of the LowRes images that cover the E15RegMap01 region show that the incidence angle is

consistently upwards of 50° in 5139r and below 30° in 5113r. This is the opposite of what the average incidence angle measurement would suggest, and can help explain why these chaos features were missed. To drive this point home, all except one of microchaos features that were omitted in the LowRes dataset were found in either 5100r or 5113r, both images that had a high incidence angle on average but a low incidence angle in the pieces of the images that covered parts of E15RegMap01. Future mapping efforts should pay careful attention to the lighting conditions of individual pixels and regions, and should restrict mapping to areas that meet particular criterion; a strong one to start with is to have incidence angles above 50°. This could also avail more images for mapping in future work.

The remaining microfeature types were found and identified correctly at varying rates. Both the rate for finding and correctly classifying domes (24.2% and 9.1%, respectively) are relatively low. These numbers together suggest that domes are difficult to identify in low-resolution images. Similarly, pits are also difficult to find and identify, with a find rate of only 5.0% and an identification accuracy of 0%. Because pits and domes are both small-scale topographic features, this suggests that low-resolution images are insufficient to pick up slight topographic variation, leading to a significant under-reporting of domes and pits in LowRes microfeature maps. Indeed, even if a feature is found and identified as a dome or a pit in a LowRes image, it is very unlikely that this feature's original classification will remain valid upon studying the feature in a higher resolution image.

Hybrids and spots are found at higher rates than domes and pits, but their identification rates are still relatively low. Hybrids were found at a rate of 65.7% but

accurately classified as hybrid features only once out of six times. Instead, hybrid features were incorrectly classified as chaos features or domes. All of the hybrid features that were missed in the LowRes mapping were characterized as Type II hybrid features, which appear as domes with cracks on their surfaces that are inconsistent with the surrounding terrain. While there is no significant difference between the normalized reflectances of Type I and Type II hybrid features, it underlines the conclusion that domes and dome-like features are generally hard to find in low-resolution images.

Spots are the rarest feature type in the RegMap dataset, so even prior to analysis, it was known that the LowRes dataset overreported the number of spots. Spots were fairly easy to find in the LowRes images (find rate = 73.9%), but roughly half of the "spots" identified in LowRes were either unclassified or phantom features (45.3%). A feature called a spot in LowRes had a high chance, roughly one in three, of being a phantom feature in RegMap images. Additionally, at least one spot was misclassified into every potential microfeature group, though the most common aside from phantom or unclassified was dome (15.1%) and chaos (13.2%). In the cases when a spot was considered a dome or a pit, it was the shadow of the topographic feature that was mapped as a spot. The LowRes "spots" that were misclassified chaos in the RegMap images adds weight to an idea from Chapter 2: that some spots could be chaos features whose interior disruption is under the resolution of the image. This is true of "spots" mapped in LowRes and RegMap images, and might explain why there appear to be a lack of small chaos features (those with less than 15 km^2; see Chapter 2 and Zamora et al. (2019) for more detail).

An argument can be made that chaos, spots, and hybrid features are inherently related due to their similar characteristics. If chaos-related features are considered approximate chaos features in RegMaps, then the chaos accuracy rate increases to 62 out of 84 times, or 73.8%. This is strong evidence that if a feature called chaos is mapped in LowRes, it has a roughly 3/4 chance of truly being chaos or a chaos-related feature. If chaos features of all sizes are considered instead of limiting it to only microchaos, then the accuracy rate for chaos and chaos-related features rises slightly to 81 out of 108 (75%).

A final important note is that the accuracy rate for microfeatures increases as size increases. This makes sense, as larger features should be easier to identify because it is possible to see more of it and details should be more apparent. There is also a size bias in microfeature type, as chaos and hybrid features tend to be significantly larger in size that pits, domes, and spots. Prior knowledge of this fact could lead to larger features being called chaos by default, unless it is clear that the feature fits better in another group. By example, in the LowRes dataset, every feature above 50 km^2 was classified as either a chaos or hybrid, despite no knowledge of the size of a feature being available until all mapping was completed. Out of the 56 microfeatures above 50 km^2, 26 features mapped in LowRes were classified incorrectly. Exactly half (13) of the time, a LowRes chaos or hybrid feature was mistaken for the other type. One of these "chaos" features was actually two individual hybrid features that are close together on Europa's surface; this is the only time it happened in the entire LowRes mapping project. The remaining times a larger microfeature was misclassified, it was a chaos or hybrid feature being called either a dome (in which case the shadow of the dome was mapped as a potential feature), an

unclassified feature, or a phantom feature. Future work will identify any commonalities in these misclassified features and provide guidelines for future LowRes mapping efforts.

3.4.2 Phantom features

The phantom features are the most concerning errors in the LowRes dataset, as they represent false positives and would greatly skew estimates of the number and locations of microfeatures on Europa's surface. A total of 51 of these features were mapped, and 46 were under the microfeature definition size cut-off. LowRes "spots" accounted for slightly more than a third of the phantom features, but features that were left unclassified in LowRes images accounted for the next largest fraction (17, or 26.1%). Following this, LowRes "chaos" features had the largest percentage (7, 15.2%). The LowRes microchaos and spots mistaken for phantom features is consistent with the high number of features reported in these categories in the LowRes dataset. These numbers suggest that as many as 37% of potential spots and roughly 15% of potential chaos features are truly non-features when viewed in superior resolution images.

About one quarter of these phantom features were truly ridges or places on Europa where multiple ridges intersect. Ridges on Europa present challenges for mapping microfeatures in LowRes images; it is possible to completely miss a feature in a mapping project if the feature is too close to the ridge and the mapper fails to recognize it as an independent feature, or a ridge could itself appear invisible aside from intermittent, dark pixels. The way to minimize this is to avoid mapping near ridges in general, or at least have as solid an understanding of where these linear features could be. This is easier to accomplish in areas for which good imaging already exists, and while this could

eliminate the need to use LowRes images in the first place, it is at least worth considering for areas that lack these images.

The other risk is that many of these phantom features are areas on Europa's surface that have no corresponding microfeature. An example of this was shown in Figure 3-9, where a darker spot in a LowRes image turned out to be a slight albedo variation in the background plains of Europa's surface. This category accounted for more than half of all phantom features. These features are primarily attributed to the difference in lighting conditions between the LowRes and RegMap images. At this time there are no obvious and quantifiable differences in the characteristics between true microfeatures and these non-features, but this could be an important area for future work.

3.4.3 Error rates

This project sought to constrain omission, accuracy, and error rates on future mapping studies that utilize low-resolution images of Europa. In terms of omission, domes and especially pits are mostly missed in low-resolution images. This suggests that for pits and domes to be found in images, there needs to be a clear topographic change in the landscape, and this change is obscured in low-resolution images. Chaos, hybrids, and spots are relatively easy to find, but 25–35% of these features are still missed in low-resolution mapping. This suggests that about a third of these microfeatures are missed in any mapping done in low-resolution. Some of these microfeatures were missed because their albedo was not significantly different in the low-resolution images, and thus did not stand out as an independent feature. The lighting conditions also contributed to some of the features, particularly chaos, going unnoticed in the low-resolution images. To

minimize this, mapping should be restricted as much as possible to areas in images where the incidence angles are above 50°.

In terms of accuracy, there is a moderate chance that if a feature is mapped as a chaos, it is truly a chaos, as chaos has a relatively high accuracy rate (59.5%). Even if a feature classified as chaos in low-resolution images is not chaos, it is most likely either a spot or a hybrid feature, which share similarities with chaos. The chance of a "chaos" feature truly being chaos or a chaos-related feature is 73.8%.

Mapping other microfeature types is less successful. Hybrids were identified as hybrids only once, but as a chaos half the time, meaning that a hybrid was identified as a chaos-related feature in 66% of cases. Spots were recognized as a spot or a chaos-related feature in roughly 33% of cases, the lowest of all the chaos-related features. A potential reason for that is because spots are defined as smooth areas of apparent low albedo. While this definition does indeed capture spots, it also means that some shadows are being confused for spots, as they are also dark areas with no apparent disruption. It is difficult to tell the difference in low-resolution images because much of the topographic information that would define a dome or a pit is under the resolution limit of the image. "Spots" in low-resolution images can also be mistaken for phantoms in RegMap images. In all but one case, a dome was not both mapped and classified as a dome, again suggesting that domes are difficult not only to find, but to accurately identify. In no cases was a pit accurately identified. The shadow of the pit or dome was mapped as a chaos, hybrid, or spot because it was distinct from the background terrain, but these classifications were false, and contribute to the more moderate accuracy rate for chaos and chaos-related features.

In terms of false positives (phantom features), there are some in particular to focus on. From this work the estimates for false positive rates are either 23.8% (for all 214 features) or 24.7% (for 186 microfeatures). Roughly a third of those features were revealed as ridges in higher resolution images, and the pieces that were mapped were the dark shadows of the ridges or an area where multiple smaller ridges intersected. While large ridges are visible even in low-resolution images, thin ridges are not always visible, contributing to this false positive rate. In areas with more ridges, this error rate is expected to be higher. Around 60% of these false positives are associated with areas on Europa's surface with no obvious microfeature present. These areas present in low-resolution images as grey smudges on the surface rather than distinct black spots. This could be a hint to future mapping studies that a feature might not be there, but albedo should not be the only reason to include or exclude a feature; some chaos features are not dark, after all. It depends on the goals of the project in question: is it better to find every potential feature, even if it means including more false positives, or to only include the features that are most likely to be a real feature? This is something to decide before mapping begins to ensure consistency within a dataset.

3.5 Conclusion

Chaos features have been mapped in multiple studies across a majority of Europa's surface, to varying success. Subsequent studies (Hoppa et al., 2001; Neish et al., 2012) show that imaging angles have a significant effect on chaos identification, more so in some cases than the resolution of the images themselves. While chaos features have been studied intently, comparatively little attention has been paid to small chaos features, domes, hybrids, pits, or spots. This work sought to fill this knowledge gap and provide

constraints for future mapping studies. The results of these mapping studies will help refine models that attempt to explain how these microfeatures form and what that implies about heat and material transport on Europa and its surface evolution.

An independent dataset was created of the E15RegMap01 region mapping features in four low-resolution images. This dataset was then compared to the E15RegMap01 dataset (see Chapter 2). Chaos, spots, and hybrid features were relatively easy to find, while pits and domes were most often missed. Chaos was also fairly easy to recognize as chaos, and approximately 60% of potential chaos features were verified as true chaos in the RegMap dataset. If hybrids and spots are considered as chaos-related features, then the accuracy rate for chaos rises to almost 75%. Pits and domes were almost never recognized as pits or domes, and thus have very low accuracy rates. On top of low find rates for both of these features, it is fair to say that pits and domes are virtually unable to be confidently found in low-resolution images. One warning is that not all dark features in low-resolution images are chaos or chaos-related features. Some of these false positives were associated with ridges, some were associated with the shadows of topographic highs and lows, and some were anomalously dark areas in Europa's plains regions that have no associated microfeature. This false positive rate could be as high as 25%.

Future mapping studies should decide in advance whether to include all potential features or to only focus on the ones that are most likely to be true features. This will affect the error rates for which This project also emphasizes the finding from Neish et al. (2012) that chaos is most easily identified in images with high (> 50°) incidence angles. This includes restricted areas within low-resolution images that otherwise have

inappropriate average incidence angles. With this knowledge there are many more places where potential microfeatures could be mapped on Europa's surface, thus dramatically increasing the amount of information available on microfeatures and providing solid constraints for modeling studies. This work will also allow for predictions to be made ahead of the Europa Clipper Flagship mission. Some of these predictions are addressed formally in the Conclusion of this document.

CHAPTER 4

QUANTITATIVE CLASSIFICATION OF MICROFEATURES

4.1 Introduction

From the mapping work presented in Chapter 2, it is clear that two main obstacles exist that prevent the identification of microfeatures in areas of Europa's surface that are not covered in RegMap mosaics: 1) the images that cover the area of Europa outside of RegMap areas are low-resolution, where microfeatures are difficult to find, let alone identify, and 2) variations always arise between qualitative datasets, creating uncertainty in classification, even in RegMap-resolution images. These problems are intertwined; quantitatively classifying features based on a series of parameters increases the accuracy on the identification of features in low-resolution (LowRes) images, and finding more features in LowRes images strengthens the classification metrics. It makes sense, therefore, to consider these questions simultaneously.

From the mapping project, there already exists a validated dataset compiled from four independently collected datasets, and there are significant differences between the microfeature groups. These differences together could be advantageously used to quantitatively classify features not just in RegMaps, but LowRes images as well. The LowRes images mapping project (Chapter 3) showed that there are many instances where one microfeature type is mistaken for another, particularly chaos being mistaken for a non-feature such as a ridge. There could be morphometric similarities in these false positives that a multivariate statistical classification approach could better detect these differences than a human could. This is the motivation behind applying multivariate statistical analyses to mapped datasets on Europa. The focus of this chapter is to

determine how useful an approach of this kind can be by developing an appropriate methodology, determining how effective and accurate this approach is, and offering suggestions for future work.

4.2 Statistical Classification Introduction

The selected multivariate analysis is a hierarchical classification analysis called discriminant function analysis (DFA). DFA is a type of multivariate analysis that is used to quantitatively sort data points of unknown origin or morphology into one of two or more user-specified groups based on similarities of the individual data point to the characteristics of those groups (Tabachnick and Fidell, 2013). It is a standard hierarchical analysis in most statistical software; the package used here is IBM SPSS 25. So long as there are significant differences between the groups, a new data point can be sorted in and assigned a most probable group. DFA has been used in other disciplines before, including geology (e.g., Roser and Korsch, 1988), but this is the first time that this kind of quantitative classification approach has been used in planetary science. The main question answered by this analysis is: can microfeatures on Europa be sorted above and beyond simple chance using a set of quantified metrics in a classification approach?

The first step in a DFA is to define the groups by populating them with the most robust features. The features mapped, classified, and defined in Chapter 2 provide the quantitative framework for these groups. A linear DFA then uses the characteristics of features within predetermined groups to test whether the discriminating variables that describe each feature can be linearly combined to separate the groups in a statistically significant way. These groups are mutually exclusive, meaning no one data point can belong to two different groups at the same time. Variables must be continuous and should

be as independent as possible, though the test is robust against variables with linear correlations less than 0.8 (Tabachnick and Fidell, 2013). Depending on the variables, the analysis may sort the data well or poorly, causing misclassification among grouped data and weak group assignments to unclassified data. Here, unclassified data refers to features that were placed into the unclassified category, while misclassification refers to data that were placed into a group originally and failed reassignment into the same group under the cross-validation test run by the DFA. In the dataset described in Chapter 2, mapped features that could not be confidently classified into one of the microfeature groups were designated as "unclassified." These features were not included in the original analysis, as they could not be used to describe the quantitative characteristics of a microfeature group, and they are not included in the DFA here.

The DFA constructs orthogonal mathematical functions that include the potentially discriminating variables, with each variable assigned a coefficient based on the effect it has on the particular discriminating function. Discriminating functions are also known as roots, canonical values, principal components, and/or dimensions depending on the statistical context in which they are formed (Tabachnick and Fidell, 2013). The number of functions produced is the lesser of either the number of discriminating variables (the predictors) or k-1, where k is the number of groups (Tabachnick and Fidell, 2013). The number of data points in the smallest group should be larger than the total number of predictors (Tabachnick and Fidell, 2013); otherwise, the results of the DFA become so overfitted that the functions are no longer generalizable to other datasets. The best functions result in well-separated groups. Functions are linearly independent from each other (orthogonal) and are linear functions, meaning no variable is

raised to a power greater than 1. The coefficient is equivalent to a weight in something like a weighted average or weighted probability calculation. Each discriminant function is designed to separate one group apart from the others in a statistically significant way (Tabachnick and Fidell, 2013). As adept as this approach is at examining relationships between groups in a multi-parameter space, the DFA is only capable of identifying linear trends in the data. Other tests such as logistic regression should be used to find non-linear patterns in the data; this can be the focus of future work.

To identify the most discriminating functions based on the predictors, the DFA evaluates each function for the individual features in the data set. If at least two functions can be produced, results are plotted with the two functions with the highest eigenvalues on each axis. Function 1 has the highest eigenvalue from the covariance matrix, function 2 has the second highest eigenvalue; this pattern continues down until all functions have been accounted for. The larger the eigenvalue of the function and the higher the canonical correlation, the better that function is at separating the groups. Even though only two functions can be displayed in a figure, mathematically there is the equivalent number of axes to the number of discriminant functions produced. To show the relationships between all the functions, multiple plots need to be produced. In the case where there is only one function calculated, no plot is produced, as the groups would be separated along a straight line, and values such as sensitivity and specificity are calculated instead. Sensitivity and specificity are discussed in more detail later.

The measure of the accuracy of these analyses is done automatically in SPSS via Leave-One-Out Cross-Validation (LOOCV). After the initial DFA is complete, each data point is removed from the dataset, and the DFA is run again, excluding that point. The

excluded point is then sorted into one of the predetermined groups, based on its function values and which probabilistic rule has been selected as part of the test:

1. Equal probability: the data point has an initially equal chance of being sorted into any of the predetermined groups
2. Weighted probability: the data point has a higher chance of being sorted into a group that has more data points in it

When the groups are close to the same size, weighted probability and equal probability will have roughly the same LOOCV percentage. A data point is sorted into the microfeature type whose group centroid (the average of the discriminant scores for each of the discriminant functions) is the least distance away from the average of the data point's discriminant scores in the k-dimensional space. Once the data point has been re-sorted, the program notes whether or not the new group matches the group the data point originally belonged to. If the two classifications match, the cross-validation was successful. There are no special problems that arise from unequal sample sizes except in the case of *a priori* classification (Tabachnick and Fidell, 2013), so weighted probability is used in this analysis.

In any statistical analysis, there is the possibility that a correct result is found by random chance. The number correct from random chance should be compared to the number that was sorted correctly overall to determine if the DFA did a better job of sorting than random chance could have done. LOOCV is one metric for this. An independent metric is to calculate the expected number sorted correctly and compare it to the actual overall sorted correctly. In the equal probability sorting case, the chance of sorting into any particular group is k^{-1}. This means that for any group, the size of that

group multiplied by k^{-1} is the number of sorted cases that could be attributed to chance. The sum of these numbers is the expected number. In the weighted probability case, calculating the expected number of sorted cases that could be attributed to chance is a bit more involved. The probability of a point being sorted into a particular group is determined as $p_i = \frac{n_i}{N}$, where N is the total number of data points in the analysis and n_i is the number of data points in that particular group. These probabilities are multiplied by the number of data points in their respective groups, and the numbers are summed to the total number of groups included in the analysis (represented by j). If the calculated number is a decimal value, the number is rounded up in every case. The equation for calculating the expected number of correctly sorted data points in a weighted probability case is therefore:

$$Expected\ number = \sum_{i=1}^{j} \left(\frac{n_i}{N}\right) * n_i$$

Other metrics of success are specificity and sensitivity, but they are values that are only calculated in two-group DFAs. In a two-group test, one group is considered the positive group, and the other, the negative. Specificity is the percentage of features sorted into the positive group that originally belonged to that group, or the true positives. The difference of this percentage from perfect is the probability of a Type I error, or the number of false positives that the test misclassified. Using Table 4-1, specificity is calculated as 100*(a/(a+c)). Sensitivity is the percentage of features sorted into the negative group that originally belonged to that group, or the true negatives. The difference of this percentage from perfect is the probability of a Type II error, or the

number of false negatives that the test misclassified. Using Table 4-1, sensitivity is calculated as 100*(d/(b+d)).

These numbers illustrate how likely a certain feature truly is what the test says it is, thus putting a measure of statistical confidence to the classifications. Depending on the goals of the analysis, the level of specificity and sensitivity necessary may change. A test with a high sensitivity means that many things are being classified into the positive group, but false positives are more likely as a result. The flip side of this is that if a high sensitivity test indicates that a data point belongs to the negative group, it is very likely that that data point is a true negative. Simply put, a high sensitivity test will also have a low Type II error rate. The same logic can be applied to the specificity measurements, where there will be more false negatives and a higher Type I error. This case would yield the conservative estimate for feature classification, as the ones that are classified as positive have a very high probability of being a true positive.

Finally, there is the overall measure of accuracy, which is simply the number of correctly classified data points divided by the total number of data points, *n*. Using Table 4-1, this value is calculated as 100*((a+d)/N), where N is the total number of features included in the analysis. This metric differs from LOOCV because it does not remove a point and reclassify it using the reassessed discriminant functions; rather, it directly calculates the classification success with all points included.

4.3 RegMap Dataset

The dataset used here is the same one that was described in Chapter 2. Univariate histograms of the area, perimeter, eccentricity, and normalized reflectance for each of the microfeature groups were produced to identify any outliers and to examine the

Table 4-1: Calculations for sensitivity and specificity in a DFA

DFA Effectiveness Measurements	DFA Classification		**TOTAL**
	Group 1	Group 1	
Group 1	a	b	a+b
Group 2	c	d	c+d
TOTAL	a+c	b+d	n

distribution of the histograms for significant deviations from a normal (Gaussian) distribution (Tabachnick and Fidell, 2013). Neither outliers nor non-normality were discovered in the microfeatures group, though when all features of all sizes were considered, the area and perimeter histograms were very right-skewed (large outliers at large sizes). This is another reason why only microfeatures should be considered in DFA analyses, especially if raw size is used as a metric. Robustness against variations in normality is highest when the number of data points in the smallest group is at least 20 and when there are five or fewer predictors (Tabachnick and Fidell, 2013). Spots is the group that fails this parameter in some cases, hence they are excluded in analyses where spots are fewer than 20 in number. For more details on this dataset, please refer back to Chapter 2.

4.4 Methods

Multiple DFAs were run in with a variety of different parameters. Only those features with areas under 100 km^2 were studied, following the definition of a microfeature. Area, perimeter, diameter, three ratios, irregularity, and eccentricity are collectively called the morphometric variables, as they are related to the size and shapes of the features. The mean, median, standard deviation, and range of a feature's normalized reflectance are collectively called the "darkness" variables. Radius was not included as a variable because it fails the statistical tolerance test, as is not linearly independent from all other variables (it is half of the diameter), and thus does not provide any new information that cannot be fully explained by another variable. Including it would violate the assumption of absence of multicollinearity in the DFA.

The three ratios are unitless ratios designed to quantify the shape of each feature in a slightly different way. Ratio 1 is calculated by the square root of the area divided by the perimeter, and relates the enclosed area to the perimeter of a feature. Ratio 2 is the length of a feature as determined by the Minimum Bounding Geometry (MBG) tool in ArcGIS divided by the perimeter of the feature, and relates the maximum lateral extent of a feature to its perimeter. Ratio 3 is calculated by the area of a feature divided by the maximum length and maximum width of a feature as determined by the MBG tool; effectively, it estimates the percentage of area that the feature covers within the rectangle made up of its maximum extent in two directions. For completeness and to refresh the reader's memory, the parameters irregularity and eccentricity are also described here. Irregularity is calculated by dividing the perimeter by the circumference of the circle with a diameter equal to the equal area diameter, which in itself is calculated from the area of the feature. The eccentricity, more accurately called the aspect ratio of a feature, is the maximum width divided by the maximum length of rectangle that encloses the feature, as determined by the MBG tool. The formulae for these metrics are given in Table 4-2.

The variables first included in all analyses were spherical area, spherical perimeter, equal area diameter, Ratio 1, Ratio 2, Ratio 3, irregularity, eccentricity (i.e., the aspect ratio), mean normalized reflectance, median normalized reflectance, standard deviation of normalized reflectance, and the total range of normalized reflectance. All of these variables were included in every analysis initially, and from each analysis a base LOOCV percentage was determined for the group combination. After the base LOOCV percentage was calculated, the non-significant and highly correlated variables were removed. The non-significant variables were determined within SPSS as part of a

Table 4-2: The formulae for the morphometric variables describing features in the DFA.

Metric	Formula
Ratio 1	$\frac{\sqrt{Area}}{Perimeter}$
Ratio 2	$\frac{Maximum\ Length}{Perimeter}$
Ratio 3	$\frac{Area}{Maximum\ Length * Maximum\ Width}$
Irregularity	$\frac{Perimeter}{\pi * Equal\ Diameter}$

univariate analysis of variance (ANOVA) using a simple F-test. Any sample of any size will have some amount of variation within a particular metric. The F-test is a basic statistical test that tests if the variation observed is above and beyond the amount of variation expected in any randomly selected sample. If the variance observed is more than could be expected from a random sample, then that variable is interpreted to sort between the microfeature groups at a statistically significant level. The chosen alpha (α) value is 0.05, so any variable with a calculated significance level ≥ 0.05 was removed because it did not significantly contribute to the separation between the groups.

The significant variables were reduced again to remove any that had a moderate correlation (over 0.4) with another. This value is conservative, as the DFA would have performed with variables that had correlations up to 0.8, and was chosen because it provides the most-conservative LOOCV with the fewest variables. In general, one variable was chosen to represent a feature's size, one was chosen to represent the normalized reflectance measurement, and one was chosen to represent its shape or irregularity. One special case of variable selection is that of mean and median of normalized reflectance. In most cases, mean and median are highly correlated (≥0.9), and thus only one was included. Median was preferred over mean because it is resistant to any outliers that may exist in the data, another conservative decision. Performing this down-selection allowed for maximum separation between the groups with the fewest number of variables. If this method is to be expanded to other areas, especially those where it is not possible to get accurate measurements for all the metrics, it is

advantageous to require the fewest number of variables that will still yield useful information.

Two-group analyses were performed first for each region individually. This means that every two-group combination for chaos, domes, hybrids, pits, and spots was tested, and for each test, LOOCV, overall success, sensitivity, and specificity were recorded. In all cases except E15RegMap01, spots were excluded from the two-group analyses because their sample size was too small for the DFA to be run. Each region was initially analyzed separately. Weighted probability was used in every analysis as it is a better reflection of the observations taken on Europa's surface than the equal probability would imply. First all two group combinations were run, excepting spots in all but E15RegMap01, as there were too few of them to run a DFA. Once the two-group tests were run, one three group test was run. These analyses included the larger supergroups of chaos/spots and pits/domes as the first two groups and hybrids as the third group. Next, either a four or five group test was run for each region individually. In the five group cases, only LOOCV and overall success were calculated, as specificity and sensitivity cannot be calculated in DFAs with more than two groups. Again, spots were excluded in most cases as there were too few of them to run a DFA with spots as a distinct group.

Once all the individual regions were analyzed, multiple grand DFAs were run by combining the data from all four RegMaps into large, comprehensive groups. Following the pattern from the RegMap analyses, first two group tests were run, followed by a three group test, and finally a five group DFA. The canonical discriminant values for each coefficient in each test, the functions' eigenvalues and canonical correlations, specificity and sensitivity (when calculated), overall accuracy, expected accuracy, and LOOCV (also

called cross-validation success rate) are given for all these analyses in Tables 4-3 to 4-7 for the Grand DFA. The results of the other tests are included in Appendix E.

4.5 Results

4.5.1 Two group tests, Grand DFA

Two group tests were run for every combination of microfeature group to get the two-group Grand DFA results. In every case, the quantitative sorting was able to sort between the groups better than simple random chance, though sometimes the difference between the expected percentage correct and the overall accuracy was not very large. In the cases where the group sizes were roughly equal, the chance of a single data point being sorted into either group during LOOCV was roughly 50%. In the cases where group sizes were greatly different, the probability of a data point being sorted into either group during LOOCV made it far more likely that the larger group would absorb more data points. Under the weighted probability sorting rules, it makes sense that more features would be sorted correctly by chance if the group sizes were exceptionally different. This is seen in cases where spots are one of the groups.

Under LOOCV, the groups that are well-sorted under LOOCV (above 80.0% correct) are chaos vs. domes, chaos vs. spots, hybrids vs. spots, and pits vs. spots. In the case of chaos vs. another microfeature type, the larger diameter of a chaos feature was the main driver of the separation in the eigenfunction; that is, it had the largest coefficient in the linear discriminant function. This was not true in the chaos vs. pits case, where it was the median normalized reflectance that drove the separation. For the other microfeature combinations, the DFA was able to separate the groups moderately well (between 60 and 80%). The DFA struggled the most with separating pits and domes, as this combination

	Diameter	Median	Std. Deviation	Ratio 1	Irregularity	Eigenvalue	Percent of Variance (%)	Canonical Correlation	Cross-validation success rate (%)
Chaos vs. Domes	0.914	-0.267	x	-0.172	x	0.616	100	0.617	80.8
Chaos vs. Hybrids	-0.578	x	0.736	0.328	x	0.139	100	0.349	74.4
Chaos vs. Pits	0.835	-0.473	x	-0.268	x	0.569	100	0.602	75.2
Chaos vs. Spots	0.860	0.429	x	x	0.108	0.353	100	0.511	90.0
Domes vs. Hybrids	0.885	-0.461	x	-0.113	x	0.412	100	0.540	74.2
Domes vs. Pits	1.000	x	x	x	x	0.027	100	0.161	65.4
Domes vs. Spots	x	0.942	x	0.434$	x	0.247	100	0.445	81.4
Hybrids vs. Pits	-0.769	0.713	x	0.198	x	0.281	100	0.468	75.7
Hybrids vs. Spots	0.844	0.425	x	x	x	0.397	100	0.533	81.6
Pits vs. Spots	0.214	0.901	x	0.393	x	0.209	100	0.416	87.9
CSH vs. DP	-0.809	0.573	x	0.259	x	0.461	100	0.562	74.2

Table 4-3: Grand DFA with all features from all RegMaps, coefficients and other technical numbers. These tests are the two-group combinations including all microfeatures mapped in all RegMaps across Europa. The "$" superscript indicates that for this test, Ratio 3 was used instead of Ratio 1.

	Group 1 n	Group 2 n	Base LOOCV (%)	New LOOCV (%)	Overall Accuracy (%)	Expected correct sorted by chance (%)	Sensitivity (%)	Specificity (%)
Chaos vs. Domes	239	116	84.1	80.8	81.7	56.1	66.9	87.6
Chaos vs. Hybrids	239	90	73.8	74.4	76.6	60.2	23.2	95.4
Chaos vs. Pits	239	217	85.0	75.2	75.9	50.2	76.6	74.3
Chaos vs. Spots	239	29	90.4	90.0	91.4	80.6	33.3	97.5
Domes vs. Hybrids	116	90	70.9	74.2	77.2	51.0	65.3	82.2
Domes vs. Pits	116	217	63.9	65.4	66.7	54.7	100.0	4.2
Domes vs. Spots	116	29	87.6	81.4	82.8	68.3	27.6	96.6
Hybrids vs. Pits	90	217	78.3	75.7	78.2	58.6	90.8	44.2
Hybrids vs. Spots	90	29	89.6	81.6	85.7	63.0	40.0	94.7
Spots vs. Pits	29	217	91.9	87.9	88.6	79.3	16.7	97.7
CSH vs. PD	358	333	80.3	74.2	75.7	50.1	73.8	75.1

Table 4-4: Grand DFA with all features from all RegMaps, descriptive numbers (sensitivity, specificity, accuracy, leave-one-out cross validation). These tests are the two-group combinations including all microfeatures mapped in all RegMaps across Europa.

Table 4-5: Three group DFA coefficients and descriptive numbers

	Diameter	Median	Ratio 1	Eigenvalue	Percent of Variance (%)	Cumulative Percent (%)	Canonical Correlation	Overall Accuracy (%)	Expected correct sorted by chance (%)	Cross-validation success rate (%)
F1	-0.807	0.560	0.283	0.478	98.4	98.4	0.569	66.0	39.9	64.7
F2	0.109	-0.559	0.818	0.008	1.6	100	0.089			

Table 4-6: Five group DFA coefficients and descriptive numbers

	Area	Median	Ratio 3	Eigenvalue	Percent of Variance (%)	Cumulative Percent (%)	Canonical Correlation	Overall Accuracy (%)	Expected correct sorted by chance (%)	Cross-validation success rate (%)
F1	0.866	-0.319	-0.384	0.546	86.0	86.0	0.594	51.4	26.4	50.4
F2	0.451	0.909	0.103	0.078	12.3	98.3	0.269			
F3	0.215	-0.270	0.918	0.011	1.7	100	0.102			

Table 4-7: Group classifications for the microfeatures using the Grand DFA framework, all microfeatures from all regions included. Variables are feature area, ratio 3, and median normalized reflectance. These only include features that were already classified in the RegMap images and reflects what the computer thought these features were. Green highlighted boxes are those that were classified correctly.

Original Group Membership	Predicted Group Membership					
	Chaos	Domes	Hybrids	Pits	Spots	Total
Chaos	174 (72.8%)	0	0	63 (26.4%)	2 (0.8%)	239
Domes	16 (13.8%)	0	0	99 (85.3%)	1 (0.9%)	116
Hybrids	52 (57.8%)	0	2 (2.2%)	36 (40.0%)	0	90
Pits	36 (16.6%)	0	0	176 (81.1%)	5 (2.3%)	217
Spots	7 (24.1%)	0	1 (3.4%)	18 (62.1%)	3 (10.3%)	29

had the lowest eigenvalue and canonical correlation out of all combinations. Moreover, none of the means of the variables were significantly different between domes and pits, which underlines how difficult it was to separate these groups. In the end, only diameter was included as a discriminating variable, but it was insufficient information to yield strong separation between pits and domes.

The trend seen in the eigenvalues and canonical correlations is mirrored in the values for specificity and sensitivity. In the cases where LOOCV was only moderately successful, either the sensitivity or the specificity was very high while the other remained relatively low (under 50%). In the chaos vs. spots case, for example, the specificity was very high, while the sensitivity was low (33.3%). This indicates that many of the chaos features are mistaken for chaos features, leading to more false positives (Type I error) in this case. This is especially apparent in the case of domes vs. pits, where the sensitivity is 100.0% but the specificity is only 4.2%. A key observation is that there are 101 more data points in the pits group than in the domes group, which is partially responsible for the high sensitivity value (large number of false negatives, Type II error), as there are preferentially more data points being sorted into the pits group rather than the domes group. This is true of the chaos vs. hybrids, spots vs. chaos and spots vs. pits cases as well, as there are significantly more features in the larger group than in the smaller group, but even in those cases there are slightly more equal values for sensitivity and specificity.

Initially it seems like the DFA struggles most to separate between chaos, hybrids, and spots, and between pits and domes. To test the test's effective at sorting between these two larger groups, a special two-group DFA was run between Chaos/Hybrids/Spots

and Domes/Pits. This analysis yielded moderate values for the eigenvalue and the canonical correlation, and high values for both specificity and sensitivity. It also had a higher-than-expected accuracy rate, where 75.7% of the features were correctly sorted against an expected correct rate of 50.1%. Thus, the DFA is able to sort between the supergroups of Chaos/Hybrids/Spots and Domes/Pits with roughly 75% confidence.

4.5.2 Three group test, Grand DFA

The three group test was made up of chaos/spots, pits/domes, and hybrids. Three is the minimum number of groups to develop a plot, as it will reveal two separate eigenfunctions. The more dominant function (F1) has an eigenvalue of 0.478 and a canonical correlation of 0.569, and explains 98.4% of the variance seen in the data. The first function was most strongly dominated by the diameter of the groups, followed by the median normalized reflectance measurement, and lastly by the area:perimeter ratio (Ratio 1). The second function (F2) had an eigenvalue of only 0.008 and a canonical correlation of 0.089. Nevertheless, it explains the remaining 1.6% of variance. The first two functions combined were significant at the $\alpha = 0.05$ level [$\chi^2(6) = 278.133$, $p < 0.001$]. The second function independently is not significant at the $\alpha = 0.05$ [$\chi^2(2) = 5.489$, $p = 0.064$], but is just beyond statistical significance. For a higher α value, the function could be interpreted as significant.

Figure 4-1 shows the plot for the three group DFA, and reveals that the chaos/spots group (purple circles) distinctly separates from the domes/pits group (red diamonds), though not completely. The hybrids group (blue triangles) almost equally straddle both groups. The LOOCV success rate of this test was 64.7%, and overall, 66.0% of the features were sorted correctly, against the expected correct sorting rate of

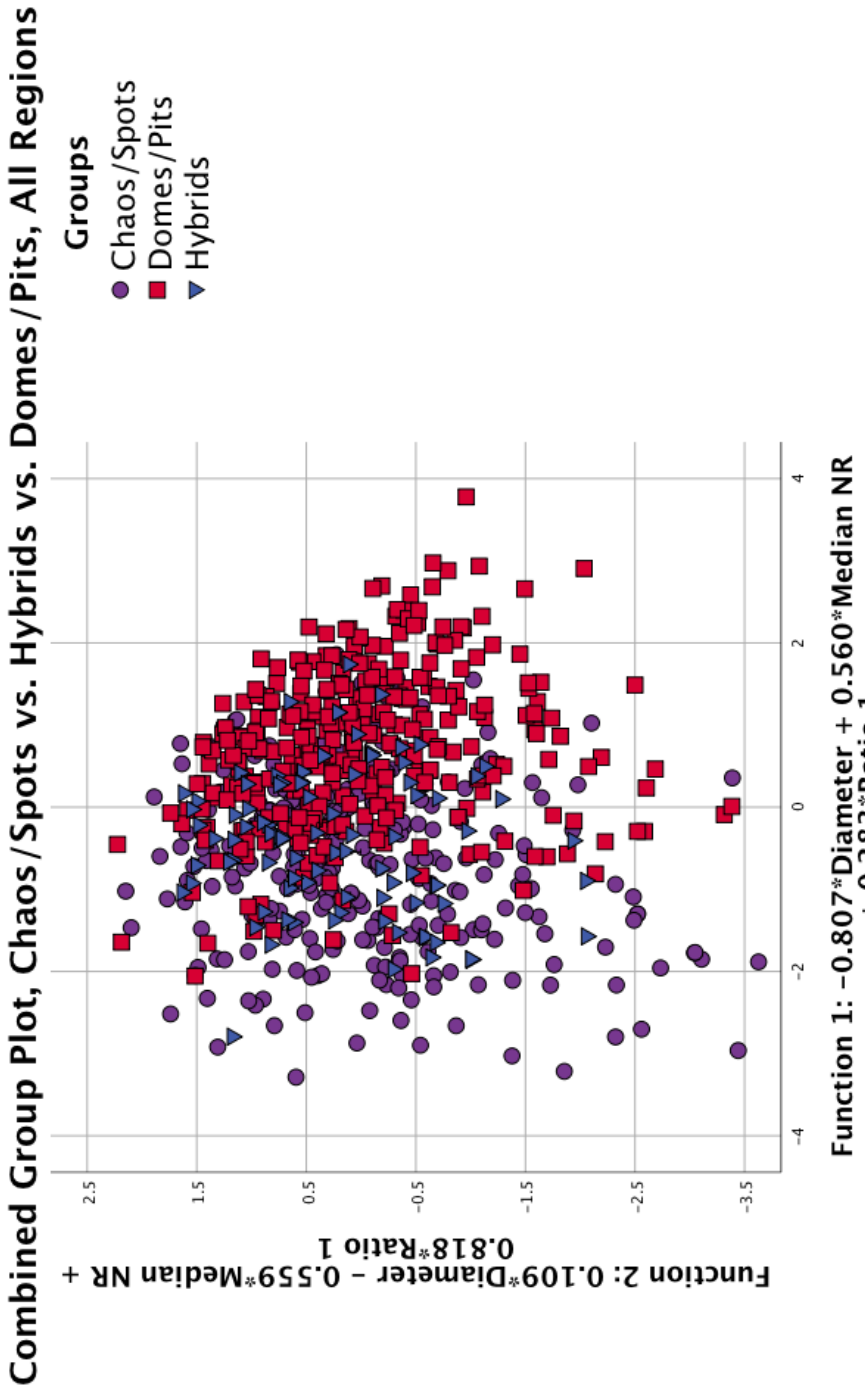

Figure 4-1: Three group Grand DFA plot. This plot combines all the microfeatures mapped in all four RegMap areas and evaluates them for differences. The three groups were selected based on the results of the two-group tests (Tables 4-3 and 4-4), and are: chaos/spots, hybrids, and domes/pits. The numerical results are given in Table 4-5.

39.9%. This test was able to correctly sort chaos/spots 184/268 times (67.9%) of the time, and was able to sort pits/domes correctly 268/333 times (80.4%). Hybrids were never correctly sorted. The reasons for this could be that the test was biased towards sorting into the two significantly larger supergroups of chaos/spots and pits/domes, but with a sample size of 90, hybrids were a sufficient group size to perform the DFA in the first place with them as a separate group. More hybrids were sorted into the chaos/spots group (54) than into the pits/domes group (36).

4.5.3 Five group test, Grand DFA

In the five group test, all microfeature types were included in the analysis as separate groups, meaning there was a total of 691 classified microfeatures included in the analysis. Such a relatively large sample size is ideal for yielding fairly robust results. As one cautionary word, the group size of spots (29) was the smallest so the results for that group are therefore the most uncertain.

The first eigenfunction (F1) was dominated by the size measurement of the feature, which in this case was the area rather than the diameter. There was no statistical reason for choosing area over diameter aside from the increased success rate of the LOOCV using area instead of diameter. F1 had an eigenvalue of 0.546 and a canonical correlation of 0.594, and explained 86.0% of the total variance in the data. The second function (F2) was dominated by the median normalized reflectance, and had an eigenvalue of 0.078, had a canonical correlation of 0.269, and explained 12.3% of the total variance in the data. The third eigenfunction was dominated by the shape ratio, Ratio 3, and had an eigenvalue of 0.011, had a canonical correlation of 0.102, and explained the remaining 1.7% of total variance in the data. All three functions together

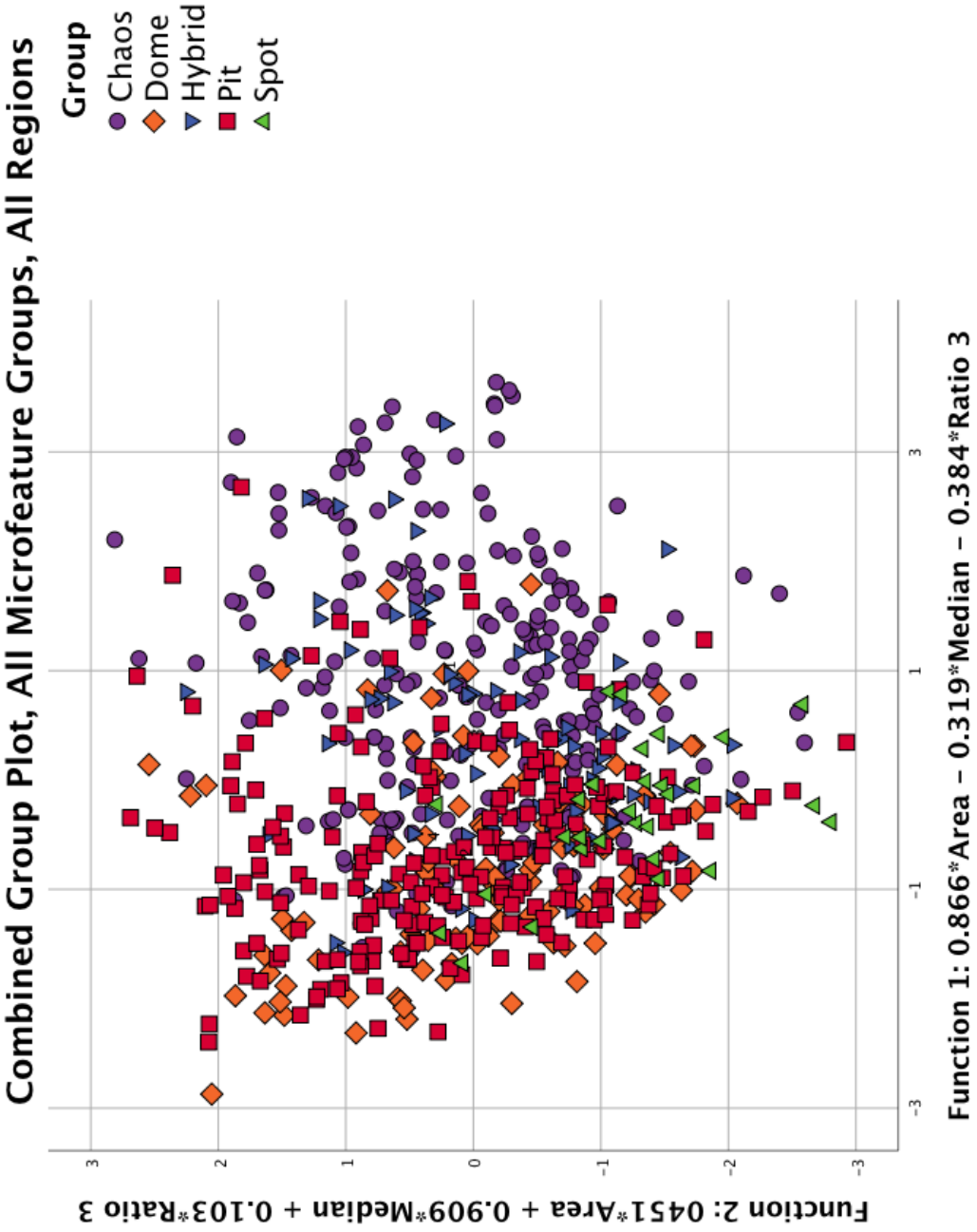

Figure 4-2: Five group Grand DFA plot. This plot combines all the microfeatures mapped in all four RegMap areas and evaluates them for differences. Each microfeature type is considered a separate group. The numerical results are given in Tables 4-6 and 4-7.

are statistically significant at the $\alpha = 0.05$ level [$\chi^2(12) = 359.078$, $p < 0.001$]. Functions 2 and 3 are also statistically significant at the $\alpha = 0.05$ level [$\chi^2(6) = 59.014$, $p < 0.001$], and Function 3 on its own is also significant at the $\alpha = 0.05$ level [$\chi^2(2) = 7.209$, $p = 0.027$].

The plot (Figure 4-2) for the five group DFA shows large amounts of overlap between the groups, though the same pattern of chaos separating out from pits/domes is also present. In this case, the spots appear to be more closely associated with the pits/domes group along the x axis (F1: feature area-dominated function), but they sort out towards the lower end of the y axis (F2: normalized reflectance dominated function). The LOOCV success rate of this test was 50.4%, and overall 51.4% of the features were sorted correctly, against the expected correct sorting rate of 26.4%. This classification was able to correctly sort chaos 174/239 times (72.8%), correctly sort hybrids 2/90 times (2.2%), correctly sort pits 175/217 times (81.0%), and correctly sort spots 3/29 times (10.3%). Domes were never sorted correctly in this analysis using these variables, despite the adequate group size. As was seen in the three group case, hybrids were split between the chaos and pits group, which are the two largest groups and therefore had the highest weighted probabilities. More hybrid features sorted into the chaos group (57.8%) than into the pits group (40.0%). The tabular write up for these overall classifications is given in Table 4-7.

4.6 Discussion

4.6.1 Summary of Results

While these features may look different to a human in RegMap images, teaching a computer to recognize these differences is a separate task. Nevertheless, all these

numbers point to a simple conclusion: that a quantitative, computer-driven classification system for microfeatures on Europa is capable of sorting between microfeature types. The effectiveness of these classifications varies based on which groups are included and which discriminant variables are used, but this classification system consistently performs at a rate that is better-than-expected from simple random guessing. This is only the first pass of classification analysis on a planetary body such as Europa, but the results are already impressive.

At the beginning, all variables were considered as potentially discriminating and were included in the initial classification. This resulted in a base LOOCV percentage. Subsequent analyses only included those which revealed a significant difference between the means of the groups for that variable (the ANOVA univariate analysis) and those that were not highly correlated to avoid any unseen errors as a result of multicollinearity. This resulted in a second LOOCV percentage. In most of the cases studied in the Grand DFAs, this new LOOCV percentage was lower than the base LOOCV. On the surface, this means the classification analysis is less effective at sorting the features in the case where only some variables are considered rather than all of them. In these cases, all it means is that the inclusion of additional variables could account for and describe more of the variation seen within the dataset. Sometimes this inherent random variation is correlated positively with excluded variables, which explains why excluding these variables decreases the LOOCV. To tailor a single model to describe a single population perfectly is overfitting. The goal of this work is to generalize to new populations, so overfitting a model based on a sample population would be antithetical to this work's purpose. While it is a good idea to have multiple variables at one's use, the most generalizable model is

the one with the fewest variables, thus requiring the least amount of information to still be effective at classification.

Consistently, a measure of the size of a feature, a measure of the normalized reflectance (a variable related to albedo), and a measure of the shape of the features is sufficient to create a significant degree of separation between the groups, though in some cases only one or two of these categories had a statistically significant variable and was used in the subsequent classification test. Overall, the classification analysis is best at sorting between chaos/spots/hybrids and pits/domes, but is less successful at sorting within those groups. This is a result that is consistent in the Grand DFA tests and in the DFAs run for each RegMap region (see Appendix E for more detail). In the test where chaos, spots, and hybrids were included in the same group and pits and domes in the second, the specificity and sensitivity values were both roughly equal and high (75.1% and 73.8%, respectively), and the LOOCV was also high at 74.2%. The accuracy is higher than could be expected from random chance. All these numbers together suggest that there are significant and important differences between these two supergroups that could be investigated further within the realm of machine learning and statistical classification analyses.

The groups where the DFA was least effective at sorting was between domes and pits. These groups are effectively identical across every variable, with non-significant ANOVA results for every potential discriminating variable. One analysis was done with one variable to have an idea of the results of a scenario with too-similar groups. The overall accuracy was above what could have been expected from random chance (66.7% vs. 54.7%, respectively), but this vastly different values between sensitivity and

specificity indicate a high chance (95.8%) of incorrectly assigning domes to the pits category. In this case, there are many falsely classified pits (false negatives). When a human mapper is identifying a pit or a dome, it is the topographical data (e.g., the position of the shadow) that informs whether or not a feature is a pit or a dome. This information is not easily attainable from simple mapping efforts that do not include photometry or some kind of altimetry measurement. In the case where this information is available, the computer should easily be able to sort these features, as the height or depth measurements would be significantly different between the two groups (negative or positive). In the absence of topography data, a human is still the best classifier.

Other cases with large differences between the sensitivity and specificity values are those where the two groups are not sufficiently different enough in one of the discriminating variables. For example, the chaos vs. spots has a high LOOCV percentage (90.0%), but a large difference between the specificity and sensitivity values (97.5% and 33.3%, respectively). The disparity could partially be attributed to the difference in group sizes, as that is what drives the weighted probability measurements and prior probabilities for group classification. It is not clear whether the difference in group size is, in itself, a significant result of a preferential formation process on Europa, or if it is a result of insufficient imaging of a majority of its surface, leading to an observationally-biased result that chaos is far more common on Europa. Regardless of the underlying reason, the result within the DFA is that some spots are incorrectly sorted into the chaos group, despite the fact that chaos is significantly larger than spots. The addition of median normalized reflectance, where chaos and spots differ less, could be confusing the analysis. To test this, a final DFA was run with only diameter and ratio 1 included as

discriminating variables. In this case, the LOOCV rose to 91.0%, the specificity rose to 99.2%, and the sensitivity dropped to 27.6%. All this shows is that excluding the normalized reflectance information did not serve to make the analysis significantly more accurate. It was better at finding chaos, perhaps, but at the cost of having more false positives. Depending on the purpose of the study, this result could be seen as an advantage (in the case where every potential chaos feature should be identified) or a disadvantage (if only the most assured chaos features should be identified).

4.6.2 Using unclassified LowRes data in a DFA

The ultimate purpose of this project is to be able to confidently classify mapped but unclassified features. Out of the 214 features that were mapped in the LowRes dataset, 111 of them were classified in both the LowRes and E15RegMap01 datasets, allowing for a direct comparison between human and computer classification according to the methodology discussed in this chapter. The 111 microfeatures were made up of 62 chaos features, 21 domes, nine hybrids, four pits, and 15 spots. No features that were unclassified or unmapped in the RegMap dataset were included. Overall, 61 out of 111 of the LowRes feature classifications (55.0%) matched their RegMap classifications. 50 out of 62 chaos features (80.6%) were accurately classified, along with one dome (4.8%), one hybrid (11.1%), nine spots (60%), but no pits. The average accuracy percentage within the microfeature groups is 31.3%. This number differs from the overall percentage correct because it examines how well a human does at classifying a data point to on particular group rather than how often the classifications were correct overall. Both numbers should be treated as important because they each address a slightly different aspect of the analysis, providing further constraints on the analysis.

The LowRes data was included in the DFA along with the microfeatures from all RegMaps (the Grand DFA dataset) as unclassified data (e.g., no prior group assignation). The LowRes data accounted for 13.8% of the data included in the total analysis (total n = 802). All data from all regions and all microfeature groups was included to set up the statistical framework for this analysis. The discriminating variables used for this analysis are the same three that were used in the initial Grand DFA to allow for direct comparison: a feature's area, the median normalized reflectance, and ratio 3. The combined group DFA plot for this analysis is shown in Figure 4-3; the black stars represent the LowRes data. A breakdown of these classifications by type and comparison to human-determined classification is provided in Table 16.

The LowRes data tend to associate more closely with the chaos and hybrid features than with the pits and domes, but there are a significant number that are located in the overlap area that includes features from all microfeature groups. Overall, the LowRes features sorted through the Grand DFA framework were all sorted into either the chaos group (64.9%) or into the pits group (35.1%). This is partially because the chaos and pits groups are the largest groups, and therefore pull the largest weighted probabilities of all the groups, but these groups are close to equal in size, and therefore have similar weighted probabilities. For so many features to be preferentially sorted into the chaos class in spite of this points again to significant and recognizable differences between the groups.

Assuming that the classification made in the RegMaps is perfectly correct, then overall, 52 out of 111 (46.8%) LowRes features were sorted correctly using only the DFA. This test was able to accurately classify 48 out of 62 chaos features (77.4%) and all

Figure 4-3: Five group Grand DFA plot with LowRes microfeatures included as unclassified data. All RegMap features made up the classification framework.

of the pits, but did not classify any of the features in any other microfeature group correctly. This averages to be a 35.5% correct classification rate across all microfeature groups, but is a bimodal distribution with values at the extreme ends of the distribution. As has been noted previously, to the computer, chaos, spots, and hybrids are virtually identical, as is the case for pits and domes. When this framework is considered and only two groups are identified in the DFA, then the accuracy of the analysis increases to and overall value of 69.4%, while the accuracy of correctly attributing a LowRes feature to the chaos/spots/hybrids group is 72.1%, and the accuracy of correctly attributing a LowRes feature to the pits/domes group is 60.0%.

Generally in statistics it is ideal to have the largest sample possible, as that would reduce the expected standard error and most instances of non-normality (via the central limit theorem). In this case, however, because all the LowRes data points came from a particular region rather than a combination of the four RegMaps, the accuracy of the classification using the DFA may change if only features from that RegMap were used to create the classification framework. In this case, that means only the data from E15RegMap01. One such analysis was run, again including the three variables used in the original five group Grand DFA: feature area, median normalized reflectance, and ratio 3. Because this analysis was done with a different dataset, the canonical values (the coefficients of the functions) are slightly different here from what they were in the Grand DFA.

The combined plot (Figure 4-4) shows the same pattern of chaos and hybrids separating out distinctly from pits and domes, with spots clustering near the lower end of the y axis. Again, there are large areas of overlap. The LowRes data (black stars) are

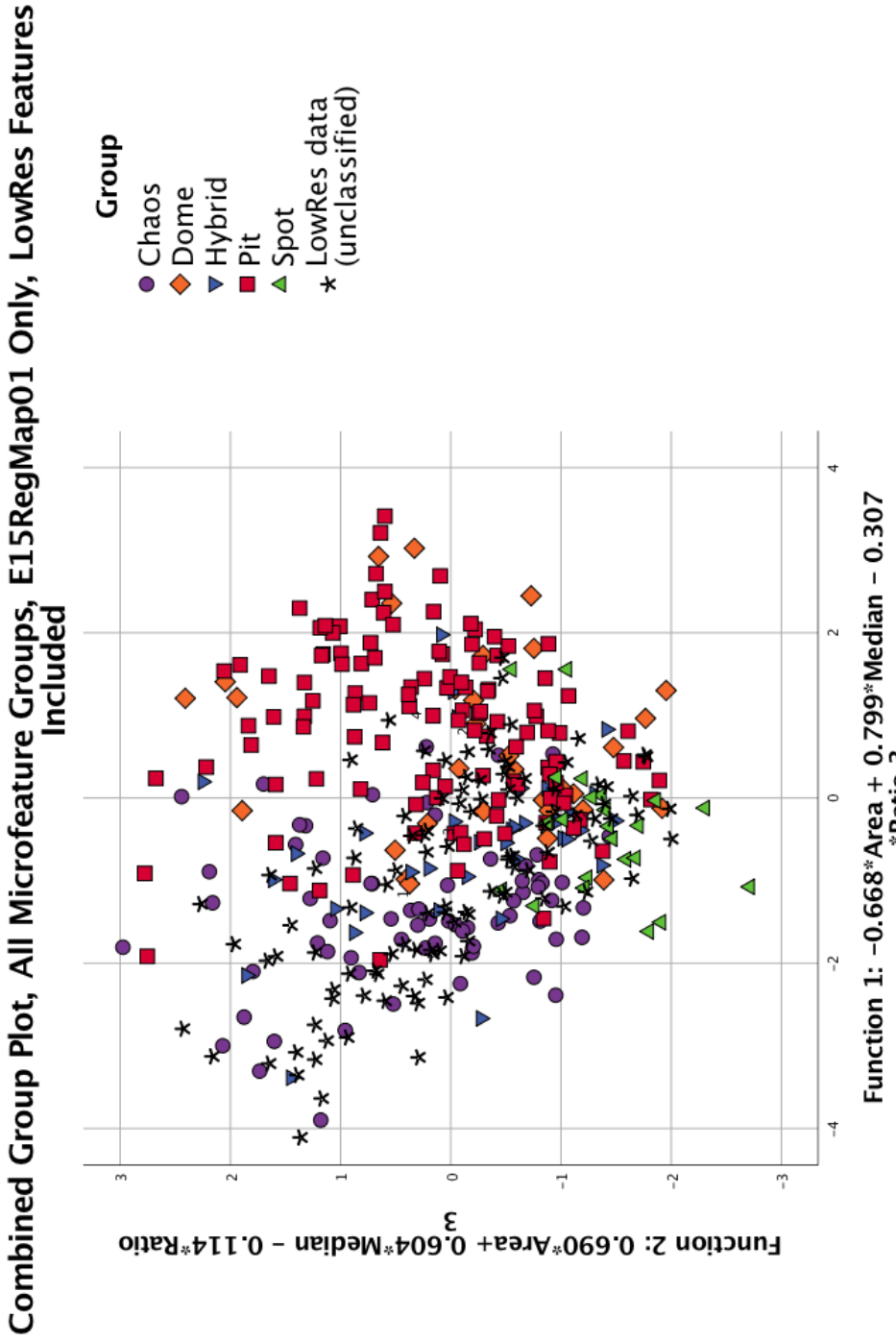

Figure 4-4: Five group Grand DFA plot with LowRes microfeatures included as unclassified data. Only E15RegMap01 features made up the classification framework here.

spread out across all microfeature groups, as they were with the overall microfeature dataset used for the Grand DFAs. Again, the LowRes features tend to more closely associate with the chaos and hybrids group over the pits and domes group (65.8% to 34.2%, respectively). These values are almost identical to the values acquired from the Grand DFA with LowRes data included.

The overall accuracy of the DFA with only E15RegMap01 data is 44.1%, with 49 out of 111 features classified correctly using the quantitative DFA. This value is lower than the overall accuracy reported for that of the Grand DFA; however, the E15RegMap dataset was able to correctly attribute hybrids and spots to their groups, something the Grand DFA framework failed to do. This DFA was able to attribute two hybrid features (22.2%) and three spots (20.0%) to their correct groups, leading to an average of 36.7% correct classification rate across all microfeature groups.

This analysis could have been actually been helped by the smaller numbers. In an analysis with large numbers of data points, the groups may show a greater degree of variation that translates to more overlap between the groups. The microfeatures of a particular type in a particular region may show more similarities with themselves, similarities that are diluted when combined with the same microfeature types from other regions on Europa. The accuracy numbers, however, do not support this overall, as they are not significantly different from the values found within the Grand DFA. When examining the efficacy of how well the more regional DFA separates between the chaos/spots/hybrids and pits/domes supergroup, the numbers are actually either identical or slightly lower than they were for the Grand DFA case. Overall, 76 out of 111 features (68.5%) were accurately attributed to their correct supergroups, with 62 out of 86

(72.1%) classified into the chaos/spots/hybrids supergroup and 14 out of 25 (56.0%) classified into the pits/domes group.

In the absence of significant changes to the accuracy rates of the classification, it is recommended that the larger datasets are used to classify features whenever possible to account for the most variation seen in between groups and to minimize the error estimates. What these DFA comparisons show is that, as of now, a human and the computer are roughly equal in their abilities to sort features mapped in low-resolution images. Depending on which number is given more weight (overall percentage correct or average percentage correct across groups), a human or a computer could be viewed as more correct. There is much promise in the heightened accuracy when considering only two supergroups, as those results yielded the highest accuracy percentages across all tests done including the LowRes dataset. The use of a statistical test that supplies a binary output (chaos/spots/hybrids vs. pits/domes) and puts constraints on the likelihood of that value being correct would be ideal in this scenario, given the available datasets and the relative simplicity of such an approach. This does assume, however, that chaos, spots, and hybrids are inherently related to each other, but given their similar morphometric characteristics as verified by the multiple two group DFAs and their likelihood to be confused for each other in low-resolution images, this is not such a stretch to consider. An example of a type of analysis that could be conducted in the future to explore this potential further would be a logistic regression test, but this approach is outside the scope of this work at present.

This work could form the basis for future, more advanced applications for quantitative classification, including but not limited to logistic regression and machine

learning to classify obscured features on the surfaces of planetary bodies. The overall goal is to use the dataset described in Chapter 2 to expand mapping to other low-resolution images across Europa's surface to search for and classify microfeatures. Between the constraints presented and described in Chapter 3 (LowRes mapping dataset) and those from here, these microfeatures will be able to be accurately attributed to at least a supergroup with upwards of 70% probability of correctness (using the values of LOOCV, specificity, sensitivity, and accuracy for the chaos/spots/hybrids vs. pits/domes cases). This represents a large increase in the amount of usable data from the low-resolution *Galileo* images, especially in terms of microfeature spatial locations. The distribution of microfeatures over Europa's surface could directly point to one of the microfeature formation models, as the distribution of microfeatures would vary depending on which process is most dominant. For example, if the microfeatures formed from diapirism, then there should be more of them in areas where diapirism should be most active. A more random distribution, however, could point to the sills model, which may not have a geographical preference. In the near future, this work could be used to classify the dataset already in existence of proposed microfeatures on Europa's surface (Leonard et al., 2018; Leonard et al., 2019) and provide solid predictions for the Europa Clipper mission and constraints for formation models.

4.8 Conclusion

This work sought to determine if microfeatures on Europa can be sorted above and beyond simple chance using a set of quantified metrics in a classification approach. The answer is an unqualified yes. Except in cases where the groups being compared were very similar (e.g., the pits and domes in multiple DFAs), the quantitative classification

was able to sort between the feature types with an accuracy that was above and beyond what could be expected from random chance. The accuracy of the classification rate depended on which groups were included in the analysis and which variables were presented as potential discriminators. In most cases, one variable from each of the following categories met the discriminating variable criteria and was included as a discriminating variable: one from the size category (feature diameter, area, or perimeter); feature normalized reflectance (median, mean, standard deviation, and range); and shape (one of the ratios, irregularity, and eccentricity/aspect ratio).

Overall the computer is adept at separating between chaos/spots/hybrids and pits/domes, but is less successful when sorting features within those groups. To the computer, pits and domes appear as the same things because of their similar size, shape, and normalized reflectance. Chaos, spots, and hybrids can also be confused for each other, but not to the degree that pits and domes are confused. In some cases, two or fewer variables are capable of sorting between feature types, an advantage in areas where detailed information is difficult to acquire because of imaging constraints.

The accuracy rate of sorting features using a quantitative classification approach was compared to a human using a traditional mapping and classification approach. To study this, the LowRes dataset was added as unclassified data and classified into groups according to the framework created by the DFA. Comparing how often domes and pits were mistakenly classified during the human classification approach, the computer actually did a better job of identifying pits and domes out from the LowRes dataset than the human did.

While this work is merely a first pass of using multivariate classification analyses and applying them to planetary bodies, there is clearly potential for something more. It will be the role of future research to take advantage of the most significant differences between the groups in the form of a more precise statistical analysis (e.g., logistic regression) and to expand the dataset of features collected in low-resolution images. In this way, more information about the spatial distribution of microfeatures on Europa's surface will be collected and used to make predictions ahead of the Europa Clipper mission and constrain existing models of microfeature formation.

CHAPTER 5

SPATIAL PATTERNS OF MICROFEATURES

5.1 Introduction

The number, characteristics, and general locations of microfeatures have now been discussed extensively in the previous chapters, as have methods designed to explore areas on Europa that lie outside of the RegMaps. The goal of this work is to provide additional constraints on microfeature formation models. This is important to do because certain models imply liquid water near Europa's surface underneath certain features. If this is true, then these targets should be prioritized for future astrobiological study. This is, of course, in addition to the better understanding that is obtained in ice-shell dynamics on ocean worlds by knowing more about the probable heat and material transport physics of these systems. What is known of Europa could then be applied to other ocean worlds in the solar system, including but not limited to Saturn's moon Enceladus fellow Galilean satellite Ganymede. Some of the implications for the microfeature formation models that the aforementioned observations create have also been discussed, but no observational predictions have been directly tested. This chapter focuses on testing predictions made by the proponents of one model in particular, as it is relatively new and has yet to be scrutinized.

The sills model of microfeature formation (Schmidt et al., 2011; Michaut and Manga, 2014; Manga and Michaut, 2017) predicts that the presence of liquid water in an elliptical sill within Europa's ice shell and its evolution over time formed the microfeatures now observed. First, liquid water enters a hollow area within the ice shell and begins to expand. This liquid water could be water that came up from the ocean

below via a dike until it reached a point of neutral buoyancy, or the liquid water could be the result of concentrated heating within the ice shell, leading to *in situ* melt. The sill grows in size over time. If the weight of this water is compensated by the underlying elastic ice shell, then as the sill expands, the surface above will be pushed upwards, forming a dome. If this process happens rapidly, the dome can crack, allowing for some of the material to spill out, potentially forming chaos and hybrid features. Small disruptions become spots. If the weight is not compensated, perhaps because the elastic ice shell is thin in that particular area, then the weight of the sill with cause the surface above to collapse, forming a pit. Eventually the liquid water will begin to freeze. Domes will retain their upwarped shape, and pits will reverse the downwarping and the surface will either return to its previous elevation or become slightly domical. The implications of this model are such that there could currently be liquid water underneath pits, as the weight of liquid water is required to downwarp the ice above, and also that these microfeatures are related to each other along a continuum, with domes and chaos being the end states.

In the paper that explains the details of the saucer sills model, Manga and Michaut (2017) outline four predictions that should be observed on Europa if the model correctly represents the microfeature formation process. First, that pits should have smaller mean radii than domes, as the downward deflection of the sill during a pit's formation should contract the lateral extent of the sill. Second, that domes should be more numerous than pits because domes should be easier to form in the ice shell and represent the final end state. As the freezing time for a sill is not indefinite, then pits should be short-lived, hence they should be less numerous. Third, that the larger sills that form the larger

microfeatures should lead to larger blocks and a greater degree of disruption, as the stresses on the overlying ice shell from a freezing sill should increase as the radius of the sill increases. Finally, that pits are clustered in space, as the sills are likely to form where there is a thin lithosphere and a high heat flux. The number of places in Europa's ice shell that meet these conditions is unknown, but so long as these places do not cover the entire moon, a distinct pit clustering pattern could hint at where these areas are.

It has been shown in previous chapters that pits and domes have very similar mean radii, at least to within statistical significance across all four RegMaps regions examined: E15RegMap01, E15RegMap02, E17RegMap01, and E17RegMap02. While this observation may at first appear to contradict the model's predictions, the authors never say by how much the radii should differ, so it is possible that the difference is undetectable even in RegMap images. It is also not generally true that domes outnumber pits, though that observation is dependent on where on Europa's surface one looks. On the whole, however, pits do outnumber domes, again contradicting a prediction of the model. Testing the third prediction rests outside the scope of this work; as there is a size cut-off imposed on the datasets here, detecting an increase in the amount of blocks with respect to size would give an incomplete picture. It was noted in Chapter 2 that there are some microchaos features that contain rafts, but these rafty microchaos are not in the majority in any of the regions studied. The dataset used here is insufficient to test this prediction at this time.

What the dataset can be used to test is the microfeature clustering prediction. Previous authors have qualitatively described microfeatures as clustered (Greeley et al., 2000; Spaun 2002; Ruiz and Tejero, 2003; Culha and Manga, 2016), but the degree of

clustering has never been quantitatively described. This work now seeks to examine to what degree microfeatures are clustered, if these clustering patterns vary by type, and if these clustering patterns vary by region. Doing so directly tests one of the predictions of a microfeature formation model. Determining how valid this assertion is could determine how robust the model itself is and suggest potential refinements to better approximate the formation processes on Europa. This could directly connect pits to liquid water on Europa and name them as astrobiological targets for future flyby (Papplardo et al., 2016; Turtle et al., 2016) and lander (Hand et al., 2017) missions, and offer suggestions for heat and material transport models for other icy satellites.

5.2 Dataset and Methods

5.2.1 Nearest neighbor clustering analysis

The dataset used here is the dataset described in Chapter 2; for ease of reading, a summary table is provided to give the total number of features in each area in Table 5-1. Separate analyses were run including all features, including the chaos and hybrid features that were above the size cut-off of 100 km^2 in area, and for microfeatures only. To test for clustering within these feature groups, multiple nearest neighbor clustering analysis tests were run. Developed by Clark and Evans (1954) to study the degree of clustering within individual species of trees in a forest, their methodology presents a straightforward way to quantitatively analyze the degree of clustering or dispersion as compared to a random population in a two-dimensional space. A variant of this test has been previously used to study the degree of clustering of potential volcanic features on Mars (Baloga et al., 2007) and of volcanoes on Europa's fellow moon Io (Hamilton et al., 2013), so the

Table 5-1: Summary of microfeatures by region and study area size

Region	Chaos (number excluded based on size cut-off)	Domes	Hybrids (number excluded based on size cut-off)	Pits	Spots
E15RegMao01 Area: 356,529.51 km^2	95 (27)	33	34 (2)	119	23
E15RegMap02 Area: 613,109.02 km^2	209 (120)	30	25 (1)	10	1
E17RegMap01 Area: 630,229.91 km^2	134 (65)	33 (1)	23 (1)	21	4
E17RegMap02 Area: 490,409.50 km^2	13	21	10	67	1

precedent for using this approach on planetary bodies has already been established, with the potential for expansion to other problems.

To understand the logic of the analysis, first assume a sample space of a given area with a given number of points contained within it. These points are initially assumed to be randomly distributed. Clark and Evans (1954) define a random distribution of points as the following:

> "In a random distribution of a set of points on a given area, it is assumed that any point has had the same chance of occurring on any sub-area as any other point, that any sub-area of specific size has had the same chance of receiving a point as any other sub-area of that size, and that the placement of each point has not been influenced by that of any other point."

Because the generation of random points is dependent on the size of the given area, this test is not scale-invariant; that is, examining some number of points in an area of a certain size would yield a different estimate of clustering if the same number of points were in an area of a different size. Therefore, it is critical that the user is careful to specify the size of the study area correctly and, in the words of Clark and Evans (1954), "with care." The most important detail is to keep the units of distance consistent across all stages of the analysis.

Once the number of points, N, and area have been determined, the next step is to calculate the average surficial density of the features per unit area, a unit called ρ. This value is used to calculate the mean distance to a point's nearest neighbor that would be expected in an infinitely large random distribution with the same density. The equation for this average value, denoted as $\bar{r}_E$, is:

$$\bar{r}_E = \frac{1}{2\sqrt{\rho}}$$

The standard error on $\bar{r}_E$ in a randomly distributed population of density ρ is:

$$\sigma_{\bar{r}_E} = \frac{0.26136}{\sqrt{N\rho}}$$

The numerical value in the numerator for the standard error and the equation for expected distance between the points are analytically derived in the Appendix of Clark and Evans (1954). These values represent an imaginary, random population and are used to compare to the observed values of the real population.

<*Special note: If you made it this far into reading the dissertation, thank you! Email me to let me know and I will respond to your email with a fun fact about Europa!*>

To determine the average distance to the nearest neighbor (the average minimum difference between points), the distances between one point and every other point are calculated, and then the minimum distance is recorded. The average of these minimum distances is calculated as a simple average, where *r* represents the individual minimum distances between the points:

$$\bar{r}_A = \frac{\sum r}{N}$$

Once this value has been calculated, the values for $\bar{r}_A$ and $\bar{r}_E$ are directly compared via a ratio, R:

$$R = \frac{\bar{r}_A}{\bar{r}_E}$$

R has a limited range of values. In a randomly distributed population, the value for R will be near 1. The minimum value R can take is 0, which signifies that all of the points occupy the same location in space. The maximum value R can take is:

$$R = \frac{1.0746}{\sqrt{\rho}} = 2.1491$$

This value represents the spread of points in an even hexagonal pattern, the orientation in which the points will be maximally separated. In this arrangement, every point is equidistant from 6 other points, and thus has a predictable value of ρ that yields the numerical value of 2.1491. The interpretation of that value is that the points are, on average, twice as far away from their nearest neighbor as they would be in a randomly distributed population. The derivation of this value is included in the Appendix of Clark and Evans (1954). Because this analysis is very sensitive to size (e.g., it is not scale-invariant), if this value of R is higher than the maximum value, it is a sign that the size of the area for computing the random sample is too large.

Once the value of R is computed, the value is standardized so as to compare it to a standard normal curve and yield a probability for observing the calculated value. This standardized normal curve has a Gaussian distribution, a mean of 0, and a standard deviation of 1. To compare a value on the standard normal curve, it is necessary to calculate the z score (standard variate) of an observed value. In this analysis, the standard variate (called c in the Clark and Evans (1954) paper) is (Mather 1947):

$$z = \frac{\bar{r}_A - \bar{r}_E}{\sigma_{\bar{r}_E}}$$

To find the probability of observing the calculated z score (the p value), a normal distribution probability table is used. For the z score to be considered significant, an alpha value α is selected ahead of time. Below this α value or above the value of $1 - \alpha$ in the case of a two-tailed test, the clustering or dispersion, respectively, is considered significant. In between the limits, the value is non-distinguishable from random, and thus

the possibility that a random distribution has been observed cannot be rejected. The α considered here is 0.05.

There is a nearest neighbor analysis tool in ArcGIS that is capable of running this test and outputting values for R and it associated p value. To run this analysis in ArcGIS, the features were converted to points, with each point representing the geographic center of its corresponding feature. The test values calculated within ArcGIS therefore only pertain to the centers of the features. There are at least two different ways to measure distances between features, then: from the center of a feature to the center of its nearest neighbor, and from the closest point along a feature's edge to the closest point along the edge of its nearest neighbor. To provide a complete picture of the degree of clustering within the dataset, the ArcGIS Near tool was used to find the minimum distances between the centers of features to its nearest neighbor, and the minimum distances between a feature's edge to the closest edge of its nearest neighbor. These values were then averaged to provide more detail regarding the average spacing of these features under both definitions of "distance to nearest feature." The standard error of these estimates was calculated as $SE = \frac{\sigma}{\sqrt{N-1}}$; these values are included alongside the average distances.

5.2.2 Monte Carlo Simulations

Finally, to fully understand the details of a randomly distributed population of features and to compare the observations to a larger range of potential observations, multiple Monte Carlo simulations were run. This code was modified from a previous variation (Wren, 2018). These codes simulated a population of points equal in number to the observed populations across a set rectangle bounded by the user-specified latitude and

longitude. For each data point, the code selects a random latitude and longitude value within the user-specified limits. These random points are pulled from a uniform distribution, so each latitude and longitude value has an equal chance of being selected on every iteration. The code is designed to calculate the distance between each point and every other point using a great circle distance calculation, find the minimum, repeat the process for every point, and then average these minimum values, enabling direct comparison to the average minimum distances calculated by the nearest neighbor analyses and the distances computed from the Near tool. The code itself is included in Appendix F.

Because of their potential relationship with liquid water, these codes were run specifically focusing on pits. One code variation approximated the regional distribution of pits in the E15RegMap01 region, which stretched between 18–60° N latitude and 212–232° W longitude at its maximal extent, covered a total area of 356,529.51 km^2, and contained 119 pits. This surface area represents 1.16% of Europa's total surface area. Because the E15RegMap01 region tapers near the top, the surface area contained in the box made up of the four pairs of latitude and longitude coordinates given previously would make a box that is too large in area. It was critical to a correct result that the specified latitude and longitude pairs in the code represent a surface area equal in size to that of E15RegMap01 relative to its reference sphere. Thus, the latitude remained at 18–60° N and the longitude was reduced to 217–232° W, a box that represents the same fractional area of Europa that E15RegMap01 covers.

The second code variation was simulated a global pits population across all of Europa between 60° S to 60° N latitude and 360° longitude. The surface area of this

segment of Europa is calculated as follows, where r = 1561 kilometers, and covers 86.6% of Europa's surface:

$$A = r^2 \int_0^{2\pi} d\phi \int_{\frac{\pi}{6}}^{\frac{5\pi}{6}} \sin(\theta)\, d\theta$$

$$A = 2\pi r^2 [-\cos\left(\frac{5\pi}{6}\right) + \cos\left(\frac{\pi}{6}\right)]$$

$$A = 2\pi r^2 [-(-0.866) + (0.866)]$$

$$A = 2.65 * 10^7\ km^2$$

The average pit density was calculated by dividing the number of pits in E15RegMap01 by the total area of that region, yielding a value of 3 x 10^{-4} pits/km^2, the highest pit density of any of the regions studied. This pit density was then multiplied by the total area of the region between 60° S to 60° N latitude and 360° longitude to find the total number of pits that could be expected, assuming a uniform pit density. This does not take into account the areas of Europa's surface that are covered with chaotic terrain, where there are very few, if any, pits to be found. Thus, the total calculated number of simulated pits in the "global" scenario is 7950. This number represents a high estimate on the total number of pits on Europa's surface because it was calculated from the highest pit density observed in the four regions studied and ignores the presence of large chaotic regions.

5.3 Results

5.3.1 Nearest neighbor clustering

The R values, p-values, and interpretations for degrees of clustering of all features studied are shown in Table 5-2. The areas used in the analysis are the corresponding areas of the RegMaps provided in Table 5-1. Most of these features have R values less than 1,

Table 5-2: The degrees of clustering of microfeatures, as determined by the nearest neighbor clustering analysis tool in ArcGIS.

Feature Type	E15RegMap01	E15RegMap02	E17RegMap01	E17RegMap02
Chaos (all)	R = 0.852 p-value = 0.006 Clustered	R = 0.739 p-value < 0.001 Strongly Clustered	R = 0.838 p-value = 0.010 Clustered	No features above 100 km^2 in this region
Chaos (small)	R = 0.842 p-value = 0.013 Clustered	R = 0.539 p-value < 0.001 Strongly Clustered	R = 1.062 p-value = 0.497 Random	R = 0.672 p-value = 0.024 Clustered
Domes	R = 0.735 p-value = 0.004 Clustered	R = 0.772 p-value = 0.017 Clustered	R = 0.838 p-value = 0.010 Clustered	R = 0.881 p-value = 0.299 Random
Hybrids (all)	R = 0.664 p-value < 0.001 Strongly Clustered	R = 0.476 p-value < 0.001 Strongly Clustered	R = 1.065 p-value = 0.536 Random	No features above 100 km^2 in this region
Hybrids (small)	R = 0.638 p-value < 0.001 Strongly Clustered	R = 0.442 p-value < 0.001 Strongly Clustered	R = 1.048 p-value = 0.666 Random	R = 1.019 p-value = 0.910 Random
Pits	R = 0.712 p-value < 0.001 Strongly Clustered	R = 0.242 p-value < 0.001 Strongly Clustered	R = 0.723 p-value = 0.015 Clustered	R = 0.539 p-value < 0.001 Strongly Clustered
Spots	R = 1.163 p-value = 0.134 Random	Too few to run analysis	R = 1.272 p-value = 0.299 Random	Too few to run analysis

suggesting that they are clustered. Pits in E15RegMap01, for example, have an R value of 0.712, and the interpretation of that value is that the average spacing between the pits is about 71% of the average distance that would be observed in a randomly distributed population. The R values differ in significance across regions partially because of the size of the study area and partially because of the difference in the number of features.

In all regions, all chaos features are observed to be clustered. This is not the case with microchaos in E17RegMap01, whose distributions are not distinguishably different from a random distribution. Hybrids are clustered in the northern hemisphere regions (E15RegMap01 and E15RegMap02), but are not distinct from randomly distributed in the southern hemisphere regions (E17RegMap01 and E17RegMap02). One special note is that for the E17RegMap02 region, no chaos or hybrid features were excluded based on size, hence why the "all" boxes are left blank. In both cases where enough spots were reported to run the clustering analysis, the observations suggest that spots are not distributed in a way that is different from random. Domes themselves also vary between clustered and random. Pits are the only features that were clustered in every region studied. The lowest R value reported is for pits in E15RegMap02 (R = 0.242). This is a large study area with only ten pits reported in it, an explanation for why the ratio is so low.

5.3.2 Near distances

The distances of these features to features of the same type are included in Tables 5-3 to 5-10. Every combination of feature type to feature type was analyzed to provide the most information about the spacing of these features relative to every other potential feature. An important note is that while it may be expected that the distance observations

between the features should be reflexively the same for each combination (e.g., the distance between chaos and pits should be the same as the distance between pits and chaos), the different sizes of the groups and their varying locations in space on Europa's surface mean that this is not the case. The average nearest neighbor distances are greater when measured from the centers of features than they are when distance is measured from the edges, as is expected. Features generally tend to be closest to other features of their own type, with the exception of spots.

5.3.3 Monte Carlo Simulations

The first Monte Carlo simulation was run approximating the study area represented by E15RegMap01. These simulations were iterated 1000 times. The ρ for this area is 3 x 10^{-4} pits/km^2, which makes the $\bar{r}_E$ for this area 28.87±1.38 km. The average minimum value of distance between the nearest neighbors ranged from 49.74–65.68 km, with an average minimum distance between two pits of 56.94±2.59 km and the R value 1.97, implying that these simulated pits are almost twice as distant from each other on average as they would be in a random distribution (e.g., they are dispersed, on average). From Table 5-3, the average minimum distance between pits in this area is 19.48±0.15 km, immediately suggesting that these pits in this region are clustered, supporting the observation of the nearest neighbor analysis. This yields a z-score of 20.30 and a p-value of <0.001 in favor of a dispersed population.

The second Monte Carlo simulation was run approximating the total area of Europa's surface that ranges between -60° S and 60° N latitude and across the full range of longitudes (0°–360° W). Because this run contained 7950 simulated pits and because

Table 5-3: Average nearest neighbor distances between centers of features, E15RegMap01. Distances are in km.

Feature Type	Chaos (all)	Chaos (small)	Domes	Hybrids (all)	Hybrids (small)	Pits	Spots
Chaos (all)	26.11 ±0.22	x	50.80 ±0.32	50.78 ±0.44	x	35.78 ±0.24	59.55 ±0.44
Chaos (small)	x	30.65 ±0.45	46.74 ±0.44	x	48.43 ±0.57	30.84 ±0.25	53.68 ±0.54
Domes	30.92 ±0.53	37.13 ±0.90	38.21 ±0.87	47.43 ±1.53	45.62 ±0.81	26.35 ±0.54	71.10 ±1.55
Hybrids (all)	28.04 ±0.53	x	45.08 ±0.67	32.07 ±0.66	x	31.98 ±0.47	60.52 ±1.22
Hybrids (small)	x	33.88 ±0.70	45.15 ±0.71	x	31.68 ±0.67	30.11 ±0.46	56.63 ±1.17
Pits	37.66 ±0.19	41.08 ±0.20	49.24 ±0.30	64.78 ±0.58	64.78 ±0.58	19.48 ±0.15	74.84 ±0.45
Spots	32.95 ±0.89	39.71± 1.54	53.95 ±1.80	51.00±1. 52	51.00 ±1.52	38.41 ±1.18	64.00 ±2.10

Table 5-4: Average nearest neighbor distances between edges of feature types, E15RegMap01. Distances are in km.

Feature Type	Chaos (all)	Chaos (small)	Domes	Hybrids (all)	Hybrids (small)	Pits	Spots
Chaos (all)	15.79 ±0.22	x	42.43 ±0.31	41.51 ±0.44	x	27.18 ±0.23	51.81 ±0.43
Chaos (small)	x	22.27 ±0.45	39.66 ±0.43	x	40.38 ±0.57	23.37 ±0.24	46.94 ±0.53
Domes	22.26 ±0.47	29.94 ±0.89	32.63 ±0.88	40.13 ±1.50	42.05 ±1.51	20.58 ±0.54	65.54 ±1.53
Hybrids (all)	18.11 ±0.51	x	38.44 ±0.67	24.18 ±0.64	x	24.50 ±0.45	53.76 ±1.21
Hybrids (small)	x	25.97 ±0.70	38.80 ±0.72	x	24.43 ±0.66	22.97 ±0.45	50.16 ±1.17
Pits	29.13 ±0.19	33.64 ±0.20	43.28 ±0.29	57.35 ±0.57	57.35 ±0.57	13.20 ±0.15	69.05 ±0.44
Spots	25.38 ±0.85	32.62 ±1.51	48.49 ±1.80	44.48 ±1.51	44.48 ±1.51	32.29 ±1.14	58.34 ±2.12

Table 5-5: Average nearest neighbor distances between centers of features, E15RegMap02. Distances are in km.

Feature Type	Chaos (all)	Chaos (small)	Domes	Hybrids (all)	Hybrids (small)	Pits	Spots
Chaos (all)	20.00 ±0.09	x	64.31 ±0.17	78.85 ±0.26	x	140.75 ±0.65	414.46 ±1.12
Chaos (small)	x	34.75 ±0.68	59.38 ±0.33	x	55.49 ±0.39	82.33 ±0.78	311.14 ±1.77
Domes	39.05 ±1.18	81.25 ±2.28	54.94 ±1.45	69.53 ±1.64	69.53 ±1.64	263.46 ±7.28	598.51 ±10.52
Hybrids (all)	30.16 ±1.15	x	56.37 ±1.21	37.38 ±1.70	x	202.39 ±7.70	487.93 ±12.06
Hybrids (small)	x	44.67 ±2.04	54.63 ±1.23	x	35.34 ±1.75	191.15 ±7.84	470.31 ±12.28
Pits	12.96 ±0.74	13.84 ±0.74	62.42 ±4.49	59.39 ±2.68	59.39 ±2.68	29.92 ±3.23	251.65 ±9.86
Spot*	16.54	33.21	92.25	147.62	147.62	114.90	x

* = only one feature was recorded in this region

Table 5-6: Average nearest neighbor distances between edges of feature types, E15RegMap02. Distances are in km.

Feature Type	Chaos (all)	Chaos (small)	Domes	Hybrids (all)	Hybrids (small)	Pits	Spots
Chaos (all)	7.67 ±0.09	x	52.36 ±0.17	65.64 ±0.26	x	129.50 ±0.65	402.57 ±1.12
Chaos (small)	x	26.93 ±0.65	52.97 ±0.32	x	48.08 ±0.40	76.52 ±0.78	305.25 ±1.77
Domes	23.88 ±0.94	74.51 ±2.28	51.17 ±1.43	63.76 ±1.63	63.76 ±1.63	259.25 ±7.28	594.20 ±10.51
Hybrids (all)	18.05 ±0.98	x	50.14 ±1.18	32.34 ±1.57	x	196.72 ±7.65	481.75 ±12.02
Hybrids (small)	x	37.01 ±2.04	48.81 ±1.22	x	30.68 ±1.64	186.01 ±7.82	464.69 ±12.26
Pits	7.71 ±0.76	8.24 ±0.73	57.32 ±4.49	55.06 ±2.73	55.06 ±2.73	27.29 ±3.08	248.15 ±9.85
Spot*	4.26	26.78	87.36	142.61	142.61	111.20	x

* = only one feature was recorded in this region

Table 5-7: Average nearest neighbor distances between centers of features, E17RegMap01. Distances are in km.

Feature Type	Chaos (all)	Chaos (small)	Domes	Hybrids (all)	Hybrids (small)	Pits	Spots
Chaos (all)	32.35 ±0.19	x	66.81 ±0.28	74.66 ±0.43	x	128.82 ±0.86	198.97 ±1.48
Chaos (small)	x	39.70 ±0.45	63.13 ±0.56	x	81.06 ±1.01	117.61 ±1.65	307.98 ±2.81
Domes	38.09 ±0.86	53.11 ±1.21	73.75 ±1.46	75.01 ±2.01	83.07 ±2.12	164.17 ±4.99	300.46 ±5.14
Hybrids (all)	35.45 ±1.07	x	65.59 ±2.23	85.90 ±1.90	x	149.80 ±4.92	247.58 ±6.77
Hybrids (small)	x	48.70 ±1.91	63.85 ±2.36	x	87.58 ±1.88	145.87 ±5.19	254.99 ±7.06
Pits	31.29 ±0.81	44.50 ±1.54	48.21 ±1.48	78.24 ±2.51	81.97 ±2.82	61.43 ±2.51	345.18 ±9.07
Spot	51.79 ±5.55	57.73 ±6.39	104.27 ±18.10	84.13 ±8.05	111.16 ±15.80	175.64 ±34.62	250.32 ±61.02

Table 5-8: Average nearest neighbor distances between edges of feature types, E17RegMap01. Distances are in km.

Feature Type	Chaos (all)	Chaos (small)	Domes	Hybrids (all)	Hybrids (small)	Pits	Spots
Chaos (all)	16.97 ±0.16	x	55.68 ±0.28	62.34 ±0.43	x	116.73 ±0.85	310.15 ±1.48
Chaos (small)	x	31.27 ±0.45	56.20 ±0.56	x	72.88 ±1.01	110.07 ±1.64	301.48 ±2.80
Domes	26.00 ±0.80	46.30 ±1.27	68.67 ±1.46	68.28 ±1.99	71.41 ±2.02	158.18 ±4.94	295.78 ±5.14
Hybrids (all)	23.60 ±1.05	x	59.06 ±2.23	77.67 ±1.90	x	141.93 ±4.84	241.27 ±6.75
Hybrids (small)	x	41.26 ±1.93	57.62 ±2.36	x	80.08 ±1.91	138.56 ±5.13	249.10 ±7.01
Pits	19.49 ±0.72	37.63 ±1.57	43.24 ±1.44	72.01 ±2.56	75.84 ±2.86	56.03 ±2.50	340.28 ±9.08
Spot	43.58 ±5.45	52.52 ±6.30	99.43 ±17.43	76.28 ±8.27	106.20 ±15.99	168.53 ±34.64	245.95 ±61.42

Table 5-9: Average nearest neighbor distances between centers of features, E17RegMap02. Distances are in km. No features in this region were excluded due to size.

Feature Type	Chaos	Domes	Hybrids	Pits	Spots
Chaos	66.55 ±4.87	96.45 ±4.07	116.61 ±7.85	68.17 ±4.06	341.29 ±16.89
Domes	129.49 ±3.95	67.13 ±2.09	113.76 ±6.93	72.99 ±4.72	509.47 ±10.92
Hybrids	76.73 ±5.30	47.18 ±5.14	112.30 ±4.27	21.88 ±1.57	459.45 ±24.31
Pits	85.40 ±0.62	66.32 ±0.67	60.96 ±0.59	23.09 ±0.40	493.11 ±3.14
Spot*	11.50	33.28	19.11	37.53	x

* = only one feature was recorded in this region

Table 5-10: Average nearest neighbor distances between edges of feature types, E17RegMap01. Distances are in km.

Feature Type	Chaos	Domes	Hybrids	Pits	Spots
Chaos	66.55 ±4.87	96.45 ±4.07	116.61 ±7.85	68.17 ±4.06	341.29 ±16.89
Domes	129.49 ±3.95	67.13 ±2.09	113.76 ±6.93	72.99 ±4.72	509.47 ±10.92
Hybrids	76.73 ±5.30	47.18 ±5.14	112.30 ±4.27	21.88 ±1.57	459.45 ±24.31
Pits	85.40 ±0.62	66.32 ±0.67	60.96 ±0.59	23.09 ±0.40	493.11 ±3.14
Spot*	11.50	33.28	19.11	37.53	x

* = only one feature was recorded in this region

of how computationally intensive it was, only 100 iterations were run in this simulation. The large number of simulated pits yielded consistent results across all 100 runs, so increasing the number of iterations would likely not have changed the overall results significantly. As the ρ for this area is the same as it was for the E15RegMap01 simulations, the $\bar{r}_E$ for this area remains at 28.87±0.17 km. The standard error has decreased in this instance because of the significant increase in the number of considered features. The observed average minimum distance between pits ranged between 57.01 and 58.13 km, with an average value of 57.50±0.25 km and a corresponding R ratio of 1.99. This yields a z-score of 169.16 and a p-value of <0.001 in favor of very significant dispersion.

5.4 Discussion

5.4.1 Implications for the sills model

The results of this analysis are straightforward, and show that pits are clustered, while other microfeature types sometimes are. In simulated populations of pits in the E15RegMap01 region, the minimum distances between randomly positioned points are significantly farther apart from each other than they are observed to be in real life, supporting the conclusion that pits are clustered in space. On a partially-global scale, these pits are likely an average of 57.50 km away from the closest pit. The global average degree of clustering of pits is difficult to determine more accurately, as pits are difficult to find in currently available images; see Chapter 2 and Noviello and Rhoden (2018) for a more thorough discussion of this. The random simulations are likely highly inaccurate, as the total number of pits was merely estimated from the region with the highest pit density, and the area included places on Europa that are already known to be covered

with chaotic terrain, where no pits have yet been observed. Still, these simulations provide a baseline estimate for the average spacing of pits on Europa in areas that have not been closely studied yet.

There are a few of explanations for why pits are observed to cluster. One potential reason is that the sills model is correct. This could either imply a large area in the brittle ice shell that allows for multiple fractures to propagate to a shallow depth within the ice shell, pushing water up from the overpressurized ocean (Manga and Wang, 2007) to a point of neutral buoyancy (Schmidt et al., 2011; Michaut and Manga, 2014; Manga and Michaut, 2017). If there are liquid water sills underneath pits, it is also possible that the water came from increased concentrations of tidal heating within the ice shell (Schmidt et al., 2011). Either of these processes could create multiple sills in a relatively small area. One other sill-related idea for pit clustering is that each small sill that creates a pit is connected to every other small sill in the area by a single larger sill that underlies them all, a scenario reminiscent of an upside-down champagne glass pyramid. As the larger, deeper sill is filled, the continued increase in pressure causes more water to be pushed upwards through additional cracks. The water finds another level of neutral buoyancy and forms another sill, which eventually creates the observed pit. If this were true, then the wider area surrounding pit clusters should be depressed, though perhaps not as distinctly or as severely as the pits themselves are.

Based on this evidence collected under multiple methodologies, it is fair to say that pits are clustered in space on Europa, an observation that has been qualitatively described in the past (Culha and Manga, 2016). Thus, the prediction of Manga and Michaut (2017) that pits are clustered on Europa has been proven true. Out of the other

three major predictions, one is outside the scope of this work, one is not supported by observations, and the third could be true. This incongruity does not mean that the model is completely wrong, however. Examining the details of the model further, it is possible that certain assumptions regarding but not limited to the shape of the liquid water sills, the freezing time of the liquid water, and the temperature and corresponding strength of the elastic ice layer could all contribute to reasons for why the observed details do not match predictions. The predictions themselves may, therefore, be incorrect. A full analysis of the sensitivity of these predictions to the inferred parameters is outside the scope of this work, but a potential place for future modeling work on the subject. It is possible that the model could describe the underlying microfeature formation process accurately with a bit of adjustment applied.

One outstanding question of microfeature formation is if these features are formed through discrete, independent processes or if they morph from one to another form along a continuum. If microfeatures are related to each other through a continuous process, then logically they should have the same clustering patterns, at least within a region of study. Across most of the four RegMaps studied, microchaos and small hybrids tend to reflect the same clustering patterns. The only region where this wasn't true was the E17RegMap02 study area, where the microchaos were clustered and the small hybrids were not distinctly different from randomly distributed. It could be that the low number of features in this area contributed to the difference, and the observed differences are because of the uncertainty present when small sample sizes are considered. If so, then this uncertainty should be applied to every group where the members were under 30 in number, as 30 is a statistical rule of thumb for adequate sample size.

The difference in degrees of clustering is not a sign that the continuum idea is invalid. As the liquid water inside of pits freeze and the sill expands, the surface could change from depressed to relatively flat, similar to how it looked before deformation. In this way pits could be erasing themselves. Pits also represent a different formation path in the sills model, and do not necessarily have to turn into domes. They could represent their own end state, in which case there is no need to reconcile the differences in the degrees of clustering. The presence of more pits in some regions over domes could also signal that these regions are comparatively younger than in regions where pits are fewer, as the pits have not had time to either erase themselves or change into domes.

An interesting note is that the sills model promoted by Manga and Michaut (2017) states that while there could be liquid water underneath chaos features, there is a higher likelihood of there being liquid water underneath pits at present. This is partially contrary to other microfeature formation models that connect liquid water directly to chaos features (Collins and Nimmo, 2009; Schmidt et al., 2011); indeed, according to the original sills model (Schmidt et al., 2011), there is active chaos formation happening now in Thera Macula. The Schmidt et al. (2011) sill formation model does focus on large chaos features, and it is not clear if microchaos would form through a similar process under their assumptions. The sills models as they are now do not include any elements of convection, although there is some evidence to suggest that clustering could be related to convection as well (Ruiz and Tejero, 2003). Determining which microfeatures are the most likely places to find liquid water is critically important for future exploration focused on constraining Europa's astrobiological potential (Chyba and Phillips, 2007). This work can also be applied to understanding Europa's ocean dynamics (Goodman et

al., 2004; Goodman and Lenferink, 2012), as the best clues at present for this are the geologic features.

5.4.2 Implications for Europa exploration with flyby mission data

The sills model has not been ruled out as possible even under closer inspection of the available data. It is important, therefore, to consider its implications for Europa exploration. Of course, the Europa Clipper mission will be able to examine 95% of the moon at resolutions of 50 m/pix or smaller (Turtle et al., 2016), so it might be trivial to find these microfeatures across the surface. The Europa Lander mission (Hand et al., 2017) is set to launch much later than the Europa Clipper mission, which should allow for full image processing and data analysis ahead of the Lander and help to select the optimum landing location. Additionally, even if the Lander launches and travels safely to Europa, there are many areas it will not be able to land because of the potential for radiation damage from Jupiter's magnetosphere (Hand et al., 2017). It is therefore important to look to other potential sources of data on the Europa Clipper mission that might identify areas where there is liquid water, or at least interesting geology that could inform about subsurface processes.

One of these alternate sources of data is that of the thermal inertia of Europa. If liquid water is present within the ice shell, it could change the thermal inertia of Europa in that area relative to areas where no liquid water is present in the shell. Surface temperature changes on a diurnal cycle is one way to retrieve the thermal inertia of a planetary body. On the *Galileo* mission, only instrument capable of measuring Europa's surface temperatures was the photopolarimeter-radiometer (PPR; Russell et al., 1992). Based on PPR observations that included both day and night temperature measurements

that happen to cover the four RegMap areas studied in this report, Rathbun et al. (2010) bracketed Europa's thermal inertia at $4 * 10^4$ to $15 * 10^4$ erg cm^{-2} $s^{-1/2}$ K^{-1}, and found a consistent drop in estimated thermal inertia along the equator, echoing the results of Spencer et al. (1999). One major difference in the results of Rathbun et al. (2010) versus those of Spencer et al. (1999) is that, while Spencer et al. (1999) proposed that endogenic heating could be responsible for the thermal inertia drop along the equator, Rathbun et al. (2010)'s models fit better if only thermal inertia variations are considered. This finding was supported by a later study that used data from Earth-based telescope observations of Europa and comparisons to models that used bolometric albedos estimated from the *Voyager* missions (Trumbo et al., 2018), though that paper noted thermal anomalies in non-equatorial areas. It is possible that there could be more liquid water sills along the equator that observably changes the modeled thermal inertia of Europa, perhaps driven by an increase in ocean dynamical activity along the equator (Soderlund et al., 2014).

The E-THEMIS instrument (Christensen et al., 2017; Bayer et al., 2018) is included as a payload instrument on the Europa Clipper mission (Pappalardo et al., 2016; Pappalardo et al., 2017). It will be an infrared spectrometer instrument specifically designed to determine Europa's surface thermal inertia. E-THEMIS will provide global mapping at resolutions of 5-10 km/pix at multiple times of day, and local observations down to resolutions of 50 m/pix, similar to the resolutions of EIS (Turtle et al., 2016). As the average diameter of microfeatures ranges between 5 and 10 km, even at a distance, E-THEMIS should be able to detect thermal anomalies at the scale of microfeatures. If this is not the case, it should still be able to detect areas of thermal anomalies that could be at the scale of microfeature clusters. At large distances from Europa's surface, E-THEMIS

may be able to identify potential anomalies in Europa's thermal inertia, which could signal the presence of liquid water underneath. If these patches are consistent with microfeature locations, as determined by the work presented here or on closer inspection by the EIS instrument (Turtle et al., 2016), then it could be evidence that liquid water within the ice shell is directly affecting the surface above. If there is an absence of these thermal anomalies that correlate to any microfeature locations, then it could be surmised that the thermal inertia variations are more likely caused by an unconsolidated regolith on the surface (Spencer et al., 1999; Rathbun et al., 2010), uncertainties in calculations of the bolometric albedo of Europa for thermal modeling work (Rathbun et al., 2010; Trumbo et al., 2018), or other physical sources of variation. It could also be strong evidence against liquid water in the shell, but only after other sources had been ruled out.

5.4.3 Implications for Europa surface in situ exploration

One of the major objectives of the Europa Lander mission is to "determine the proximity to liquid water and recently erupted materials at the Lander's location" (Hand et al., 2017). One named sub-objective specifically states that the Lander should "search for any subsurface liquid water within 30 km of the lander, including the ocean" (Hand et al., 2017). The 30 km requirement primarily stems from the high estimates for ice shell thickness (Pappalardo et al., 1998; Schenk, 2002) from surface to the ocean, as the ocean is the likeliest place for there to be large amounts of liquid water. To investigate potential locations for liquid water pockets within the ice shell and the distance to the underlying ocean, the lander will use passive seismology to detect seismic and acoustic waves as they travel through the ice shell. These waves travel spherically outward from their source and are affected by the material through which they travel in terms of phase,

direction, and speed. Measuring the scattering and refraction of these waves will help to identify areas in the ice shell where there are pockets of liquid water, slush, or ice of different densities; however, with one seismometer and a detection range of 30 km, it will be difficult to determine the subsurface physical properties of an entire ice shell.

To ensure the success of the mission, the Lander should choose a landing site carefully. This landing site should have a high probability of liquid water within 30 km. If the sills model holds up to further scrutiny, then pits could be a likely place to study liquid water. Even landing near a different type of microfeature could still yield results that point to the presence of a since frozen sill, but pits and liquid water would fulfill the main Lander mission objective to find subsurface liquid water at present (Hand et al., 2017). This liquid water is likely to be fairly close to the surface as well; Manga and Michaut (2017) predict a relationship of $R \approx 2.4d$ between the radius of a feature and the depth of its corresponding sill (Figure 1-6). To determine the presence of liquid water within the ice shell versus below the ice shell, the Lander should prioritize landing within 30 km of a pit.

To determine the probability of the Lander landing within 30 km of a pit, at least within the confines of the RegMaps studied here, arrays whose centers were 30 km apart were constructed in ArcGIS using the fishnet tool (Figures 5-1 to 5-4). Table 5-11 shows the probability of a random point contained within the RegMap falling within a certain radial distance from the nearest pit. These percentages are cumulative; each line contains the points counted in the rows above it, aside from the last row, which notes the percentage of points that are greater than 100 km from the nearest points. Of course,

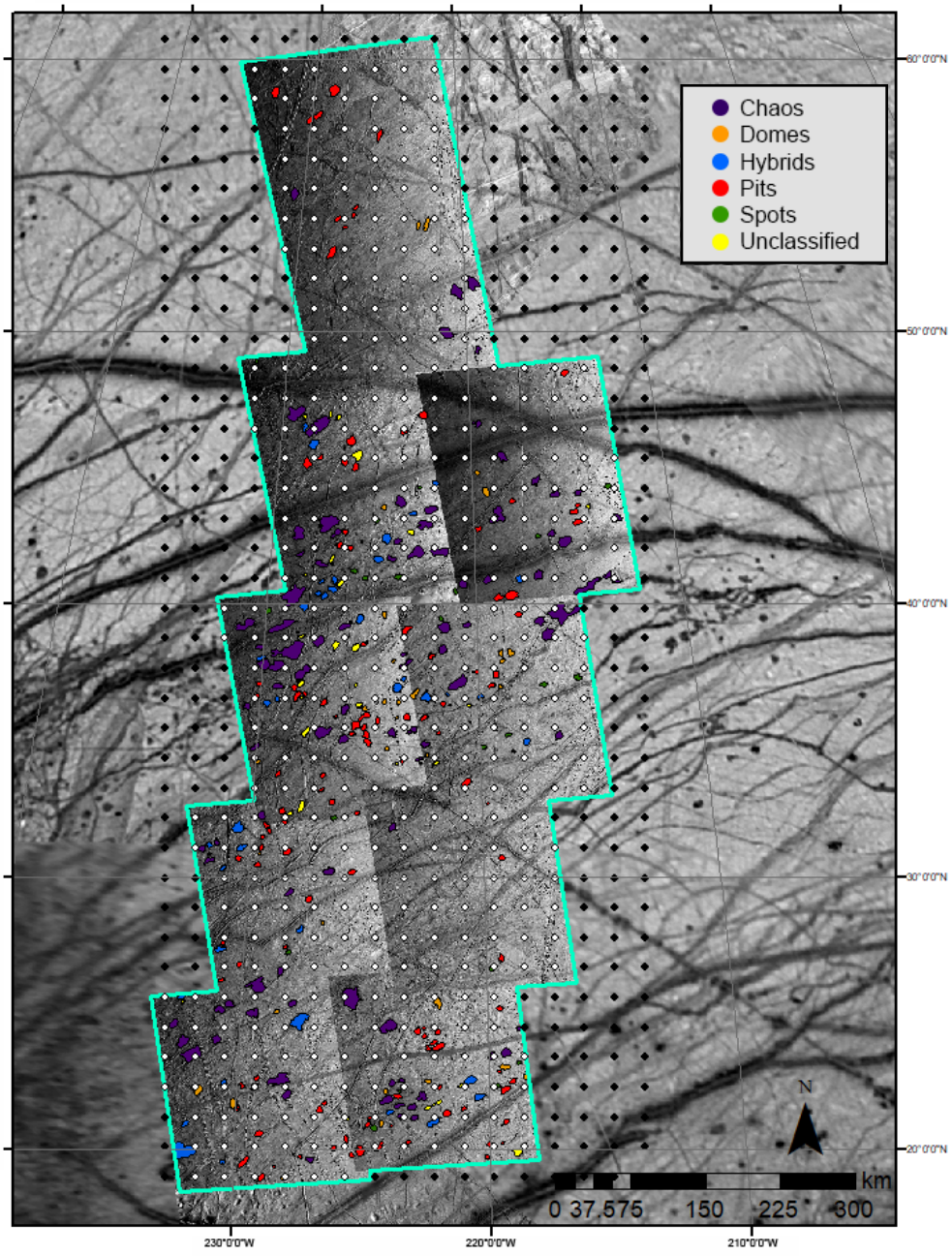

Figure 5-1: E15RegMap01 map with fishnet grid overlain. The points are 30 km apart and represent any potential landing sites for a Europa lander mission. The black dots extend beyond the RegMap perimeter, the white dots are those that lie entirely inside the RegMap.

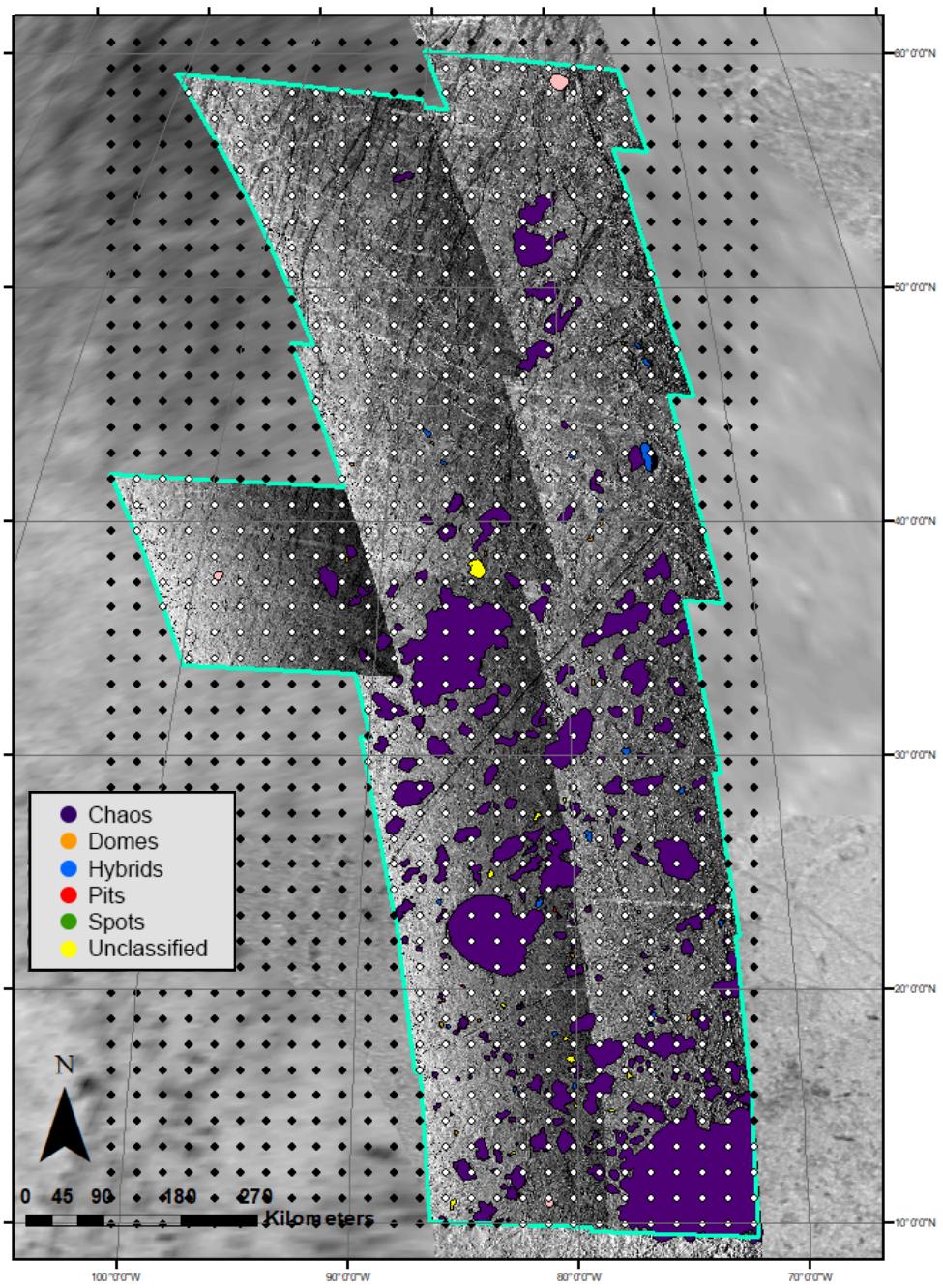

Figure 5-2: E15RegMap02 map with fishnet grid overlain. The points are 30 km apart and represent any potential landing sites for a Europa lander mission. The black dots extend beyond the RegMap perimeter, the white dots are those that lie entirely inside the RegMap.

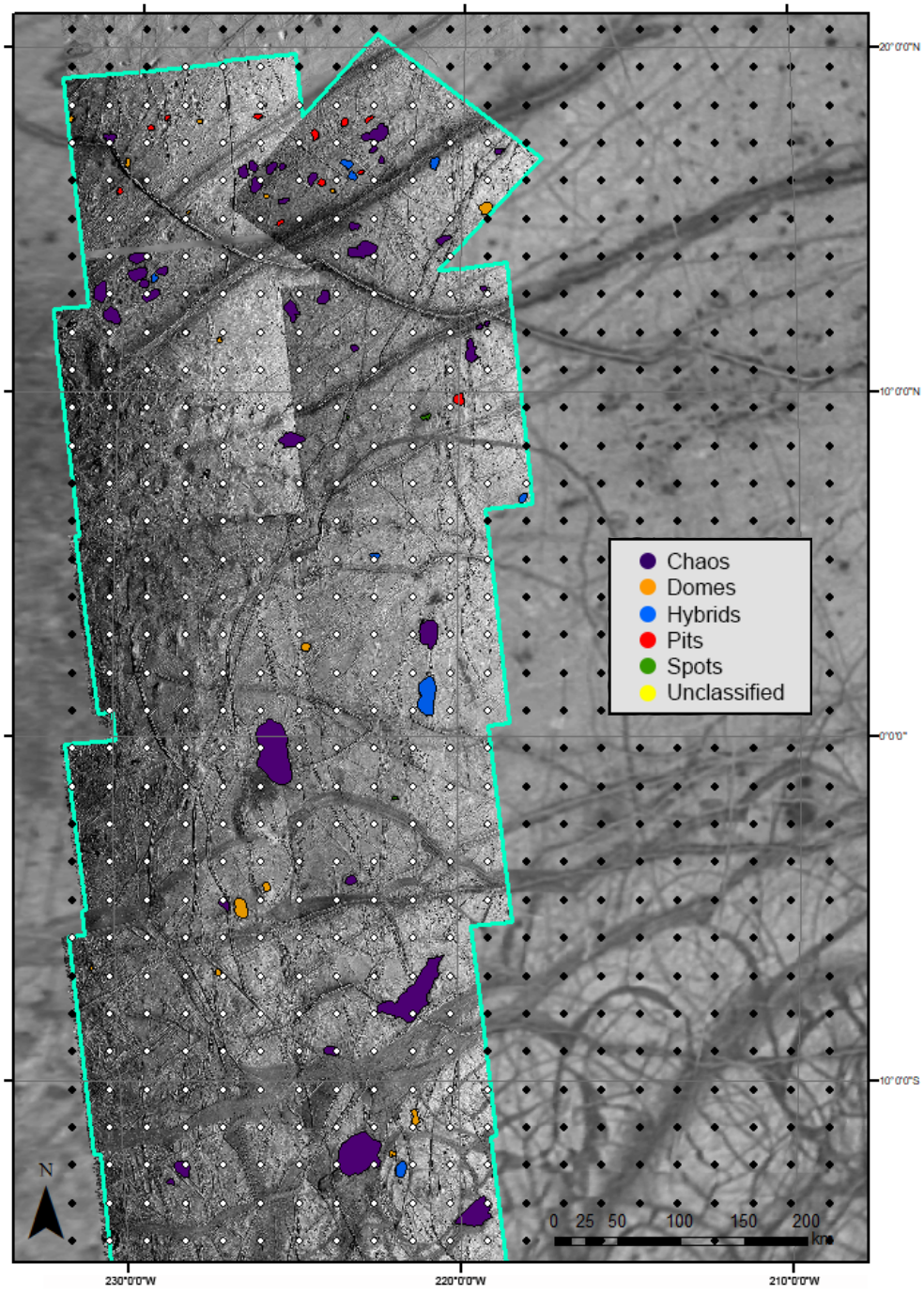

Figure 5-3A: E17RegMap01 map with fishnet grid overlain. The points are 30 km apart and represent any potential landing sites for a Europa lander mission. The black dots extend beyond the RegMap perimeter, the white dots are those that lie entirely inside the RegMap.

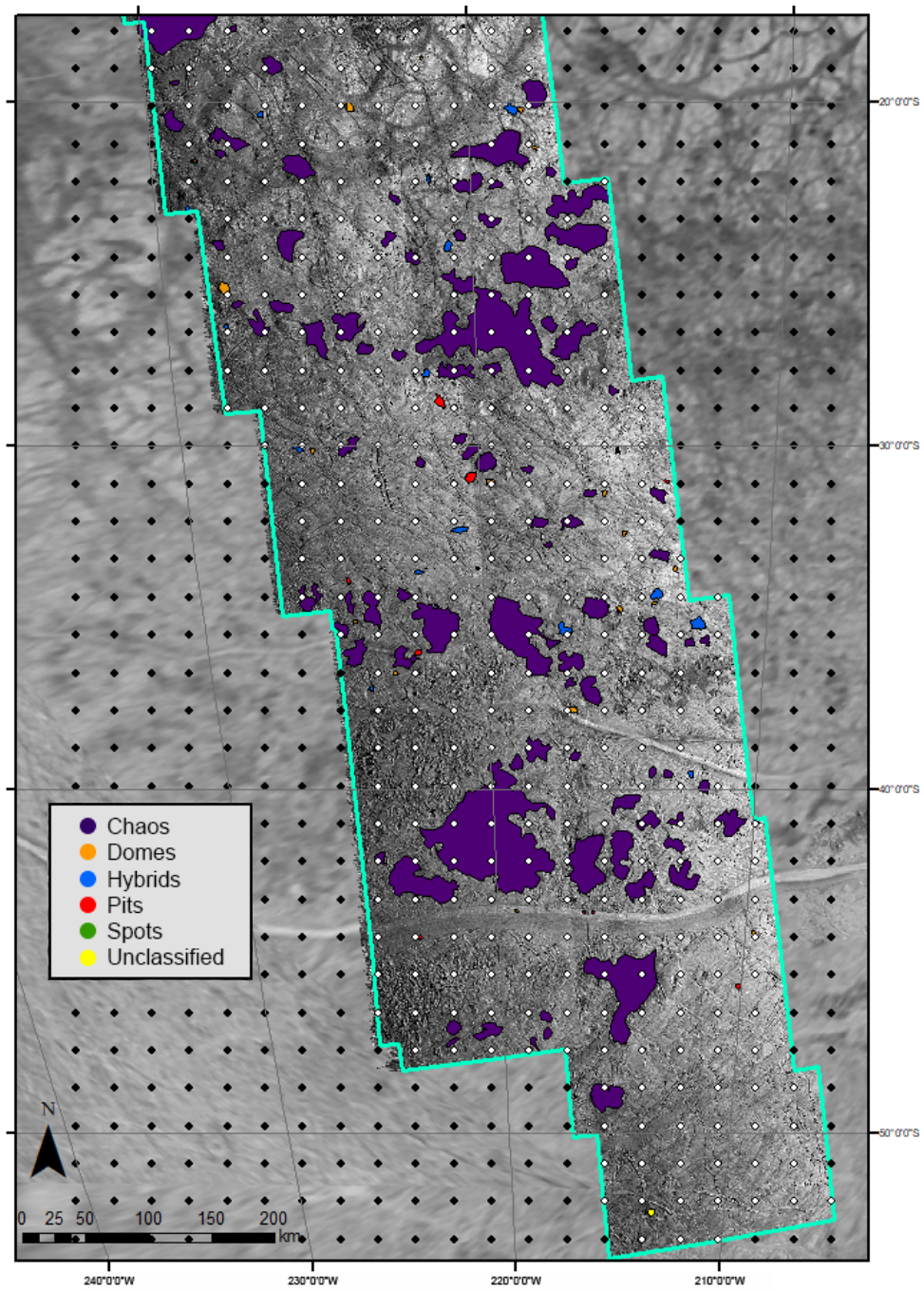

Figure 5-3B: E17RegMap01 map with fishnet grid overlain. The points are 30 km apart and represent any potential landing sites for a Europa lander mission. The black dots extend beyond the RegMap perimeter, the white dots are those that lie entirely inside the RegMap.

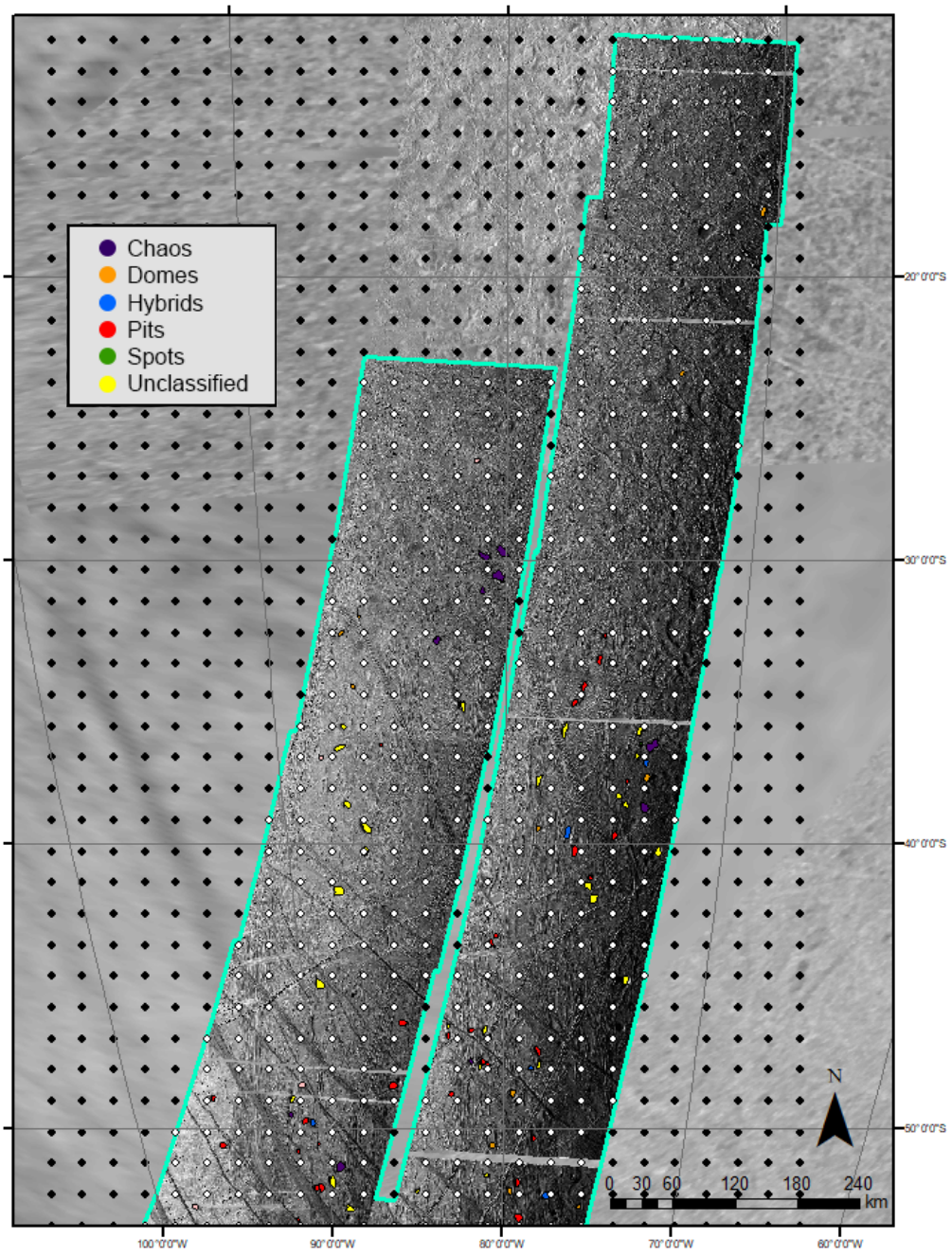

Figure 5-4A: E17RegMap02 map with fishnet grid overlain. The points are 30 km apart and represent any potential landing sites for a Europa lander mission. The black dots extend beyond the RegMap perimeter, the white dots are those that lie entirely inside the RegMap.

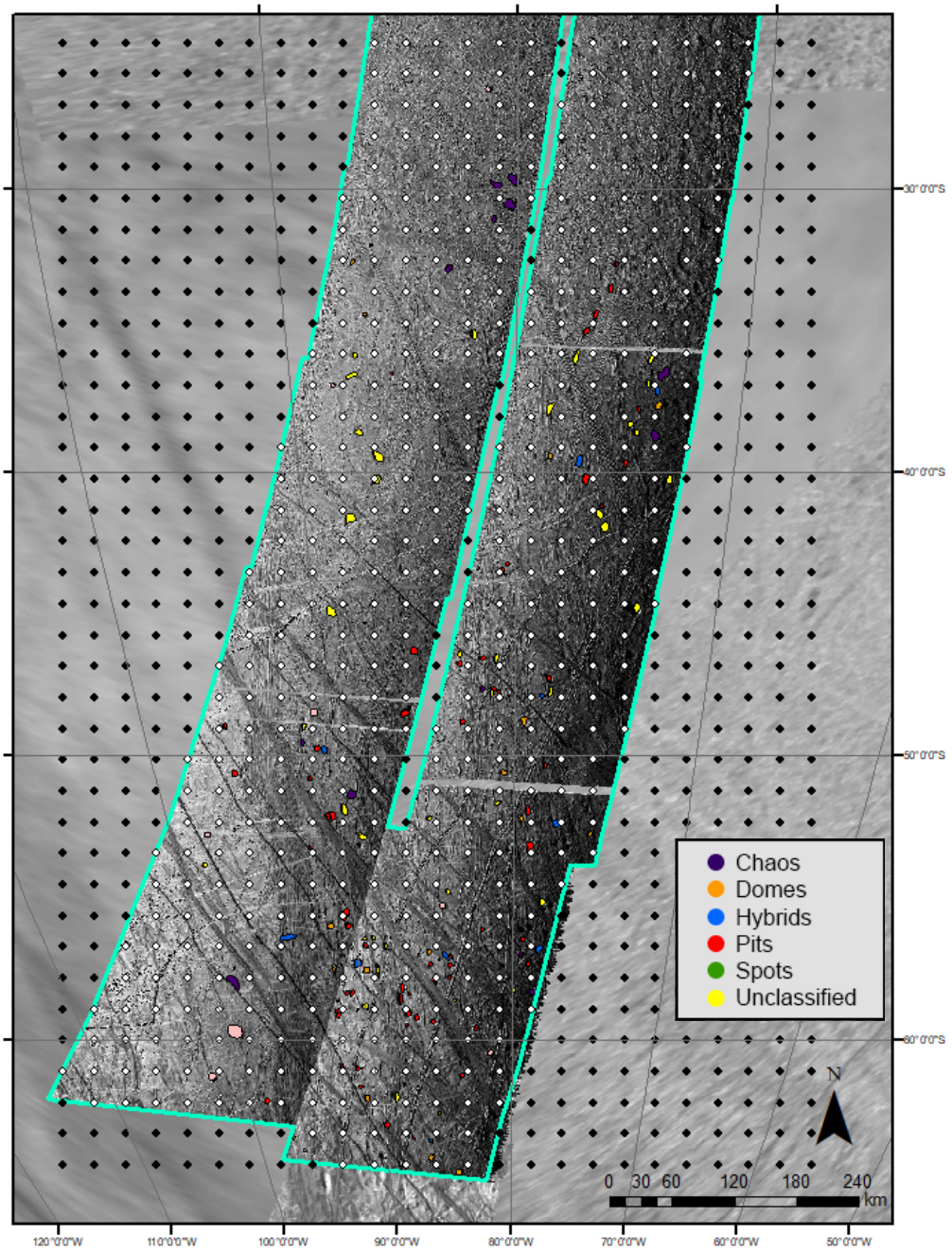

Figure 5-4B: E17RegMap02 map with fishnet grid overlain. The points are 30 km apart and represent any potential landing sites for a Europa lander mission. The black dots extend beyond the RegMap perimeter, the white dots are those that lie entirely inside the RegMap.

Table 5-11: Pit distance probabilities from points in the fishnet array. The points represent a potential landing site for the Europa Lander mission. Only points that fell within the RegMap (the white dots in the fishnet array) are considered in these calculations.

Distance	E15RegMap01	E15RegMap02	E17RegMap01	E17RegMap02
≤ 10 km	15.33	0.73	1.00	4.79
≤ 20 km	33.17	2.06	4.87	13.26
≤ 30 km	50.50	3.67	8.74	23.39
≤ 40 km	63.57	5.87	13.32	30.20
≤ 50 km	73.12	8.08	17.48	38.49
≤ 60 km	83.67	10.72	22.49	45.12
≤ 70 km	89.70	13.66	26.93	49.91
≤ 80 km	94.22	16.59	31.23	54.88
≤ 90 km	96.98	18.80	35.10	59.48
≤ 100 km	97.74	22.32	39.11	61.88
> 100 km	2.26	77.68	60.89	38.12

these percentages vary because the number of pits vary across the four RegMaps, so the chance of a point falling within 30 km of a pit varies from 3.67% to 50.5%. Granted, these percentages would likely be higher if all microfeatures were considered and not simply pits, but this shows that the Lander mission requires an appropriate targeted landing spot to ensure mission success.

Assuming once more that the sills model is correct, then it is possible to model the subsurface structure assuming the relationship between a feature's radius and the proposed depth of its sill. Doing so provides seismology models data that are used to create synthetic seismographs and train the seismology instrument on the Europa Lander to analyze real signals in the future. This modeling work is outside the scope of this project, but it is still helpful to visualize what the subsurface of Europa might look like. Figure 5-5 shows the area covered by the *Galileo* image 1865r (E15RegMap01), and Figure 5-6 shows its potential subsurface structure. This region was selected because of the high density and variety of microfeatures. Note that the majority of features are related to sills less than 2.5 km in depth from the surface of Europa, and that the larger features correspond to deeper sills. While this image extrapolates much about Europa's subsurface and represents the sills as spheres rather than ellipses, it serves as a first glimpse of what could be underneath Europa's icy exterior.

5.5 Conclusions

This project sought to determine which features, if any, are associated with liquid water at or near Europa's surface by examining the prediction made by Manga and Michaut (2017) that pits are clustered in space. All microfeature types in four RegMaps (E15RegMap01, E15RegMap02, E17RegMap01, and E17RegMap02) were analyzed

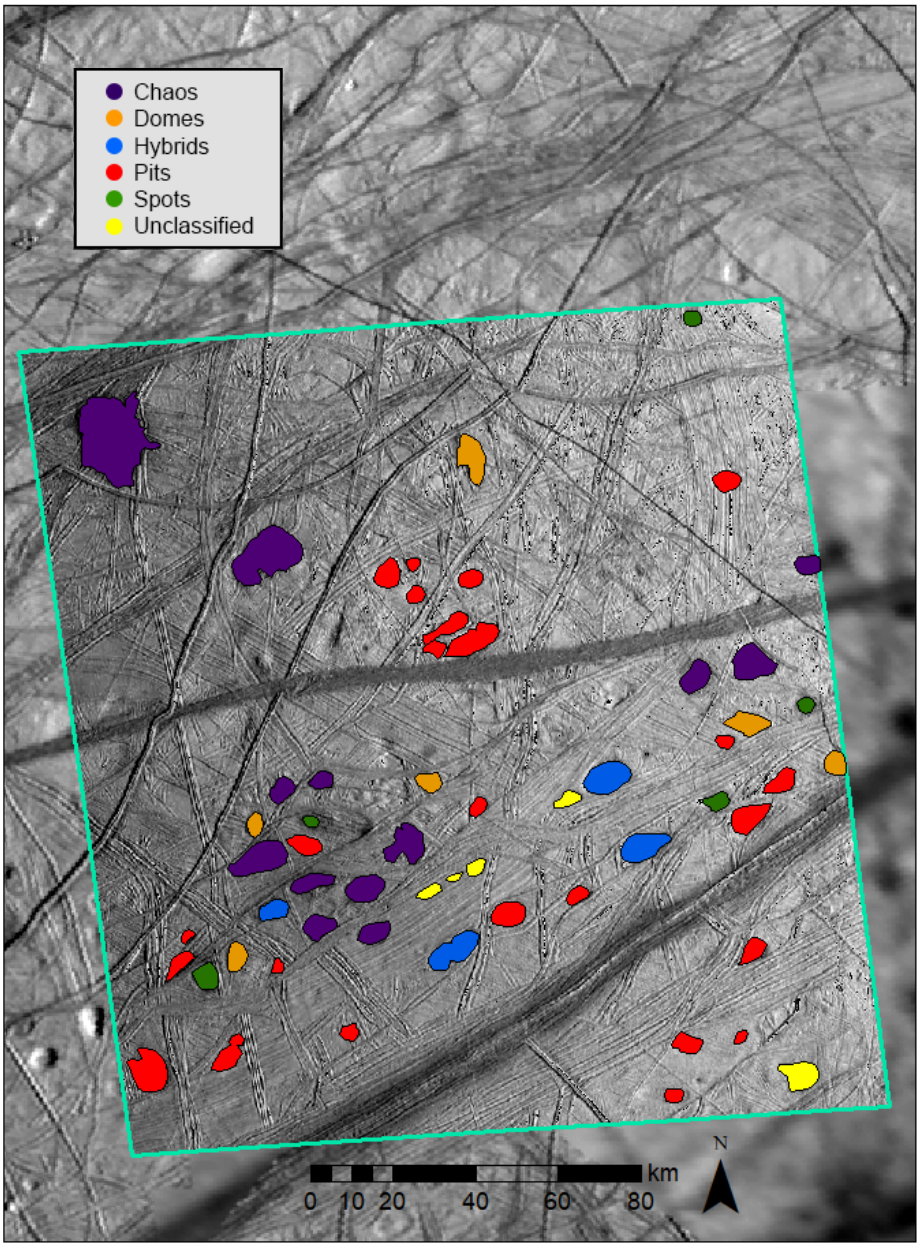

Figure 5-5: The study area of *Galileo* image 1865r (turquoise outline), at the southernmost extent of E15RegMap01. This area was selected for further study because of the abundance of verified microfeatures and because all microfeature types are represented.

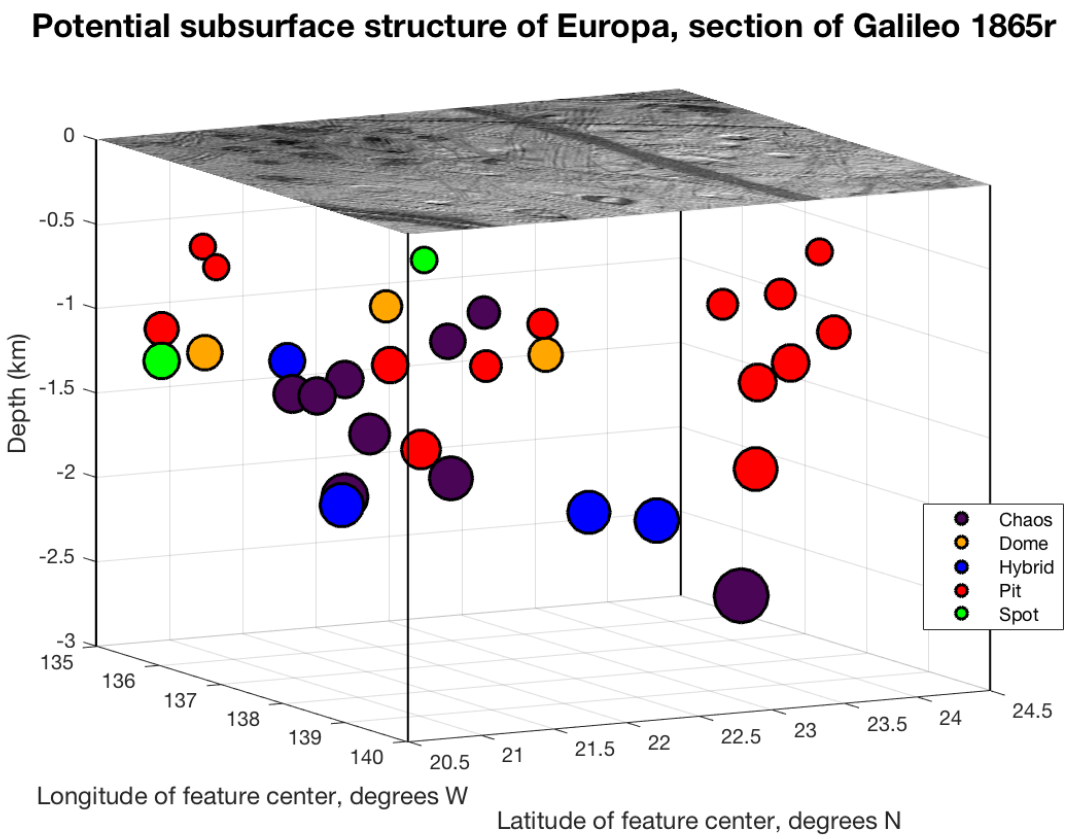

Figure 5-6: The potential subsurface structure underneath the study area of *Galileo* image 1865r. The colors represent to the microfeature types; the red dots represent sills that correspond to pits directly above them. Note that the majority of these sills are projected to be under 2 km from the surface of Europa's ice shell.

using the nearest neighbor to detect the degrees of clustering among these features. While in general all microfeature types were reported as clustered, pits were the only ones that were clustered in all four RegMaps studied. The average minimum distances between pits to other pits were consistently lower than the average minimum distances between pits to any other feature type. Finally, Monte Carlo analyses were run to simulate other populations with the same number of pit density. These runs consistently had average minimum distances that were significantly larger than the observed distances. This is all evidence that shows that pits are indeed clustered in space over the areas where they were mapped on Europa's surface.

This information was then used to explore the implications of the sills model on future exploration of Europa. One piece of data that could be used to further test the potential relationship between pits and liquid water is *Galileo*'s PPR measurements, which are fine enough to detect thermal anomalies that may be correlated with microfeature clusters. Future missions to Europa will be able to test this idea further with more sensitive measurements of thermal inertia, superior thermal models informed by better parameter estimates of bolometric albedo, and a relative abundance of imaging data across a majority of Europa's surface. This work is also relevant to future surface exploration of Europa's ice shell, as the presence of liquid water in the ice shell should be visible in seismology experiments conducted by a potential Lander mission. It also provides the first view of Europa's potential subsurface informed by observations and makes testable predictions for future missions.

CHAPTER 6

CONCLUSION

6.1 Background Summary

Europa is a planetary body that commands attention. The *Galileo* mission provided enough data to hint at an ocean world with curious dynamics, unique geology, and the potential for habitability, but difficulties with the spacecraft itself prevented complete data return (Alexander et al., 2009). Even with these constraints, the *Galileo* dataset remains the best one collected of Europa to date, and with it planetary scientists have investigated a myriad of questions regarding the formation and evolution of many outer solar system satellites.

One of the key attributes that makes Europa unusual is the presence of a global liquid water ocean underneath a thin layer of ice (Khurana et al., 1998; Kivelson et al., 1999; Kivelson et al., 2000). This liquid water ocean could be a place where extraterrestrial life is viable (Chyba and Phillips, 2007; NRC, 2011). Europa's geology is a direct connection to the subsurface activity of Europa that could provide more evidence for or against the hypothesis that Europa is a habitable world, as the surface geology will change based on the dynamics that drive their formation and even tectonism (Kattenhorn and Prockter, 2014). This work focused on the small-scale geologic features on Europa's surface to investigate claims related to Europa's heat and material transport dynamics and, by extension, its potential for habitability.

Europa's icy chaos has been tied to heat and surface modification since the *Voyager* mission era. As adding heat to solid ice causes melting, icy chaos could be a place to directly measure Europa's habitability or search for evidence of biosignatures.

Chaos' association with salts suggests they may also be connected to material transport from the salty ocean to the surface. Understanding how chaos forms would answer important questions regarding Europa's dynamics and significantly lower the uncertainty surrounding other aspects of the moon, including its potential for habitability. At present there is currently no single model that fully explains all instances of icy chaos (Collins and Nimmo, 2009). At small sizes (under 100 km^2 in area), these microchaos features occur alongside several other types of endogenic surface features that are roughly the same sizes. These microfeatures include uplifts and domes, pits, spots (areas of consistently low albedo but no obvious topography), and hybrid features, which have morphological aspects of both chaos and domes. Formation models of these microfeatures often link them together because of their comparable sizes and generally close proximity to one another, and also invoke material transport and potential liquid water deposits in Europa's ice shell (Collins and Nimmo, 2009; Schmidt et al., 2011; Manga and Michaut, 2017).

Microfeatures are clearly visible in the areas of Europa's surface that are covered by *Galileo* images on the order of ~230 m/pixel; these areas are called the regional mosaics, or RegMaps. Unfortunately, these images only cover about 10% of Europa's surface (Doggett et al., 2009), but low-resolution images cover almost all of Europa. It could be possible to find microfeatures in these low-resolution images to some level of confidence. Finding microfeatures outside of RegMaps would provide new observational constraints for microfeature formation models, as certain patterns of microfeature distribution across Europa's surface could be indicative of a particular formation process.

For example, if microfeatures formation is dominated by diapirism, there should be more microfeatures in areas with more proposed diapiric activity (Collins and Nimmo, 2009).

This work sought to: 1) quantitatively describe the different microfeature groups that differentiate between them; 2) test the limits of mapping microfeatures in low-resolution images, both in terms of missed features and classification accuracy; 3) develop a method to quantitatively sort between microfeature groups that can be used to sort features mapped in both RegMap and low-resolution images; and 4) examine the spatial relationships between and among microfeature groups. These answers help constrain the presence of liquid water in the ice shell and to better understand heat and material transport from the ocean to the surface on Europa. Knowing that information will refine microfeature formation models and better the assessment of Europa's potential for habitability. This work also makes predictions for the NASA Europa Clipper mission (Pappalardo et al., 2016; Pappalardo et al., 2017), the ESA JUICE mission (ESA, 2005), and the potential NASA Europa Lander mission (Hand et al., 2017).

6.2 Results Summary: Implications for Microfeature Formation Models

To quantitatively describe Europa's microfeatures, first the microfeatures needed to be mapped and analyzed. A total of 691 classified microfeatures were identified across four of Europa's RegMaps, which in total cover 6.43% of Europa's total surface area. Initially one dataset was collected which was then validated against three other published manuscripts (Greenberg et al., 2003; Culha and Manga, 2016; Singer et al., in review) to create a complete dataset with robust classifications. Overall, the most numerous feature type was microchaos (239), almost equaled in number by pits (217), followed by domes (116), hybrids (90), and spots (29). The region with the highest number of microfeatures

was E15RegMap01. Chaos and hybrid features are 50% larger on average than the other microfeatures, and also have lower average normalized reflectance values. Chaos and hybrid features are also significantly more irregularly shaped. Finally, there are two distinct types of hybrid features, one more chaos-like (Type I) and the other more dome-like (Type II). The Type II hybrids outnumber the Type I hybrids roughly 3:1. Pits and domes are similar in size, aspect ratio, and normalized reflectance, and the only major difference between them is the topography. Spots are not only the darkest and smallest of the features, but the least common as well. In terms of locations, microfeatures are more numerous in the northern hemisphere when considering latitudinal variation, and more numerous in the trailing hemisphere when considering longitudinal variation.

These findings are most consistent with the liquid water sills model and the cryovolcanism model of microfeature formation, though there is also the question of whether different microfeatures are the result of different variations of the same process or if these microfeatures are different stages along a continuum. Pappalardo et al. (1998) first suggested that the different microfeatures are genetically related, and that domes and chaos were especially indicative of a warm-ice diapir within a convecting ice shell between 3 and 10 km thick. Based on the current modeling results, the small sizes and prevalence of pits and domes are inconsistent with the diapir formation model. However, because chaos features and hybrids are typically larger than other microfeature types, diapirism cannot be ruled out as a formation mechanism for chaos. Cryovolcanism models (Quick and Marsh 2016; Quick et al., 2017) are able to recover the topographic signatures of domes and can explain the presence of salts and lower normalized reflectance within chaos and Type I hybrid features. These models fail to fully explain all

microfeatures, though the current model's predictions match well with observations. Finally, the sills model (Schmidt et al., 2011; Manga and Michaut, 2017) invokes the presence of a liquid water sill, in which the depth of the sill relative to the surface and the strength of the ice layer containing the sill control the microfeature formed. This model also details how microfeatures can change morphology over time. It successfully predicted that chaos would be larger than other microfeature types, but inaccurately predicted that domes will be more numerous and larger than pits. Other predictions were evaluated in other chapters.

Even with the microfeatures in the RegMaps confidently mapped, it was not enough information to narrow down the potential formation models. More data were required, which meant mapping was expanded to include low-resolution (> 1 km/pixel) images. To investigate the different sources of error and the corresponding error rates, an independent dataset was created of the E15RegMap01 region mapping features in four low-resolution images; this dataset was then compared to the RegMap dataset. A total of 214 features were mapped in these LowRes images, and 186 of them were below the microfeature size cut-off of 100 km^2 in area. A total of 193 microfeatures that were mapped in the RegMap dataset were missed in the LowRes dataset. The majority of the mapped microfeatures were classified as either chaos or spots because of the prominence of these features relative to the background terrain. Partially for this reason, chaos, spots, and hybrids that were mapped in the RegMap dataset were also mapped in the LowRes dataset at high percentages (77.9%, 65.7%, and 73.9%, respectively). Only 5% of pits and 24.2% of domes were recovered in the LowRes dataset. Moreover, chaos features were accurately called chaos 59.5% of the time, while the other feature types had relatively

low accuracy percentages. This shows that chaos is relatively easy to both find and identify even in low-resolution images. However, there is a 25% chance that features mapped in low-resolution images are false positive phantom features; that is, they are features mapped in low-resolution images that have no corresponding morphology in the RegMaps. “Spots” mapped in low-resolution images were most likely to be phantom features.

This work quantified error estimates and identified sources of error for maps that include microfeatures outside of RegMap areas (Leonard et al., 2018). It revealed that almost no pits or domes are mapped in low-resolution images, and that even when they are mapped, they are almost never classified accurately. On the other hand, chaos, hybrids, and spots are mapped and accurately classified at high rates. This suggests that as many as a third of chaos, hybrids, and spots are left unmapped in low-resolution images while almost all domes and pits are left unmapped. It also found that so long as features have apparent albedos that are distinct from that of the background terrain, features as small as 2.5 km in diameter can be mapped. Finally, phantom features are mapped as much as 25% of the time, and often turn out to be dark areas along ridges, but can also be areas that are not associated with a microfeature in the RegMap images.

Creating a quantified framework for classifying these microfeatures could result in a higher accuracy across all feature types. Using a hierarchical classification analysis called a discriminant function analysis (DFA), the microfeatures were evaluated for their statistically significant quantitative differences and how well those differences separated the microfeature groups. The variables that were included in the analysis were size (area, perimeter, diameter), normalized reflectance (mean, median, standard deviation, and

range), and shape (three ratios, aspect ratios, and irregularity). In general, the quantitative classification was able to sort between the feature types with an accuracy that was above and beyond what could be expected from random chance. The classification was easily able to sort between chaos/spots/hybrids and pits/domes, but had difficulty sorting within those groups. To the computer, pits and domes are almost identical, echoing the results of the RegMap mapping study.

The LowRes dataset was then added into the analysis as unsorted data points so the classification from the quantified approach could be compared to the actual classification from the RegMaps. The computer was comparable to the human mapper at classifying features mapped in the low-resolution images, but accurately classified pits and domes significantly more often than the human did. When the LowRes microfeatures were sorted into either chaos/spots/hybrids or domes/pits, 76 out of 111 of them were accurately attributed to their correct supergroup, 62 out of 86 (72.1%) classified into the chaos/spots/hybrids supergroup and 14 out of 25 (56.0%) classified into the pits/domes group. This work could form the basis for future, more advanced applications for quantitative classification, including but not limited to logistic regression and machine learning to classify obscured features on the surfaces of planetary bodies. More immediately, however, this work can be used to improve the accuracy of the classification of features mapped in low-resolution images when expanding mapping to new areas.

Finally, one of the predictions of the sills model (Schmidt et al., 2011; Manga and Michaut, 2017), that pits are clustered in space, was evaluated in more detail. This model is particularly compelling as it implies the presence of liquid water currently underneath

pits. If this is true, then pits should be considered an important target for future astrobiological studies. To test for clustering within these feature groups, multiple nearest neighbor clustering analysis tests were run on every microfeature type to study the degree of clustering across Europa's RegMaps. The average minimum distances for each feature type to every other feature type were also calculated. Finally, multiple Monte Carlo simulations were run to create additional datasets for comparison to the observed distribution of microfeatures. While other microfeature types vary between clustered and randomly distributed in their regions, pits are consistently clustered across all four RegMaps studied. Additionally, the average minimum distances between pits to other pits were consistently lower than the average minimum distances between pits to any other feature type. The Monte Carlo simulations also showed that the observed average minimum distances were significantly smaller than the expected distances in simulations that approximated the size of a RegMap and the entire global area between 60ºS and 60ºN latitude. All this evidence points to the conclusion that pits are clustered in space on Europa.

This information was then used to explore the implications of the sills model on future exploration of Europa. Examining the thermal measurements taken by *Galileo* could identify clusters of pits even in areas outside of the RegMaps, another idea that could be tested with the E-THEMIS instrument on the Europa Clipper mission. Assuming once more that the sills model is correct, then it is possible to model the subsurface structure assuming the relationship between a feature's radius and the proposed depth of its sill. A lander mission should be able to determine the presence of liquid water in the sill from seismology measurements, assuming that there is liquid water present at all. The

probability that the lander will be within 30 km of a pit ranges from 3.67–50.5%, depending on which RegMap the lander is assigned to land in. It also provides the first view of Europa's potential subsurface informed by observations and makes testable predictions for future missions.

6.3 Predictions for Future Exploration of Europa

Looking ahead to future missions that will study Europa's geology and subsurface structure with the knowledge acquired from this work, here are some predictions regarding Europa and its underlying processes:

1. **Spots do not exist.** Spots are defined as small, flat areas with no obvious interior disruption and exceptionally low normalized reflectance values relative to other microfeature types, including chaos and hybrids. The RegMap dataset shows that there are no spots above 35 km^2 in area, and that there is a significant drop in the overall number of chaos features below 25 km^2. Additionally, spots and chaos are easily confused for each other in low-resolution images, and the quantitative classification analysis showed low specificity when sorting between chaos and spots, partially because of the larger number of chaos features included, but also because these two microfeature types are morphologically similar. In fact, the biggest difference between chaos and spots is that chaos is typically larger. Chaos and spots are uncommon in images with resolutions under 100 m/pixel (Zamora et al., 2019), though the completeness of the microfeature dataset at small sizes is uncertain. Knowing how similar these features are and the apparent size trade-off between the two microfeature types, it is likely that spots do not exist as a separate feature type. It is likely that spots are actually small chaos features whose

rough interiors are not resolvable even in the RegMap images. Further analysis searching for chaos and spots in high-resolution images can test the veracity of this prediction, though this approach is hindered by the small amount of surface area they cover. If these images prove insufficient to answer this question, it will be up to Europa Clipper's Europa Imaging System instrument (EIS; Turtle et al., 2016) to provide the necessary instruments.

2. **Features are forming along a continuum.** Instead of these microfeatures forming as the end result of variations of the same process, it is more likely that these features are evolving and morphing into each other as part of a continuous process. The most compelling evidence for this is the presence of the hybrid features. They come in two types, one that is more chaos-like and the other that is more dome-like, and could be evidence of a transition from domes to chaos or vice versa. Moreover, the quantifiable similarities that hybrids have between chaos and domes is visible even in statistical classification tests. These microfeatures generally have the same clustering patterns as well; if a feature changed from one feature type to another, so long as all features in the vicinity changed at the same rate, then the clustering patterns of the original feature type should be preserved in the new type. The way that a future flyby mission could test this is to simply re-image the surface and count the number of hybrid features that now exist in the current RegMap boundaries. If the ratio between the two types of hybrids has changed significantly or if there are different features in place of where hybrids used to be, then it is evidence that the features are evolving into each other and the direction of that evolution. This finding would

support the sills model over the other microfeature formation models, and would therefore heavily imply that there is liquid water underneath pits and some chaos features. To test this prediction further, images taken of the same place on Europa at two significantly different times (e.g., years apart) could be studied for noticeable differences that would suggest a change in the surface. Such an approach has been applied to identify new craters on Earth's moon using data from the Lunar Reconnaissance Orbiter Camera (LROC) over the course of a decade (Speyerer et al., 2016).

3. **There are upwards of 8,000 pits, 8,000 microchaos features, 2500 domes, and 2700 hybrid features within 60ºS and 60ºN latitude globally on Europa.** These are estimates taken from the microfeature density values in E15RegMap01 scaled linearly up to the total area of this region on Europa. These are rough estimates, as many areas in between these lines of latitude are presumed to be covered with large chaotic areas where microfeatures probably will not be found. The geographical limits of these chaotic regions, however, is not well known because of the lack of RegMap-comparable images in these areas. It is possible these areas of large chaos are overestimated. In addition, even if microfeatures are sought in these low-resolution images that span these previously unstudied regions, it is very likely that pits and domes will not be mapped at all. It will therefore be up to the EIS to return images ≤ 50 m/pix in resolution over 95% of Europa's surface. These images will likely be taken during low-altitude flybys that will happen later in the mission. To study this prediction earlier in the mission, chaos and hybrid features can be mapped in low-resolution images and classified either by human

eye or with a quantitative sorting test (either discriminant function analysis or a more advanced test such as logistic regression). This can constrain areas where microfeatures might be. As these microfeatures tend to cluster with each other in general, these areas found in low-resolution could be highlighted as areas for further study during low-altitude flybys or potentially even surface exploration with the Europa Lander mission (Hand et al., 2017).

4. **Pit clusters will be correlated with thermal inertia hot spots.** If the sills model is true, then pits will have liquid water in relative shallow (≤ 2 km) pockets within Europa's ice shell. The thermal signature of liquid water in the ice shell should be visible in the surface temperatures and the thermal inertia measurements even at large distances from Europa. Measurements at this scale may be too coarse to resolve the signatures of individual pits, but if microfeatures are clustered across Europa, then they should have a large collective heat signature detectable even from large distances. These thermal signatures will be taken with the E-THEMIS instrument. Locating these hot spots and then examining that surface area closer with the EIS instruments will verify this prediction. Additionally, the REASON radar sensing instrument will be able to detect the presence of liquid water in these hot spot regions; as radar waves cannot travel through liquid, these areas should be straightforward to detect. If these radar-lacking areas also correlated with the thermal inertia hot spots, then even before EIS images the area, it is strong evidence of liquid water within the ice shell. EIS can confirm whether or not these signatures are due to a locally thin ice shell (which could be an alternate explanation for these potential observations) or if they are truly due to sills

forming microfeatures. Some of these areas could be found with thermal data from *Galileo*, though the Europa Clipper will give better data due to better constraints on bolometric albedo that is necessary to accurately predict thermal inertia measurements on Europa.

6.4 Final Thoughts

Despite their small size, microfeatures on Europa are a large part of the story of Europa's evolution, geologic processes, and ice shell dynamics. At the moment they are some of the best clues available to study the subsurface activity and Europa's ocean, but many models have previously excluded them. They vary in morphologies and distribution and clustering, but they are likely related to each other in a fundamental way, and should be included as equally valuable pieces of Europa's story alongside large chaos, ridges, and cycloids. This work sought to understand them better and connect it back to the bigger picture questions regarding Europa: How do Europa's geologic microfeatures form? Are they related to each other in any way, and if so, how? Is their formation related at all to the subsurface ocean? And what do they say about Europa's potential for habitability? Europa is known to be a dynamic world. If it is habitable, how can we confirm it? What should we as scientists and explorers look for, and where?

It is impossible to know what Galileo the scientist would think of these discoveries. It is equally impossible to know exactly what future exploration of Europa will uncover, though some predictions have been made here. This research is the foundation for future study of Europa's microfeatures, but it builds on the work of many other scientists and observers who have come before, stretching back to 1610. It is with great pride and hope that this work is submitted for academic consumption. Now is the

time to turn towards the future and seek discoveries with carefully trained but open minds, just as Galileo himself did on a cold January night long ago.

REFERENCES

Alexander, C., Carlson, R., Consolmagno, G., Greeley, R., and Morrison, D., 2009. The exploration history of Europa. In: Pappalardo, R.T., McKinnon, W.B., and Khurana, K.K. (Eds.), Europa. The Univ. of Arizona Press, Tucson, AZ, pp. 3–26.

Anderson, J. D., Schubert, G., Jacobson, R. A., Lau, E. L., Moore, W. B., Sjogren, W. L., 1998. Europa's Differentiated Internal Structure Inferences from Four Galileo Encounters. Science 281, 2019–2022.

Allu Peddinti, D. A. and McNamara, A. K., 2019. Dynamical investigation of a thickening ice-shell: Implications for the icy moon Europa. Icarus 329, 251–269.

Anderson, J. D., Schubert, G., Jacobson, A., Lau, E. L., Moore, W. B., and Sjogen, W. L., 1998. Europa's differentiated internal structure: Inferences from four Galileo encounters. Science 281, 2019–2022.

Anderson, J.A., et al. (2004) Modernization of the Integrated Software for Imagers and Spectrometers. Lunar Planet. Sci. XXXV, Houston, TX, Abstract #2039.

Baloga, S. M., Glaze, L. S., and Bruno, B. C., 2007. Nearest-neighbor analysis of small features on Mars: Applications to tumuli and rootless cones. J. Geophys. Res. 112, DOI: 10.1029/2005JE002652.

Bayer, T., et al., 2018. Europa Clipper mission update: Preliminary design with selected instruments. IEEE Aerospace Conference, 8396629.

Bierhaus, E. B., Zahnle, K., and Chapman, C. R., 2009. Europa's Crater Distributions and Surface Ages. In: Pappalardo, R.T., McKinnon, W.B., and Khurana, K.K. (Eds.), Europa. The University of Arizona Press, Tucson, pp. 161–180.

Belton, M. J. S., et al., 1992. The Galileo solid-state imaging experiment. Space Sci. Rev. 60, 413–455.

Buffo, J. J., Schmidt, B. E., Huber, C., and Walker, C. C., 2019. Entrainment and dynamics of ocean derived impurities within Europa's ice shell. Lunar Planet. Sci. L, Houston, TX, Abstract #2191.

Bunte, M. K., 2013. Utilizing Science and Technology to Enhance a Future Planetary Mission: Applications to Europa. Ph.D. thesis, Arizona State University, Tempe, Arizona. 279 pp.

Buratti, B., Golombek, M., 1988. Geologic implications of spectrophotometric measurements of Europa. Icarus 75, 437–449.

Carlson, R. W., Johnson, R. E., and Anderson, M. S., 1999. Sulfuric acid on Europa and the radiolytic sulfur cycle. Science 286, 79–99.

Carlson, R. W., Anderson, R. E., Johnson, R. E., Schulman, M. B., and Yavrouian, A. H., 2002. Sulfuric acid production on Europa: The radiolysis of sulfur in water ice. Icarus 157, 456–463.

Carlson, R. W., Anderson, M. S., Mehlman, R., Johnson, R. E., 2005. Distribution of hydrate on Europa: Further evidence for sulfuric acid hydrate. Icarus 177, 461–471.

Carlson, R. W., et al., 2009. Europa's surface composition. In: Pappalardo, R.T., McKinnon, W.B., and Khurana, K.K. (Eds.), Europa. The Univ. of Arizona Press, Tucson, AZ, pp. 283–327.

Carr, M. H., et al., 1998. Evidence for a subsurface ocean on Europa. Nature 391, 363–365.

Cassen, P., Reynolds, R. T., and Peale, S. J., 1979. Is there liquid water on Europa? Geophys. Res. Lett. 6, 731–734.

Cassen, P., Peale, S. J., and Reynolds, R. T., 1980. Tidal dissipation in Europa: A correction. Geophys. Res. Lett. 7, 987–988.

Cassen, P. M., Peale, S. J., Reynolds, R. T., 1982. Structure and thermal evolution of the Galilean satellites. In: D. Morrison (Ed.), Satellites of Jupiter, Univ. of Arizona Press, Tucson, AZ, pp. 93-128.

Christensen, P. R., Hamilton, V. E., Edwards, C. S., Spencer, J. R., 2017. Looking Forward: A Next Generation of Thermal Infrared Planetary Instruments. Am. Geophys. Union, Fall Meeting, Abstract #P33H-01

Chyba, C. F. and Phillips, C. B., 2007. Europa. In: Sullivan, W. T. III and Barross, J. A., Planets and Life: The Emerging Science of Astrobiology. Cambridge Univ. Press, Cambridge, UK, pp. 388–423.

Collins, G. C., Head, J. W., Pappalardo, R. T., and Spaun, N. A., 2000. Evaluation of models for the formation of chaotic terrain on Europa. J. Geophys. Res. 105, 1709–1716.

Collins, G. and Nimmo, F., 2009. Chaotic Terrain on Europa. In: Pappalardo, R.T., McKinnon, W.B., and Khurana, K.K. (Eds.), Europa. The University of Arizona Press, Tucson, pp. 259–281.

Clark, P. J. and Evans, F. C., 1954. Distance to Nearest Neighbor as a Measure of Spatial Relationships in Populations. Ecology 35, 445–453.

Craft, K. L., Patterson, G. W., Lowell, R. P., Germanovich, L., 2016. Fracturing and flow: Investigations on the formation of shallow water sills on Europa. Icarus 274, 297–313.

Croft, S. K., Lunine, J. I., Kargel, J. S., 1988. Equation of state of ammonia-water liquid: Derivation and planetological applications. Icarus 73, 279–293.

Culha, C. and Manga, M., 2016. Geometry and spatial distribution of lenticulae on Europa. Icarus 271, 49–56.

Dalton, J. B., Prieto-Ballesteros, O., Kargel, J. S., Jamieson, C.S., Jolivet, J., and Quinn, R., 2005. Spectral comparison of heavily hydrated salts with disrupted terrains on Europa. Icarus 177, 472–490.

Desch, S. J., and Neveu, M., 2017. Differentiation and cryovolcanism on Charon: A view before and after New Horizons. Icarus 287, 175–186.

Doggett, T., Greeley, R., Figueredo, P, and Tanaka, K., 2009. Geologic Stratigraphy and Evolution of Europa's Surface. In: Pappalardo, R.T., McKinnon, W.B., and Khurana, K.K. (Eds.), Europa. The University of Arizona Press, Tucson, pp. 137–159.

Domingue, D. L., Hapke, B. W., Lockwood, G. W., and Thompson, D. T., 1990. Europa's Phase Curve: Implications for Surface Structure. Icarus 90, 30–42.

The European Space Agency Publications Division, ESTEC, 2005. Cosmic Vision: Space Science for Europa 2015–2025. ISBN: 92-9092-189-6.

Fagents, S. A., Kadel, S. D., Greeley, R., Kirk, R. L., Team, G. S., 1998. Styles of cryovolcanism on Europa: Summary of evidence from the Galileo nominal mission. Lunar Planet. Sci. XXIX, Abstract #1721.

Fagents, S. A., 2003. Considerations for effusive cryovolcanism on Europa: the post-Galileo perspective. J. Geophys. Res. 108, 10.1029/2003JE002128

Fanale. F. P., Johnson, T. V., and Matson, D. L., 1974. Io: A Surface Evaporite Deposit? Science 186, 922–925.

Figueredo, P. H., Chuang, F. C., Rathbun, J., Kirk, R. L., and Greeley, R., 2002. Geology and origin of Europa's "mitten" feature (Murias Chaos). J. Geophys. Res. 107, DOI: 10.1027/2001JE001591.

Figueredo, P. H. and Greeley, R., 2004. Geology and origin of Europa's "mitten" feature (Murias Chaos). J. Geophys. Res. 107, 10.1027/2001JE001591.

Figueredo, P. H. and Greeley, R., 2004. Resurfacing history of Europa from pole-to-pole geological mapping. Icarus 167, 287–312.

Fimmel, R. O., Swindell, W., and Burgess, E., 1977. Pioneer Odyssey: Encounter with a giant. NASA-SP-349, NASA Scientific and Technical Information Office, Washington, D.C.

Fimmel, R. O., Van Allen, J. A., and Burgess, E., 1980. Pioneer: First to Jupiter, Saturn and Beyond. NASA SP-446, NASA Scientific and Technical Information Office, Washington, D.C.

Galilei, G., 1610. Siderius Nuncius, translated by E. S. Carlos, 1929. In: H. Shapley and Howarth, Eds., A Source Book in Astronomy. McGraw-Hill, New York, NY.

Geissler, P. E., 2000. Cryovolcanism in the outer solar system. In: Sigurdsson, H. Encyclopedia of Volcanoes, pp. 785–800. Academic Press, San Diego, CA.

Goodman, J. C., Collins, G. C., Marshall, J., and Pierrehumbert, R. T., 2004. Hydrothermal plume dynamics on Europa: Implications for chaos formation. J. Geophys. Res. 109. DOI: 10.1029/2003JE002073.

Goodman, J. C. and Lenferink, E., 2012. Numerical simulations of marine hydrothermal plumes for Europa and other icy worlds. Icarus 221, 970–983.

Grasset, O., et al., 2013. JUpiter ICy moons Explorer (JUICE): An ESA mission to orbit Ganymede and to characterise the Jupiter system. Planet. Space Sci. 78. 1–21.

Greeley, R., et al., 1998. Europa: Initial Galileo geological observations. Icarus 135, 4–24.

Greeley, R., et al., 2000. Geologic mapping of Europa. J. Geophys. Res. 105, 22559–22578.

Greenberg, R., Hoppa, G. V., Tufts, B. R., Geissler, P., Riley, J., and Kadel, S., 1999. Chaos on Europa. Icarus 141, 263–286.

Greenberg, R., Geissler, P., Hoppa, G., and Tufts, B. R., 2002. Tidal-tectonic processes and their implications for the character of Europa's icy crust. Rev. of Geophys. 40, 1.1–1.33.

Greenberg, R., Leake, M. A., Hoppa, G. V., and Tufts, B. R., 2003. Pits and uplifts on Europa. Icarus 161, 102–126.

Hamilton, C. W., et al., 2013. Spatial distribution of volcanoes on Io: Implications for tidal heating and magma ascent. Earth Planet. Sci. Lett. 361, 272–286.

Han, L. and Showman, A. P., 2005. Thermo-compositional convection in Europa's icy shell with salinity. Geophys. Res. Lett. 32, doi:10.1029/2005GL023979

Han, L. and Showman, A. P., 2010. Coupled convection and tidal dissipation in Europa's ice shell. Icarus 207, 834–844.

Hand, K. P. and Carlson, R. W., 2015. Europa's surface color suggests an ocean rich with sodium chloride. Geophys. Res. Lett. 42, 3174–3178.

Hand, K. P., the Europa Clipper Project Science Team, and the Project Engineering Team, 2017. Report of the Europa Lander Science Definition Team. Posted February 2017. https://europa.nasa.gov/resources/58/europa-lander-study-2016-report/

Hartman, B., and Domingue, D., 1998. Scattering of Light by Individual Particles and the Implications for Models of Planetary Sciences. Icarus 131, 421–448.

Head, J. W., et al., 1999. Europa: Recent Geological History from Galileo Observations. Lunar Planet. Sci. XXX, Abstract #1404.

Head, J. W., Pappalardo, R. T., 1999. Brine mobilization during lithospheric heating on Europa: Implications for formation of chaos terrain, lenticula texture, and color variations. J. Geophy. Res. 104, 27143–27155.

Helfenstein, P. and Parmentier, E. M., 1985. Patterns of fracture and tidal stresses due to nonsynchronous rotation: Implications for fracturing on Europa. Icarus 61, 175–184.

Hoppa, G. V., Greenberg, R., Riley, J., and Tufts, B. R., 2001. Observational selection effects in Europa image data: Identification of chaotic terrain. Icarus 151, 181–189.

Hussman, H., Spohn, T., and Wieczerkowski, K., 2002. Thermal equilibrium states of Europa's ice shell: Implciations for internal ocean thickness and surface heat flow. Icarus 156, 143–151.

Jenness, J., 2011. Tools for Graphics and Shapes [Computer Software]. Version 2.1.85. Retrieved from: http://www.jennessent.com/arcgis/shapes_graphics.htm

Kattenhorn, S. and Prockter, L. M., 2014. Evidence for subduction in the ice shell of Europa. Nature Geoscience 7, 762–767.

Kargel, J. S., et al., 2000. Europa's crust and ocean: Origin, composition, and the prospects for life. Icarus 148, 226–265.

Kempf, S., et al., 2014. SUDA: A Dust Mass Spectrometer for Compositional Surface Mapping for a Mission to Europa. European Planet. Sci. Congress 9, Abstract #229.

Khurana, K. K., et al., 1998. Induced magnetic fields as evidence for subsurface oceans in Europa and Callisto. Nature 395, 777–780.

Kivelson, M. G., et al., 1999. Europa and Callisto: Induced or intrinsic fields in a periodically varying plasma environment. J. Geophys. Res. 104, 4609–4625.

Kivelson, M. G., et al., 2000. Galileo magnetometer measurements: A stronger case for a subsurface ocean at Europa. Science 289, 1340–1343.

Leonard, E. J., Patthoff, D. A., Senske, D., Collins, G. C., 2017. The First USGS Geologic Map of Europa. American Geophysical Union Fall Meeting 2017, Abstract #P33A-2862.

Leonard, E. J., Collins, G., Senske, D., Patthoff, D. A., 2018. The Global Geology of Europa: Units, their Distribution, and Implications for Formation Processes. COSPAR Sci. Assem. XLII, Abstract #B5.3-14-18.

Lowell, R. P., and DuBose, M., 2005. Hydrothermal systems on Europa. Geophys. Res. Lett. 32. DOI: 10.1029/2005GL022375

Lucchita, B. K. and Soderblom, L. A., 1982. The geology of Europa. In: Satellites of Jupiter. University of Arizona Press, Tucson, AZ, p. 521-555, 940, 941.

Manga M. and Wang, C.-Y., 2007. Pressurized oceans and the eruption of liquid water on Europa and Enceladus. Geophys. Res. Let., 34. doi:10.1029/2007GL029297

Manga, M. and Michaut, C., 2017. Formation of lenticulae on Europa by saucer-shaped sills. Icarus 286, 261–269.

Mather, K., 1947. Statistical analysis in biology. Interscience Publishers Inc. New York, NY.

McCord, T. B., et al., 1998a. Non-water-ice constituents in the surface material of the icy Galilean satellites from the Galileo near-infrared mapping spectrometer investigation. J. Geophys. Res. 103, 8603–8626.

McCord, T. B., et al,. 1998b. Salts on Europa's surface detected by Galileo's Near Infrared Mapping Spectrometer. Science 280, 1242–1245.

McCord, T. B., Teeter, G., Hansen, G. B., Sieger, M. T., Orlando, T. M., 2002. Brines exposed to Europa surface conditions. J. Geophys. Res. 107, DOI: 10.1029/2000JE001453

Michaut, C. and Manga, M., 2014. Domes, pits, and small chaos on Europa produced by water sills. J. Geophys. Res. 119, 550–573. DOI: 10.1002/2013JE004558.

Mitri, G. and Showman, A. P., 2008. A model for the temperature-dependence of tidal dissipation in convection plumes on icy satellites: Implications for Europa and Enceladus. Icarus 195, 758–764.

Neish, C. D., Prockter, L. M., and Patterson, G. W., 2012. Observational constraints on the identification and distribution of chaotic terrain on icy satellites. Icarus 221, 72–79.

National Research Council of the National Academies, 2011. Vision and Voyages for Planetary Science in the Decade 2013–2022. https://solarsystem.nasa.gov/resources/598/vision-and-voyages-for-planetary-science-in-the-decade-2013-2022/

Nimmo, F. and Giese, B., 2005. Thermal and topographic tests of Europa chaos formation models from Galileo E15 observations. Icarus 177, 327–340.

Neveu, M. and Desch, S. J., 2015. Geochemistry, thermal evolution, and cryovolcanism on Ceres with a muddy ice mantle. Geophys. Res. Lett. 42, 10,197–10,206. DOI: 10.1002/2015GL066375.

Noviello, J. L., Rhoden, A. R., Torrano, Z. A., and Manga, M., 2017. The Inferred Distribution of Liquid Watter in Europa's Ice Shell: Implications for the Europa Lander Mission. American Geophys. Un. XCIX, Abstract #232681.

Noviello, J. L., and Rhoden, A. R., 2018. Identification of Microfeatures on Europa in Low-resolution Galileo images: Successes, Limits, and Implications for Europa's Exploration. Lunar Planet. Sci. XLIX, Abstract #2707.

Noviello, J. L., Torrano, Z. A., Rhoden, A. R., and Singer, K. N. Mapping Europa's microfeatures in regional mosaics: new constraints on formation models. Icarus, vol. 329, 101–123.

O'Brien, D. P., Geissler, P., and Greenberg, R., 2002. A melt-through model for chaos formation on Europa. Icarus 156, 152–161.

Oeter, H., Kipfstuhl, J., Determann, J., Miller, H., Wagenbach, D., Minikin, A., and Graft, W. Evidence for basal marine ice in the Filchner-Ronne ice shelf. Nature 358, 399–401.

Ojakangas, G. W., and Stevenson, D. J., 1989. Thermal state of an ice shell on Europa. Icarus 81, 220–241.

Pappalardo, R. T., et al., 1998. Geological evidence for solid-state convection in Europa's ice shell. Nature 391, 365–368.

Pappalardo, R. T., et al., 1999. Does Europa have a subsurface ocean? Evaluation of the geological evidence. J. Geophys. Res. 104. 24015–25055.

Pappalardo, R. T., Barr, A. C., 2004. The origin of domes on Europa: The role of thermally induced compositional diapirism. Geophys. Res. Lett. 31, doi: 10.1029/2003GL019202.

Pappalardo, R. T., et al., 2013. Science Potential from a Europa Lander. Astrobiology 13, 740–773. DOI: 10.1089/ast.2013.1003

Pappalardo, R. T. et al., 2016. Science Objectives and Capabilities of the NASA Europa mission. Lunar Planet. Sci. XLVII, Abstract #3058.

Pappalardo, R. T., et al., 2017. The Europa Clipper Mission: Exploring the Habitability of a Unique Icy World. European Planet. Sci. Congress 11, Abstract #304.

Phillips, C. B. and Pappalardo, R. T. 2014. Europa Clipper Mission Concept: Exploring Jupiter's Ocean Moon. Eos 95, No. 20, pgs. 165–167.

Prockter, L. M., et al., 1999. Europa: Stratigraphy and geological history of the anti-Jovian region from Galileo E14 solid-state imaging data. J. Geophys. Res. 104, 16,531–16,540.

Prockter, L. M. and Schenk, P., 2005. Origin and evolution of Castalia Macula, an anomalous young depression on Europa. Icarus 177, 305–326.

Quick, L. C. and Marsh, B. D., 2016. Heat transfer of ascending cryomagma on Europa. J. Volcanology and Geotherm. Res. 319, 66–77.

Quick, L. C., Glaze, L. S., Baloga, S. M., 2017. Cryovolcanic emplacement of domes on Europa. Icarus 284, 477–488.

Rathbun, J. A., Musser, G. S., Squyres, S. W., 1998. Ice diapirs on Europa: Implications for liquid water. Geophys. Res. Lett. 25, 4157–4160.

Rathbun, J. A., Rodriguez, N. J., and Spencer, J. R., 2010. Galileo PPR observations of Europa: Hotspot detection limits and surface thermal properties. Icarus 210, 763–769.

Riley, J., Hoppa, G. V., Greenberg, R., Tufts, B. R., and Geissler, P., 2000. Distribution of chaotic terrain on Europa. J. Geophys. Res. 105, 22599–22615.

Roser, B. P. and Korsch, R. J., 1988. Provenance signatures of sandstone-mudstone suites determined using discriminant function analysis of major-element data. Chemical Geology 67, 119–139.

Ruesch, O., et al., 2016. Cryovolcanism on Ceres. Science 353, 1005–1013. DOI: 10.1126/science.aaf4286

Ruiz, J. and Tejero, R. Heat flow, lenticulae spacing, and possibility of convection in the ice shell of Europa. Icarus 162, 262–373.

Russell, E. E., et al., 1992. Galileo photopolarimeter/radiometer experiment. Space Sci. Rev. 60, 531–563.

Schenck, P. M., 2002. Thickness constraints on the icy shells of the Galilean satellites from a comparison of crater shapes. Nature 417, 419–421.

Schenk, P. M. and Pappalardo, R. T., 2004. Topographic variations in chaos on Europa: Implications for diapiric formation. Geophys. Res. Lett. 31, DOI: 10.1029/2004GL019978.

Schenck, P., Matsuyama, I., and Nimmo, F., 2008. True polar wander on Europa from global-scale small-circle depressions. Nature 453, 368–371.

Schmidt, B. E., Blankenship, D. D., Patterson, G. W., and Schenk, P. M., 2011. Active formation of ‘chaos terrain’ over shallow subsurface water on Europa. Nature 479, 502–505.

Schroeder, D. M., et al., 2016. Assessing the potential for passive radio sounding of Europa and Ganymede with RIME and REASON. Planet. Space Sci. 134, 52–60.

Seidelmann, P. K., et al., 2007. Report of the IAU/IAG Working Group on Cartographic Coordianates and Rotational Elements: 2006. Celestial Mechanics and Dynamic Astronomy 98, 155–180.

Shepard, M. K., and Helfenstein, P., 2007. A test of the Hapke photometric model. J. Geophys. Res. 112, DOI: 10.1029/2005JE002625.

Showman, A. P. and Han, L., 2004. Numerical simulations of convection in Europa's ice shell: Implications for surface features. J. Geophys. Res. 109, DOI: 10.1029/2003JE002103.

Showman, A. P. and Han, L., 2005. Effects of plasticity of convection in Europa's ice shell: Implications for surface features. Icarus 177, 425–437.

Singer, K. N., McKinnon, W. B., and Schenk, P. M., 2010. Pits, spots, uplifts, and small chaos regions on Europa: Evidence for diapiric upwelling from morphology and morphometry. Lunar Planet. Sci. XLI, Abstract #2195.

Singer, K. N., et al., 2016. Pluto's putative cryovolcanic constructs. Ann. Plant. Geologic Mappers Meeting, Abstract #7017.

Singer, K. N., McKinnon, W. B., and Schenk, P. M., 2019. Pits, Uplifts and Small Chaos Features on Europa: Evidence for Diapiric Upwelling from Morphology and Morphometry. In review to Icarus, submitted for publication.

Snyder, J. P., and Voxland, P. M., 1994. An Album of Map Projections. United States Geological Survey Professional Paper, 1453.

Soderlund, K. M., Schmidt, B. E., Wicht, J., and Blankenship, D. D., 2014. Ocean-driven heating of Europa's icy shell at low latitudes. Nature Geosci. 7, 16–19. DOI: 10.1038/NGEO02021.

Sotin, C., Head, J. W., Tobie, G., 2002. Europa: Tidal heating of upwelling thermal plumes and the origin of lenticulae and chaos melting. Geophys. Res. Lett. 29, DOI:0094-8276/02/2001GL013844.

Spencer, J. R., Tamppari, L. K., Martin, T. Z., Travis, L. D., 1999. Temperatures on Europa from Galileo PPR: Nighttime thermal anomalies. Science 284, 1514–1516.

Squyres, S. W., Reynolds, R. T., Cassen, P. M., Peale, S. J., 1983. Liquid water and active resurfacing on Europa. Nature 301, 225–226.

Spaun, N. A., Head, J. W., Collins, G. C., Prockter, L. M., and Pappalardo, R. T., 1998. Conamara Chaos region, Europa: Reconstruction of mobile polygonal ice blocks. Geophys. Res. Lett. 25, 4277–4280.

Spaun, N. A., Prockter, L. M., Pappalardo, R. T., Head, J. W., Collins, G. C., Antman, A., and Greeley, R., 1999. Spatial distribution of lenticulae and chaos on Europa. Lunar Planet. Sci. XXX, Abstract #1847.

Spaun, N. A., 2002. Chaos, lenticulae, and lineae on Europa: Implications for geological history, crustal thickness, and the presence of an ocean. Ph.D. thesis, Brown University, Providence, Rhode Island.

Spaun, N. A., Head, J. W., and Pappalardo, R. T., 2004. Europan chaos and lenticulae: A synthesis of size, spacing, and areal density analyses. Lunar Planet. Sci. XXXV, Abstract #1409.

Speyerer, E. J., Povilaitis, R. Z., Robinson, M. S., Thomas, P. C., and Wagner, R. V., 2016. Quantifying crater production and regolith overturn on the Moon with temporal imaging. Nature 548, 215–218.

Tabachnick, B. G. and Fidell, L. S., 2013. Discriminant Analysis. In: Using multivariate statistics, 6th ed., 377–438.

Thomson, R. E., and Delaney, J. R., 2001. Evidence for a weakly stratified Europan ocean sustrained by seafloor heat flux. J. Geophys. Res. 106, 12,335–12,365.

Tobie, G., Choblet, G., and Sotin, C., 2003. Tidally heated convection: Constraints on Europa's ice shell thickness. J. of Geophys. Res. 108. DOI: 10.1029/2003JE002099.

Tognetti, L., Rhoden, A., and Nelson, D., 2017. Investigating a link between large and small-scale chaos features on Europa. American Geophysical Union Fall Meeting 2017, Abstract #P43C-2904.

Torson, J.M., and Becker, K.J. (1997) ISIS - A Software Architecture for Processing Planetary Images. Lunar Planet. Sci. XXVIII, Houston, Texas, Abstract #1219.

Trumbo, S. K., Brown, M. E., and Butler, B. J., 2018. ALMA thermal observations of Europa. The Astro. Journal 156, 161–167.

Turtle, E. P., et al., 2016. The Europa Imaging System (EIS): High-resolution Imaging and Topography to Investigate Europa's Geology, Ice Shell, and Potential for Current Activity. Lunar Planet. Sci. XLVII, Houston, Texas, Abstract #1626.

U.S. Geological Survey, 2002, Controlled photomosaic map of Europa, Je15M CMN: U.S. Geological Survey Geologic Investigations Series I–2757, available at http://pubs.usgs.gov/imap/i2757/

Westlake, J. H., et al., 2016. The Plasma Instrument for Magnetic Sounding (PIMS) on The Europa Clipper Mission. American Astronomical Society, DPS meeting #48, id.123.27

Wren, P. F., 2018. Constraining the small binary asteroid population of the main belt using doublet craters on Ceres. MS Thesis, University of North Dakota, Grand Forks, North Dakota. 140 pp.

Zahnle, K., Schenk, P., Levison, H., and Dones, L., 2003. Cratering rates in the outer Solar System. Icarus 163, 263–289.

Zamora, C. A, Noviello, J. L., and Rhoden, A. R., 2019. Identification of Microfeatures on Europa's Surface in High-Resolution Images: Assessing the Completeness of Available Datasets. Lunar Planet. Sci. L, Houston, Texas, Abstract #2096.

APPENDIX A

COAUTHOR PERMISSION FOR INCLUDING PREVIOUSLY PUBLISHED WORK

The contents of Chapter 2 have been previously published in a manuscript to the journal Icarus, vol. 329, pages 101–123 under the title of: "Mapping Europa's microfeatures in regional mosaics: new constraints on formation models." The permissions of all coauthors—Z. A. Torrano, K. N. Singer, and A. R. Rhoden—are included in this Appendix. All coauthors have given their consent for that work to be repurposed here. The additional information about the custom MATLAB codes was not included in the published material and is only reported here (Appendix D).

The contents of other chapters have been given in abstracts but have not formally been published in any scientific journal. Content from Chapters 3 and 4 will be published in either one or two upcoming manuscript(s) about the limits of mapping microfeatures in low-resolution images and further results of the DFA tests. This publication will be supplemented by the results of mapping another area (E17RegMap01) in low-resolution images to provide contrast for the E15RegMap01 area.

Noviello, J. L., Rhoden, A. R. (*in preparation; to be submitted fall 2019*). Mapping microfeatures in low-resolution *Galileo* images. Likely submission to Icarus.

Noviello, J. L., Rhoden, A. R. (*in preparation; to be submitted fall/winter 2019*). Quantitative classification of microfeatures on Europa: Expanding geomorphic mapping to low-resolution images. Likely submission to Icarus or EPSL.

Finally, the contents of Chapter 5 will be submitted as a separate manuscript. This work will be supplemented by additional Monte Carlo analyses that will examine all microfeatures, as well as identify the probability of finding the degree of clustering within an area equal to the size of the E15RegMap01 area. Finally, this model will include modifications to the Manga and Michaut (2017) model to fit the updated

observations, especially those regarding the quantitative clustering measurements of all microfeatures.

This manuscript should include new numerical simulations that should further constrain the timeline of microfeature formation. Additionally, this would could expand on the idea that multiple microfeatures combine with each other on the surface to form larger chaos features by modeling and studying the combination of sills in the subsurface or by determining how closely sills can be spaced. Finally, it is important to determine the smallest sized microfeature that the sills model could produce, which leads to assumptions regarding the strength of different layers within the ice shell (i.e., whether or not a brittle upper layer could form and retain a sill).

Noviello, J. L., Rhoden, A. R., Manga, M., Michaut, C. (*in preparation; to be submitted spring 2020*). The spatial distribution of microfeatures on Europa: Implications for subsurface structure. Likely submission to J. Geophys. Res.

Jessica Noviello <jlnoviel@asu.edu>

Permission to use the Europa Mapping paper as a thesis chapter

Zachary Torrano <ztorrano@asu.edu> Mon, May 13, 2019 at 10:18 AM
To: Jessica Noviello <jlnoviel@asu.edu>

Permission granted!
[Quoted text hidden]
--
Zachary Torrano
Ph.D. Candidate
School of Earth and Space Exploration
Arizona State University
ztorrano@asu.edu

PermissionFrom_EuropaMapping_TorranoSigned.pdf
134K

The School of Earth and Space Exploration
Arizona State University
781 E. Terrace Mall, Rm. 795
Tempe, AZ 85287-6004

On Behalf of: Jessica L. Noviello

By signing below, I willingly give permission for Jessica L. Noviello to use the previously published work as a chapter in her dissertation, named here: Mapping Europa's microfeatures in regional mosaics: New constraints on formation models.

This paper was published in the journal *Icarus* (vol. 329, pp. 101–123) and is available digitally at the following link:
https://www.sciencedirect.com/science/article/pii/S0019103518306572?via%3Dihub

Print name: _____

Signed name: Zachary Torrano

Date: _____

Jessica Noviello <jlnoviel@asu.edu>

Permission to use the Europa Mapping paper as a thesis chapter

Kelsi Singer <kelsi.singer@gmail.com> Mon, May 20, 2019 at 11:50 AM
Reply-To: kelsi.singer@gmail.com
To: Jessica Noviello <jlnoviel@asu.edu>
Cc: Alyssa Rhoden <arhoden@asu.edu>

Hi Jessica,

Sorry I thought you could use the previous e-mail, but here is an official permission:

I, Kelsi Singer, approve the inclusion of previously published work in this dissertation.

Thanks,
~Kelsi

Kelsi N. Singer
Senior Research Scientist, SwRI Boulder, CO
Deputy Project Scientist and Co-I on New Horizons Mission
Office Phone: 303-226-5910 (in SwRI ext. 7258)

[Quoted text hidden]

Jessica Noviello <jlnoviel@asu.edu>

Permission to use the Europa Mapping paper as a thesis chapter

Alyssa Rhoden <arhoden@asu.edu> Fri, May 24, 2019 at 4:11 PM
Cc: Jessica Noviello <jlnoviel@asu.edu>

I approve of the inclusion of previously published work in this dissertation.

~Alyssa
[Quoted text hidden]

APPENDIX B

COMPLETE DETAILS OF IMAGES USED FOR REGMAP MAPPING

Appendix Table B-1: E15RegMap01 images used for mapping

Image ID	Incidence Angle	Emission Angle	Phase Angle	Pixel Resolution	Center Longitude (360 W)
1800r	80.77	27.42	62.79	231.58	229.16
1814r	80.77	27.42	62.79	231.58	228.01
1827r	80.00	32.49	62.91	231.69	226.62
1840r	79.63	38.82	63.04	232.12	225.86
1852r	79.87	46.48	63.17	232.97	224.88
1865r	81.15	55.96	63.29	234.39	222.08
1879r	74.47	24.29	63.10	228.46	220.47
1901r	74.47	24.29	63.10	228.46	218.62
1914	73.81	30.30	63.22	228.64	216.69

Appendix Table B-2: E15RegMap02 images used for mapping

Image ID	Incidence Angle	Emission Angle	Phase Angle	Pixel Resolution	Center Longitude (360 W)
4252r	21.76	81.75	232.23	232.30	77.40
4265r	28.22	75.09	233.49	233.58	84.41
4278r	26.16	81.60	233.79	233.87	77.88
4300r	32.07	74.87	235.09	235.19	85.38
4313r	31.74	81.57	235.59	235.69	78.68
4326r	37.10	74.72	236.93	237.06	86.17
4339r	38.31	81.45	237.68	237.80	79.03
4352r	43.34	74.58	239.09	239.26	87.69
4365r/4366r *	45.30	82.46	240.00	240.17	78.52
4378r	49.90	75.48	241.45	241.69	88.88
4401r	100.24	54.69	82.36	243.31	80.45
4413r	100.68	59.65	75.16	245.20	93.46
4426r	100.16	67.05	82.32	248.90	82.27
4439r	101.22	50.21	68.70	243.96	97.64

Appendix Table B-3: E17RegMap01 images used for mapping

Image ID	Incidence Angle	Emission Angle	Phase Angle	Pixel Resolution	Center Longitude (360 W)
4152r/4153r*	81.27	28.67	71.31	227.98	228.12
4165r/4166r*	81.28	22.37	71.23	226.75	227.81

4178r/4179r*	74.78	20.72	71.67	226.07	221.31
4200r/4201r*	75.35	14.20	71.56	225.06	222.15
4213r/4214*	75.49	8.54	71.51	224.25	222.03
4226r/4227r*	76.39	5.09	71.41	223.63	222.31
4253r/4254r*	76.41	7.16	71.38	222.65	221.58
4265r/4266r*	75.83	12.02	71.41	222.36	220.43
4278r/4279r*	74.85	17.69	71.50	222.23	218.26
4300r/4301r*	74.50	23.95	71.55	222.32	216.47
4313r/4314r*	74.23	31.07	71.63	222.62	213.92
4326r/4327r*	75.07	38.34	71.64	223.22	212.49
4340r	75.97	46.68	71.68	224.16	210.37
4500r[&]	77.91	25.78	100.15	202.63	222.21
4552r	80.73	17.37	70.63	212.45	227.47
4565r	81.17	13.24	70.54	211.66	227.68
4578r	81.51	11.23	70.48	211.05	227.65
4600r	81.37	11.60	70.47	210.56	227.03
4613r	81.00	14.34	70.49	210.21	226.01
4626r	80.40	18.66	70.55	210.01	224.73
4639r	79.82	23.77	70.61	209.99	223.20
4652r	79.09	29.64	70.71	210.17	221.08
4665r	80.16	36.44	70.67	210.61	220.65

& = taken on E19 orbit of the Galileo mission

Appendix Table B-4: E17RegMap02 images used for mapping

Image ID	Incidence Angle	Emission Angle	Phase Angle	Pixel Resolution	Center Longitude (360 W)
6752r	83.22	12.27	91.81	217.87	72.92
6778r	83.25	17.44	91.85	219.23	73.99
6800r	77.32	26.79	92.28	220.66	82.38
6813r	83.29	23.54	91.88	220.81	74.50
6826r/6827r*	77.24	33.11	92.32	222.50	84.05
6839r	83.29	30.32	91.92	222.63	75.51
6852r/6853r*	77.16	40.28	92.35	224.65	86.20
6865r	83.24	37.77	91.95	224.74	76.79
6878r/6879r*	76.95	48.79	92.39	227.24	90.46
6900r/1901r*	83.18	46.34	91.99	227.27	79.24
6913r/6914r*	76.67	59.42	92.42	230.55	97.61
7052r	83.01	56.85	92.20	235.09	85.00

* = these images were mosaicked together to create a complete image of the area

APPENDIX C

DETAILS REGARDING PHOTOMETRIC CORRECTIONS IN ISIS3

The two-term Henyey-Greenstein (2T-HG) photometric function was applied to each image, defined by the following function:

$$P(\alpha) = \frac{(1+c)}{2}\frac{1-b^2}{(1+2b\cos\alpha+b^2)^{\frac{3}{2}}} + \frac{(1-c)}{2}\frac{1-b^2}{(1-2b\cos\alpha+b^2)^{\frac{3}{2}}}$$

In this equation, α represents the phase angle of an image, b is the approximate widths of the two independent scattering lobes, and f is the partition coefficient. The values for the parameters named here are c = 0.113 for the leading hemisphere, c = 0.391 for the trailing hemisphere, b = -0.429 for the leading hemisphere, and b = -0.443 for the trailing hemisphere (Domingue et al., 1990). The differences between the parameters for the leading and trailing hemispheres are due to the increased amount of ionic bombardment present on the trailing hemisphere. Multiple studies (Hartman and Domingue, 1997; Shepard and Helfenstein, 2007) show that there is no improvement in the model fit between the 2T-HG function over the three-term Henyey-Greenstein (3T-HG) function when phase angles are <130°; hence, we opted for the simpler 2T-HG equation.

APPENDIX D

CUSTOM MATLAB CODES FOR IMAGE CORRECTION

These MATLAB codes were custom written to remove the linear shadow gradient present in the *Galileo* RegMap images. There are three codes that are run sequentially to remove the linear gradient. An example of a before and after image is shown in Figure D-1. Figures D-2 and D-3 shows that after the image is broken into eight or more strips, there is no improvement in the linear model that describes the shadow gradient; for this reason, 10 was determined as the appropriate number of strips to split the images into while correcting them with these codes.

All these codes do is remove the linear trend in the data (Appendix Figure D-4) while maintaining the residuals (Appendix Figure D-5), where the variations in normalized reflectances lie. The codes are provided after the images. A user guide for these codes is available upon request.

First, the code breaks the image down into strips according to an equal number of pixels. Next, the mean and standard deviation of the digital numbers (DNs) of each strip were calculated and plotted against the strip's center longitude. A simple linear model with a slope and y-intercept was created of the DNs vs. longitude. The difference between the model predicted maximum DN and the actual mean DN of that strip is the residual, δ (Figure D-5). This value of δ was applied to every DN in the strip to correct the values to maintain the variations in DNs across strips while correcting them to fluctuate around the same value and brighten the entire image to a uniform value (Appendix Figure D-5). The strips were then put back into a single image which could then be projected using the ISIS3 commands.

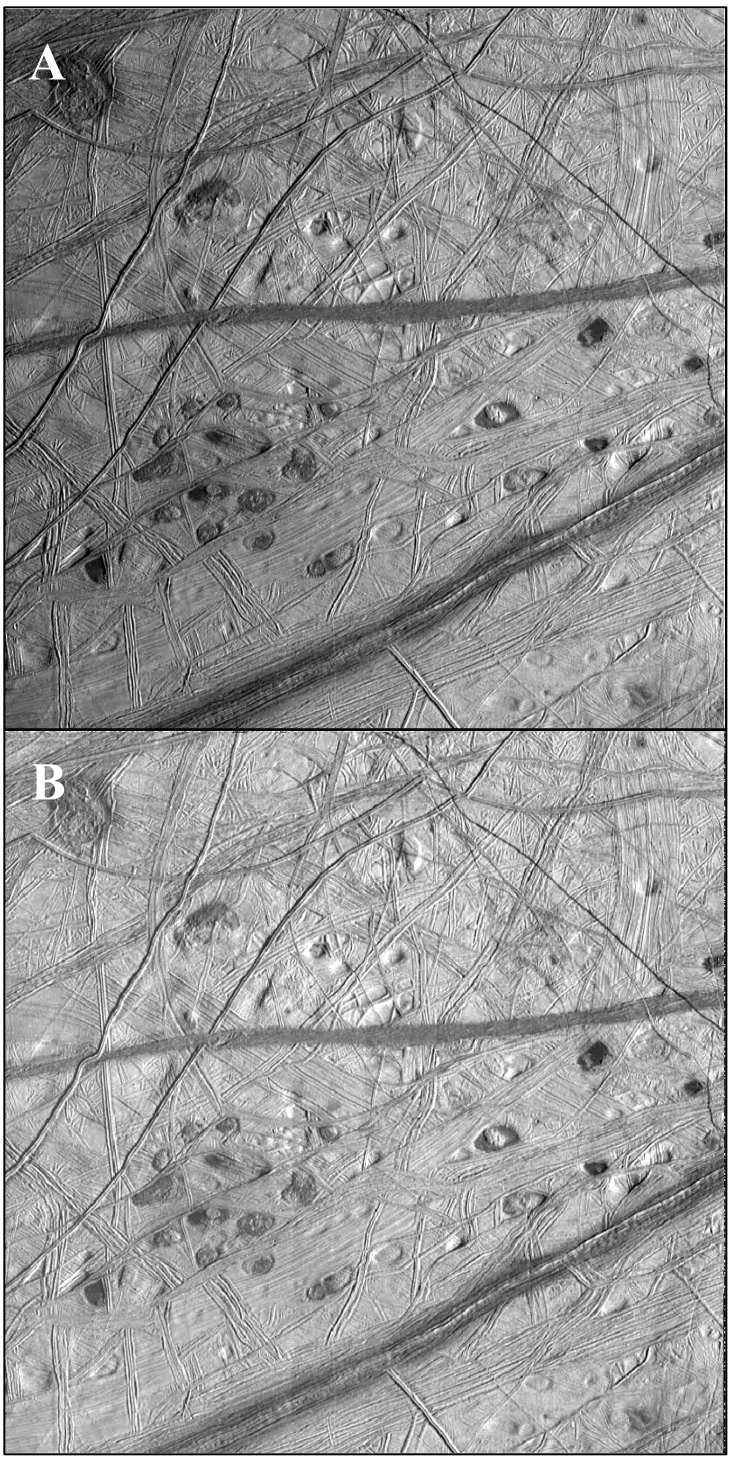

Appendix Figure D-1: Before and after MatLab code correction. A) Uncorrected *Galileo* image 1865r. B) MatLab corrected *Galileo* image 1865r.

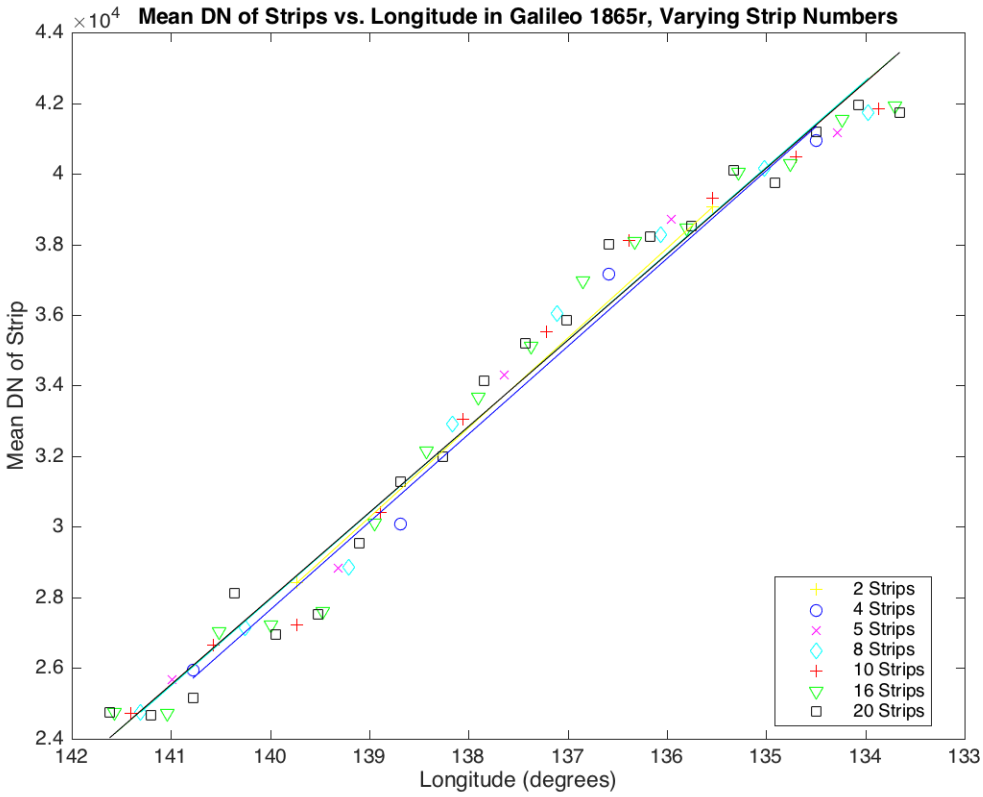

Appendix Figure D-2: The change in mean DN values of image strips vs. longitude in *Galileo* image 1865r under varying strip numbers. At small numbers of strips, the calculated linear slope is more variable, but stabilizes after 8 strips.

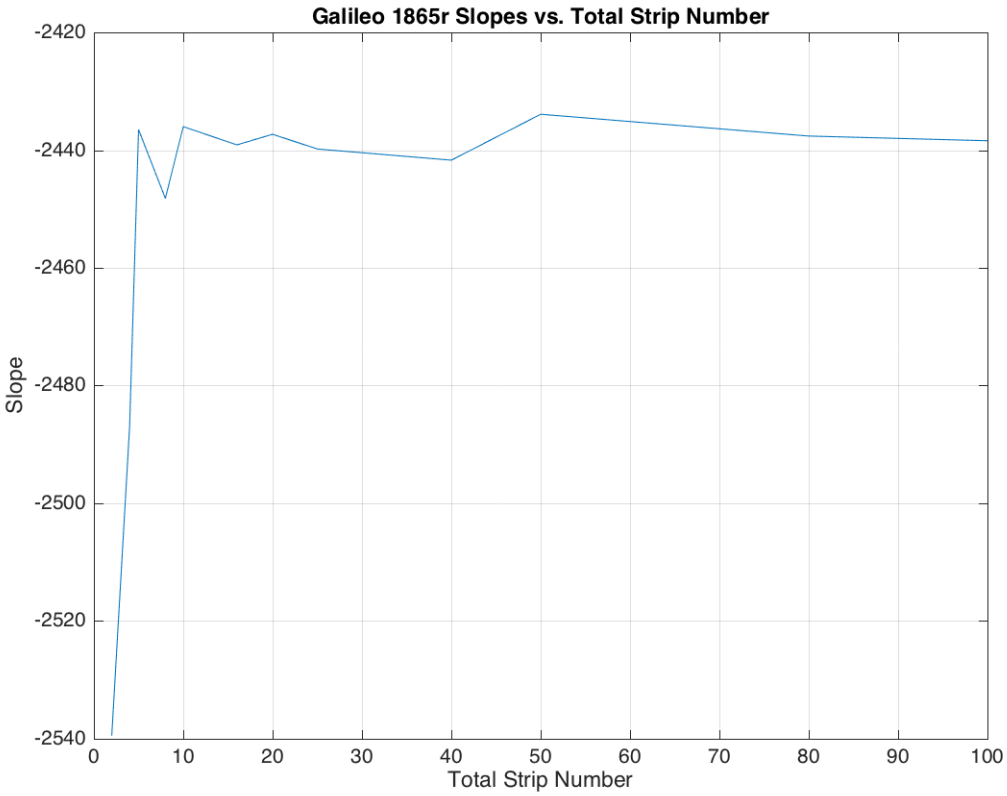

Appendix Figure D-3: The value of the calculated linear slope as a function of number of image strips. Note that after eight strips, the value of the slope plateaus and the value of the slope does not significantly change. Hence, any value of strip numbers above eight is appropriate for use.

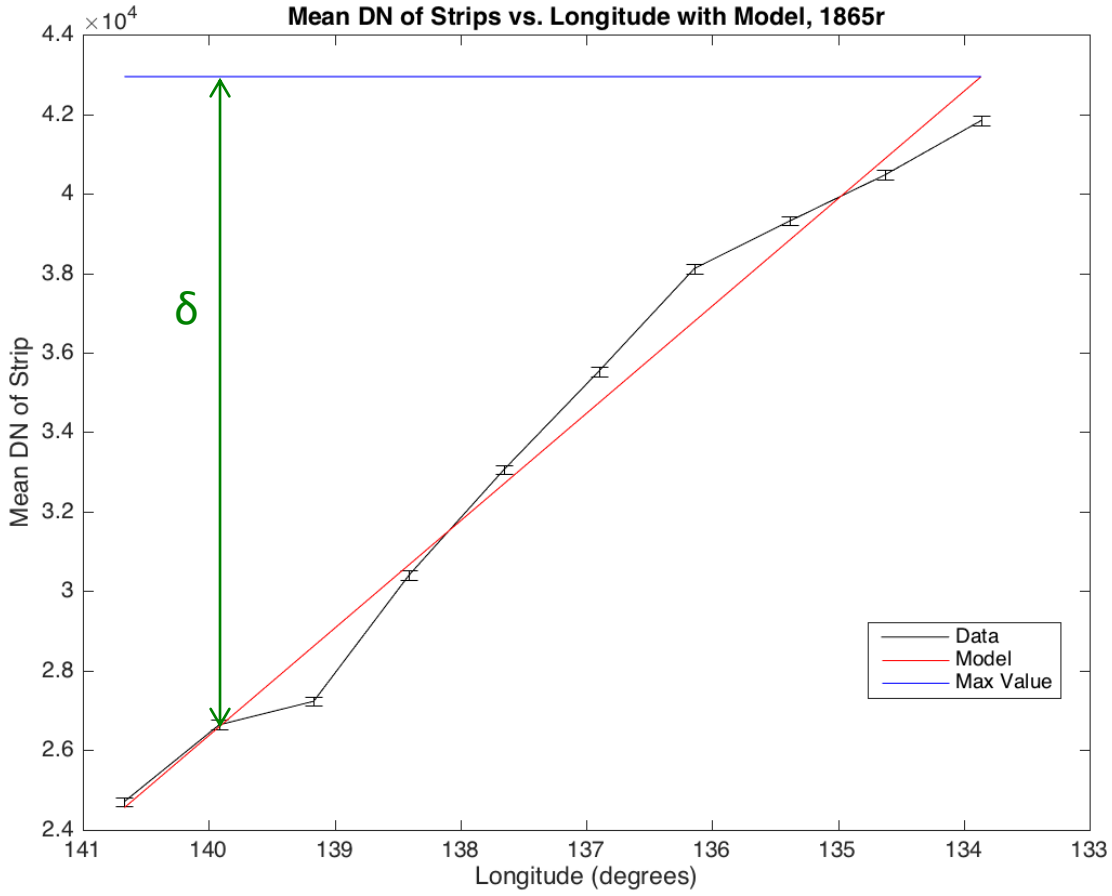

Appendix Figure D-4: Graphical representation of the MatLab code's function. The model (red line) is fit to the data (black line), and then the maximum DN value of the brightest strip (blue line) is used to correct the other strips according to a calculated δ value (green). This preserves the variation between the strip DNs but brightens the image to a uniform value for easy comparison between features in different locations in the image.

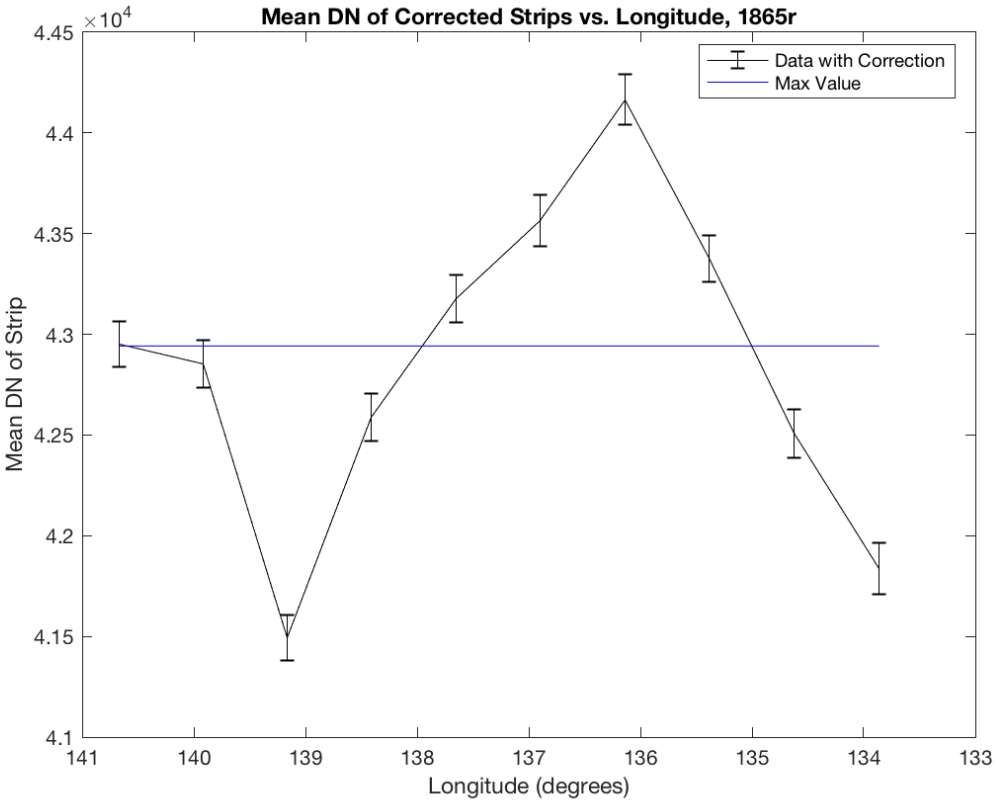

Appendix Figure D-5: The preservation of variation after MatLab correction for *Galileo* image 1865r. The blue line represents the maximum value as predicted by the model (red line) seen in Figure D-4; note that the data varies above and below the line, but the horizontality of the blue line shows that the linear gradient has been removed.

StripTest.m

```
%I_start=imread('1865r.png'); %import the test image; this is if .png
files are used (turns out, unlikely)

%This part sets up the binary file for analysis
row=800;  col=800;
fid=fopen('1865r_calIF.raw','r');
img=fread(fid, [col row],'uint16=>uint16');
I_start=img';
%fclose('1865r.raw');
imshow(I_start);

%I=imrotate(I_start,180);%rotates image to how it appears in Europa
basemap
%(only used for E15RegMap01 images, as E15RegMap02 doesn't need it)
%I=I_start; %only for images that need not be rotated to align in
Europa
%basemap.
%Assumption is that darker strips will be on the left side of the
image.
imshow(I)
title('Galileo image 1865r')
xlabel('Longitude')
ylabel('Latitude')

%Divide the image into strips
[r,c,p]= size(I);%r-rows,c-columns,p-planes
%I(I==0) = NaN; Might as well NaN everything before the strips are made

% 1865r_mean=zeros(size(I)); %make an array to put the elements that
aren't equal to zero
%
% for element in I
%     if element~=0;
%

figure();
%suptitle('Galileo 1865r in Strips')
% suplabel('Latitidue','y')
% suplabel('Longitude')
A=I(:,1:c/10,1);
subplot(1,10,1);
%subplot(1,2,1);
% n = sum(x~=0); This was the internet fix, but it only returned the
% columns without 0s, which is not what I wanted. I am disappointed.
Will
% seek additional advice from people who know better.
% n(n==0) = NaN;
% q = sum(x) ./ n;
imshow(A);
mean1865r_A=mean(A(:));
std1865r_A=std2(A(:));
```

```
B=I(:,c/10+1:c/10+80,1);
subplot(1,10,2);
%subplot(1,2,1);
imshow(B);
mean1865r_B=mean(B(:));
std1865r_B=std2(B(:));

C=I(:,c/10+81:c/10+160,1);
subplot(1,10,3);
%subplot(1,2,1);
imshow(C);
mean1865r_C=mean(C(:));
std1865r_C=std2(C(:));

D=I(:,c/10+161:c/10+240,1);
subplot(1,10,4);
%subplot(1,2,1);
imshow(D);
mean1865r_D=mean(D(:));
std1865r_D=std2(D(:));

E=I(:,c/10+241:c/10+320,1);
subplot(1,10,5);
%subplot(1,2,1);
imshow(E);
mean1865r_E=mean(E(:));
std1865r_E=std2(E(:));

F=I(:,c/10+321:c/10+400,1);
subplot(1,10,6);
%subplot(1,2,1);
imshow(F);
mean1865r_F=mean(F(:));
std1865r_F=std2(F(:));

G=I(:,c/10+401:c/10+480,1);
subplot(1,10,7);
%subplot(1,2,1);
imshow(G);
mean1865r_G=mean(G(:));
std1865r_G=std2(G(:));

H=I(:,c/10+481:c/10+560,1);
subplot(1,10,8);
%subplot(1,2,1);
imshow(H);
mean1865r_H=mean(H(:));
std1865r_H=std2(H(:));

J=I(:,c/10+561:c/10+640,1);
subplot(1,10,9);
%subplot(1,2,1);
imshow(J);
mean1865r_J=mean(J(:));
std1865r_J=std2(J(:));
```

```
K=I(:,c/10+641:c/10+720,1);
subplot(1,10,10);
%subplot(1,2,1);
imshow(K);
mean1865r_K=mean(K(:));
std1865r_K=std2(K(:));

%COLORBAR TIME

%Divide the image into strips
[r,c,p]= size(I);%r-rows,c-columns,p-planes, don't always need this

figure();
subplot(1,10,1);
imagesc(A,[min(round(mean1865r_A - std1865r_A)), max(round(mean1865r_A
+ std1865r_A))]); colorbar

subplot(1,10,2);
imagesc(B,[min(round(mean1865r_B - std1865r_B)), max(round(mean1865r_B
+ std1865r_B))]); colorbar

subplot(1,10,3);
imagesc(C,[min(round(mean1865r_C - std1865r_C)), max(round(mean1865r_C
+ std1865r_C))]); colorbar

subplot(1,10,4);
imagesc(D,[min(round(mean1865r_D - std1865r_D)), max(round(mean1865r_D
+ std1865r_D))]); colorbar

subplot(1,10,5);
imagesc(E,[min(round(mean1865r_E - std1865r_E)), max(round(mean1865r_E
+ std1865r_E))]); colorbar

subplot(1,10,6);
imagesc(F,[min(round(mean1865r_F - std1865r_F)), max(round(mean1865r_F
+ std1865r_F))]); colorbar

subplot(1,10,7);
imagesc(G,[min(round(mean1865r_G - std1865r_G)), max(round(mean1865r_G
+ std1865r_G))]); colorbar

subplot(1,10,8);
imagesc(H,[min(round(mean1865r_H - std1865r_H)), max(round(mean1865r_H
+ std1865r_H))]); colorbar

subplot(1,10,9);
imagesc(J,[min(round(mean1865r_J - std1865r_J)), max(round(mean1865r_J
+ std1865r_J))]); colorbar

subplot(1,10,10);
imagesc(K,[min(round(mean1865r_K - std1865r_K)), max(round(mean1865r_K
+ std1865r_K))]); colorbar
```

```
%close all
```

Variable.m

```
%Script to take the means and standard deviations out of the workspace
and
%into a usuable format for the normalized reflectance graph
%The longitude must be manually entered by the user in column 1

Image1865r=zeros(10,4);

%Longitude must be answered manually. Best to save this information in
an Excel
%document so it can be entered in again easily.

%put all the means into a column
Image1865r(1,2)=mean1865r_A;
Image1865r(2,2)=mean1865r_B;
Image1865r(3,2)=mean1865r_C;
Image1865r(4,2)=mean1865r_D;
Image1865r(5,2)=mean1865r_E;
Image1865r(6,2)=mean1865r_F;
Image1865r(7,2)=mean1865r_G;
Image1865r(8,2)=mean1865r_H;
Image1865r(9,2)=mean1865r_J;
Image1865r(10,2)=mean1865r_K;

%put all the standard deviations into a column
Image1865r(1,3)=std1865r_A;
Image1865r(2,3)=std1865r_B;
Image1865r(3,3)=std1865r_C;
Image1865r(4,3)=std1865r_D;
Image1865r(5,3)=std1865r_E;
Image1865r(6,3)=std1865r_F;
Image1865r(7,3)=std1865r_G;
Image1865r(8,3)=std1865r_H;
Image1865r(9,3)=std1865r_J;
Image1865r(10,3)=std1865r_K;

%calculate the error
error=Image1865r(:,3)./(800*40)^(1/2);
Image1865r(:,4)=error;
```

Plotting.m

```
%Will linearly correct the Galileo images, assuming brightness going
from left
%to right within the image.

%Plotting the norm refl. data vs. longitude
imshow(I)
title('Galileo image 1865r')
xlabel('Longitude')
```

```
ylabel('Latitude')

longitude=Image1865r(:,1);
norm_refl=Image1865r(:,2);
std_dev=Image1865r(:,3);
error=Image1865r(:,4);

figure()
%plot(flip(longitude),norm_refl)
plot(longitude,norm_refl,'k')
title('Mean DN of Strips vs. Longitude');
set(gca,'Xdir','reverse')
xlabel('Longitude (degrees)');
ylabel('Mean DN of Strip');
saveas(gcf,'ImageData1865.png')
x=Image1865r(:,1);
y=Image1865r(:,2);
%b1=x\y; %Just to get the simple slope, not best practice
%The \ operator performs a least-squares regression.
%calculate y intercept by padding x with a column of 1s and using the
LSR operator
X = [ones(length(x),1) x];
b = X\y;

model=X*b;
y_int=b(1);
m=b(2);
%plot(longitude,model,'r-')

%calculate R^2 yourself
Rsq = 1 - sum((y - model).^2)/sum((y - mean(y)).^2);

% 95% confidence interval
figure()
errorbar(longitude,norm_refl,2.*error,'k')
title('Mean DN of Strips vs. Longitude, 1865r');
set(gca,'Xdir','reverse')
xlabel('Longitude (degrees)');
ylabel('Mean DN of Strip');
%scatter(x,y);
hold on
plot(longitude,model,'r-')
legend('data','model','Location','best');
saveas(gcf,'ImageDataModel1865.png')

%text(141,160,'model = -11.653*x + 1727.2')
%text(141,155,'R^2 =')

%Time to normalize the images
Image1865r(:,5)=zeros; %create a new column in the image variable for
predicted values
Image1865r(:,5)=y_int+(x.*m);
%create a new column for the residuals
Image1865r(:,6)=zeros;
Image1865r(:,6)=Image1865r(:,5)-Image1865r(:,2); %anomalies
```

```
%Figure out what the max is and then add the differences into a new
column
Image1865r(:,7)=zeros;
%max model value
max_value=Image1865r(10,1)*m+y_int;
%calculate the model's residual from the max
Image1865r(:,7)=max_value-Image1865r(:,5);
%Show the max vs. the model vs. the data
figure()
errorbar(x,y,2.*error,'k')
set(gca,'Xdir','reverse')
title('Mean DN of Strips vs. Longitude with Model, 1865r');
xlabel('Longitude (degrees)');
ylabel('Mean DN of Strip');
hold on
plot(x,model,'r-')
%make a column to call x1, for the reference line
Image1865r(:,8)=ones;
x1=Image1865r(:,8);
max_line=Image1865r(:,8).*max_value;
plot(x,max_line,'b')
legend('Data','Model','Max Value','Location','best');
saveas(gcf,'ImageDataModelFit1865.png')

%apply the image corrections to the strip matrices
CorA=A+Image1865r(1,7);
CorB=B+Image1865r(2,7);
CorC=C+Image1865r(3,7);
CorD=D+Image1865r(4,7);
CorE=E+Image1865r(5,7);
CorF=F+Image1865r(6,7);
CorG=G+Image1865r(7,7);
CorH=H+Image1865r(8,7);
CorJ=J+Image1865r(9,7);
CorK=K+Image1865r(10,7);

%now the MosaicM script is used to put the strips back together into a
%single image of size(800,800,1).
Corrected = uint16(zeros(size(I)));
Corrected(:,1:80,1)=CorA;
Corrected(:,81:160,1)=CorB;
Corrected(:,161:240,1)=CorC;
Corrected(:,241:320,1)=CorD;
Corrected(:,321:400,1)=CorE;
Corrected(:,401:480,1)=CorF;
Corrected(:,481:560,1)=CorG;
Corrected(:,561:640,1)=CorH;
Corrected(:,641:720,1)=CorJ;
Corrected(:,721:800,1)=CorK;

Corrected_1865r16=Corrected(:,:,1);

% %Ensure the anomalies are preserved by one last graph
 %only corrections
Image1865r(:,9)=zeros;
```

```
Image1865r(:,10)=zeros;
%means
Image1865r(1,9)=mean(CorA(:));
Image1865r(2,9)=mean(CorB(:));
Image1865r(3,9)=mean(CorC(:));
Image1865r(4,9)=mean(CorD(:));
Image1865r(5,9)=mean(CorE(:));
Image1865r(6,9)=mean(CorF(:));
Image1865r(7,9)=mean(CorG(:));
Image1865r(8,9)=mean(CorH(:));
Image1865r(9,9)=mean(CorJ(:));
Image1865r(10,9)=mean(CorK(:));

%std deviations (for completeness)
Image1865r(1,10)=std2(CorA(:));
Image1865r(2,10)=std2(CorB(:));
Image1865r(3,10)=std2(CorC(:));
Image1865r(4,10)=std2(CorD(:));
Image1865r(5,10)=std2(CorE(:));
Image1865r(6,10)=std2(CorF(:));
Image1865r(7,10)=std2(CorG(:));
Image1865r(8,10)=std2(CorH(:));
Image1865r(9,10)=std2(CorJ(:));
Image1865r(10,10)=std2(CorK(:));

figure()
corr_c=Image1865r(:,9);
errorbar(x,corr_c,2.*error,'k-')
set(gca,'Xdir','reverse')
title('Mean DN of Corrected Strips vs. Longitude, 1865r');
xlabel('Longitude (degrees)');
ylabel('Mean DN of Strip');
hold on
%plot(x,corr_ac,'r-')
%make a column to call x1, for the reference line
plot(x,max_line,'b')
legend('Data with Correction','Max Value','Location','best');
saveas(gcf,'ImageSquiggle1865.png')

% %If you need it, make another variable so you can do imrotate(x,180)
figure()
imshow(Corrected_1865r16) %change file name here, but that's all.
Assuming you do each image individually.
title('Corrected Galileo image 1865r')
xlabel('Longitude')
ylabel('Latitude')
saveas(gcf,'CorrectedImage1865.png')

%Rotate array to get it back to "raw" appearance and save matrix as
image
I_fin=imrotate(Corrected_1865r16,180);
fid=fopen('1865r_corr.raw','w+');
cnt=fwrite(fid,I_fin','uint16');

fclose(fid);
```

```
%close all

reg1=fitlm(longitude,norm_refl);
save('Galileo1865r_test.mat')
%clear all
```

APPENDIX E

TABULAR RESULTS OF ALL DFA TESTS FOR ALL REGMAPS

	Diameter	Median	Std. Deviation	Ratio 1	Eigenvalue	Percent of Variance (%)	Canonical Correlation	Cross-validation success rate (%)
Chaos vs. Domes	0.240	0.671	x	-0.878	1.026	100	0.712	89.4
Chaos vs. Hybrids	-0.456	x	0.743	0.419	0.334	100	0.501	72.9
Chaos vs. Pits	-0.671	0.766	x	0.349	1.047	100	0.715	84.2
Chaos vs. Spots	0.920	0.109	x	-0.329	0.958	100	0.699	87.2
Domes vs. Hybrids	0.826	-0.704	x	x	0.473	0.567	100	73.9
Domes vs. Pits	0.657	0.663	x	x	0.046	100	0.210	77.9
Domes vs. Spots	x	1.000	x	x	0.518	100	0.584	75.0
Hybrids vs. Pits	-0.568	0.905	x	x	0.366	100	0.518	81.9
Spots vs. Pits	0.236	0.941	x	x	0.551	100	0.596	88.9

Appendix Table E-1: E15RegMap01 two group classification tests, standardized discriminant function coefficients.

	Group 1 n	Group 2 n	Base LOOCV (%)	New LOOCV (%)	Overall Accuracy (%)	Expected correct sorted by chance (%)	Sensitivity (%)	Specificity (%)
Chaos vs. Domes	68	33	86.5	89.4	92.1	56.4	79.4	94.3
Chaos vs. Hybrids	68	34	71.0	72.9	76.5	55.9	54.1	84.3
Chaos vs. Pits	68	119	91.1	84.2	86.6	53.5	89.2	78.6
Chaos vs. Spots	68	23	86.2	87.2	94.5	62.6	83.3	94.3
Domes vs. Hybrids	33	34	71.0	73.9	76.8	50.7	83.3	69.7
Domes vs. Pits	33	119	73.4	77.9	78.3	65.8	100.0	0.0
Domes vs. Spots	33	23	75.0	75.0	78.6	51.6	78.3	78.8
Hybrids vs. Pits	34	119	83.2	81.9	84.3	65.4	93.3	50.0
Spots vs. Pits	119	23	88.9	88.9	90.1	72.5	95.8	54.2

Appendix Table E-2: E15RegMap01 two group classification tests, descriptive numbers.

	Diameter	Median	Std. Deviation	Ratio 3	Eigenvalue	Percent of Variance (%)	Canonical Correlation	Cross-validation success rate (%)
Chaos vs. Domes	0.879	x	-0.542	0.083	0.755	100	0.656	86.6
Chaos vs. Hybrids	x	x	0.823	0.551	0.118	100	0.324	75.2
Chaos vs. Pits	0.944	-0.352	x	x	0.501	100	0.578	96.0
Domes vs. Hybrids	0.962	-0.241	x	x	0.566	100	0.601	68.5
Domes vs. Pits	No variables separated these groups sufficiently well							
Pits vs. Hybrids	0.927	-0.456	x	x	1.310	100	0.753	91.2

Appendix Table E-3: E15RegMap02 two group classification tests, standardized discriminant function coefficients.

	Group 1 n	Group 2 n	Base LOOCV (%)	New LOOCV (%)	Overall Accuracy (%)	Expected correct sorted by chance (%)	Sensitivity (%)	Specificity (%)
Chaos vs. Domes	89	30	87.4	86.6	86.6	62.2	60.0	95.5
Chaos vs. Hybrids	89	24	73.5	75.2	77.0	66.4	8.3	95.5
Chaos vs. Pits	89	10	96.0	96.0	97.0	81.8	70.0	100.0
Domes vs. Hybrids	30	24	72.2	68.5	70.4	50.0	58.3	80.0
Domes vs. Pits	No variables separated these groups sufficiently well							
Hybrids vs. Pits	24	10	88.2	91.2	91.2	58.8	80.0	95.8

Appendix Table E-4: E15RegMap02 two group classification tests, descriptive numbers

	Area	Diameter	Std. Deviation	Ratio 1	Eigenvalue	Canonical Correlation	Cross-validation success rate (%)
Chaos vs. Domes	-0.627	x	0.854	0.451	1.900	0.809	90.2
Chaos vs. Hybrids	0.844	x	-0.824	x	0.251	0.448	79.6
Chaos vs. Pits	x	-0.763	0.806	0.346	1.226	0.742	91.1
Domes vs. Hybrids	-0.437	x	0.660	0.768	0.936	0.695	82.5
Domes vs. Pits	No variables separated these groups sufficiently well						
Pits vs. Hybrids	-0.519	x	0.518	0.729	0.465	0.563	73.3

Appendix Table E-5: E17RegMap01 two group classification tests, standardized discriminant function coefficients. Spots are excluded from these tests because there were insufficient data points.

	Group 1 n	Group 2 n	Base LOOCV (%)	New LOOCV (%)	Overall Accuracy (%)	Expected correct sorted by chance (%)	Sensitivity (%)	Specificity (%)
Chaos vs. Domes	69	32	90.2	90.2	91.1	56.4	78.8	95.7
Chaos vs. Hybrids	69	22	76.3	79.6	81.3	63.7	36.4	95.7
Chaos vs. Pits	69	21	88.9	91.1	91.1	64.4	71.4	97.1
Domes vs. Hybrids	32	22	80.7	82.5	90.6	52.8	86.4	90.6
Domes vs. Pits	No variables separated these groups sufficiently well							
Hybrids vs. Pits	22	21	64.4	73.3	76.7	51.2	66.7	79.2

Appendix Table E-6: E17RegMap01 two group classification tests, descriptive numbers.

	Diameter	Std. Deviation	Median	Ratio 3	Eigenvalue	Canonical Correlation	Cross-validation success rate (%)
Chaos vs. Domes	-0.525	0.726	x	0.021	1.027	0.712	79.4
Chaos vs. Hybrids	x	0.959	x	0.083	0.738	0.652	78.3
Chaos vs. Pits	0.836	-0.722	-0.078	x	0.959	0.700	90.0
Domes vs. Hybrids	0.919	x	-0.408	x	0.407	0.538	71.0
Pits vs. Hybrids	0.952	x	-0.303	x	0.251	0.448	85.7
Chaos/Hybrids vs. Domes/Pits	0.949	x	-0.291	x	0.442	0.554	85.6

Appendix Table E-7: E17RegMap02 two group classification tests, standardized discriminant function coefficients. Spots are excluded from these tests because there were insufficient data points.

	Ratio 2	Aspect Ratio	Eigenvalue	Percent of Variance (%)	Canonical Correlation	Cross-validation success rate (%)
Domes vs. Pits	2.258	1.350	0.068	100	0.252	76.1

Appendix Table E-8: The unusual case of Domes vs. Pits in E17RegMap02, where variables that have never been significant before are now significant to separate between domes and pits.

	Group 1 n	Group 2 n	Base LOOCV (%)	New LOOCV (%)	Overall Accuracy (%)	Expected correct sorted by chance (%)	Sensitivity (%)	Specificity (%)
Chaos vs. Domes	13	21	76.5	79.4	85.3	52.9	85.7	84.6
Chaos vs. Hybrids	13	10	69.6	78.3	82.6	52.2	80.0	84.6
Chaos vs. Pits	13	67	90.0	90.0	90.0	72.5	97.0	53.8
Domes vs. Hybrids	21	10	58.1	71.0	74.2	54.8	50.0	85.7
Domes vs. Pits	21	67	68.2	76.1	76.1	63.6	100.0	0.0
Pits vs. Hybrids	67	10	88.3	85.7	85.7	77.9	20.0	95.5
Chaos/Hybrids vs. Domes/Pits	23	88	85.6	85.6	85.6	67.6	95.5	47.8

Appendix Figure E-9: E17RegMap02 two group classification tests, descriptive numbers

APPENDIX F

PYTHON CODE USED FOR MONTE CARLO CLUSTERING ANALYSES

EuropaPits_montecarlo_allofEuropa.py

```
import csv
import math
import numpy as np
import random
# import statistics
# import scipy.stats as st

# ********************************************************************
# * Function to compute distance between two lat/lon points on Europa
# ********************************************************************
def separation( lon1, lat1, lon2, lat2 ):
   radius = 1561       # Europa mean radius in km
   lon1 = float(lon1)
   lat1 = float(lat1)
   lon2 = float(lon2)
   lat2 = float(lat2)

   diflat = math.radians(lat2-lat1)
   diflon = math.radians(lon2-lon1)

   a = math.sin(diflat/2) * math.sin(diflat/2) + \
      math.cos(math.radians(lat1)) * math.cos(math.radians(lat2)) * \
      math.sin(diflon/2) * math.sin(diflon/2)
   c = 2 * math.atan2(math.sqrt(a), math.sqrt(1-a))
   d = radius * c
   return d

# ********************************************************************
# * Function to compute the locations of random pits and bin them
# ********************************************************************

def sim_pits(log_bins):
   random_pits = []     # [ longitude, latitude ]
   pit_pairs = []   # [ pit1, lon1, lat1, pit2, lon2, lat2, separation ]

   # randomized pit locations
   num_pits = 7950
   minlon = 0.0
   maxlon = 360.0
   minlat = -60.0
   maxlat = 60.0

   for x in range(0, num_pits):
```

```
        randlon = random.uniform(minlon, maxlon)
        randlat = random.uniform(minlat, maxlat)
        row = [randlon, randlat]
        random_pits.append(row)

    num_rows = len(random_pits)

    binnable_sep = []
    return_vals = [] # mean, stdev
    # create pit pairs and separations
    for x in range (0, num_rows-1):
        shortest = 100000.0;
        for y in range (x+1, num_rows):
            n1 = x+1
            lon1 = random_pits[x][0]
            lat1 = random_pits[x][1]
            n2 = y+1
            lon2 = random_pits[y][0]
            lat2 = random_pits[y][1]
            sep = separation(lon1, lat1, lon2, lat2)
            # sep = int(sep)
            if sep < shortest:
                shortest = sep
        binnable_sep.append(shortest)
    # bin
#    binned = np.histogram(binnable_sep, bins=log_bins)
#    print ("Separations=",binnable_sep)
    sep_mean = np.mean(binnable_sep)
    sep_stdev = np.std(binnable_sep)
    sep_min = np.min(binnable_sep)
    sep_max = np.max(binnable_sep)
    return_vals.append(sep_mean)
    return_vals.append(sep_stdev)
    return_vals.append(sep_min)
    return_vals.append(sep_max)
#    print ("Mean=",sep_mean)
    return return_vals

# ************************** MAIN ************************************

out2 = open('Europapits_montecarlo_global.csv', 'w')
csvwriter = csv.writer(out2, delimiter=',')

# Create the bins
bins = np.logspace(0.0, 1.3, num=11)
```

```
csvwriter.writerow(["Run","Mean nearest neighbor distance", "StDev", "Min","Max"])

# Execute the simulation runs
number_runs = 100   # 1000
sim_runs = []
for i in range(0, number_runs):
    run_results = sim_pits(bins)
    sim_runs.append(run_results)
    csvwriter.writerow([i+1,run_results[0], run_results[1], run_results[2], run_results[3]])
```

EuropaPits_MonteCarlo_E15RM01.py

```
import csv
import math
import numpy as np
import random
# import statistics
# import scipy.stats as st

# ******************************************************************
# * Function to compute distance between two lat/lon points on Europa
# ******************************************************************
def separation( lon1, lat1, lon2, lat2 ):
   radius = 1561       # Europa mean radius in km
   lon1 = float(lon1)
   lat1 = float(lat1)
   lon2 = float(lon2)
   lat2 = float(lat2)

   diflat = math.radians(lat2-lat1)
   diflon = math.radians(lon2-lon1)

   a = math.sin(diflat/2) * math.sin(diflat/2) + \
      math.cos(math.radians(lat1)) * math.cos(math.radians(lat2)) * \
      math.sin(diflon/2) * math.sin(diflon/2)
   c = 2 * math.atan2(math.sqrt(a), math.sqrt(1-a))
   d = radius * c
   return d

# ******************************************************************
# * Function to compute the locations of 119 random pits and bin them
# ******************************************************************

def sim_pits(log_bins):
   random_pits = []     # [ longitude, latitude ]
   pit_pairs = []   # [ pit1, lon1, lat1, pit2, lon2, lat2, separation ]

   # randomized pit locations
   num_pits = 119
   minlon = 127.0
   maxlon = 142.0
   minlat = 18.0
   maxlat = 60.0

   for x in range(0, num_pits):
```

```
        randlon = random.uniform(minlon, maxlon)
        randlat = random.uniform(minlat, maxlat)
        row = [randlon, randlat]
        random_pits.append(row)

    num_rows = len(random_pits)

    binnable_sep = []
    return_vals = [] # mean, stdev
    # create pit pairs and separations
    for x in range (0, num_rows-1):
        shortest = 100000.0;
        for y in range (x+1, num_rows):
            n1 = x+1
            lon1 = random_pits[x][0]
            lat1 = random_pits[x][1]
            n2 = y+1
            lon2 = random_pits[y][0]
            lat2 = random_pits[y][1]
            sep = separation(lon1, lat1, lon2, lat2)
            # sep = int(sep)
            if sep < shortest:
                shortest = sep
        binnable_sep.append(shortest)
    # bin
#    binned = np.histogram(binnable_sep, bins=log_bins)
#    print ("Separations=",binnable_sep)
    sep_mean = np.mean(binnable_sep)
    sep_stdev = np.std(binnable_sep)
    sep_min = np.min(binnable_sep)
    sep_max = np.max(binnable_sep)
    return_vals.append(sep_mean)
    return_vals.append(sep_stdev)
    return_vals.append(sep_min)
    return_vals.append(sep_max)
#    print ("Mean=",sep_mean)
    return return_vals

# ************************** MAIN ************************************

out2 = open('Europapits_montecarlo_E15RM01.csv', 'w')
csvwriter = csv.writer(out2, delimiter=',')

# Create the bins
bins = np.logspace(0.0, 1.3, num=11)
```

```
csvwriter.writerow(["Run","Mean nearest neighbor distance", "StDev", "Min","Max"])

# Execute the simulation runs
number_runs = 1000   # 1000
sim_runs = []
for i in range(0, number_runs):
    run_results = sim_pits(bins)
    sim_runs.append(run_results)
    csvwriter.writerow([i+1,run_results[0], run_results[1], run_results[2], run_results[3]])
```

APPENDIX G

COPYRIGHT CONSIDERATIONS

All images used in this dissertation that were not created by the author are in the public domain (e.g., those available through the NASA Planetary Data System repository, published in an official NASA report, or used under the NASA Media Usage Guidelines). A list of these figures with their permissions are included below.

Figure 1-1

Descrption: The first spacecraft image of Europa taken by the *Pioneer 10* mission

Date: December 1973

Source: NASA

Copyright: Public domain, commons license

Figure 1-3

Descrption: Conamara Chaos as imaged by the *Galileo* mission

Date: February 1997

Source: NASA/JPL/University of Arizona

Copyright: Public domain

Figure 1-4

Descrption: Cross section of Europa's theorized ice shell, ocean, and ocean floor

Date: February 2017

Source: NASA report on the potential Europa Lander mission Pre-phase A report (Hand et al., 2017)

Author: Kevin P. Hand, JPL/NASA

Copyright: Public domain

Figure 1-5

Descrption: Thera Macula chaos on Europa

Date: November 16, 2011

Source: Paul Schenk/NASA

Copyright: Public domain

Figure 1-7

Description: Proposed instruments of the NASA *Europa Clipper* Flagship mission

Date: February 21, 2018

Source: NASA

Copyright: Public domain